Title
Sodium-Oxygen and Magnesium Metal Electrochemistry for Energy Storage Applications

Author
Nichols, Jessica Ellen

Publication Date
2018

Peer reviewed|Thesis/dissertation

Sodium-Oxygen and Magnesium Metal Electrochemistry for Energy Storage Applications

by

Jessica Ellen Nichols

A dissertation submitted in partial satisfaction of the

requirements for the degree of

Doctor of Philosophy

in

Chemical Engineering

in the

Graduate Division

of the

University of California, Berkeley

Committee in charge:

Professor Bryan D. McCloskey, Chair
Professor David B. Graves
Professor Mark Asta

Summer 2018

Sodium-Oxygen and Magnesium Metal Electrochemistry for Energy Storage Applications

Abstract

Sodium-Oxygen and Magnesium Metal Electrochemistry for Energy Storage Applications

by

Jessica Ellen Nichols

Doctor of Philosophy in Chemical Engineering

University of California, Berkeley

Professor Bryan D. McCloskey, Chair

A major challenge facing larger-scale and more widespread use of electric vehicles is the practical energy density of current battery technology. While significant improvements in lithium-ion technology have been achieved over the past few decades, a dramatic increase in battery capacities and decrease in cost will be required to increase market penetration for electric vehicles. This dissertation focuses on deepening the fundamental understanding of two systems, the sodium-oxygen battery and the magnesium metal electrochemistry, which are highly relevant in potential low-cost, high-energy-density battery applications.

Metal-air, or metal-O_2 batteries, have been intensely studied in recent decades due to their high theoretical energy densities. Of these, the nonaqueous sodium-oxygen (Na-O_2) battery offers improved stability, higher full-cycle efficiencies, and higher reversible capacities on both discharge and charge than similar nonaqueous metal-O_2 technologies. However, the Na-O_2 battery is afflicted by a "sudden death" during discharge at a capacity significantly lower than that predicted from complete conversion of the active materials. This sudden death effectively limits the achievable battery capacity on discharge, and has been previously linked to the electrochemistry occurring at the Na-O_2 cathode, where the sodium superoxide (NaO_2) discharge product is formed. I studied the dependence of this sudden death on the discharge current density under constant-pressure conditions, and found that at high current densities, the maximum capacity on discharge was limited by passivation of the cathode surface by insulating NaO_2 films. The capacity on discharge could be enhanced by decreasing the current density, and at low current densities the capacity was limited by pore clogging by large NaO_2 crystals.

I further examined the dependence of the sudden death on other operating and design parameters of the cell, and in particular explored the influence of O_2 pressure on the maximum discharge capacity. I observed that, at a given current density, there exists a transition between the mechanisms of sudden death with O_2 pressure, as a result of phenomena related to the deposition of the NaO_2 discharge product. Cells operated at low O_2 pressures were more susceptible to failure due to surface passivation by thin NaO_2 films; increasing the O_2 pressure at the same current density caused an increase in capacity and a transition to failure

due to pore clogging from NaO_2 crystal deposition. I correlated the transition between failure mechanisms with the spatial deposition of NaO_2 through the cathode, and associated it with a combination of electron and mass transfer effects.

The Na-O_2 battery is also subject to a sudden death during charge, which typically occurs at a capacity lower than the prior discharge capacity of the cell. I observed that the discharge and charge current densities both influenced the attainable charge capacity prior to sudden death. These variables were associated with changes in the deposition and oxidation of the NaO_2 discharge product. I proposed a charge mechanism consistent with my data, where a concerted surface oxidation mechanism and dissolution-oxidation mechanism contributed to the observed potentials. Sudden death on charge resulted when these two pathways could not support the applied current rate. Informed with this understanding of the Na-O_2 capacity limitations on charge, I explored the utility of both redox mediation and modified charging schemes in preventing sudden death and enhancing the achievable charge capacity. While I found the introduction of redox mediators typically did not result in a significant enhancement in cell performance, the use of a combined constant-current/constant-potential charging scheme led to improved charge capacity, reversibility, and overall performance.

A separate metal-O_2 chemistry, magnesium-O_2, represents one of several hypothetical magnesium (Mg) batteries. Mg metal offers numerous advantages over other related battery materials, including high abundance, light weight, low toxicity, and ease of safe handling. Both rechargeable and non-rechargeable Mg batteries are of interest for energy storage applications. However, a particular challenge affecting aqueous Mg batteries is the corrosion of Mg in the presence of water, which decreases the battery's efficiency. Unusually, this corrosion is exacerbated during oxidative polarization of the Mg metal, such as during discharge of a Mg-O_2 battery, where increasing currents result in increasing hydrogen (H_2) evolution. This phenomenon is referred to as the negative difference effect (NDE), and has been the subject of research for more than a century, with no consensus on its precise mechanisms and cause.

To investigate the NDE, I designed an electrochemical cell that enabled quantitative study of the NDE under various pH and electrolyte compositions. I quantified H_2 evolution due to the NDE in high pH conditions, and observed that in electrolytes of a sufficiently low bulk pH, the NDE disappears. This observation has significant implications with respect to the possible mechanism of the NDE.

To my parents,
without whom far more than this dissertation
would be existentially challenged.

Contents

List of Figures

List of Tables

Acknowledgments

I could not ask for better colleagues, collaborators, labmates, and friends than I have found in the members of the McCloskey Lab at U.C. Berkeley. Special thanks goes to Colin M. Burke and Sara E. Renfrew for their invaluable collaboration during our five years as graduate students and peers at U.C. Berkeley. We constructed the DEMS as a team during our early months in the lab, established lab procedures, practices, and culture, and shared the highs and lows of fundamental research on many occasions. Our collaboration has been a source of constant personal support and countless scientific insights. Particular thanks also goes to labmate and coauthor Dr. Kristian B. Knudsen, for his many helpful discussions regarding electrochemistry, impedance spectroscopy, experimental configurations, and instrument maintenance. I also thank Elyse A. Kedzie for her experimental collaboration on alternate charging schemes and redox mediators in Na-O_2 cells, and Keren Zhang for his collaboration on and assistance with experimental setups for studies of corrosion. Thanks are also owed to Rickey C. Terrell for measuring the viscosity of electrolytes used in my Mg corrosion work.

Particular gratitude is owed to my advisor, Professor Bryan D. McCloskey. His guidance and mentorship have seen me through the challenging transition from a wide-eyed junior graduate student to an experienced junior scientist. His unfailing patience and good humor have been the perfect compliment to his brilliant scientific insights, his willingness to answer any and all questions, and his earnest engagement in every peer-to-peer scientific discussion in which we engaged. I will always be grateful for his knowledge, expertise, and guidance, and know that his work with me has left an enduring mark upon me and my career.

I also thank my home institutions, the Department of Chemical & Biomolecular Engineering at University of California, Berkeley, and the Energy Storage & Distributed Resources Division at the Lawrence Berkeley National Laboratory. Finally, I gratefully acknowledge Alan Luntz and Venkat Viswanathan for valuable discussion regarding the discharge and charge mechanism of Na-O_2 cells.

Last, but certainly not least, are the friends and family who helped every step of the way, especially Hannah Reese, Brian Perea, and Margaret Hwang.

The material concerning Na-O_2 batteries and Mg corrosion is based upon work supported by the National Science Foundation Graduate Research Fellowship Program under Grant No. DGE-1106400 and the National Science Foundation under Grant No. CBET-1604927. Work in Chapter 4, particularly the contributions of co-author Kristian B. Knudsen, was additionally supported by the NASA Ames Research Center under contract #NNX16AR82A. Any opinion, findings, and conclusions or recommendations expressed in this material are those of the author and do not necessarily reflect the views of the National Science Foundation. The construction of the DEMS, development of titration protocol, and early study of Na-O_2 batteries, was supported in part by the Laboratory Directed Research and Development Program of Lawrence Berkeley National Laboratory under U.S. Department of Energy Contract No. DE-AC02-05CH11231.

Chapter 1

Introduction

1.1 Research in Rechargeable Battery Technology

Since their commercialization in the 1990s, Li-ion batteries have become the most important energy-storage technology for mobile applications, especially for electric vehicles and portable electronic devices.[3,4] Advances continue to be made in Li-ion technology, with dramatic improvements to processing efficiency, electrolyte performance, and cathode material optimization.[3,5] While research efforts over the past two decades have lead to significant increases in Li-ion power density (i.e., the battery's ability to quickly charge or discharge), improvements to both the achievable volumetric and gravimetric energy densities (i.e., the amount of energy stored for a given volume or mass of material, respectively) have been relatively small.[5] Indeed, the practical energy densities of Li-ion batteries are approaching their attainable limits.[6,7]

As a result, an ongoing focus in rechargeable battery research is the identification of new materials and chemistries that could enable higher energy densities and increased power densities while lowering processing and material costs compared to present Li-ion technology.[3,8–11] These "beyond Li-ion" technologies could potentially offer the dramatic increase in capacity required to increase market penetration of electric vehicles and the dramatic decrease in cost that may enable large-scale and widespread applications.[3,4] Improvements in rechargeable batteries would also be welcomed for other technologies, including both portable electronics and grid storage.[9]

One promising class of beyond Li-ion chemistries is the metal-air or metal-O_2 battery, where the active material of the cathode is replaced with a porous support on which O_2 is reduced.[12] Researchers in the field sometimes use the terms metal-air and metal-O_2 interchangeably, though metal-air is often taken to imply an atmospheric O_2 source and a

battery that "breathes," as opposed to a dedicated O_2 reservoir. The fundamental promise of metal-air batteries is that of higher gravimetric energy densities, due to the inherently lightweight nature of one or more of the active materials (i.e., O_2 gas) as compared to the transition metal oxides common in metal-ion batteries.[12] Indeed, a metal-air battery that utilizes O_2 drawn from the air might have an enormous weight advantage, since the active cathode material need not be carried around with the device being powered.[13] Many such systems may also be inherently lower-cost depending on the materials involved.[3,8,13] Of the various metal-air batteries proposed, only one has been successfully commercialized: the primary (non-rechargeable) Zn-air battery, which employs an alkaline aqueous electrolyte.[12] Secondary (rechargeable) Zn-air batteries remain an active field of research, as are metal-air batteries utilizing Li, Na, Mg, and Al.

The general operating principle of a metal-air battery is the use of a lightweight, porous material as the cathode, on which O_2 is reduced to a solid species on discharge and, in the case of secondary batteries, oxidized reversibly to O_2 on charge.[12] Many proposed designs also utilize lightweight metal anodes (e.g., Li, Na, Mg, or Al) to further reduce the mass of material required in the battery; these metals are oxidized on discharge and their metal ions are reduced to their metal state on charge. The metal-air chemistry introduces challenges that are often unlike those in the research of other battery systems. Foremost among them is the fact that electrochemical measurements alone are inadequate to assess the performance and rechargeability of metal-air batteries. The quantity of O_2 consumed on discharge and the efficiency of its conversion into a corresponding metal-oxide species is an essential figure of merit in assessing the performance of the cell for both primary and secondary battery chemistries.[9] These values may be obtained using combinations of gas, chemical, and materials analysis techniques.[14] Furthermore, quantifying O_2 evolution on charge from the reverse reaction is equally essential, due to the likelihood of parasitic side reactions in the cell. In some metal-air batteries, these reactions are known to occur at potentials similar to the charging potential of the cell.[9] Assessing a battery's performance in this respect requires quantitative gas analysis because electrochemical evidence alone is frequently misleading.[15–18] Likewise, in the event of gas-producing side reactions or corrosion at the anode, characterization of the gases present in a cell's headspace on discharge or charge clarifies the extent to which these reactions may be occurring for a given cell configuration.[19] The ratio between O_2 consumed on discharge and produced on charge serves as an excellent indication of a cell's rechargeability, and in a perfectly rechargeable battery this ratio is equal to 1.[9]

1.2 The Nonaqueous Li-O_2 and Na-O_2 Battery Chemistries

Of all the beyond Li-ion chemistries, the nonaqueous aprotic Li-O_2 battery offers the highest theoretical energy density (3456 Wh kg^{-1} Li_2O_2).[20] In Li-O_2 batteries employing a suitably stable electrolyte and a porous, conductive cathode, the dominant reversible cell chemistry

has been demonstrated to be the reduction of O_2 to Li_2O_2 via a two-electron process on discharge, with the reverse oxidation of Li_2O_2 on charge,[8,9,15,21,22]

$$2Li^+ + O_{2(g)} + 2e^- \rightleftharpoons Li_2O_{2(s)} \qquad E^0 = 2.96\ V \text{ vs. } Li/Li^+ \tag{1.1}$$

Both the production and oxidation of Li_2O_2 lead to significant challenges. These include the instability of battery components in the presence of Li_2O_2 and its reaction intermediates, as well as limitations on rechargeability, capacity, and efficiency.[14,15,23–28]

A similar battery system, the nonaqueous aprotic Na-O_2 battery, offers potential advantages over analogous Li-O_2 systems, including improved stability and full-cycle efficiency.[11,29–31] Despite its lower theoretical specific energy (1605 Wh kg^{-1} Na_2O_2 or 1105 Wh kg^{-1} NaO_2), sodium's natural abundance and lower cost make large-scale implementation economically attractive.[8,13,32,33] The product analogous to the Li-O_2 system has been reported:[11,34–36]

$$2Na^+ + O_{2(g)} + 2e^- \rightleftharpoons Na_2O_{2(s)} \qquad E^0 = 2.33\ V \text{ vs. } Na/Na^+ \tag{1.2}$$

This two-electron formation of Na_2O_2 is thermodynamically preferred, but its production and oxidation are associated with many of the same challenges as Li_2O_2 production and oxidation in Li-O_2 technology.[35–38] Furthermore, it has been widely accepted that in Na-O_2 batteries employing an electrolyte with a suitably stable, nonaqueous solvent, the dominant cell chemistry is instead the one-electron reduction of O_2 to NaO_2,[29,39–46]

$$Na^+ + O_{2(g)} + e^- \rightleftharpoons NaO_{2(s)} \qquad E^0 = 2.27\ V \text{ vs. } Na/Na^+ \tag{1.3}$$

Multiple explanations for the differences in electrochemistry between the Li and Na systems have been proposed, including kinetic, catalytic, or nucleation effects, and subtle differences in electrolyte chemistry, cell configuration, trace contaminants, and cathode selection.[8,35,36,38,41,42,47,48] Regardless, cells operating with an NaO_2 discharge product have been widely reported to exhibit lower overpotentials, particularly on charge, improved stability, higher full-cycle efficiencies, and higher capacities as compared to those of their Li-O_2 and two-electron Na-O_2 counterparts.[35,36,38,49,50] Subsequent studies have shown that Na-O_2 batteries producing NaO_2 can be highly sensitive to operating conditions and contaminants, leading to changes in cell capacity, discharge product morphology, efficiency, and rechargeability.[1,2,38,40,41,45,47,49–54] Additional stability concerns exist surrounding the solubility of NaO_2 in the battery electrolyte and its reactivity to other cell components, and numerous research efforts into these challenges are underway.[45,46,53,54]

1.3 The Na-O_2 Sudden Death Phenomena

Typical laboratory Na-O_2 cells are fed with an excess of O_2, such that discharge could theoretically proceed until all Na metal at the anode is consumed.[40] However, Na-O_2 cells have been widely observed to undergo a "sudden death" during discharge at a capacity significantly

lower than that predicted from complete Na metal conversion.[8,39,40,44] Furthermore, sudden death is also observed in cells fed with a limited O_2 supply prior to the consumption of all O_2 available.[1,40] This sudden death is a precipitous decrease in potential that signifies the end of discharge, and is reminiscent of similar behaviors observed in Li-O_2 batteries.[55]

The Na-O_2 sudden death on discharge has been observed to occur due to the deposition of solid NaO_2 on the cathode surface. As NaO_2 deposits, it could either passivate the electrode surface (due to its electronically insulative nature) or clog the pores of the cathode.[1,2,51,56] Early studies of room-temperature Na-O_2 cells demonstrated successful discharge in mixtures of N_2 and O_2 of varying composition, including with O_2 partial pressures near those of ambient air.[40] However, the achievable galvanostatic discharge capacity prior to sudden death was observed to depend significantly on the partial pressure of O_2 provided to the cell, even though the O_2 supply was never completely consumed.[40] Other reports indicated that O_2 pressures may influence the nucleation and growth rates of NaO_2.[47] Since these early studies, the influence of pressure effects in Na-O_2 cells has been largely neglected. In many studies, O_2 pressure is not monitored or reported, and the pressures utilized are significantly higher than those of ambient O_2, with the intent of providing an ideal discharge environment. The impact of O_2 pressure on discharge capacity and overpotentials and its relation to the causes of sudden death were not, prior to our reports, firmly established.

Unlike in Li-O_2 cells, a poorly understood sudden death is also observed on charge in Na-O_2 cells, where a precipitous increase in voltage occurs and does not necessarily correspond to the full discharge capacity.[1,8,38] Charge following sudden death is possible, but is accompanied by evolution of undesired side products not observed prior to sudden death.[1] Delaying the charge sudden death to allow a low charging voltage for the full capacity attained during discharge is desirable to improve energy efficiency and rechargeability. Several approaches have been proposed or demonstrated, including alternate charging schemes and the incorporation of redox mediators, but few have been studied in detail.[1,8] Further work improving the Na-O_2 capacity on charge is best informed by a clear mechanistic understanding of the charge sudden death phenomenon and quantitative study of the gases evolved to assess cell performance.

1.4 Mg Energy Storage and the Negative Difference Effect

Mg has received considerably less recent interest in research for energy storage applications, despite the fact that Mg offers numerous advantages, including its high abundance, light weight, low toxicity, and inherently safer properties compared to other active metals.[57,58] Because of these properties, design of a breathing Mg-O_2 battery is less complicated, especially for primary (non-rechargeable) batteries, and could be similar to the design of commercialized Zn-O_2 batteries. The present Mg-O_2 battery is generally a primary battery, with so-called "mechanical rechargeability" enabled by the physical replacement of the spent Mg anode and electrolyte.[59] Electrochemically rechargeable Mg batteries, including both nonaqueous and

aqueous battery chemistries, are an active area of research.[19,57,58] A particular challenge affecting aqueous Mg batteries is the corrosion of Mg in the presence of the electrolyte, which decreases the faradaic efficiency of the battery.[60] Parasitic corrosion reactions occurring on the Mg anode are given below for neutral, basic, and acidic electrolytes:

$$\text{Oxidation}: \quad \mathrm{Mg} \rightarrow \mathrm{Mg^{2+}} + 2\mathrm{e^-} \tag{1.4}$$

$$\text{Reduction (neutral, basic)}: \quad 2\mathrm{H_2O} + 2\mathrm{e^-} \rightarrow \mathrm{H_2} + 2\mathrm{OH^-} \tag{1.5}$$

$$\text{Reduction (acidic)}: \quad 2\mathrm{H^+} + 2\mathrm{e^-} \rightarrow \mathrm{H_2} \tag{1.6}$$

$$\text{Overall (neutral, basic)}: \quad \mathrm{Mg} + 2\mathrm{H_2O} \rightarrow \mathrm{H_2} + \mathrm{Mg(OH)_2} \tag{1.7}$$

$$\text{Overall (acidic)}: \quad \mathrm{Mg} + 2\mathrm{H^+} \rightarrow \mathrm{H_2} + \mathrm{Mg^{2+}} \tag{1.8}$$

For more than a century, attempts have been made to understand the fundamental corrosion reaction of Mg in aqueous electrolytes.[61–71] The standard reduction potential of Mg is -2.37 V vs. the standard hydrogen electrode (SHE). Because this value is highly negative, the evolution of H_2 from the Mg electrode at open-circuit potential is unsurprising, and a classical understanding of electrochemistry suggests that anodic (oxidative or positive) polarization of the electrode should result in a decreased corrosion rate.[72] However, the corrosion rate of Mg is observed to increase on the Mg anode during oxidation, a peculiar phenomenon referred to as the negative difference effect (NDE) and first reported by Beetz in 1866.[61,73–75] The NDE is particularly unfortunate for aqueous Mg battery applications, because it means that the corrosion rate increases during battery discharge, decreasing the capacity and efficiency of both primary and secondary battery configurations.[19,57]

While the NDE and other so-called difference effects are not unique to Mg,[64,76] unraveling the fundamental causes behind the Mg NDE has proven to be an ongoing challenge in corrosion and electrochemical research. Despite the long history of research into the subject, disagreement regarding the mechanism of the NDE continues, and numerous possible mechanisms have been put forward. One of the most controversial and divisive mechanisms was first introduced in 1954, and involves the oxidation of Mg as a short-lived, unipositive Mg^+ ion, which may be oxidized in turn to Mg^{2+} either chemically or electrochemically.[63,65] Later reports disputed the possibility of Mg dissolution as a unipositive ion, instead suggesting mechanisms associated with film disruption, disintegration of the anode, and "chunk" or spalling effects, where the corrosion of fine Mg particles expelled from the surface accounts for the NDE.[66,67] Other hypothesized mechanisms involve the formation of MgH_2,[77] the damage and repair of surface films,[78,79] and the influence of elemental impurities in the metal,[80,81] with each report offering fresh experimental and theoretical evidence for their assertions.[75] Reports as recent as the past few years continue to posit novel mechanisms for the NDE and dispute previously postulated mechanisms, including those in support of unipositive Mg dissolution[82–85] and those opposed to it.[71,73,86–90] No consensus has been reached.

Given the potential importance of the Mg anode in electrochemical energy storage, further quantitative investigation of the NDE and its fundamental underlying mechanisms could provide much-needed clarity in the field. In addition, while we acknowledge the NDE's

relevance in electrochemical energy storage as the primary motivation in this work, it is worthwhile to note that Mg and its alloys are also of interest in numerous other engineering applications due to their high specific strength, light weight, electromagnetic shielding, recyclability, and other valuable properties.[75] Areas of possible utility include structural, transportation, electronic, medical, and biodegradable applications.[91–94] Like pure Mg, Mg alloys are typically also subject to the NDE, and a fundamental understanding of its mechanism is therefore critical to enabling these applications and extending the lifetime and safety of Mg-containing products.[57,59,60,62,85,95,96]

1.5 Aims

The aims of this dissertation were therefore: (1) to characterize the Na-O_2 cell behavior and sudden death phenomena on discharge and charge; (2) to develop mechanisms consistent with this characterization; (3) to apply an understanding of these mechanisms in attempts to improve Na-O_2 cell capacity, particularly on charge; (4) to quantitatively examine the negative difference effect on Mg metal electrodes in various electrolyte environments; and (5) to apply these quantitative observations in a critical analysis of the negative difference effect mechanisms under consideration by the field at large.

Chapter 2 leads the reader through a detailed discussion of the experimental methods utilized in the subsequent chapters, including the instrumental configuration, cell design, and further *in situ* and *ex situ* characterizations. The rationale behind important design decisions and the chosen methods is also discussed.

Chapter 3 explores in detail the Na-O_2 sudden death phenomenon on discharge, particularly with respect to the influence of current density. The evidence presented suggests that sudden death on discharge was caused primarily by pore clogging at low current densities due to the formation of large NaO_2 crystals and by cathode passivation at high current densities due to the formation of conformal NaO_2 films. Because changes in current density were observed to result in different failure mechanisms, we considered it likely that the rate of reaction as compared to the rate of diffusion of reactants played a significant role in the mechanism of sudden death on discharge. This possibility is examined in Chapter 4, with particular emphasis on the influence of O_2 pressure on the mechanism of sudden death. It was observed that, at a given current density, there exists a transition between failure mechanisms with O_2 pressure as a result of phenomena related to the deposition of NaO_2.

In Chapter 5, the discussion shifts to the Na-O_2 sudden death phenomenon on charge. These current-density-dependent sudden deaths were observed to occur when the combined rates of NaO_2 film oxidation and the dissolution and reaction of NaO_2 crystals could no longer support the applied current density. Improving the achievable capacity on charge prior to sudden death might be achieved through several approaches; preliminary results from the study of two such approaches, alternate charging schemes and the introduction of redox mediators, are presented and discussed in Chapter 6.

Chapter 7 shifts the focus of the discussion to Mg corrosion and the negative difference effect (NDE), with a focus on its behavior in solutions containing Cl^-. This chapter leads the reader through quantitative evidence of the NDE, demonstrating that the quantities of Mg reacted, H_2 evolved, and charge passed through the system were consistent with a 1:1 ratio of corroded Mg to H_2 and a 2:1 ratio of oxidized Mg to e^-. Furthermore, the NDE was not observed to occur in solutions of sufficiently low pH. The implications of these observations with respect to proposed NDE mechanisms are discussed.

Chapter 2

Experimental Methods

As discussed in the previous chapter, quantitative study of the chemistry of metal-air electrochemical systems is essential in developing an understanding of the processes taking place in any given metal-air cell. In this chapter, we will discuss in detail the instrumental configuration used in the study of both the Na-O_2 and Mg metal electrochemical systems and the design and assembly of the electrochemical cells themselves. In addition, we will detail further *in situ* characterizations and *ex situ* techniques used in the quantitative and qualitative study of their electrochemistry.

2.1 Instrumental Configuration

A differential electrochemical mass spectrometer (DEMS) of a custom design was constructed for the work described in this study. A schematic diagram of the DEMS design is given in Figure 2.1 below. A design of this type was first reported by McCloskey et al.,[15] and the DEMS described herein comprises a later iteration of the same concept, developed with the permission of the original authors. The DEMS design depicted in Figure 2.1 is readily modifiable for analysis of evolved and consumed gases in electrochemical or chemical systems using pressure-based techniques alone by omission of the leak valve and other components specific to the mass spectrometer capabilities (designated "MS-specific components" as indicated in Figure 2.1). Though specialized for *in situ* analysis of evolved gases from a metal-air electrochemical cell, this DEMS design has also been applied in the quantification of evolved gases from chemical systems. The instrument may be operated in two general modes for quantification of evolved or consumed gases depending on the positions and settings of its valves: pressure-rise/pressure-decay or differential electrochemical mass spectrometry. The operation of the instrument will be discussed in greater detail in the following sections.

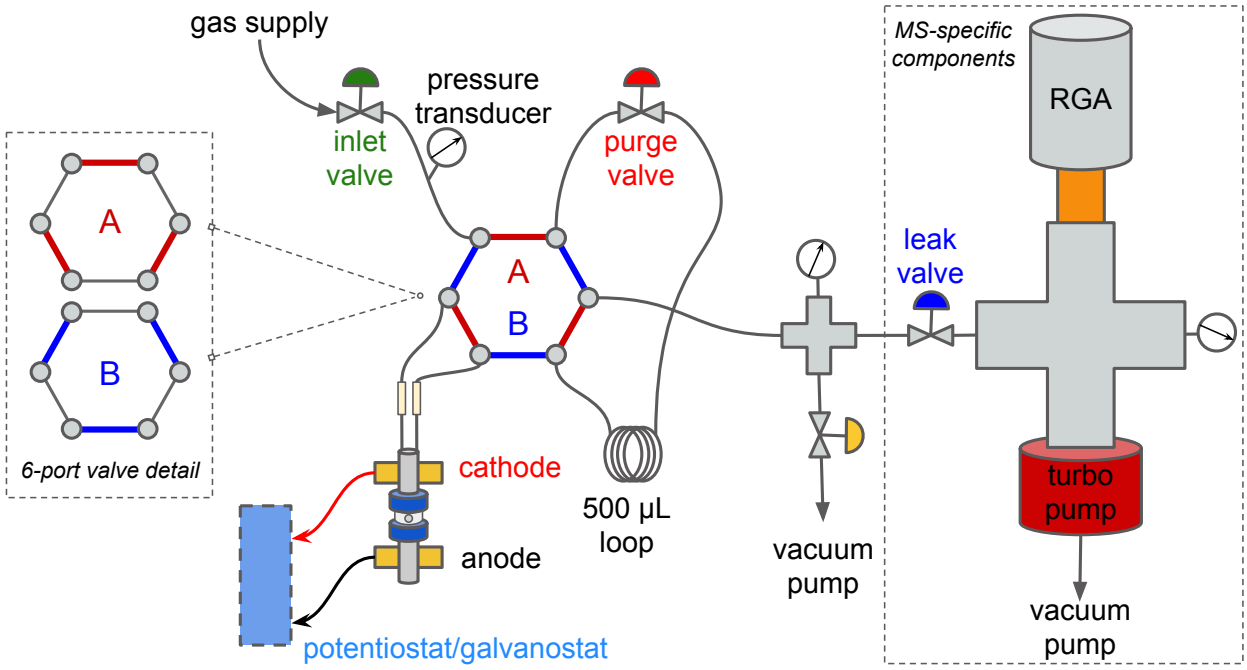

Figure 2.1: Schematic of the differential electrochemical mass spectrometer (DEMS) and pressure-rise/decay gas analysis setup. Components specific to the mass-spectrometer capability are indicated in the box on the right. A detail of the two possible positions of the six-port valve are given in the box on the left. An example of a Swagelok electrochemical cell as in Figure 2.2 is shown connected to the DEMS. A thermocouple (not pictured) was used to monitor cell operating temperatures.

Gas was supplied to the DEMS via copper and stainless steel tubing. An in-line purifier downstream of the gas cylinder regulator removed residual water from the gas prior to delivery to the DEMS. In all electrochemical experiments, either research-grade Ar (6.0 RS, Praxair) or O_2 (5.0 RS, Praxair) was employed. Additional gases (i.e., CO_2 and H_2, Praxair) were likewise connected to the DEMS system for use in calibration of the mass spectrometer. A manual selector valve (Valco) determined which gas was supplied to the system; all gas transfer lines downstream of the selector valve were 1/16-inch SS capillaries unless otherwise noted. Downstream of the selector valve, a needle valve ("inlet valve") controlled flow of gas to the cell. An in-line pressure transducer (Omega Engineering Inc.) monitored the pressure of the gas. In Figure 2.1, a Swagelok-type cell is shown in place on the instrument, with the cathode and anode connected by brass current collectors; see section 2.2 for an in-depth discussion of this and other cell designs. Other key components surrounding the cell included a 500 μL standard volume loop (Valco) and a needle valve ("purge valve") that controlled flow of gas to the downstream sample cross and dry scroll vacuum pump. A six-port valve controlled the direction of gas flow through the system and cell. It could be set to two positions, A or B, as shown in the detail in Figure 2.1 In position A, an attached cell's headspace was isolated, and the 500 μL loop was open to the sample cross and vacuum

pump. In position B, the cell could be charged with gas via the inlet valve, and gases from the cell could flow to the 500 μL loop; so long as the purge valve was closed the cell and its headspace were isolated from the vacuum pump.

The pressure in the central sample cross (KF25, stainless steel) was monitored by an in-line capacitance manometer (Baratron, MKS Instruments). A variable leak valve allowed a portion of the gases in the sample cross to enter the mass spectrometer chamber, pumped by an ultra-high vacuum turbomolecular pump (Pfeiffer Vacuum, HiPace 80, Asslar, Germany). The base pressure in the mass spectrometer chamber was $< 10^{-9}$ Torr whenever the instrument was not analyzing a sample, as measured by an ion gauge. The mass spectrometer is indicated in Figure 2.1 by the abbreviation RGA for "residual gas analyzer" (Stanford Research Systems, RGA200, Sunnyvale, CA).

To ensure the DEMS system was hermetically sealed, a dry capillary was affixed to the system in place of an electrochemical cell, and the setup was pumped down for several hours and He-leak checked in-place using the system's mass spectrometer. The sample cross, transfer lines, and cell headspace volumes were calibrated by attaching standard volume loops (between 25 and 2000 μL, Valco) to the DEMS instead of a cell. They were then charged with a known pressure of Ar with both the inlet and purge valves closed. This gas was then expanded into the evacuated sample cross and the pressure measured by the capacitance manometer. Performing this procedure with different standard volume loops allowed for the calculation of the sample cross volume and the volume of the transfer lines between the inlet and purge valves, excluding the volume of whatever cell or standard loop was connected to the instrument. The same volume expansion technique may then be performed using a dry cell (i.e., a cell assembled without electrolyte or reactive materials) to calculate the volume of the cell headspace. The estimated variance of the various volumes calculated in this manner was less than $\pm 2\%$ of the measured values.

Any cell or hermetically sealed vessel with 1/16-inch stainless steel capillaries could be connected to the DEMS via two plastic high-pressure PEEK fittings (Valco). Cells were connected to the DEMS while flowing the chosen analysis gas (O_2 or Ar) to prevent atmospheric contamination; this was accomplished by opening the inlet valve and placing the six-port valve in position B prior to cell connection. The purge valve was closed while the cell was attached to prevent evacuating the cell headspace and evaporating any electrolyte, since the sample cross and vacuum pumps were downstream of the purge valve. Once the cell was connected, the cell headspace was flushed by alternating the six-port valve position from A to B. When the six-port valve was switched to position A, the 500 μL loop was evacuated by the vacuum pump. Upon switching back to position B, gas flowed from the cell to the 500 μL loop, and fresh gas flowed from the gas supply through the open inlet valve to replenish it. Repeating this procedure multiple times replaced the cell headspace with the chosen analysis gas in a controlled manner, without exposing the cell to vacuum. Similarly, following discharge or charge of a cell under a given gas headspace, the cell could be isolated by setting the six-port valve to position A and the gas supply switched to another gas (e.g., switching from O_2 to Ar). With the purge valve closed and inlet valve open, the new gas was flushed through the cell in a controlled manner by repeatedly switching the

six-port valve from position A to B. Approximately 10 repetitions of the procedure above were found to achieve adequate replacement of the headspace gas with another gas for a cell of an approximately 400 μL headspace volume or less.

2.1.1 Pressure-rise/pressure-decay measurements and analysis

Measurement of the quantity (but not identity) of evolved gases was possible with the DEMS as depicted in Figure 2.1 without the use of any MS-specific components. This capability was limited to the detection of gases that behave as ideal gases at room temperature; however, the gases of greatest interest (O_2, CO_2, and H_2) all behave reasonably ideal at room temperature and were therefore possible to quantify using pressure-rise/pressure-decay (or pressure-rise/decay) techniques. In this mode of operation, following the controlled flushing of a cell with the desired headspace gas as described above, the six-port valve was placed in position B, and the inlet valve was closed. The in-line pressure transducer monitored the pressure in the cell's effective headspace, the volume of which was equivalent to the total volume of the transfer lines, the 500 μL loop, and the cell's individual headspace. Discharge, charge, or other electrochemical analyses (see section 2.3) were then performed; simultaneously, the pressure of the cell and temperature were recorded by a PC running Labview software (National Instruments, Austin, TX, USA). The pressure, temperature, and calibrated volume of the cell headspace were used to determine the quantity of gas consumed or evolved by the ideal gas law.

2.1.1.1 Constant-pressure operation

While pressure-rise/decay operation allowed for quantification of evolved or consumed gases, operation at an approximately constant pressure helped eliminate mass transfer and the concentration of dissolved gas, especially O_2, as variables in cell performance. Cells were operated under an approximately constant O_2 pressure by adjusting the pressure of the gas supply (i.e., the O_2 gas cylinder regulator), closing the purge valve as in pressure-rise/decay operation, and opening the inlet valve. The inlet valve was allowed to remain open during cell operation, and consumed gases are continuously replenished. In the absence of a control system, the pressure of the cell was observed to increase or decrease during discharge. The DEMS allowed for continuous monitoring of the cell pressure, and typical pressure variations during so-called constant-pressure operation were less than 0.04 atm total (30 Torr). Representative galvanostatic discharges with accompanying pressure data under these conditions are available in Figure 4.1. As with cells operated under pressure-rise/decay conditions, all cells were thoroughly leak-tested at an above-atmospheric pressure before the O_2 supply pressure was adjusted to the desired level. Constant-pressure galvanostatic discharges were performed under pure O_2 at a pressure in one of four approximate ranges: 0.3-0.5, 0.7-0.9, 1.3-1.5, and 2.0-2.1 atm O_2. For the sake of brevity, these are indicated

elsewhere in this text by representative pressures 0.4, 0.8, 1.4, and 2.0 atm.[a]

2.1.2 Differential electrochemical mass spectrometry

The differential electrochemical mass spectrometry (DEMS) mode of operation allowed for *in situ* measurement of the quantity and identity of gases evolved from a cell during electrochemical operation with isotopic sensitivity. DEMS measurements were performed during charge of Na-O_2 cells following discharge under either pressure-decay or constant-pressure operation in a pure O_2 atmosphere. When discharge was completed, the cell was isolated (the six-port valve was set to position A) and the gas supply was switched from O_2 to Ar. The cell headspace was flushed with Ar as described above, by switching the six-port valve repeatedly between positions A and B, finishing in position A prior to beginning instrument operation in DEMS mode.

While the instrument operated in DEMS mode, the inlet valve was opened and the purge valve closed. The six-port valve was set to position A to isolate the cell; the cell accumulated evolved gases during this time, and the valve leading from the sample cross to the vacuum pump was open to evacuate the sample cross of any residual gases. The six-port valve was then switched to position B, causing a sample of gas to flow to the 500 μL loop while fresh gas from the gas supply and open inlet valve replenished the gas in the cell. After a few seconds, the six-port valve was switched back to position A and the valve leading from the sample cross to the vacuum pump was closed. The gas sample accumulated in the 500 μL loop therefore expanded to fill the sample cross, resulting in a pressure of $\sim 6\text{x}10^{-3}$ atm. The variable leak valve was set to allow the gas in the sample cross to enter the turbo-pumped mass spectrometer chamber, increasing the pressure to $\sim 8\text{x}10^{-10}$ atm ($\sim 6\text{x}10^{-7}$ Torr), which was the optimum pressure for the sensitivity and dynamic range for the mass spectrometer. Mass spectral data were recorded by a PC running Labview software. All mass-to-ion ratios from 2 to 80 were recorded, skipping the most abundant mass of the carrier gas (e.g., 40 for Ar). Following acquisition of the mass spectrometer data, the valve from the sample cross to the vacuum pump was opened and the above procedure repeated.

The mass spectrometer was calibrated to determine the partial pressures of CO_2, H_2, and O_2 using mixtures of gas between 0.5% and 10% by volume of each of these gases in Ar. The estimated accuracy of the gas partial pressures and DEMS calibration was approximately $\pm$%5 of the measured values. The accuracy of the calibration and of the measured quantities of evolved gases were verified with multiple pressure-rise measurements of identically prepared cells.

[a] In our previous publications, the pressure here abbreviated as "1.4 atm" was referred to as "$\sim$1000 Torr"[51] or "1,000-1,100 Torr".[1] The abbreviated pressures discussed here will be used throughout this work.

2.2 Electrochemical Cell Design and Materials

The bulk of experimental work for this dissertation was performed in one of two different cell configurations: first, nonaqueous Na-O_2 cells in a two-electrode Swagelok-type assembly for study of the chemistry of the Na-O_2 cathode; and second, aqueous three-electrode Mg cells for study of Mg oxidation and corrosion.

2.2.1 Two-electrode Na-O_2 cells

A two-electrode cell design offers numerous advantages for the study of the Na-O_2 system. Two-electrode cells are relatively simple to assemble, requiring only an anode and cathode. This avoids the complexity of choosing an appropriate reference electrode and positioning said electrode within a hermetically sealed environment. Unfortunately, the absence of a reference electrode means that the potential of the working electrode must be measured relative to the counter electrode, and the overpotential contributions of the working and counter electrode are not easily distinguished.[72] As will be discussed later (see section 2.3.2), electrochemical impedance spectroscopy and an appropriate equivalent circuit model may be used to determine the overpotentials of the anode and cathode, and validated with appropriate three-electrode cells.[1,51] In most cases, changes in the overpotential of the cathode were responsible for changes in the total cell potential, and the overpotential of the anode remained relatively constant throughout cell discharge or charge. Given this, a two-electrode cell was appropriate for characterization of the Na-O_2 cathode electrochemistry.

2.2.1.1 Cell design

A custom-built cell of a modified Swagelok™ design was used to study capacity dependencies of the Na-O_2 system and to discharge cathodes for study by *ex situ* techniques including quantitative titrations (Section 2.4) and scanning electron microscopy (Section 2.5). This cell design has been previously described in detail, particularly as applied to the Li-O_2 electrochemistry.[15,30] Previous reports have also utilized this basic cell design for the study of Na-O_2, Li-ion, and Mg-O_2 cells.[19,30,97]A schematic of the cell as assembled for study of the Na-O_2 electrochemistry is given in Figure 2.2; substitution of different metal foils or anodes, separators, or cathode materials enables study of other chemistries using the same parts and similar assembly procedures.

The active cell components consisted of a metal foil anode (Na, in the case of Na-O_2), a separator (glass fiber), and a porous cathode (carbon paper). The metal anode was pressed onto a stainless steel (SS) alloy 20 anode current collector tip. A piece of SS mesh was placed over the carbon paper cathode to provide even distribution of current and protect the carbon paper from damage when the cell was pressed together. A SS ring on top of the SS mesh provided a gas reservoir directly over the cathode and electrical connection to the current collector. These cell components were assembled dry in an argon-filled glovebox (<0.1 ppm H_2O, <0.1 ppm O_2 content). The cell components were placed on the anode current collector

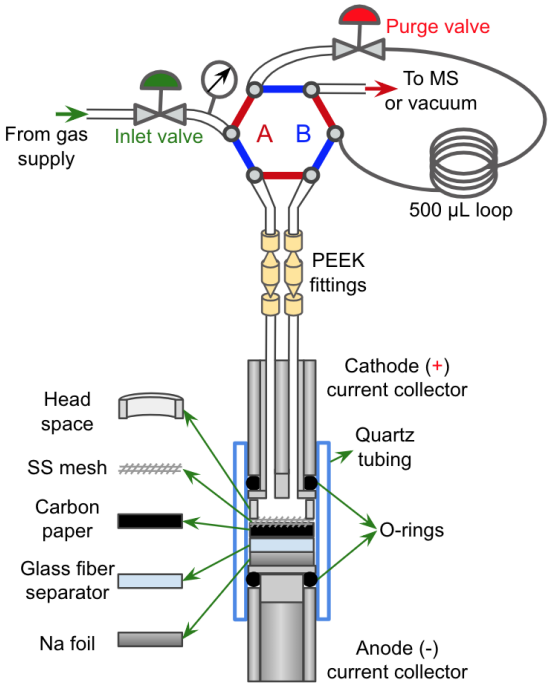

Figure 2.2: Schematic diagram of a Swagelok-type Na-O_2 cell. Substituting the Na foil and carbon paper cathode for alternate materials allows for testing of other cell configurations or chemistries. The cell is affixed to the gas analysis system depicted in Figure 2.1 by plastic high-pressure PEEK fittings; a simplified schematic of the instrumental configuration during cell operation is shown. Figure not to scale.

and contained within a 25-mm-long section of quartz tubing (13 mm interior diameter, 15 mm exterior diameter). Following assembly of the dry active components, the nonaqueous electrolyte was added to the assembled dry cell, so that the electrolyte completely flooded the separator and cathode. After addition of electrolyte, a SS alloy 20 cathode current collector was inserted into the quartz tubing. A hermetic seal between the cathode and anode current collectors and the quartz tubing was achieved using compressed Markez O-rings (Marco Rubber), which were selected due to their high resistance and thermal stability. The cathode current collector features two SS 1/16-inch capillaries silver-soldered into the cathode tip, for addition of reagent gases and removal of evolved gases. The cell is held together by a plastic Swagelok collar (not pictured in Figure 2.2). The headspace volume of the cell was determined using pressure-expansion techniques with a dry cell as discussed in section 2.1, and the active headspace volume of the cell used in pressure-rise/decay measurements was calculated by the dry cell volume minus the added electrolyte volume.

2.2.1.2 Materials and cell assembly

1,2-dimethoxyethane (DME, BASF) was used as received. Sodium trifluoromethanesulfonate (NaOTf, Sigma Aldrich) was dried in a vacuum oven at 80°C and <1 Torr for 12 hours prior to direct transfer to an argon-filled (<0.1 ppm H_2O, <0.1 ppm O_2 content) glovebox without exposure to atmosphere. Samples of NaOTf were titrated using hydrochloric acid (HCl, Sigma Aldrich) and determined to contain <0.7% base by mass, assuming NaOH is the major impurity. NaOTf was weighed by analytical balance inside an argon-filled glovebox, and DME measured by volumetric pipet to prepare electrolyte solutions of the desired concentration (0.1, 0.2, or 0.5 M). The prepared NaOTf in DME electrolytes had ∼100 ppm H_2O as determined by Karl Fischer titration. We note that prior reports indicate water impurities at this concentration have no significant influence on the chemistry of the cell.[45]

Na foil anodes were prepared by roll pressing a piece of Na (GalliumSource) between two pieces of Celgard 2500, then cut into 7/16-inch discs. 12 mm diameter AvCarb P50 carbon paper discs (Fuel Cell Earth) were used as cathodes; typical cells utilized one P50 disc, though some cells utilized two (see below, Section 2.2.1.3). All current densities and capacities reported in this work are normalized on the basis of their geometric cross-sectional area (1.13 cm^2). The cathodes were washed repeatedly in isopropanol and acetone before being dried first at 120°C in a vacuum oven, then at 200°C inside an argon-filled glovebox immediately prior to use. 12 mm cathodes were measured to be 6.2 ± 0.1 mg on average, and prior measurements of identically prepared cathode surface areas by BET estimate a surface area of 88 ± 3 cm^2/mg.[51] Whatman glass fiber filters (QM-A grade, VWR) were used as separators. The separators were cut into 1/2-inch discs and cleaned and dried following a similar procedure to the cathodes. 80 μL of electrolyte (NaOTf in DME) was used in cells where one P50 disc was employed as the cathode, while 90 μL of electrolyte was used in measurements utilizing two P50 discs (as described below).

2.2.1.3 Cells containing multiple P50 discs as the cathode

Typical cells utilized a single P50 disc as the cathode. This provided a reasonable surface area and pore volume for deposition of discharge product. In addition, the single P50 disc allowed for discharge to the maximum achievable capacity in a reasonable amount of time to allow for a high experimental throughput; the longest-duration discharge in this work was 64 hours (5.66 mAh/cm^2 at 88 $\mu A/cm^2$), and the shortest only a few minutes (e.g., a <0.5 mAh/cm^2 at 3500 $\mu A/cm^2$). However, multiple P50 discs could be used as the cathode instead; no binder or additional current collectors between the two discs were required. This provided a significant enhancement to the maximum achievable capacity and a corresponding increase in the length of time required for a single discharge or charge. The maximum achievable capacity was not observed to scale linearly with the number of cathodes included, likely due to limitations in mass transport through the thicker cathode.

To give quantitative insight into NaO_2 deposition trends throughout the cathode, some

cells were assembled using two P50 discs instead of one. Upon cell disassembly in the glovebox, these discs were separated for quantification of the discharge products by a titration-based assay (see section 2.4). Because both cathode surface area and thickness were approximately doubled by the addition of a second P50 disc, the results at a stated two-cathode current density were not directly analogous to single-cathode discharges at either the same or half the cross-sectional current density. While direct quantitative comparisons were difficult to draw, the overall trends in relative deposition of the discharge product under constant-pressure conditions were likely conserved between the single- and double-cathode systems. Likewise, similar trends in discharge and cell failure mechanisms with changes in cell operating pressure and current density were expected with one or two P50 discs.

2.2.1.4 Considerations for charging of cells

In our previous reports, we observed that Na-O_2 cells frequently failed due to dendrite formation on charge, especially at higher capacities.[1,51] For this reason, this work considered only cells discharged to moderate- or low-capacity (typically Q$\leq$0.88 mAh/cm^2). Where possible, these cells were also discharged under constant O_2 pressure to control for the influence of NaO_2 deposition on the charge behavior, with separate pressure-decay and titration experiments to confirm the discharge chemistry. Furthermore, all cells were charged under an Ar headspace to reduce the likelihood of catastrophic cell failure. As this dissertation is concerned largely with the first discharge and charge cycle, we utilized for all charge experiments a high cutoff potential of 5.0 V, except where otherwise noted. Short-circuiting due to dendrite formation was regularly observed at charge current densities at or above 1800 μA/cm^2, even following a modest discharge of 0.88 mAh/cm^2. Dendrite formation prior to or during the high-potential charge plateau following sudden death was observed in all the highest current density charges (currents greater than or equal to 3500 μA/cm^2) attempted in this work. Galvanostatic charge profiles for these current densities may therefore end before reaching the cutoff potential of 5.0 V or the full charge capacity, indicating that the cell experienced short-circuiting. Upon disassembly of every short-circuited cell, dendrites were readily visible in the cell separator (see Figure A.1b). Finally, as recent reports have indicated NaO_2 is subject to degradation during extended rest periods following discharge, cells were not allowed to rest more than 2 hours between discharge and charge, with an average resting period of 30 min.[46,53]

2.2.1.5 Testing of potential redox mediators

Sodium iodide (NaI), sodium bromide (NaBr), ferrocene, and thianthrene were purchased from Sigma Aldrich. NaI and NaBr were dried at 80°C for 12 hours prior to direct transfer to an argon-filled (<0.1 ppm H_2O, <0.1 ppm O_2 content) glovebox without exposure to atmosphere; ferrocene was used as received, as its tendency to sublimate prohibited drying under vacuum. Thianthrene was recrystallized in hexane, dried, transported to the lab in a sealed container, and dried again following the same procedures as with NaI and NaBr.

NaI, ferrocene, and thianthrene were added to 0.5 M NaOTf in DME solutions prepared as described above (Section 2.2.1.2) to create either 0.2 M NaI, 0.2 M ferrocene, or 50 mM thianthrene. NaBr was observed to have a sparing solubility in DME; a quantity of NaBr adequate to make a 0.2 M solution was added to 0.5 M NaOTf in DME and no significant dissolution of the NaBr crystals was observed. The solution was allowed to rest over four days, during which time it was periodically stirred to ensure NaBr saturation. Cells were assembled with these electrolytes (0.2 M NaI, saturated NaBr, 0.2 M ferrocene, or 50 mM thianthrene with 0.5 M NaOTf in DME) following procedures identical to those described in Section 2.2.1.2.

2.2.2 Three-electrode H-cells for study of Mg corrosion

Accurate study of the negative difference effect (NDE) during Mg oxidation requires analysis of the gas evolved at the Mg anode separate from any other gas that is consumed or evolved in the cell. During Mg oxidation, a reductive potential is required at the Pt counter electrode, resulting in the evolution of H_2 gas. To prevent interference with measurements of H_2 gas evolved as a result of the Mg NDE, the working and counter electrodes must be spatially segregated. Furthermore, while Mg may be utilized as an anode in a battery, the chemistry of potential cathodes is beyond the scope of this study, and would complicate the study of the NDE. Additionally, accurate measurements of the potential at the Mg electrode can be critical to understanding the corrosion phenomena taking place under given electrochemical conditions. For this reason, a Swagelok setup as described in section 2.2.1.1 is not ideal for the focused study of the Mg NDE, though it was previously utilized in Mg batteries with sufficiently NDE-suppressing electrolytes.[19] Instead, a three-electrode cell configuration was selected, with a Mg working electrode, appropriate reference electrode, and Pt counter electrode arranged in an H-cell. The H-cell configuration provided the required spatial separation and was deemed most suitable for accomplishing the objectives of this study.

2.2.2.1 Tradeoffs in cell design

An H-cell configuration as depicted in Figure 2.3 was previously reported for use in the study of the Mg NDE.[19] Cells of similar design have also been used to study other electrochemical and electrocatalytic systems.[98] This small-volume three-electrode glass H-cell was custom designed and constructed by Adams & Chittenden Scientific Glass (Berkeley, CA), and utilized ∼5 mL of electrolyte in the working electrode (WE) chamber and a similar quantity in the counter electrode (CE) chamber. An ion exchange membrane separated the two chambers to prevent crossover of gases. The WE chamber included both a Mg foil electrode (∼1 cm^2 exposed to the electrolyte) and a Ag/AgCl reference electrode (RE). A stainless steel sample holder and current collector was used to hold the Mg foil WE immersed in the electrolyte, but no portion of the current collector was in contact with in the electrolyte. (Note that an Al sample holder may also be used.[19]) In Figure 2.3, capillaries are shown affixed to the top port of the WE chamber for addition or sampling of gases to the DEMS;

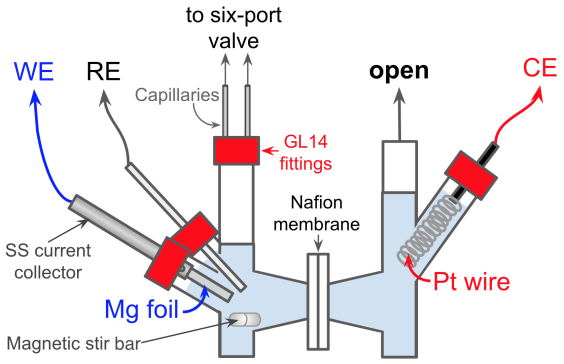

Figure 2.3: Schematic of a small-volume three-electrode glass H-cell for study of Mg corrosion.

capillaries may alternately or additionally be affixed to the open port of the CE chamber. During typical operation, the CE chamber top port was allowed to remain open so that gases evolved at the Pt wire CE could escape. GL14 fittings were used to ensure leak tight connections at the current collector ports and top port, and an NW14 flange set joined the two cell chambers.

This small H-cell design had several notable advantages for study of the Mg system and was successfully utilized in previous work.[19] It was designed with a small-volume chamber, requiring only small quantities of electrolyte. For cases where high-value electrolytes were to be used, a cell configuration like this was optimal. In addition, the small volume allowed the accumulation of trace products to reasonably high concentrations, permitting their later analysis, as has been previously demonstrated.[19,98] The relatively small electrolyte volume and total WE chamber volume resulted in small headspace volumes ($\lesssim$5 mL), enabling high-precision measurements of gas evolved from the Mg WE. Unfortunately, this small electrolyte volume was sensitive to changes in the electrolyte composition, especially changes in pH resulting from the reduction of H^+ or H_2O to H_2 gas. The evolution of H_2 due to the Mg NDE resulted in a steady increase in pH, and depending on the initial pH of the electrolyte, the Mg electrode could experience dramatically different, uncontrolled chemical environments during the course of a single experiment. Finally, the small chamber size allowed the Mg WE and Ag/AgCl RE to be positioned within millimeters of each other; this decreased the ohmic losses in the cell, but increased the risk of H_2 bubbles interfering with the RE's measurements. A magnetic stir bar in the base of the WE chamber helped to mitigate this risk and to prevent concentration gradients in the cell, but the rate and efficacy of agitation was somewhat limited.

A modified design (Adams & Chittenden Scientific Glass, Berkeley, CA) was developed to provide a pseudo buffer capacity in the form of a higher electrolyte volume. This design is depicted in Figure 2.4. A to-scale schematic of the cell design with dimensions is provided in Figure A.2. In this modified design, the volume of the WE chamber was significantly increased from $\sim$5 to $\sim$230 mL electrolyte, with a cell headspace of 10 to 15mL. This

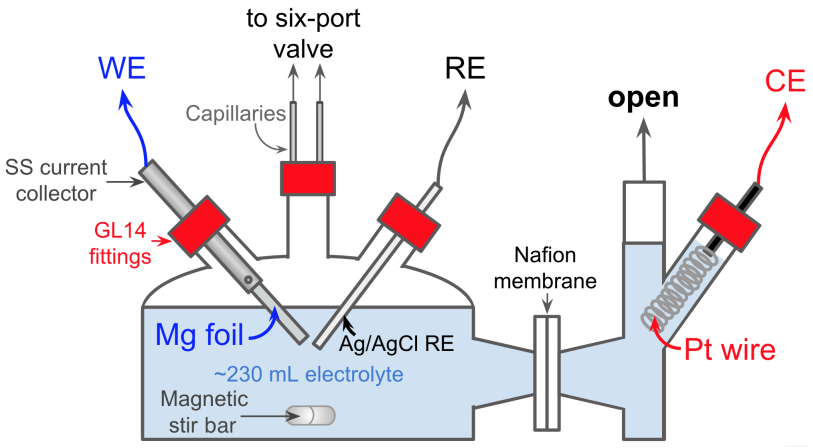

Figure 2.4: Schematic of a large-volume three-electrode glass H-cell for study of Mg corrosion, particularly in unbuffered or near-neutral-pH electrolytes. Figure is not to scale.

increased electrolyte volume prohibited the use of high-cost electrolytes, and the increased cell headspace volume decreased the sensitivity of gas evolution measurements. However, the larger electrolyte volume was largely insensitive to changes in pH over time, except in pH ranges where miniscule variations in H^+ and OH^- concentration have significant effect (i.e., pH 5-9). In addition, the WE and RE were positioned, on average, slightly further apart than in the small-volume cell, increasing ohmic losses but decreasing the risk of H_2 bubbles interfering with the RE. Finally, despite the larger volume to be mixed, the cell could accommodate a larger magnetic stir bar, which stirred the electrolyte at higher rotation rates than in the small cell. Because a primary objective in this work was to characterize the NDE in different pH environments, the large-volume H-cell was utilized for all the data presented.

Correction of H_2 pressure-rise/decay data using Henry's Law. Due to the large electrolyte-to-headspace volume ratio in the large-volume three-electrode H-cell, measurement of the quantity of gas by pressure-rise/decay alone was not necessarily adequate; the ideal gas assumption did not apply in the case of gases which were soluble in the electrolyte. The analyte gas of interest in Mg corrosion measurements, H_2, was soluble in the electrolyte to a significant degree, and pressure-rise/decay measurements significantly under-predicted the quantities of H_2 produced. In order to correct for this, a correction using the H_2 Henry's law solubility coefficient and the measured partial pressure of H_2 was applied. The Henry's law coefficient was determined using a literature value for the H_2 Bunsen coefficient in NaCl solutions.[99] Though most of the data presented were collected in KCl solutions of various concentration, this Bunsen coefficient was regarded as an adequate approximation.

2.2.2.2 Materials and cell assembly

NaCl (99.5%), KCl (99.5%), concentrated HCl, 0.1 N HCl, and KOH (88.5%) were purchased from Fischer Scientific and used as received. NaOH (99.0%) was purchased from EMD and used as received. $MgCl_2 \cdot 6H_2O$ (99.0%) was purchased from Sigma Aldrich and used as received. Electrolytes were prepared by mixing these salts or diluting these acids with ultrapure water (18.2 MΩcm, Millipore) to the desired concentration; concentrations varied from 0.3 M to 3.0 M, and electrolytes included mixtures of salt and the corresponding acid or base to adjust the pH (e.g., KCl and KOH, or NaCl and HCl). Electrolyte pH was determined immediately prior to and following any Mg experiment using pH multi-indicator paper where low precision was required (pH-Fix 0-14 test strips, Macherey-Nagel) or using an intelligent pH probe with a Pt temperature sensor (Metrohm iUnitrode with Pt1000 probe, controlled via a Titrando titrator and Tiamo titration software, v2.2).

High purity planar Mg sheets (250 μm thick) were purchased from Gallium Source and used in all experiments. From the manufacturer's specifications, the impurities in the Mg were as follows: 30 ppm Al, 50 ppm Mn, 50 ppm Si, 40 ppm Ca, 30 ppm Fe, 2 ppm Ni, 5 ppm Pb, and 50 ppm Zn. Mg electrodes were cut from the planar Mg sheets with scissors and their dimensions measured with calipers prior to and following all experiments; typical Mg electrodes were 3-6 mm wide and 20-35 mm long, with larger or smaller dimensions selected depending on the intended experiment. Prior reports indicate that polishing the surface of Mg alloys, such as with high-grade sandpaper, has been shown to decrease the initial corrosion rate due to removal of contaminants on the alloy surface,[96] but other reports have indicated that polished samples may produce significantly different corrosion rates.[19]

Instead of physical polishing, a chemical polishing/conditioning procedure was devised to pre-treat every electrode immediately prior to electrochemical measurement. Mg electrodes were washed in a well-mixed 0.1 M HCl and 0.4 M KCl or NaCl solution for approximately 30 seconds to remove surface oxide layers and contaminants. The salt (KCl or NaCl) was selected such that the cation was the same as in the electrolyte in which the Mg electrode would be tested so as avoid trace cross-contamination. Following acid washing, the electrode was placed in a well-mixed solution of 0.5 M KCl or NaCl, again consistent with the electrolyte in which the electrode would be tested. The pH of this solution was generally observed to be ∼10 due to corrosion of the Mg electrode during pretreatment, regardless of initial pH. The electrode was allowed to rest in this solution for 5-10 minutes; the initial corrosion rate of the electrode was found to be relatively insensitive to changes to the length of time within that range. Following this pretreatment, the electrode was dried with a clean laboratory Kimwipe™ and weighed, then immediately inserted into the cell. Typical electrodes weighed between 20 and 50 mg following pre-treatment. All electrodes were pre-treated with the exception of electrodes tested in a pH 1 (0.1 M HCl) electrolyte; these were not pre-treated because our pre-treatment procedure was observed to increase the initial rate of open-circuit Mg corrosion in these electrolytes, increasing the rate of H_2 evolution and the hazards associated with cell assembly.

The H-cell (either as in Figure 2.3 or 2.4) was assembled with a 28 mm diameter Nafion

117 membrane (Ion Power) between the WE and CE chambers. The Nafion membrane was placed on the WE side of the NW10 flange set between the two chambers, as this was generally observed to lead to superior hermetic integrity. A coiled Pt wire (23 cm) counter electrode and a Ag/AgCl reference electrode with glass frit were purchased from BASi Inc. Due to the small headspace-to-electrolyte volume ratio of the large-volume H-cell, significant pressure variations were observed in the sealed cell due to dissolution and equilibration of the headspace gas with the electrolyte. To ensure the cell was at equilibrium prior to measurement, the large-volume H-cell was assembled with capillaries on the top port of the WE chamber, the CE in place in its chamber, and capped GL14 fittings on all remaining ports. The WE chamber headspace was alternately flushed with Ar and evacuated to ∼0.15 atm total pressure to allow outgassing of atmospheric O_2 and N_2. Following five Ar flushing/low pressure cycles, the cell was charged with ∼1.3 atm Ar, sealed, and allowed to equilibrate overnight (> 12 hours). Typical cell pressure following overnight equilibration was 1.05-1.25 atm. Following equilibration, the plug was removed from the top port of the CE chamber. The RE and WE were inserted into the WE chamber while Ar was actively flowed into the cell to prevent atmospheric contamination. The WE chamber pressure was adjusted to match the equilibrated Ar pressure prior to electrochemical analysis.

Due to the cell geometry, approximately half of the electrode as-cut was submerged in the electrolyte, while the remainder was inactive. The active electrode area was determined by measurement of the dimensions of the unreacted electrode that had not been submerged in electrolyte, or by measurement of the submerged electrode, which typically had a different appearance from unreacted Mg. Examples of electrodes following electrochemical characterization at a number of different pH are available in Figure 7.2. Films and accumulated material were observed on the surface in nearly every case, and were observed to be black, grey, or white. The appearance of these films was consistent with prior reports, which suggest they were comprised of $Mg(OH)_2$ containing small particles of metallic Mg.[62,67] Lighter-colored films likely contained little to no metallic Mg with darker-colored films containing more numerous and densely packed metallic Mg particles. These films could also incorporate trace amounts of other Mg salts (e.g., $MgCl_2$). For cases where few films were apparent (e.g., pH 1-2 in Figure 7.2), a change in surface luster or evidence of dissolution distinguished the active and inactive surface area; in the latter case, the initial surface area was more determined by subtraction of the inactive surface area from the initial surface area. Finally, the darker surface films visible at the top of the electrodes in Figure 7.2 indicate the appearance of the Mg as-received, whereas the lighter color just below indicates the appearance following pre-treatment and conditioning.

Electrodes were dried with a Kimwipe™ and weighed following electrochemical analysis. However, the change of the electrode's mass was generally observed to be a poor indication of the quantity of Mg that had been oxidized, except in cases where the entirety of the active electrode was deliberately oxidized or dissolved. We attributed this inconsistency to the accumulation of the aforementioned $Mg(OH)_2$ films on the electrode surface, the possibility of H_2O incorporated into the films, and the potential inclusion of electrolyte salts and spectator ions (e.g., NaCl, KCl, or $MgCl_2$).

2.2.2.3 *In situ* calibration of large-volume cells

The large-volume H-cell could be calibrated using volume expansion techniques similar to those utilized for calibrating the Swagelok cells and the DEMS transfer lines. However, this measurement required the use of a dry electrochemical cell, and the uncertainty of the volume calculation was approximately ±2% of the measured quantity. The total dry volume of the WE chamber of the large-volume H-cell was determined to be approximately 240 mL, with an error of up to ±5 mL. Since the electrolyte volume was ∼230 mL, the calculated headspace volume on the basis of this calibration would have an error on the same order as the volume itself, rendering pressure-rise/decay measurements essentially meaningless.

An alternate *in situ* calibration procedure was devised for use in the large-volume H-cell, and is illustrated in Figure 2.5. The fully assembled cell was charged with gas, with the six-port valve in position B and the purge valve closed. The inlet valve was closed, and the pressure recorded (P_{B1}, Figure 2.5a). The six-port valve was then switched to position A. This caused the 500 μL loop to be evacuated, and expanded the gas in the transfer line between the inlet valve and six-port valve into the transfer line between the six-port valve and the purge valve; this pressure was recorded (P_A, Figure 2.5b). The six-port valve was then switched into position B, expanding the gas in the cell and in the transfer lines between the inlet valve and the six-port valve into the 500 μL loop, and this pressure was recorded (P_{B2}, Figure 2.5c). This procedure was repeated with a standard volume loop to determine the volume of the transfer line between the inlet valve and six-way valve (V_1) and of the transfer lines between the cell and six-port valve (V_2). The total volume of the transfer lines open to the cell with the six-port valve in position B (V_T) was known from previous

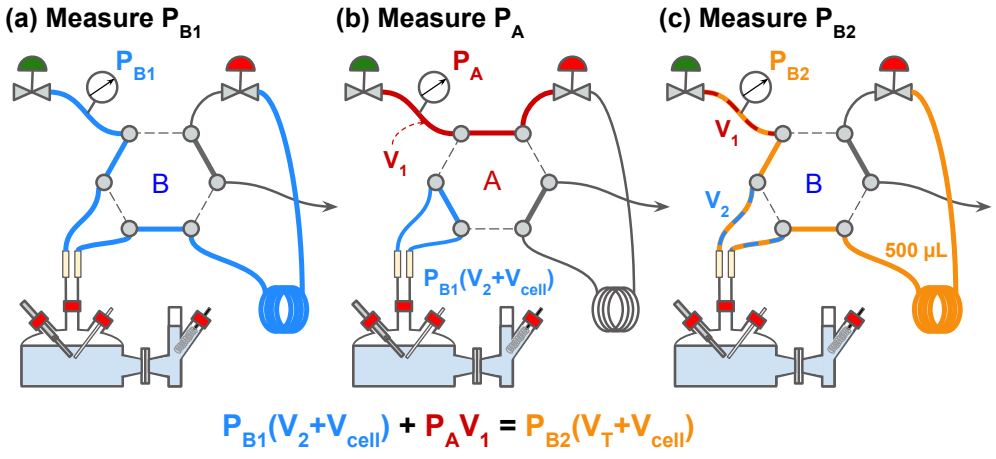

Figure 2.5: Illustration of the *in situ* volume calibration procedure for large-volume three-electrode glass H-cells. The equation given assumes constant temperature, ideal gas behavior, and no transfer of gas between ports on the six-port valve during switching, and may be rearranged to give equation 2.1.

volume-expansion calibration of the instrument. Assuming no gas was transferred between ports on the six-port valve during switching, the volume of the cell was then calculated to be:

$$V_{cell} = \frac{P_{B2}V_T - P_{B1}V_2 - P_A V_1}{P_{B1} - P_{B2}} \tag{2.1}$$

The above calibration procedure was repeated multiple times and the average calculated volume used for analysis of pressure-rise/decay data. The estimated accuracy of this headspace volume calibration was approximately ±5% of the measured value; however, as this approach directly measured the cell headspace, this error was typically $\lesssim$0.5 mL. To eliminate systemic error, this calibration was performed under experimental conditions that would not lead to significant changes in pressure due either to evolution of H_2 gas or to re-equilibration with the gas headspace. Ultimately, the cell was operated as shown in Figure 2.5c, with the total cell headspace volume for calculation of gas evolved or consumed given by:

$$V_{headspace} = V_T + V_{cell} = (V_1 + V_2 + 500\mu L) + V_{cell} \tag{2.2}$$

2.3 Electrochemical Methods

All electrochemical experiments were performed using a Bio-Logic VSP potentiostat/galvanostat connected to a PC running EC-Lab® software. With few exceptions, the electrochemical experiments in this work may be generally broken into several distinct categories. In the study of Na-O_2 batteries, first, galvanostatic (constant-current) discharges and charges were performed on Na-O_2 cells to analyze cell performance, both to a limited capacity and to the failure or "sudden death" of the cell (Section 2.3.1). Second, electrochemical impedance spectroscopy was performed on Na-O_2 cells to elucidate the contributions to the cell overpotential and causes of sudden death (Section 2.3.2). Third, some additional discharge/charge cycling, linear sweep voltammetry, and alternate charging schemes were also performed with Na-O_2 cells (Section 2.3.3). In the study of Mg corrosion, the non-polarizable behavior of the Mg electrode makes analysis of electrochemical data more nuanced. Various electrochemical impedance spectroscopy techniques were employed to clarify whether changes in the measured potential of the cell were due to changes in the chemistry or increases in the series resistance (Section 2.3.4). Finally, electrochemical tests to determine mass-transfer coefficients in the large-volume H-cell were performed using the limiting current technique and used in support of a simple model of pH changes at the Mg electrode surface (Section 2.3.5).

2.3.1 Galvanostatic discharge and charge of Na-O_2 cells

Due to widely reported instabilities of the NaO_2 discharge product and the potential variables introduced by cycling an Na-O_2 cell more than once, the focus of this study was the first discharge-charge cycle.[1,8,30,38,39,46,49,53] Most Na-O_2 cells were discharged or charged

galvanostatically (i.e., at a constant current). Na-O_2 cells as-assembled contained no discharge product (NaO_2) and therefore were discharged prior to charge; charge without prior discharge was possible but resulted in degradation of the electrolyte. Additionally, the rate and depth of discharge can alter a cell's behavior on charge.[1] For this reason, discharge and charge were studied as independently as possible, with cells discharged at one of only a few current densities to a set capacity (0.88 mAh/cm^2) under controlled conditions prior to charge.

The discharge capacity at sudden death was taken to be the total capacity of the cell when its full-cell potential reached 1.0 V, since discharge at lower potentials was likely to result in undesired side reactions or degradation of the electrolyte. Achieving 1.0 V typically coincided with the precipitous decrease in potential characteristic of sudden death. Discharges were performed at constant current densities between 88 μA/cm^2 and 3500 μA/cm^2. While it was observed that discharge at higher current densities was possible and still resulted in consumption of O_2 at rates consistent with the formation of NaO_2, these higher current densities generally resulted in full cell potentials less than 1.0 V. Thus, current densities above 3500 μA/cm^2 were largely excluded from this study.

The charge capacity at sudden death was generally taken to be the capacity when the cell potential underwent a precipitous increase from its lower-potential charge plateau. Where a specific capacity was needed for analysis, this point was defined as when the full-cell potential exceeded 4.0 V, as this generally represented a capacity before the onset of undesirable electrochemical processes. However, as charge following sudden death was possible and was demonstrated to coincide with continued evolution of O_2, charge was typically continued to a maximum cutoff potential of 5.0 V or until the cell shorted due to dendrite growth.[1] Thus, charge profiles may generally be divided into two clear regions, prior to and following sudden death. Charges were generally performed following discharge at either 440, 880, or 1800 μA/cm^2. Charge current densities between 88 μA/cm^2 and 7100 μA/cm^2 were studied. Higher charge current densities at full cell potentials below 5.0 V were observed to be possible, but these cells were observed to rapidly short due to dendrite formation and were not studied further due to safety concerns. We note that protection of the anode to prevent dendrite growth could enable the safe study of higher-current discharges.

2.3.2 Electrochemical impedance spectroscopy for analysis of Na-O_2 cell failure

Electrochemical impedance spectroscopy (EIS) was performed at open-circuit potential using an AC amplitude of 10 mV that varied from 100 kHz to 50 mHz with 9 points/decade and 3 cycles/frequency. EIS performed galvanostatically was conducted at an AC amplitude equal to 10% of the DC current. The frequency varied from 100 kHz to 320 mHz with 9 points/decade and 4 cycles/frequency; the relatively high lower frequency was chosen as no additional processes were monitored in cells tested down to 5 mHz.[51] The impedance spectra were fitted with equivalent circuit models that relied on Levenberg-Marquardt complex nonlinear least-squares minimization algorithm using software programmed in Python.[100] An

equivalent circuit diagram is shown in Figure 2.6 and further discussion of the equivalent circuit and normalization of parameters is given below. The error related to the impedance measurements originates from the precision of the potentiostat and is stated to be <0.3% by the manufacturer. The largest source of error in fitted quantities was the BET surface area, and the error bars (e.g., in Figures 4.6 and 4.10 to 4.12) are based on this uncertainty.[51]

2.3.2.1 The equivalent circuit and parameter normalization

The equivalent circuit of the reacting cathode used in the study of the electrochemical impedance of Na-O_2 cells is given in Figure 2.6. A detailed description of normalization and fitting can be found in Knudsen et al.;[51] a brief discussion is included here, but the deeper nuances of EIS of two-electrode Na-O_2 systems are considered beyond the scope of this dissertation. The sodium anode behaves faradaically at all potentials as Na^+ moves through the SEI to sustain charge neutrality. The equivalent circuit therefore contains a resistor (R_{Na}) to represent the movement of the Na^+ and a capacitor (C_{Na}) in parallel to represent sodium's double-layer capacitance. The equivalent circuit of the cathode was based on the porous electrode theory model developed by de Levie and Delahay, since the cathode exhibits distinct responses related to its flooded pores.[51,101] The equivalent circuit therefore contains an ionic resistance (R_i) within the electrolyte-filled pores of the cathode. In addition, the interfacial impedance of the cathode is controlled by the applied DC potential, and during discharge or charge, this interface behaves faradaically. Thus, a resistor (R_{CT}) is applied to represent the rate of O_2 reduction and the rate of formation of NaO_2 in parallel with a capacitor ($C_{Cathode}$), which is related to the pristine cathode/electrolyte interface, the formation of NaO_2, and the NaO_2 interface with the electrolyte. The series resistance R_s is governed by the thickness of the separator and the conductivity of the electrolyte. Finally, the equivalent circuit applied for the interfacial impedance of the non-reacting cathode measured at open-circuit potential was a constant phase element -(Q)-.[51]

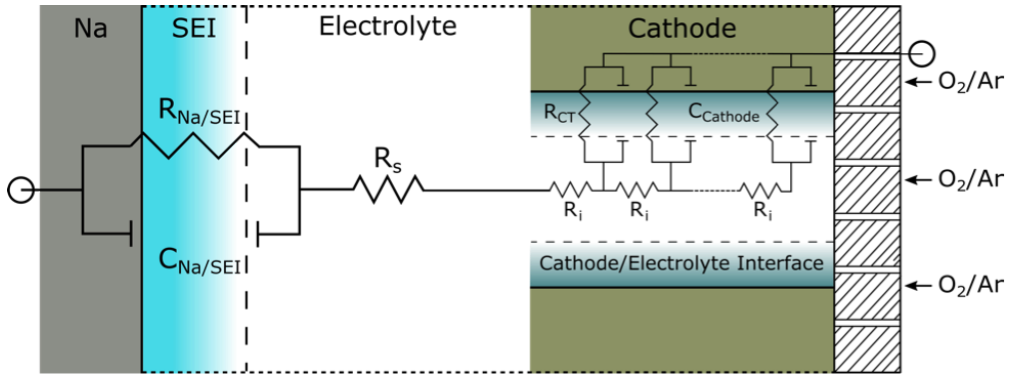

Figure 2.6: A schematic representation of the equivalent circuit that describes the two-electrode cell with a sodium anode and a reacting porous carbon cathode.

During fitting, the capacitors in the equivalent circuit were exchanged with constant phase elements and their exponents (n) were kept between 0.7-1.0. As de Levie and Delahay's porous model was utilized for the cathode impedance, the units of R_{CT}, R_i, and $C_{Cathode}$ were normalized to the thickness of the cathode as Ω/cm, Ωcm, and $\frac{s^n}{\Omega cm}$, respectively.[101] For the purpose of relating these parameters to the surface area of the cathode, the resistors were normalized using the thickness of the cathode (L_c, cm), as reported in Knudsen et. al, and the BET surface area of the cathode.[51] The capacitance was normalized to the effective capacitance using methods described by both Brug et al. and Hirschhorn et al.[102,103] Equations (2.3) to (2.5) describe the normalization in detail, where R'_{CT}, R'_i, and $C'_{Cathode}$ are the output parameters of the ionic resistance, charge-transfer resistance, and the interfacial constant phase element, respectively, with the aforementioned units. Other parameters include the mass of the P50 carbon cathode (m_{carbon}, mg) and the BET surface area of the cathode (A_{BET}, cm^2/mg).

$$R_i = R'_i L_c m_c A_{BET} \qquad [\Omega cm^2] \tag{2.3}$$

$$R_{CT} = \frac{R'_{CT}}{L_c} m_c A_{BET} \qquad [\Omega cm^2] \tag{2.4}$$

$$C_{Cathode} = C'^{\frac{1}{n}}_{Cathode} L_c \left(\frac{R_s R_{CT}}{R_s + R_{CT}}\right)^{\frac{1-n}{n}} \frac{1}{m_c A_{BET}} \qquad [Fcm^{-2}] \tag{2.5}$$

2.3.3 Additional electrochemical analyses of Na-O_2 cells

2.3.3.1 Linear sweep voltammetry

To probe the stability and activity of electrolytes and redox mediators on charge in the Na-O_2 system, oxidative linear sweep voltammetry (LSV) was performed on assembled Swagelok cells under an Ar headspace without exposure to O_2 or prior discharge. The scan rate was 5 mV/s, and the linear sweep was performed from the open-circuit potential of the cell as-assembled (between 2.5 and 3.0 V), to a 5.0 V maximum. LSV data was acquired for cells assembled with the following electrolytes: 0.5 M NaOTf in DME, 0.2 M NaI with 0.5 M NaOTf in DME, saturated NaBr with 0.5 M NaOTf in DME, and 0.2 M ferrocene with 0.5 M NaOTf in DME.

2.3.3.2 Cycling of cells to examine viability of redox mediators

Cells assembled with a 0.5 M NaOTf in DME electrolyte and a saturated NaBr with 0.5 M NaOTf in DME were cycled for a total of up to four discharge/charge cycles. The first discharge/charge cycle was performed as for all Na-O_2 cells; however, a 4.0 V cutoff voltage was employed on charge to prevent electrolyte degradation. On each subsequent cycle, the cell was discharged to a capacity representing 102% of the charge capacity of the previous cycle. The additional 2% capacity was included to represent losses of NaO_2 to instability and dissolution, such that the quantity of NaO_2 present on the cathode prior to charge was

approximately equal for every cycle. The additional capacity was not observed to dramatically impact the capacity at which sudden death occurred on the subsequent cycles. Both discharge and charge were performed under pressure-rise/decay mode for acquisition of gas consumption and evolution data.

2.3.3.3 Chronoamperometic alternate charging schemes

To explore the viability of charging cells by using chronoamperometry (i.e., potentiostatic charging, or charging at a constant potential), Na-O_2 cells were first discharged at either 880 or 1800 μA/cm^2 to 0.88 mAh/cm^2. Cells were then charged galvanostatically 1800 μA/cm^2 to 3.0 V. Immediately upon achieving the cutoff potential, the cell was switched to charge potentiostatically at 3.0 V. The current density was observed to decrease over time. Charge was allowed to continue until the cell reached a current of 15 μA/cm^2, at which time charge was ceased. This cutoff current was selected based on the current achieved in Na-O_2 cells during LSV prior to the onset of electrolyte degradation. This combined chronopotentiometry-chronoamperometry charging scheme was tested under pressure-rise/decay mode for quantification of consumed and evolved gases.

2.3.4 Electrochemical impedance spectroscopy for accurate measurement of Mg electrode potentials

Mg anodes exhibit characteristics consistent with a non-polarizable system, such that a significant current can be passed on oxidation without the change in overpotential predicted by models such as Butler-Volmer or Tafel kinetics.[71,72]The primary goal of electrochemical impedance spectroscopy in the Mg system was the accurate measurement of the Mg electrode's potential by accounting for the overpotential loss incurred due to the solution resistance or series resistance (R_s). This resistance was overwhelmingly due to ion transport through the electrolyte between the Mg working electrode (WE) and the Ag/AgCl reference electrode (RE). While it is possible a junction potential at the Ag/AgCl reference electrode existed, since most electrolytes contained a significant concentration of Cl^- ions, this junction potential was likely small.[72] Due to varying electrode sizes, the cell geometry, and the difficult-to-control positioning of the WE and RE, the distance between the tip of the WE and the RE varied from approximately 2 mm to ~2 cm. Additionally, different electrolytes could have significantly lower conductivities and higher solution resistances. For example, in two identically assembled cells, a 0.3 M KCl electrolyte was observed to lead to $R_s = 10\ \Omega$ while a 3.0 M KCl electrolyte resulted in $R_s = 1\ \Omega$. EIS was therefore necessary for more nuanced electrochemical characterization.

Several EIS techniques and IR-correction approaches were employed in this work as described below. In principle, R_s may be determined by calculating the real component of the impedance when the imaginary component is zero, or by determining the x-intercept of a Nyquist plot of the impedance spectrum. Where more than one x-intercept occurred, as has been reported to be the case for Mg electrodes, the highest-frequency x-intercept

gave R_S.[71,72,87,104] In cases where no x-intercept was observed on the Nyquist plot, R_S was determined by extrapolating the available data to zero. These extrapolated R_S values were used with extreme caution because this extrapolation could be imprecise, especially for noisy data.

Generally, data at frequencies below ~1 Hz were observed to be too noisy to allow analysis or fitting with an equivalent circuit model. In spite of these issues, qualitative characteristics of the impedance spectra were consistent with prior reports, including the appearance of induction loops at low frequencies.[71,87] We attribute data quality issues relative to prior reports to differences in electrode geometry and the subsequent current distribution across the electrode, possible transport effects due to electrolyte stirring and agitation, a cell configuration poorly optimized for impedance spectroscopy, and non-optimal experimental parameters.

2.3.4.1 Potentiostatic EIS at OCV

Potentiostatic electrochemical impedance spectroscopy (PEIS) was performed before or after polarization of the Mg electrode at open-circuit potential using an AC amplitude of 10 mV. Identical frequencies were observed to produce different results under different pH conditions and electrolyte concentrations, and so a range of high-frequency limits and low-frequency limits between 200 kHz and 50 mHz were employed with 8 points per decade. Because of the poor quality of data at lower frequencies, data acquired at frequencies between 150 and 10 kHz were used to acquire the R_S.

Some irregularities were observed in the IR-corrected data using the resistances determined by PEIS at open-circuit potential. In particular, some electrodes were observed to exhibit apparently decreasing overpotentials with increasing currents. In these cases, PEIS performed following polarization was observed to produce higher values of R_S than those acquired prior to polarization, suggesting R_S increased during data acquisition. Consequently, impedance spectra acquired during polarization away from open-circuit potential are recommended, including SPEIS or GEIS at nonzero currents, as described below.

2.3.4.2 Staircase potentiostatic EIS

Staircase potentiostatic electrochemical impedance spectroscopy (SPEIS) was performed in an effort to quantify changes in the series resistance during anodic polarization of the Mg electrode. These changes might be attributed to film accumulation on the electrode surface or to decreases in electrolyte conductivity as the pH increases, among other possible, uncontrolled effects. In SPEIS, PEIS was performed at a linearly increasing series of potentials, like a staircase, to some potential limit. For each "step" of the staircase, the potential was held constant for between 15 to 30 seconds before acquiring a single impedance spectra by PEIS at an AC amplitude of 10 mV that varied from 200 kHz to 20 kHz with 8 points per decade. The high lower frequency limit was chosen because of the aforementioned inconsistencies at lower frequencies, and because the goal of the SPEIS technique was to determine R_S alone.

Because of the relatively high frequencies, most impedance spectra were acquired in less than 20 seconds. The length of the constant-potential period before PEIS was varied together with the number of steps in the staircase and the potential window such that the length of time the electrode was polarized approximated a linear sweep through the same potential window at 5 mV/s. Representative values were 21 steps with 20 seconds of constant-potential polarization prior to EIS.

For each step, the average current and potential were calculated, and the potential was IR-corrected according to R_s as measured at that step. These corrections were generally observed to exhibit fewer or less pronounced irregularities in the current-potential relationship than corrections based on an R_s determined at open-circuit potential by PEIS. However, typical resistances in cells containing the same electrolyte were observed to vary by as much as 10 Ω, largely correlated with the distance between the WE and RE. As a result, the currents observed and the IR-corrected potential window explored during SPEIS could vary widely. For experiments where a direct comparison between the performance of two electrodes was desired, GEIS techniques were preferred, as described below.

2.3.4.3 Galvanostatic EIS and complete dissolution of Mg electrodes

Galvanostatic electrochemical impedance spectroscopy (GEIS) was performed at currents between 5 mA and 150 mA; when normalized to the initial surface area of a given Mg electrode, the oxidative current densities were between 2 mA/cm^2 and 450 mA/cm^2. The AC amplitude was was equal to 5% of the DC current, and the frequency varied from 150 kHz to 10 kHz with 8 points per decade. GEIS was performed according to different experimental schemes that fall into two categories: application of current alternating with open-circuit relaxation, or constant-current until the Mg electrode had completely oxidized or dissolved. In the first scheme, oxidative GEIS was performed for several minutes at a given current density (usually 6 cycles), after which the electrode was relaxed to open-circuit for a short rest (usually 5 minutes). These experiments were used to compare the rate of H_2 evolution at different current densities on the same electrode. Due to the relatively short period over which GEIS was performed, the surface area of the Mg electrode remained approximately constant. In the second scheme, oxidative GEIS was performed repeatedly, up to several hundred cycles, until the Mg electrode completely dissolved. This second approach allowed for precise measurement of the quantities of oxidized and corroded Mg, the quantity of evolved H_2, and the capacity passed through the electrode (taken to be the average current multiplied by the length of time during which GEIS at that average current was performed). During Mg electrode dissolution, the GEIS approach allowed continuous monitoring of R_s and therefore calculation of the electrode's operating potential. These experiments approximated a constant-current oxidation of the Mg electrode; however, it should be noted that they do not represent a constant current density, particularly in the cycles immediately preceding the complete dissolution of the electrode. The initial active surface area was determined by subtraction of the remaining surface area from the initial total area of the electrode, and the mass of Mg dissolved was determined by weighing the electrode prior to insertion in the cell

and following oxidation/dissolution.

2.3.5 Limiting current measurements and calculation of mass-transfer coefficients in the large-volume H-cell

Battery-grade Cu foil (99.99% pure) was used as-received, and cut to dimensions comparable to those of Mg electrodes in the large-volume H-cell (approximately 2 by 30 mm). A large-volume three-electrode H-cell was assembled with ∼230 mL of 1 M KCl electrolyte and equilibrated overnight under an O_2 headspace (as opposed to the typical Ar headspace). The cell was assembled and the electrode inserted as described for Mg electrodes, and stirred at the same rate as during all Mg dissolution experiments. The limiting current of O_2 reduction on Cu was measured by cyclic voltammetry from -0.45 V to -0.2 V vs. Ag/AgCl at a scan rate of 0.1 mV/s. These potentials were selected to avoid the onset potentials of the H_2 evolution reaction on Cu.[105]

2.3.5.1 Determination of mass-transfer coefficients by correlation

Relevant mass-transfer coefficients were determined from the limiting current by use of the Sherwood (Sh), Reynolds (Re), and Schmidt (Sc) numbers of the cell and the correlation between them for mass transfer occurring to or from a flat plate:[106]

$$\mathrm{Sh} = 0.664\mathrm{Re}^{1/2}\mathrm{Sc}^{1/3} \tag{2.6}$$

The dimensionless groups were calculated as follows:

$$\mathrm{Re} = \frac{\mathrm{lv}\rho}{\mu} \tag{2.7}$$

$$\mathrm{Sh} = \frac{\mathrm{k_x l}}{\mathrm{D_x}} = \frac{\mathrm{i_L l}}{\mathrm{nFC_{x,\infty}D_x}} \tag{2.8}$$

$$\mathrm{Sc} = \frac{\mu}{\rho \mathrm{D_x}} \tag{2.9}$$

where l is the characteristic length (the width of the electrode); v is the velocity of the fluid parallel to the plate; ρ and μ are the density and viscosity of the electrolyte, respectively; k_x and D_x are the mass-transfer and diffusion coefficients of species x, respectively; i_L is the limiting current density; n is the number of electrons in the electrochemical reaction (for O_2 reduction on Cu, n = 4); F is Faraday's constant; and $C_{x,\infty}$ is the bulk concentration of species x. The equivalence in equation 2.8 is true when operating at the limiting current density.[72]

In order to determine the mass-transfer coefficient of H^+ in the large-volume H-cell, the limiting current acquired as described above and equation 2.6 were used to determine the value of Re in the cell, with the value of the diffusion coefficient for O_2 determined from the literature.[107] The bulk concentration of O_2 was determined from the pressure in the cell

at the limiting current and a literature value for the Henry coefficient of O_2 (H_{O_2}).[108] The viscosity and density of the electrolyte were measured experimentally. Since the limiting current was acquired on a similarly-sized electrode using the same stir bar rotation speed, Re should be the same between both the O_2 reduction experiments and the Mg oxidation experiments. Using a literature value for the diffusion coefficients of H^+,[109] and determining the bulk concentration according to the bulk pH, equations (2.6), (2.8) and (2.9) were used to estimate the mass-transfer coefficient. Once acquired, the mass-transfer coefficient was used to calculate the concentration of the species x at the surface, C_x:

$$N_x = k_x(C_{x,\infty} - C_x) \tag{2.10}$$

The flux, N_x, was determined based on the rate of H_2 evolution and a set of simplifying assumptions. Values of key parameters used in these calculations and the calculated dimensionless groups are available in Table 2.1.

Table 2.1: Typical experimental, calculated, and literature values for relevant parameters in our model to estimate the pH at the surface of dissolving Mg electrodes. Experimental values acquired for this study are indicated "Expt." Values for each dimensionless quantity outlined above are also included.

Parameter	Value	Units	Source
i_L	-2.02	mA/cm^2	Expt.
l	2.2 to 3.8	mm	Expt.
ρ	1.05	g/mL	Expt.
μ	1.03	cP	Expt.
D_{H^+}	$9.311x10^{-5}$	cm^2/s	[109]
D_{O_2}	$1.42x10^{-5}$	cm^2/s	[107]
H_{O_2}	$7.84x10^{-6}$	mol/m^3Pa	[108]
Re	1100	-	-
Sc_{O_2}	691	-	-
Sc_{H^+}	105	-	-
Sh_{O_2}	192	-	-
Sh_{H^+}	104	-	-

Viscosity and density of KCl electrolyte. The viscosity of the 1.0 M KCl electrolyte, a necessary parameter in the determination of the mass-transfer coefficient, was measured with an electromagnetically spinning viscometer (EMS-1000, Kyoto Electronics Manufacturing Co., Ltd., Tokyo, Japan).[b] The viscosity was determined to be 1.03 cP at 25°C as the average of ten measurements, with a standard deviation of <0.01 cP and a standard error of ≪0.01 cP. The density of the 1.0 M KCl electrolyte was measured by pipetting the electrolyte into

[b]Viscosity measurement courtesy of Rickey C. Terrell.

a volumetric flask on a tared analytical balance. 10 mL and 50 mL volumetric flasks were used and an average density of 1.05 g/mL was determined from several measurements, with a standard deviation of <0.01 g/mL.

2.4 Quantification of Discharge Products by *Ex Situ* Titration

Further quantification of the Na-O_2 system may be accomplished through the application of a titration-based assay, which provides independent validation of findings from pressure-rise/decay measurements or DEMS. This technique was previously described as applied to the Li-O_2 system[14] and later adapted for the Na-O_2 system.[1,30] Titrations of the extracted cathodes as described below may be used to confirm the identity of the discharge product, the efficiency of O_2 conversion to discharge product, or the quantity of discharge product remaining on a discharged cathode following other electrochemical treatments (e.g., charge or open-circuit relaxation). Additionally, these titrations may be applied to detect the presence of NaO_2 in electrolyte-soaked cell separators or samples of electrolyte. Though the approach has been applied to both Li-O_2 and Na-O_2 cells, the procedures and reactions described below will focus on the chemistry in the Na-O_2 case, as it is the focus of this dissertation.

2.4.1 Titration-based assay outline and procedures

Following electrochemical analysis, each cell or sample to be titrated was flushed with Ar gas and sealed for transfer into the glovebox. Cathodes were extracted from the cell in an Ar-filled glovebox using clean stainless steel tweezers, then placed in an unsealed vial. For typical titrations of Na-O_2 cells, the time between the end of a cell discharge or charge and the extraction of the cathode was less than half an hour, and could be as little as five minutes. Short wait times between the conclusion of electrochemical analysis and extraction of the cathode were recommended, since the primary discharge product NaO_2 is known to be sparingly soluble in the electrolyte and may suffer from chemical instability over long periods of time, as has been previously reported.[46]

Extracted cathodes were dried under vacuum in the glovebox antechamber for approximately five minutes to evaporate excess electrolyte solvent. The analyte vial was sealed with a silicone septa lid for transfer out of the glovebox, ensuring protection from atmospheric contamination and potential side reactions with O_2, CO_2, or H_2O in the atmosphere. 2 mL ultrapure water (18.2 MΩcm, Millipore) was injected into the sealed vial using a syringe. The expected primary discharge product, NaO_2, reacts with neutral water via reaction 2.11:

$$2NaO_2 + 2H_2O \rightarrow 2NaOH + H_2O_2 + O_2 \tag{2.11}$$

If instead the discharge product were the thermodynamically preferred Na_2O_2, two other reactions may occur. The first is analogous to that observed in the Li-O_2 system,[14] and is

distinguished from 2.11 by the absence of evolved O_2.

$$Na_2O_2 + 2H_2O \rightarrow 2NaOH + H_2O_2 \tag{2.12}$$

A small side reaction could also occur for the Na_2O_2 case:

$$Na_2O_2 + H_2O \rightarrow \frac{1}{2}O_2 + 2NaOH \tag{2.13}$$

However, in the analogous case of Li_2O_2, no evidence of reaction 2.13 was reported, suggesting that it would also not occur for Na_2O_2.[14]

Significant O_2 evolution was observed in every Na-O_2 titration performed; the depressed plunger of the syringe used to inject water was typically allowed to rise to relieve pressure inside the vial due to gas evolution. This qualitative observation does not support the occurrence of reaction 2.12. Furthermore, evidence of stoichiometric quantities of H_2O_2 in the analyte, as will be discussed below, support the hypothesis that reaction 2.11 is occurring, rather than reaction 2.13, and that the discharge product is NaO_2. Therefore, the results of this titration technique not only allow quantification of the discharge product, but also provide a qualitative indication of its identity. Significant deviations from stoichiometric quantities of NaOH and H_2O_2 were never observed.

The contents of the vial were vigorously stirred for 30 seconds after apparent evolution of gas ceased, after which the vial was opened. NaOH formed by reaction 2.11 was titrated with a standardized HCl solution dispensed by a digital titrator (Hirschmann Solarus, 20mL) using a phenolphthalein endpoint indicator, according to reaction 2.14:

$$NaOH + HCl \rightarrow NaCl + H_2O \tag{2.14}$$

Typical standardized titrant concentrations for cells in this work varied from 0.005 M to 0.01 M; higher concentrations were ideal for titration of high-capacity cells, as they reduced the amount of titrant required, whereas lower concentrations were ideal for low-capacity cells or cells where greater precision was required due to small quantities of analyte. (See section 2.4.2 for a discussion of standardization procedures.) In addition to reacting with NaOH, the HCl could react with products from parasitic reactions of NaO_2 with the electrolyte or cathode. Furthermore, NaOH is a common contaminant in Na^+ salts that are good candidates for Na-O_2 battery salts, particularly in NaOTf that has not been recrystallized.[1,30] Potential contamination and parasitic side reactions lead to artificially high percent yields of NaO_2, which can reach and even exceed 110% of the amount of NaO_2 expected to form given the total Coulombic capacity of the discharge. This yield was observed to vary slightly depending on the conditions in which the cell was prepared, and was higher for lower-capacity cells, consistent with a systemic error due to electrolyte contamination. As such, the use of the titration described by reaction 2.14 was insufficient to quantify an NaO_2 discharge product on its own, but was useful as a means of confirming other results. Significant changes in the yield between cells of similar capacity would serve as a warning as to the extent of decomposition or contamination in the cell.

Quantification of H_2O_2 formed by reaction 2.11 was achieved using an iodometric titration technique, as applied previously.[14,30] Following titration with HCl, three reagents were added in succession: 1 mL of a 2 wt% solution of KI in H_2O, 1 mL of 3.5 M H_2SO_4, and a $\sim 50\mu$L drop of a molybdate-based catalyst solution. The KI and H_2SO_4 in these quantities were typically present in considerable excess of that required to consume all H_2O_2. The catalyst solution was prepared by dissolving 0.5 g ammonium molybdate in 5 mL of 6N ammonium hydroxide, then adding 1.5 g ammonium nitrate and diluting the solution to 25 mL total using ultrapure H_2O. Upon reagent addition, the solution turned yellow-brown due to I_2 formation:

$$H_2O_2 + 2KI + H_2SO_4 \rightarrow I_2 + K_2SO_4 + 2H_2O \tag{2.15}$$

The I_2 formed in reaction 2.15 was immediately titrated to a faint straw color using a standardized 0.01 N $Na_2S_2O_3$ solution (see section 2.4.2) dispensed by a digital titrator (Hirschmann Solarus, 20mL), according to the following reaction:

$$I_2 + 2Na_2S_2O_3 \rightarrow Na_2S_4O_6 + 2NaI \tag{2.16}$$

Once the solution was a faint straw color, $\sim$0.5 mL of a 1% starch indicator was added to the solution, which turned a dark blue; the titration was continued until the solution was clear. Because the only source of H_2O_2 in this assay is the Na-O_2 discharge products, the iodometric titration alone was used to determine how much discharge product (i.e., NaO_2) was in the cell at the time of cell disassembly. In this work, we generally define the percent yield of NaO_2 as the ratio of NaO_2 detected by iodometric titration to the quantity of NaO_2 expected given the total Coulombic capacity of the discharged cell.

Iodometric titrations must be performed rapidly to ensure no desorption of I_2 from the solution. Furthermore, excess KI is known to react spontaneously to form I_2, particularly upon exposure to light, water, and reducing environments. Based on experiments using ultrapure water instead of an H_2O_2-containing analyte, this reaction did not occur significantly on the order of a few minutes, but could affect the titration outcome if the analyte and reagents were allowed to rest for 10 minutes or more. This was further evidenced by the change in color of titrated solutions following endpoint; a titrated analyte allowed to rest eventually developed the deep blue color characteristic of the iodine-starch complex used as an indicator. Potassium iodide, sulfuric acid, hydrochloric acid, sodium thiosulfate, 1 wt% starch in H_2O, and ammonium molybdate were all purchased from Sigma Aldrich.

2.4.2 Standardization

The titration methods described above required the use of standardized titrant solutions. Because of the low concentration of analytes and titrants, small inaccuracies in the reported concentration of as-received standardized solutions could lead to significant deviations in reported yields, and standardization procedures were performed in-lab for each batch of titrant.

2.4.2.1 Standardization of HCl titrant

Potassium hydrogen phthalate (KHP, Sigma Aldrich) is a non-hygroscopic, monoprotic acidic salt compound. A solution of KHP of known concentration between 0.01 to 0.03 M was prepared using an analytical balance and a certified volumetric flask. Additionally, a fresh solution of NaOH was prepared at a concentration of approximately 0.01 to 0.03 M, though this concentration could not be measured precisely due to the hygroscopic and reactive nature of NaOH. Between fifteen and thirty aliquots of 1mL to 4mL NaOH were measured by volumetric pipet and titrated with KHP in a random order. A phenolphthalein indicator was used, with the pink-to-clear transition taken to be the titration's endpoint. These titrations were used to ascertain the precise concentration of the NaOH solution according to the stoichiometry of the KHP-NaOH reaction:

$$KHC_8H_4O_4 + NaOH \rightarrow NaKC_8H_4O_4 + H_2O \tag{2.17}$$

Following this titration, between fifteen and thirty 1 mL to 3 mL aliquots of the now known-concentration NaOH solution were titrated with the HCl to be standardized, again using a phenolphthalein indicator. These titrations were used to ascertain the precise concentration of the HCl solution according to reaction 2.14. Because NaOH solutions can form sodium carbonates over time upon exposure to air, and because they may attack glass and quartz containers, a fresh NaOH solution was utilized for each standardization, and both the KHP-NaOH titrations and the HCl-NaOH titrations were completed within a few hours of one another.

2.4.2.2 Standardization of $Na_2S_2O_3$ titrant

Potassium iodate (KIO_3, Sigma Aldrich) is reasonably non-hygroscopic and stable to air. A potassium iodate solution of known concentration between 0.05 and 0.02 M was prepared using an analytical balance and a certified volumetric flask. Between fifty and thirty 100 to 400 μL aliquots were measured by volumetric pipette to be titrated in a random order. For each titration, 5 mL of a 2 wt% solution of KI in H_2O and 5 mL of 3.5 M H_2SO_4 were added to the KIO_3 aliquots to provide an excess of I^- and H^+ for the following reaction:

$$IO_3^- + 5I^- + 6H^+ \rightarrow 3I_2 + 3H_2O \tag{2.18}$$

The I_2 produced was titrated with the $Na_2S_2O_3$ to be standardized, following reaction 2.16. The concentration of the $Na_2S_2O_3$ solution was then determined by the stoichiometry of reactions 2.16 and 2.18.

2.5 Scanning Electron Microscopy

Scanning electron microscopy (SEM) measurements were performed on cathodes extracted from Na-O_2 cells both following discharge at various O_2 pressures and following discharge

and (partial or complete) charge. The methods described here are consistent with those reported in our prior studies.[1,2,51] Following electrochemical measurements, the cells were flushed with Ar and transferred to an Ar-filled glovebox. The cells were disassembled and the cathodes were extracted and rinsed briefly in DME to remove residual electrolyte salts. The cathode was placed in a clean glass vial and transferred to a vacuum chamber connected to the glovebox for ∼5 min of drying to remove residual solvent. Following drying, the vials were removed from the vacuum chamber to the glovebox and the cathodes were mounted on an SEM sample holder. Some cathodes were cut in half with a pair of clean scissors and mounted with opposite sides face-up for direct comparison between the two sides of the cathode. As a control, a pristine cathode was mounted as prepared for use in a cell, without exposure to electrolyte or rinsing in solvent.

To prevent exposure to ambient atmosphere, the sample holder was stored in an airtight glass bottle under an Ar atmosphere for transport to the SEM facility, and then transferred rapidly into the SEM chamber. The time from opening the glass bottle to the commencement of the SEM loading chamber pump down was less than 1 min. This brief exposure prohibited quantitative chemical analysis in the SEM (e.g., by energy-dispersive X-ray spectroscopy), but any change in the morphology of the NaO_2 discharge product was likely negligible during this time.

Measurements were performed using a JEOL JSM-7500F SEM operating in gentle beam (GB) mode with an emission electron current of 10.0 μA, an accelerating voltage of 1.00 kV, a sample bias voltage of 1.50 kV, and a work distance between 6.0 mm and 8.0 mm. These acquisition parameters were observed to minimize beam damage to the samples due to NaO_2's low electronic conductivity. However, some beam damage to visible NaO_2 crystals was observed in every case, and could be used as a qualitative indicator of the presence or absence of NaO_2. The images presented in this work were acquired with a through-lens secondary electron detector.

2.6 Conclusion

In this chapter, I have presented the experimental methods used to obtain the results discussed in this dissertation. In addition, I have presented the reasoning and decisions behind novel cell designs, experimental or theoretical approaches, and the acquisition and analysis of data. Reference will be made in later chapters to relevant sections of this chapter. In the following chapters I will discuss the experimental results and the conclusions drawn from them, as well as future studies that may provide further insight into the fundamental electrochemistries of the Na-O_2 and Mg systems.

Chapter 3

The Discharge Sudden Death Phenomenon in Na-O_2 Batteries

This chapter adapted with permission from Nichols, J. E.; McCloskey, B. D. *J. Phys. Chem. C* **2017**, *121* (1), 85–96.

3.1 Abstract

Metal-air (O_2) batteries have been studied over the past decade as potential high-energy alternatives to current state-of-the-art Li-ion batteries. Although Li-O_2 batteries possess higher theoretical specific energies, Na-O_2 cells have been reported to achieve higher capacities on discharge and exhibit much lower overpotentials on charge than analogous Li-O_2 cells. Nevertheless, sudden and large overpotential increases ("sudden deaths") occur in Na-O_2 cells on both discharge and charge, substantially limiting achievable capacity on discharge and increasing the average charge voltage, thereby reducing round-trip energy efficiency. In this chapter, we unravel the origins of the sudden death phenomenon on discharge, which have been previously linked to the electrochemistry occurring at the cathode. The maximum capacity on discharge was limited by pore clogging at low current densities and by surface passivation at high current densities, with concentration polarization playing only a small role in limiting the achievable capacity.

3.2 Introduction

Among the various "beyond Li-ion" battery technologies, the highest theoretical specific energies are those of the nonaqueous metal-O_2 batteries, such as the Li-O_2 and Na-O_2 batteries. While nonaqueous Li-O_2 batteries in which Li_2O_2 is formed as the discharge product have a very high theoretical specific energy,[9,24,25,110] the nonaqueous Na-O_2 battery has been reported as a possible alternative.[11,29,32,33] Despite its lower theoretical specific

energy (1100 Wh kg^{-1} for Na-O_2 vs. 3450 Wh kg^{-1} for Li-O_2), sodium's natural abundance and lower cost make large-scale implementation economically attractive.[8] Recent studies on the Na-O_2 battery chemistry have reported potential advantages over analogous Li-O_2 systems, including improved stability and lower overpotentials, particularly on charge.[14,15,28–31] These advantages are at least partially attributed to the differences in discharge products between the two systems.[30] In batteries employing an electrolyte with an anhydrous ethereal solvent, the Na-O_2 battery reaction has been convincingly shown to be the one-electron reduction and oxidation of O_2 to NaO_2:[30,39,40,43,45]

$$Na^+ + O_{2(g)} + e^- \rightleftharpoons NaO_{2(s)} \qquad E^0 = 2.27\,V \text{ vs. } Na/Na^+ \tag{3.1}$$

In addition, subsequent studies have shown that Na-O_2 batteries are highly sensitive to operating conditions and contaminants, leading to changes in capacity, discharge product morphology, and overall cell performance.[38,40,41,50,52,53]

As discussed in Section 1.3, typical Na-O_2 cells are observed to undergo a "sudden death" during discharge at a capacity well below what would be expected from either complete Na or O_2 consumption.[1,8,39,40,44] This sudden death is a precipitous decrease in potential which signifies the end of discharge, and is reminiscent of a similar phenomenon observed during discharge in Li-O_2 batteries.[55]

In this chapter, we examine in detail the sudden death occurring on the first discharge of the Na-O_2 battery. We consider the maximum cell capacity achieved on discharge and the associated deposition of NaO_2 at various current densities. By examining the discharge product and cell behavior preceding and following sudden death, we provide insight into the factors limiting overall cell discharge capacity. In particular, our evidence suggests that sudden death on discharge is caused primarily by pore blocking or clogging due to large NaO_2 crystal formation at low current densities and by passivation due to a more conformal NaO_2 film deposition at high current densities. These findings are consistent with our prior report.[51]

3.3 Methods

Experimental methods are discussed in detail in Chapter 2. A custom-built cell of a modified Swagelok design was used in this study and has been previously described in detail (Section 2.2.1.1).[15,30] Materials and cell assembly procedures are given in Section 2.2.1.2 and are consistent with our prior report.[51] Constant-pressure galvanostatic discharges were performed under pure O_2 at pressures around 1.4 atm as described in Section 2.1.1.1. Quantitative iodometric titrations of hydrogen peroxide formed from extracted cathodes were used to verify the identity of the discharge product and efficiency of O_2 conversion to NaO_2 as described in Section 2.4 and as previously applied in the Na-O_2 and Li-O_2 systems.[14,30] Additional quantitative characterizations of cell performance during discharge were performed using pressure-rise/decay techniques (Section 2.1.1), which we have previously described.[15,30] Electrochemical methods are described in Section 2.3.1, and the discharge capacity at sudden

death was taken to be the total capacity of the cell at 1.0 V. Samples for characterization with scanning electron microscopy (SEM) were prepared using methods described in Section 2.5 and consistent with our prior study.[51]

3.4 Results and Discussion

3.4.1 Influence of discharge current density on discharge sudden death

Representative constant-current discharge profiles are given in Figure 3.1a. O_2 reduction to form NaO_2 was the dominant process in all of these measurements. Iodometic titrations on discharged cathodes confirm high conversion of O_2 to NaO_2, averaging 94% yield regardless of current density. Furthermore, cells titrated following sudden death show no significant quantitative differences in discharge product formation yields relative to cells discharged to capacities prior to sudden death. Separate pressure decay experiments to sudden death demonstrate an average 1.02 $\pm$ 0.02 e^-/O_2 consumption (Figure 3.2), with most of the deviation from ideal occurring in the final 5% of discharge; this is in part an experimental artifact due to evaporation of the electrolyte at low pressures, and titration of similarly prepared cells indicated typical 94% yields for NaO_2 formation both prior to and following sudden death under pressure decay and constant-pressure conditions. The slightly lower capacity in Figure 3.2 than that achieved under constant pressure is consistent for all cells discharged under pressure decay conditions and is a consequence of O_2 consumption resulting in a lower operating pressure; the influence of pressure on cell capacity will be discussed in detail in Chapter 4. These O_2 consumption values and NaO_2 yields are consistent with previous results when using NaOTf that had been rigorously purified,[30] indicating that minor impurities have little influence on final product composition on the first discharge, in agreement with another study.[45] We note that extraordinary electrolyte purification procedures have resulted in differences in the electrochemistry, as have large H_2O concentrations.[41,43,50,111] We consider these impurity ranges outside the scope of this work. We also note that proton induced phase-transfer catalysis, as described by Xia et al.,[41] is essentially equivalent to enhancing solubility of reduced oxygen species, such that if this phase transfer catalyst mode is active, it would simply enhance the rate of any solution-based mechanisms that we hypothesize here.

A few clear observations are derived from Figure 3.1. First, as the current rate increases, the capacity at sudden death decreases (Figure 3.1b). Second, at moderate and low current densities, a voltage plateau is observed throughout most of discharge, with the plateau voltage decreasing with increasing current. Third, the occurrence of sudden death is marked by a precipitous drop in voltage, reminiscent of the sudden death also observed in Li-O_2 batteries.[9,55,112] This behavior has previously been observed in other Na-O_2 batteries under comparable discharge conditions.[29,30,40,41,44] Fourth, at higher current densities (1800 $\mu A/cm^2$, 3500 $\mu A/cm^2$), no plateau is observed; instead, a monotonically decreasing cell

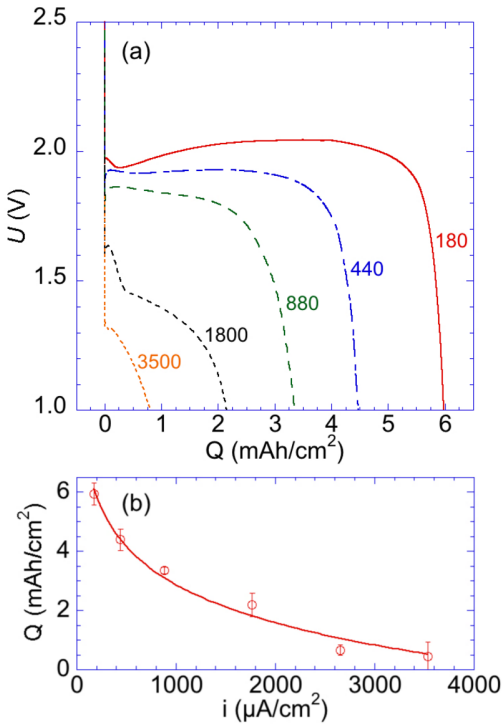

Figure 3.1: (a) Representative galvanostatic discharge profiles of Na-O_2 cells at various currents under 1.4 atm O_2. Numbers on each curve represent the current density, in $\mu A/cm^2$, normalized to the geometric surface area of the cathode. Voltages are reported as a full cell potential (i.e., without reference electrode). (b) Average cell discharge capacity at 1.0 V (sudden death) as a function of current. Error bars represent one standard deviation of between 2 and 6 cells. The line in (b) is solely to guide the eye.

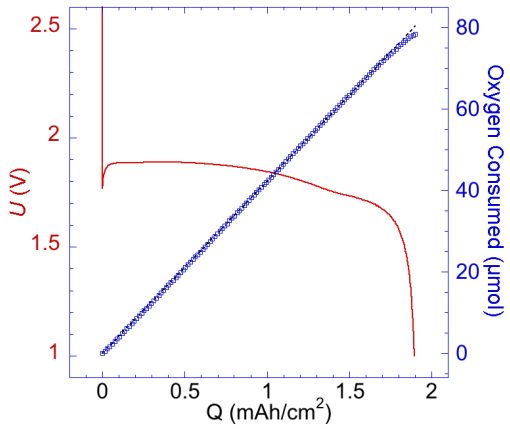

Figure 3.2: Discharge to sudden death with accompanying quantitative O_2 consumption data. The cell was discharged galvanostatically at 880 $\mu A/cm^2$ under a static, pure O_2 headspace. Overall O_2 consumption was 1.02±0.02 e^-/O_2 for the entire discharge. An ideal 1 e^-/O_2 process is indicated (dashed line).

potential rapidly falls to 1.0 V (taken to be sudden death). These profiles illustrate the results of several competing effects, and taken on their own do not strictly clarify the cause of the sudden death behavior. Prior studies have suggested a variety of causes, including pore clogging in the cathode decreasing the availability of O_2 and Na^+ for reduction and charge-transfer resistances at the cathode surface due to the deposition of solid, electronically insulating NaO_2.[37,41,56,113] Our recent impedance studies indicate that charge-transfer resistance is the most significant effect at current densities above 880 μA/cm^2 and pore clogging is most significant at lower current densities (440 μA/cm^2 and below) for our specific cell configuration.[51] The following sections will describe our efforts to further understand the mechanism of Na-O_2 deposition and isolate the causes for sudden death on discharge.

3.4.2 Influence of discharge current density on NaO_2 morphology

Na-O_2 cells were discharged at a variety of current densities to the same capacity (0.88 mAh/cm^2), and the cathodes were extracted for SEM imaging as described previously (Section 2.5).[51] In addition, the cathode of a cell discharged to sudden death at 3500 μA/cm^2 was imaged, as it was of comparable capacity (1.03 mAh/cm^2). Some variation in crystal morphology and size was found to occur on a given cathode, depending on location and other uncontrolled factors, and representative images collected from the side of the cathode facing

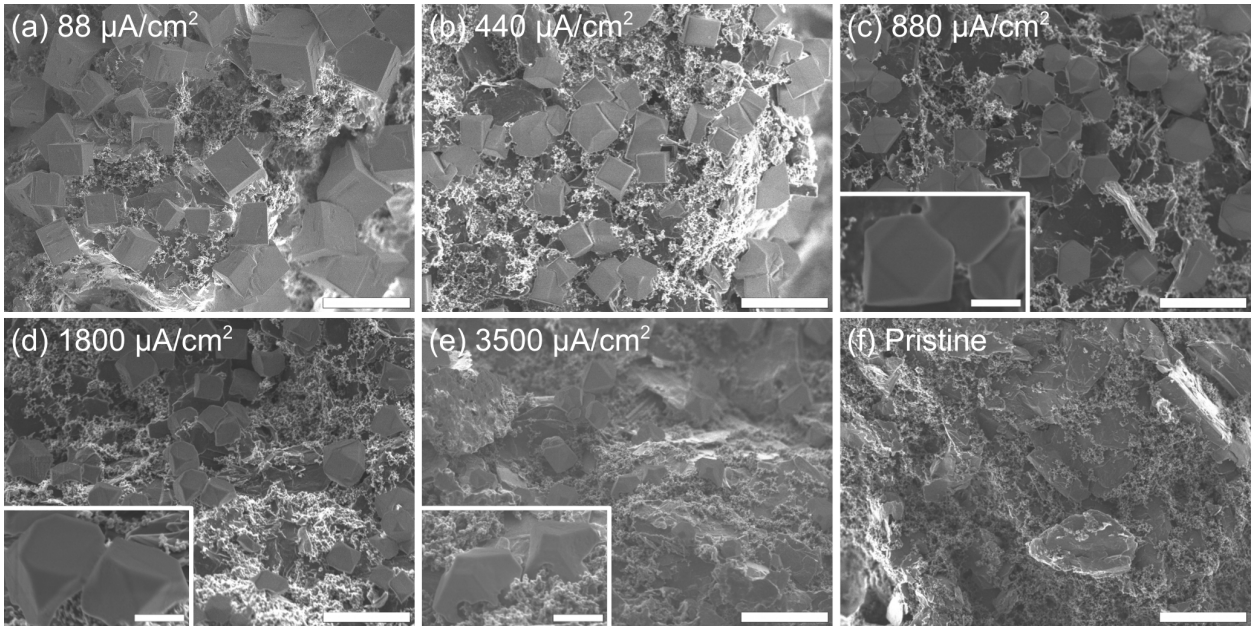

Figure 3.3: SEM images from cathodes discharged under 1.4 atm O_2 to 0.88 mAh/cm^2 at (a) 88 μA/cm^2, (b) 440 μA/cm^2, (c) 880 μA/cm^2, and (d) 1800 μA/cm^2. The discharge to sudden death at (e) 3500 μA/cm^2 and 1.03 mAh/cm^2 is also included as it represents a similar capacity. (f) A pristine cathode, included for comparison. Scale bars are 5 μm; inset scale bars are 1 μm.

the separator are presented in Figure 3.3. At low current densities (Figure 3.3a-b), the NaO_2 crystals are predominantly cubic, as has been widely reported, and relatively large (1μm - 5μm, depending on current density).[29,39,43,52] As the current density increases, fewer cubic structures are evident, and the appearance of smaller, truncated cubic structures becomes prominent (Figure 3.3c-d and insets). Qualitatively similar structures have been previously reported.[52] At high current densities, irregularly shaped small particles are observed, in addition to truncated cubic structures bearing some resemblance to those present at lower current densities (Figure 3.3e and inset). A clear general trend is that cathodes discharged at low current densities show significantly larger crystals than those at higher current densities. Indeed, at the highest current densities (e.g., 3500 $\mu A/cm^2$) the crystals can be difficult to distinguish from the pristine P50 surface. Comparable images collected from the side of the cathode facing the O_2 supply are presented in Figure 3.4. In general, crystals facing the separator are observed to be slightly smaller and more regularly shaped than those on the opposite side, though the general trend of decreasing crystal size with increasing current density is preserved.

Noting again that cathodes shown in Figure 3.3 all have statistically equal amounts of NaO_2 deposited on them, Figure 3.3 suggests that, as current rate increases, a larger amount of NaO_2 is deposited as a thin, unobservable conformal film rather than large crystals. This observation is supported by the fact that sample surface charging between visible NaO_2 crystals in the SEM was observed on all cathode surfaces shown in Figure 3.3, as would be expected if solid NaO_2, a wide bandgap insulator,[37,56,113,114] was conformally deposited on much of the cathode surface; no charging was observed when acquiring data from pristine samples of P50 cathodes. The trend of increasing NaO_2 deposition as a thin conformal coating with increasing current is reminiscent of similar observations in certain Li-O_2 cell compositions. A lithium superoxide dissolution-disproportionation electrochemical pathway has been proposed to explain these results.[23,26,115,116]

As previous reports also indicate,[41,43,46,50,53,113] a similar solution-based mechanism is clearly active in the Na-O_2 cells, albeit with two notable differences compared to Li-O_2 cells: 1) NaO_2 has been reported to be substantially more soluble than LiO_2 and Li_2O_2 in ether based electrolytes,[9,46,54,113] and 2) NaO_2 is the ultimate discharge product rather than Na_2O_2 in our cell configuration. Li_2O_2 solubility is not detectable in ether-based electrolytes,[9] and the solubility of LiO_2 is not known and difficult to measure. Nevertheless, it is likely less soluble than NaO_2 given that NaO_2 crystals grow to substantially larger sizes than Li_2O_2 toroids at similar discharge current rates, though this may also be due to NaO_2's superior stability.[9] Of note, after immersing a fully discharged Na-O_2 cathode (440 $\mu A/cm^2$) into $\sim$1 mL of fresh electrolyte, we could barely detect superoxide in the electrolyte using our titration protocol, allowing us to place an absolute upper limit for the saturated NaO_2 concentration in our electrolyte at 1 mM, consistent with a previously reported value of $\sim$0.1 mM.[113]

Given that NaO_2 is the ultimate discharge product, crystal growth occurs via a diffusion-nucleation/growth mechanism. Precipitation of NaO_2 occurs when its concentration saturation limit is achieved, which occurs very quickly even at the lowest rates used in this study.[41,50,113] For example, at a 100 μA discharge rate (i.e., 88 $\mu A/cm^2$), a 1 mM NaO_2

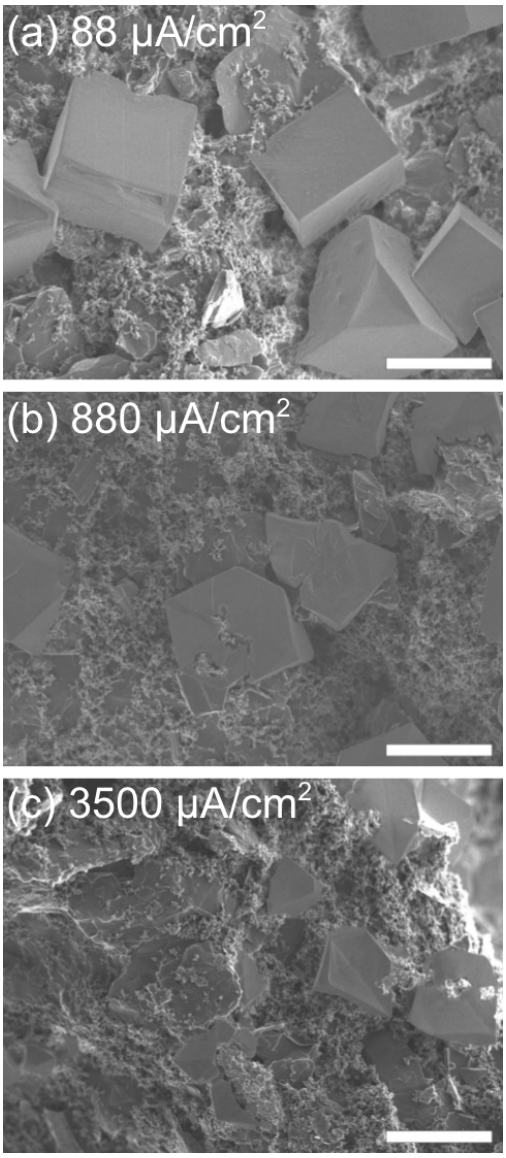

Figure 3.4: SEM images from the gas-facing side of cathodes discharged under 1.4 atm O_2 to 0.88 mAh/cm^2 at (a) 88 μA/cm^2 and (b) 880 μA/cm^2, and discharged to (c) 1.03 mAh/cm^2 at 3500 μA/cm^2 (sudden death). Scale bars are 5 μm.

saturation limit would be achieved in roughly 80 s in the electrolyte volume employed in our cells (80 μL). Of course, the dissolution-nucleation/growth mechanism results in the formation of large NaO_2 crystals at low rates, as would be expected from established crystal growth theory (Figure 3.5a).[117] At high rates, NaO_2 film deposition is similar to the aforementioned analogous surface mechanism in Li-O_2 batteries. If the current rate is sufficiently high (e.g., >880 μA/cm^2), saturation of NaO_2 likely occurs in thin electrolyte layers close to the cathode surface, thereby allowing more NaO_2 to deposit at the site where it is initially formed (i.e.,

at a growing NaO_2 film, Figure 3.5b). Nevertheless, truncated cubic NaO_2 crystals are still observed, indicating that the solution growth mechanism still accounts for a substantial fraction of NaO_2 formation, even at the highest currents rates studied.

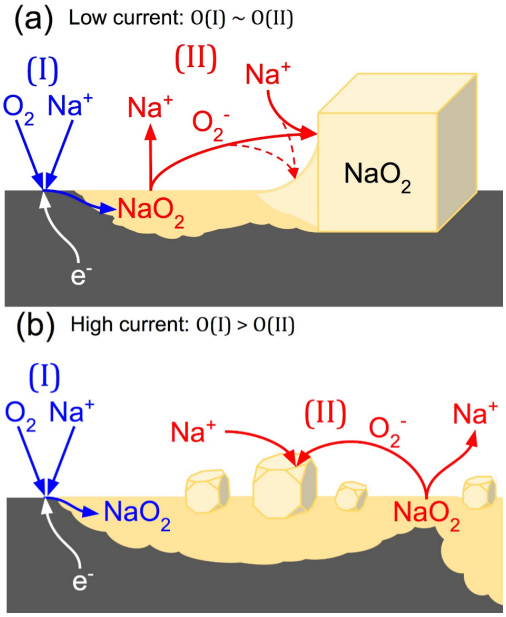

Figure 3.5: The proposed mechanism during discharge. O(x) indicates the order of magnitude of the overall rate of process x. (a) At low current rates, large cubic NaO_2 crystals form through a three-step process: the reduction of O_2 to NaO_2 (I), the dissolution and diffusion of O_2^-, and the nucleation/growth of large NaO_2 cubes (II) or thicker, porous films (dashed), which grow between crystals towards the end of discharge. Both NaO_2 films and NaO_2 cubes are observed to grow at low currents, although most NaO_2 likely deposits as large crystals. (b) At high currents, the same pathways occur, but the fraction of NaO_2 deposited as a thin film substantially increases. Therefore the initial step (I) proceeds at a much faster rate than the subsequent O_2^- dissolution/diffusion/crystal growth step (II).

3.4.3 NaO_2 crystal and film growth during discharge

Consistent with the observations from Figure 3.3, the NaO_2 films and large observable crystals both continuously grow during the course of discharge, as shown in Figure 3.6. During early stages of discharge, small NaO_2 crystals were observed to nucleate and grow (Figure 3.6b). As discharge continues, the additional capacity appears primarily due to the growth of existing crystals, as evident in the steady increase of crystal size in Figure 3.6b-d. At later stages of discharge, a thick surface film becomes visible between the crystals (Figure 3.6d inset). It appears that large crystal growth discontinues at some point during discharge in favor of growth of a very thick, porous film, which at sudden death (Figure 3.6e) has completely covered the cathode surface between the large crystals. The reason

for this transition is not entirely clear, although it may be a result of crystal site poisoning that inhibits large cubic crystal growth. At these rates, this clearly observable thick film very likely grows through the solution mechanism, since the surface mechanism would only allow approximately nanometer-thick films to grow.[55] For comparison, the morphology of deposited NaO_2 observed at sudden death following discharge at 3500 μA/cm^2 (Figure 3.3e) is consistent with a conformal coating formed through the surface mechanism, whereas the sudden death image at 880 μA/cm^2 (Figure 3.6e) is indicative of the thick film formed through a solution mechanism.[51,115]

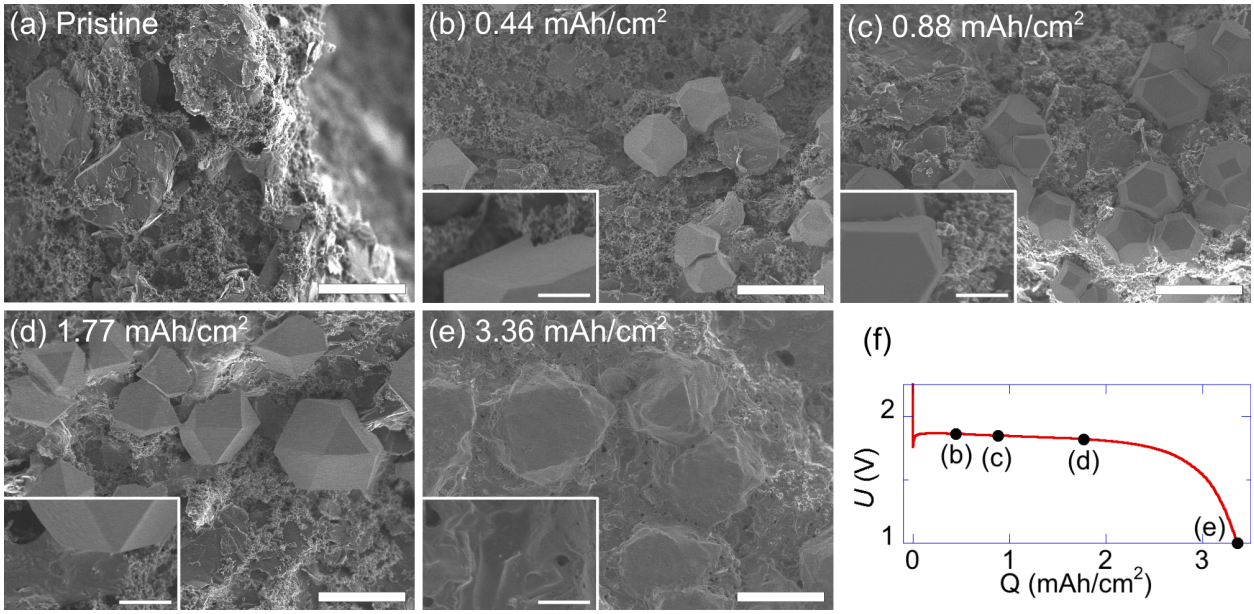

Figure 3.6: SEM images from cathodes discharged under an approximately constant 1.4 atm O_2 at 880 μA/cm^2 to a series of increasing capacities: (a) a pristine cathode, (b) 0.44 mAh/cm^2, (c) 0.88 mAh/cm^2, (d) 1.77 mAh/cm^2, and (e) sudden death at 3.36 mAh/cm^2. Scale bars are 5 μm; inset scale bars are 1 μm. The associated representative discharge profile (f) with capacities indicated.

3.4.4 Relaxation studies to elucidate the influence of surface passivation vs. pore clogging

Surface NaO_2 coatings could result in sudden death from either pore clogging or an increased charge transfer resistance due to surface passivation. Two relaxation studies were performed to further examine the causes of sudden death at various current rates (Figure 3.7). In the first, a cell was discharged to sudden death at 440 μA/cm^2; upon reaching sudden death, the current density was immediately decreased to 180 μA/cm^2, then again to 88 μA/cm^2 when sudden death was observed. This cell achieved little additional discharge capacity upon decreasing the current, suggesting that the cause for sudden death at 440 μA/cm^2 and below is pore clogging. Constriction of pores eliminates Na^+ and O_2 transport to the

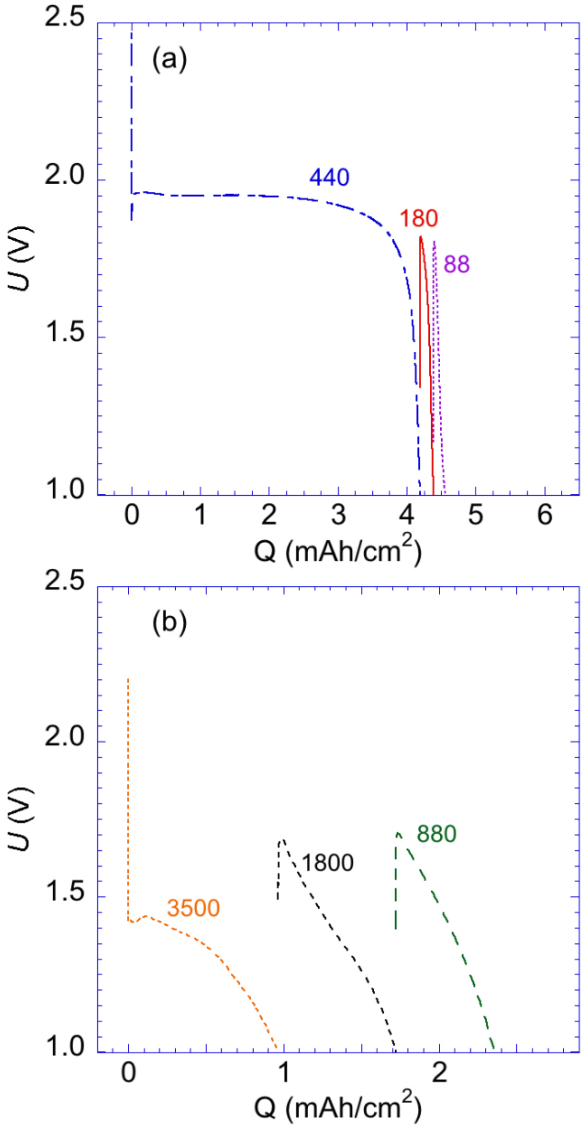

Figure 3.7: (a) Discharge profiles for a cell initially discharged to sudden death at 440 μA/cm^2. Upon achieving a 1.0 V full cell potential (i.e. sudden death), the current was immediately decreased to 180 μA/cm^2, then again to 88 μA/cm^2. (b) Analogous discharge profiles for a cell discharged to sudden death at 3500 μA/cm^2, then at 1800 μA/cm^2 and 880 μA/cm^2. Both cells were discharged under approximately constant O_2 pressure (1.4 atm). Current densities for each discharge are indicated in μA/cm^2.

cathode surface, thereby disallowing further discharge regardless of current rate. Of note, a simple calculation indicates that roughly 35% of the P50 pore volume is occupied by NaO_2 following the sudden death at 440 μA/cm^2 (assuming a pore volume percent of 80% in the P50, a thickness of 130 μm, and NaO_2 density of 2.2 g/cm^3). Substantial pore volume is still available for NaO_2 deposition, implying that optimizing the electrode porosity could further

improve cell capacity.

Using a similar relaxation measurement on cells discharged at higher currents (Figure 3.7b), a greater than twofold increase in total capacity was observed following discharge to sudden death at 3500 μA/cm^2 by successively relaxing to 1800μA/cm^2, then to 880 μA/cm^2. Following the initial 3500 μA/cm^2 sudden death in Figure 3.7b, the pore volume is estimated to be only approximately 9% occupied, roughly a fourth of the volume occupied when pore clogging was the primary cause of sudden death in Figure 3.7a. In this case, our results suggest that surface passivation by insulating NaO_2 films is primarily responsible for sudden death, and therefore decreasing the current density reduces the overpotential due to charge-transfer resistance and allows further discharge. Both relaxation results in Figure 3.7 agree with our previous impedance spectroscopy study.[51] Also of note, Na^+, O_2, and O_2^- concentration gradients appear to contribute to sudden death, although only to a minor extent. Following sudden death, relaxation at open-circuit potential is expected to alleviate any O_2, O_2^- or Na^+ polarization contributions. However, little additional discharge capacity (13%, 4%, and 2% at 3500, 1800, and 880 μA/cm^2, respectively) is observed when discharge is attempted again at the original current rate following an hour relaxation to open-circuit potential (Figure 3.8).

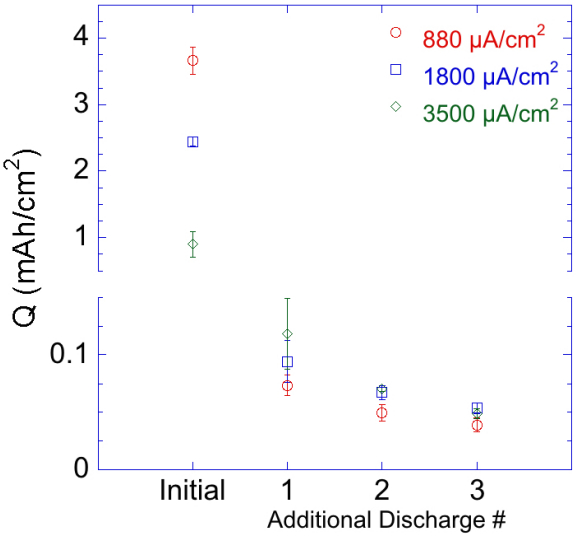

Figure 3.8: Capacities of cells discharged initially to sudden death, then discharged again at the same current after 1 hour of relaxation. Relaxation and attempted discharge were repeated twice more. Note the axis break and change in scale; little additional discharge capacity was achieved following sudden death.

3.5 Conclusions

In this chapter, we have examined the possible causes and mechanisms of the sudden death of Na-O_2 cells on discharge, and the relationship between discharge current density and sudden death. We confirm previous reports of the 1 e^-/O_2 reduction to NaO_2 on discharge with minor parasitic side reactions. The achievable Na-O_2 discharge capacity significantly decreases with increasing current density, and our data suggest that NaO_2 deposition occurs through a combined surface and solution mechanism that deposits NaO_2 as a thin conformal film and large cubic crystals, with the relative extent of each depending on current density. At low current densities, we confirm pore clogging is the primary limiting factor to capacity, whereas at high current densities, passivation is the primary limiting factor. These limitations result from the morphologies of the electronically insulating NaO_2 formed during discharge. At low current densities we observe the formation of large, cubic NaO_2 crystals that can constrict overall porosity, whereas at high current densities we observe small, irregularly shaped particles interspersed in a thin, conformal NaO_2 layer that coats the cathode. In fact, in all cases, we observe evidence of a thin NaO_2 conformal layer between larger NaO_2 particles, which grows thicker and eventually covers the surface at sudden death. A very thick porous film, which is clearly observable at sudden death, can also grow between large crystals through the solution-mediated process at low and moderate current densities. While NaO_2 is only minimally soluble in the electrolyte, this solubility appears sufficient to promote the formation of large crystals at low current densities and support the solution mechanism on discharge. Though sparing, NaO_2 solubility appears to be significantly greater than that of the intermediates and discharge products in Li-O_2 cells,[113] accounting for the larger NaO_2 crystals that result in the pore-clogging sudden death mechanism observed at low current rates; note that no such pore clogging has been reported in similar Li-O_2 cells.[118] In addition, we demonstrate that O_2, O_2^-, and Na^+ polarization are not significant limiting factors to cell discharge capacity, only contributing a small fraction to the overall capacity limitations on discharge even at high current rates. In the following chapter we will continue our discussion of the Na-O_2 sudden death phenomenon on discharge, with particular attention to the interaction between current density and O_2 pressure.

Chapter 4

The Influence of O_2 Pressure on Spatial NaO_2 Deposition and the Sudden Death Mechanism

This chapter adapted with permission from Nichols, J. E.; Knudsen, K. B.; McCloskey, B. D. *J. Phys. Chem. C* **2018**, *122* (25), 13462–13472.

4.1 Abstract

Over the past decade, metal-O_2 batteries have been studied as potential high energy density alternatives to current state-of-the-art Li-ion batteries. Of these, nonaqueous Na-O_2 batteries offer high stability, improved full-cycle efficiency, and lower overpotentials, particularly on charge, when compared to the higher-energy-density Li-O_2 system. However, Na-O_2 batteries exhibit sudden and large overpotential increases or "sudden deaths" on discharge, substantially limiting the achievable capacity. In this chapter, we expand upon the previous chapter by examining the influence of O_2 pressure effects in Na-O_2 batteries and the mechanism of sudden death at different O_2 pressures and current density regimes. We observe that at a given current density, there exists a transition between failure mechanisms with O_2 pressure as a result of different phenomena related to the deposition of the solid discharge product, sodium superoxide (NaO_2). Cells operated at a lower O_2 pressure are more susceptible to failure due to surface passivation resulting from thin NaO_2 film coverage, whereas cells

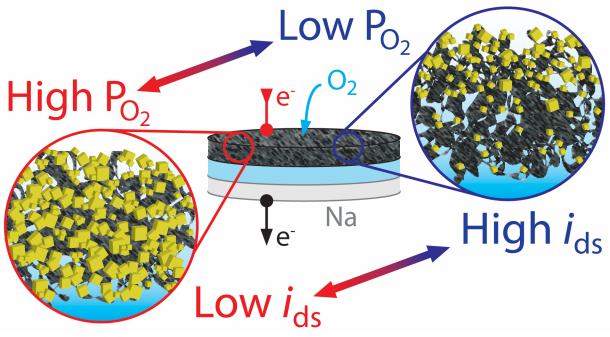

operated at a higher O_2 pressure achieve higher capacities but are increasingly subject to failure due to pore clogging from substantial solid NaO_2 deposition. We associate the transition between these failure mechanisms with a combination of electron and mass transfer effects, leading to dramatic differences in the spatial deposition of NaO_2 through the cathode.

4.2 Introduction

In the preceding chapter, we considered the discharge sudden death phenomenon of a Na-O_2 battery employing a nonaqueous ethereal solvent at a single pressure regime ($\sim$1.4 atm O_2).[1,51] Under these conditions, we reported two sudden death mechanisms, depending on the applied discharge current density. It is generally accepted that NaO_2 forms during discharge via a combined surface and solution mechanism, wherein O_2 is reduced to O_2^- at the cathode surface, and may form either NaO_2 surface films or dissolve and crystallize in larger cubic structures.[1,41,48,50,113] In general, we observed that at lower discharge current densities, cells were prone to failure due to blocking or "clogging" of the pores by large NaO_2 crystal growths, whereas at higher discharge current densities, cell failure resulted from passivation of the cathode surface due to the buildup of NaO_2 thin films. These findings are consistent with the observations of other studies.[39,41,50,52]

Because changes in current density result in different failure mechanisms, it is likely that the kinetic rate of reaction as compared to the rate of diffusion of reactants plays a significant role in the mechanism of sudden death. Thus, we chose to focus on the dependence of the sudden death capacity on the concentration of available reactants, and particularly the partial pressure of O_2, which could vary over an enormous range. While high O_2 concentration and more rapid O_2 flux in the liquid phase are expected at high pressures, higher-pressure O_2 supplies are also likely to carry greater costs and decrease the practical energy density of Na-O_2 batteries due to the requirement of additional gas handling equipment. It is essential, therefore, to examine the dependence of Na-O_2 cell discharge capacity and sudden death on the O_2 partial pressure.

In this chapter, we examine the performance of the Na-O_2 cell chemistry under four significantly different O_2 partial pressures to evaluate cell discharge capacity and determine the causes for cell failure for each region. We observe that at a given current density, a transition in the sudden death failure mechanism occurs. At low pressures, Na-O_2 cells are more susceptible to failure as a result of surface passivation, while at high pressures, Na-O_2 cells exhibit increased resistance within the pores of the cathode consistent with a pore-clogging failure mechanism. The transition pressure between failure mechanisms depends on the current density, with failure due to pore clogging becoming evident at lower pressures for lower current densities. These findings emphasize the importance of monitoring and reporting cell operating pressure when studying capacity limitations in the Na-O_2 battery system and the need to engineer cathodes with appropriate porosities to accommodate the discharge product.

4.3 Methods

Experimental methods are discussed in detail in Chapter 2. A custom-built cell of a modified Swagelok design was used in this study and has been previously described in detail (Section 2.2.1.1).[15,30] Materials and cell assembly procedures are given in Section 2.2.1.2 and are consistent with our prior report.[51] Prior to discharge, all cells were thoroughly leak-tested at an above-atmospheric pressure. Constant-pressure galvanostatic discharges were performed under pure O_2 at pressures around 0.4, 0.8, 1.4, and 2.0 atm as described in Section 2.1.1.1. Pressure data and discharge profiles for representative cells at each pressure regime used in this work are available in Figure 4.1. Separate quantitative characterizations of cell performance during discharge were performed using pressure-rise/decay techniques (Section 2.1.1), which we have previously described (Chapter 3).[1,15,30] Samples for characterization with scanning electron microscopy (SEM) were prepared using methods described in Section 2.5 and consistent with our prior study.[51]

Quantitative iodometric titrations of hydrogen peroxide formed from extracted cathodes were used to verify the identity of the discharge product and efficiency of O_2 to NaO_2 as discussed in Section 2.4 and as previously described.[1,14,30] Additionally, to give quantitative insight into NaO_2 deposition trends throughout the cathode, some cells were assembled using two carbon paper discs instead of one, as described in Section 2.2.1.3. Upon cell disassembly, these discs were separated for iodometric titration. We emphasize that because both cathode surface area and thickness are approximately doubled in this case, the results at a stated two-cathode current density are not directly analogous to single-cathode discharges at either the same or half the cross-sectional current density. For consistency, current densities and capacities in these cells are normalized to the geometric cross-sectional area of the cathode.

Electrochemical methods for galvanostatic discharge are described in Section 2.3.1, and the discharge capacity at sudden death was taken to be the total capacity of the cell at 1.0 V. Electrochemical impedance spectroscopy (EIS) was performed as described in Section 2.3.2; an equivalent circuit diagram is shown in Figure 2.6, and this section discusses in detail the normalization and fitting of the parameters. The main source of error in these calculations was the BET surface area and the error bars in Figures 4.6 and 4.10 to 4.12 are based on this uncertainty.[51]

4.4 Results and Discussion

4.4.1 Overall trends observed with O_2 pressure

4.4.1.1 NaO_2 is observed as the dominant discharge product regardless of current density or O_2 pressure

The cells considered throughout this chapter were operated at a constant pressure; however, separate pressure decay measurements of otherwise identical cells indicate that a 1 e^-/O_2 reduction of O_2 to form NaO_2 was the dominant reaction (see Figure 3.2).[1,30] Iodometric

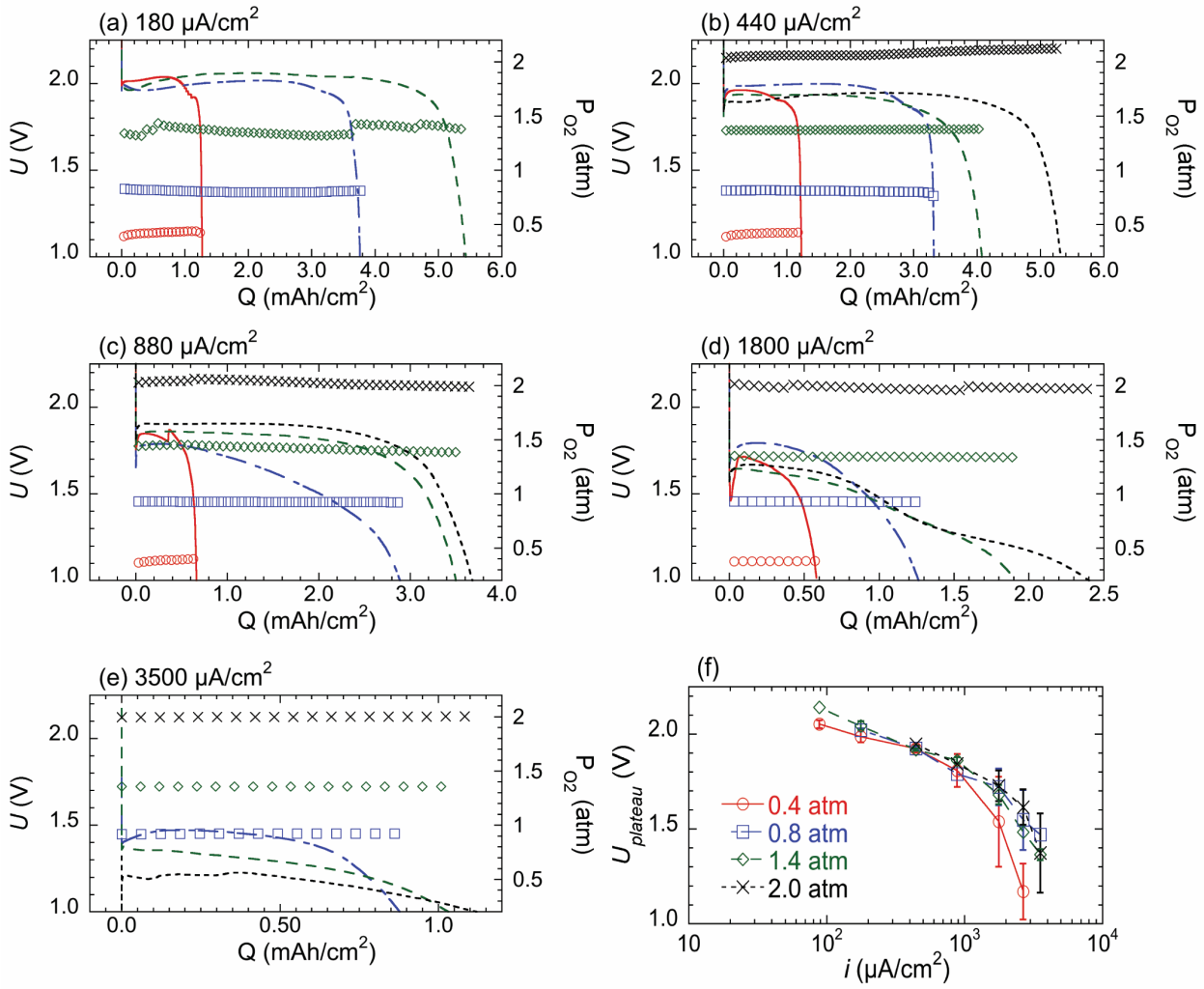

Figure 4.1: Representative discharge profiles for cells discharged at (a) 180 μA/cm^2, (b) 440 μA/cm^2, (c) 880 μA/cm^2, (d) 1800 μA/cm^2, and (e) 3500 μA/cm^2 under approximate pressures of 0.4 atm (red —, circles), 0.8 atm (blue - –, squares), 1.4 atm (green - -, diamonds), and 2.0 atm (black —, x's). Pressure data acquired during discharge is given on the right-hand axis and indicated by points. In most cases, O_2 pressure varied by less than 0.04 atm during any given discharge. (f) Average highest potential achieved during discharge ($U_{plateau}$), where error bars indicate standard deviation of multiple cells. Points without error bars correspond to single measurements. The only cells with statistically different plateau potentials are those discharged at 0.4 atm and discharge current densities well above 10^3 μA/cm^2.

titrations confirm an average 94 ± 4% yield of NaO_2, depending slightly on pressure and current density, a dependence which will be discussed in greater detail later. These results are consistent with our previously reported results at 1.4 atm (Chapter 3),[1] and with other reports.[29,30,39,41,43,44] No evidence of Na_2O_2 formation was observed even at very low operating pressures, suggesting that a scarcity of O_2 as a reactant is not sufficient to drive further reduction of NaO_2, in agreement with prior studies.[40,42] Even if the cell pressure decreases below 0.25 atm during the operation of a pressure-decay cell, the primary cell reaction is a 1 e^-/O_2 process.[1] Additionally, since the cells throughout this study were operated at an approximately constant pressure, cell failure did not occur in any instance because of a total depletion of the O_2 supply.

4.4.1.2 Slightly lower NaO_2 yields are observed at lower current densities.

Since decreasing the current density significantly increases the time required for a same- or higher-capacity discharge, very low current densities approach timescales on which prior studies have indicated NaO_2 solubility and stability are of concern.[46] Accordingly, we observe slightly differing yields for conversion of O_2 to NaO_2 with decreasing current density, as measured by iodometric titration. For instance, cells discharged at low current densities (88 and 180 $\mu A/cm^2$) to very high capacities (>5 mAh/cm^2) consistently exhibit NaO_2 yields around 88-90%, compared to those at higher current densities and lower capacities, which can achieve 92-97% yield, averaging 94% overall in agreement with our prior study.[1,30] We note that we define yield as the ratio of actual amount of NaO_2 formed to NaO_2 expected to form given the total Coulombic capacity of the discharge. We attribute the difference in yields largely to the solubility of NaO_2 and the overall stability of the cell chemistry, such as NaO_2 diffusion to the sodium anode or to the instabilities of other cell components including the solvent and salt.[46,54] Since titrations of extracted separators indicate that little if any NaO_2 was present in the separator at the time of cell disassembly, dissolved NaO_2 that diffuses from the cathode is likely unstable. Overall, the titration data indicate that at all current densities, capacities, and pressures involved, the primary discharge product was NaO_2, and that electrochemical conversion of O_2 to NaO_2 is improved at high current densities.

4.4.1.3 Increasing O_2 pressure increases attainable capacity, particularly at low discharge current densities

To elucidate the overall dependence of discharge capacity on operating pressures, Na-O_2 cells were discharged at six current densities and four discharge pressure regimes. The resulting average discharge capacities versus the O_2 pressure are summarized in Figure 4.2. At nearly all current densities studied, increases in pressure result in an increase in discharge capacity. This change was most dramatic for cells discharged at low current densities (e.g., 180 and 440 $\mu A/cm^2$), where an approximately threefold increase in achievable discharge capacity over the range of pressures studied was obtained. At moderate to high current densities (e.g., 880 to 1800 $\mu A/cm^2$), beyond a certain pressure the gains resulting from increases in pressure

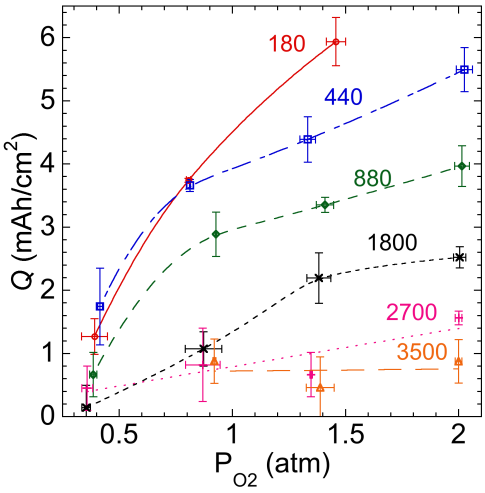

Figure 4.2: Average sudden-death discharge capacity of Na-O_2 cells at various current densities (indicated in μA/cm^2) as a function of average discharge pressure (P_{O2}). Discharge pressure was maintained to be approximately constant for each cell. At low discharge currents a strong dependence of capacity on O_2 pressure is observed; at high discharge currents this dependence is weaker. Note that lines are intended solely to guide the eye. Y error bars represent standard deviations of multiple cells for capacities and x error bars represent the pressure variation of those cells.

are limited, while at the highest current densities (e.g., 2700 μA/cm^2 and greater), little to no advantage in capacity was gained by increasing the discharge pressure. This result was not surprising if, like in our previous studies at 1.4 atm, sudden death at higher current densities was primarily due to an increase in the carbon/electrolyte interfacial charge-transfer resistance, and thus independent of mass transport.

Notably, the highest discharge capacity observed was roughly 6 mAh/cm^2, regardless of current density or O_2 pressure, which corresponds to roughly 50% of the total cathode porosity being occupied by insoluble NaO_2 at the end of discharge (assuming a pore volume percent of 80% in the P50, a thickness of 130 μm, and an NaO_2 density of 2.2 g/cm^3). While lower current densities might be expected to increase the capacity at sufficiently high pressures, this does not appear to be the case. For example, a cell discharged at 88 μA/cm^2 near 1.4 atm resulted in a capacity of 5.7 mAh/cm^2 (Figure 4.3), which is statistically comparable to or less than the capacity of cells discharged at 180 μA/cm^2 (Figure 4.2). This finding reiterates our prior suggestion that optimizing the porosity of the cathode may be important in maximizing the achievable discharge capacity, and suggests that pore clogging is primarily responsible for cell failure at low current densities and high pressure regimes.[1,51]

4.4.2 Na-O_2 cell behavior by pressure regime

While the trend in capacity with operating pressure is clear from a galvanostatic discharge study (Figure 4.2), its cause is not immediately apparent. Additionally, while our prior

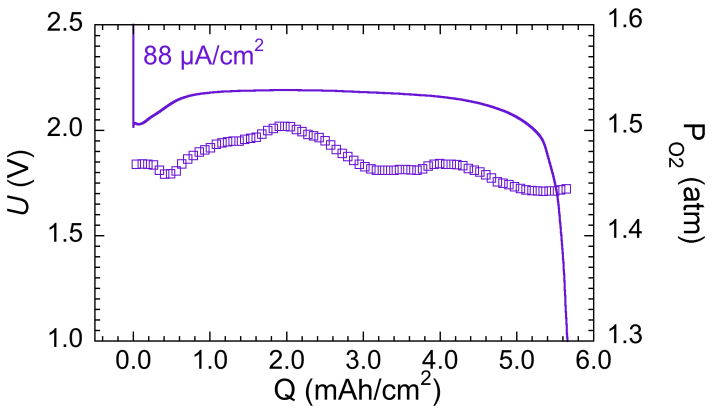

Figure 4.3: Discharge of a cell to sudden death (5.66 mAh/cm^2) at 88 μA/cm^2 with accompanying pressure data. Temperature variations over the course of the 64-hour discharge affected the pressure of the O_2 supply, resulting in the slightly higher O_2 pressures than the typical 1.4 atm cell.

studies elucidated the behavior of the Na-O_2 system, we considered only one pressure regime (1.4 atm, Chapter 3). We sought to elucidate the results at all pressure regimes with a combined EIS and SEM study. EIS was performed at four different current densities between 180 and 1800 μA/cm^2 and at four different pressure regimes from 0.4 to 2.0 atm. These conditions allowed a sufficient discharge capacity for a larger number of impedance spectra, making it possible to study the mechanism of failure. We studied cathodes of cells discharged at low current densities (180 and 440 μA/cm^2) using SEM, as these exhibited the greatest variation in discharge capacities over the full range of pressures (0.4 to 2.0 atm). To capture possible variations in product morphology across the cathode, SEM data were acquired from both sides of the cathode, with the side adjacent to the separator designated the "Na side" and the side facing the O_2 headspace designated the "O_2 side." The results of the SEM study are presented in Figure 4.4, which shows SEM images of discharged cathodes at sudden death (1.0 V) at 440 μA/cm^2, while Figure 4.5 presents images of cathodes discharged at 180 μA/cm^2 to sudden death and a pristine cathode for comparison (Figure 4.5g). Across the full range of pressures considered we observe that at both 180 and 440 μA/cm^2 product deposition, distribution, and morphology depends strongly on O_2 pressure. The details and implications of this observation are discussed below in the context of the EIS results for each pressure regime.

4.4.2.1 Na-O_2 cell behavior at low O_2 pressures (0.4 atm)

Figure 4.6 presents the evolution of three key parameters (R_{CT}, R_i, and $C_{Cathode}$) contributing to the changes in the cell's potential during discharge at 0.4 atm. R_{CT}, the charge-transfer resistance at the cathode surface, corresponds to the rate of O_2 reduction and NaO_2 formation at the cathode. Increases in R_{CT} are generally indicative of passivation of the active cathode surface, such as by the deposition of electronically insulating films. R_i represents the ionic

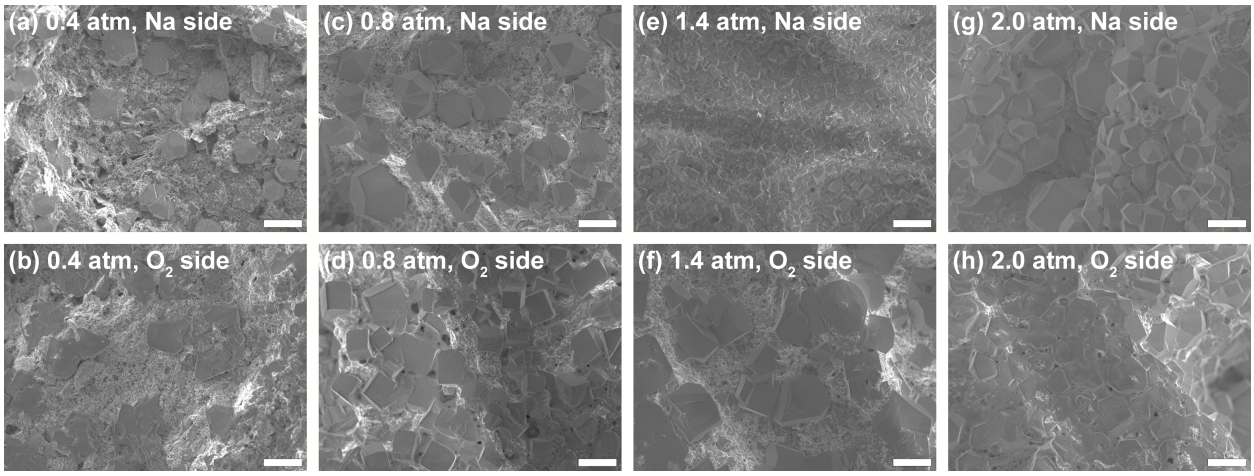

Figure 4.4: SEM images of cathodes following discharge to sudden death (1.0 V) at 440 μA/cm^2. Each cell was discharged under an approximately constant O_2 pressure and a sudden death capacity of (a-b) 0.4 atm and 1.23 mAh/cm^2, (c-d) 0.8 atm and 3.32 mAh/cm^2, (e-f) 1.4 atm and 4.08 mAh/cm^2, and (g-h) 2.0 atm and 4.76 mAh/cm^2. For each cathode, the side facing the separator and anode (a,c,e,g) and the side facing the current collector and gas supply (b,d,f,h) are imaged separately. Scale bars are 10 μm.

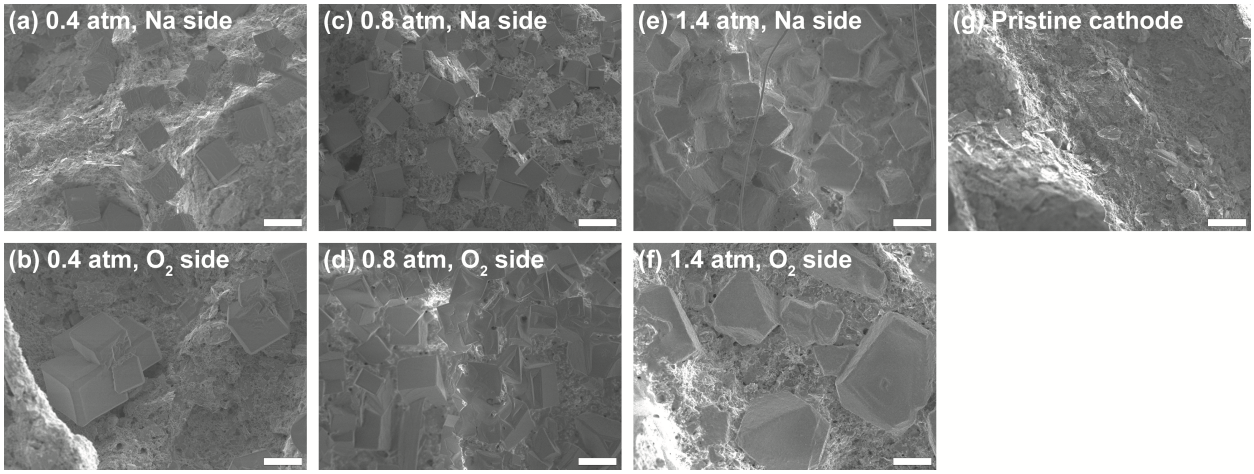

Figure 4.5: SEM images of cathodes following discharge to sudden death (1.0 V) at 180 μA/cm^2. Each cell was discharged under an approximately constant O_2 pressure and a sudden death capacity of (a-b) 0.4 atm and 1.26 mAh/cm^2, (c-d) 0.8 atm and 2.49 mAh/cm^2, and (e-f) 1.4 atm and 5.56 mAh/cm^2. For each cathode, the side facing the separator and anode (a,c,e) and the side facing the current collector and gas supply (b,d,f) are imaged separately. A pristine P50 cathode (g) is included for comparison. Scale bars are 10 μm.

resistance within the pores of the cathode. Increases in R_i generally indicate the blocking or clogging of the cathode pores, such as by growing NaO_2 crystals. $C_{Cathode}$ is a capacitance related to the cathode/electrolyte interface, the formation of NaO_2, and the NaO_2 interface with the electrolyte. Decreases in $C_{Cathode}$ are consistent with the passivation of the pristine cathode surface, typically by deposition of insulating films, and cathodes with a lower value of $C_{Cathode}$ are generally less active overall and accumulate less NaO_2. It should be noted that some limitations exist in employing EIS to examine cell failure. These become particularly evident at 0.4 atm, where EIS was only possible at 180 and 440 $\mu A/cm^2$ because the relative residuals from linear Kramers-Kronig transformations at higher current densities were too large as a result of the increasing overpotential.[104] Further details regarding EIS, including the equivalent circuit (Figure 2.6) and the parameter normalization and fitting are available in Section 2.3.2. Representative Nyquist and Bode plots at 0.4 atm corresponding to the data in Figure 4.6 are available in Appendix A.3 (Figure A.3).

Based on the observations in Figure 4.6, in cells operated at low O_2 pressures the discharge capacity is limited by an increase in the carbon/electrolyte charge-transfer resistance (R_{CT}), relative to those discharged under higher O_2 pressures. At these low O_2 partial pressures, the ionic resistance within the pores (R_i) and R_{CT} are similar during the early stages of discharge, but R_{CT} dominates the cell death. This indicates that the NaO_2 interface shunts electron transport and forces an increase in overpotential, and suggests that insoluble NaO_2 does not occupy a significant fraction of the pore volume. At 0.4 atm, SEM evidence (Figure

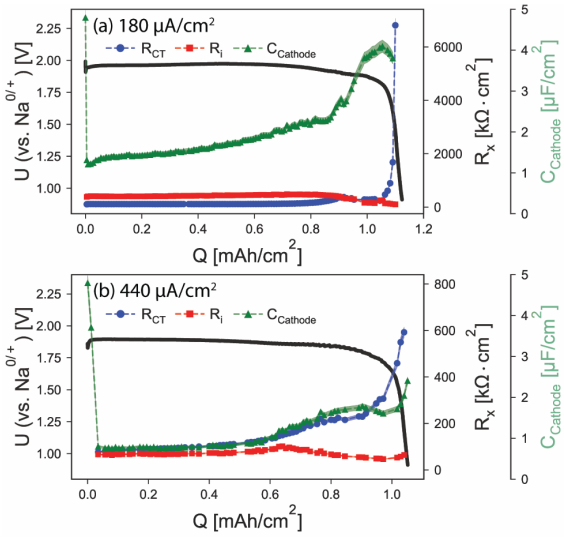

Figure 4.6: Electrochemical impedance spectroscopy analyses for cells discharged at an approximately constant pressure around 0.4 atm and an average current density of (a) 180 $\mu A/cm^2$ and (b) 440 $\mu A/cm^2$. The output resistances (charge-transfer resistance R_{CT}, and the ionic resistance within the pores R_i) from the impedance fits are plotted on the secondary axis R_x, while the effective capacitance of the cathode ($C_{Cathode}$) is plotted in green and corresponds to the third axis. The uncertainty of each variable is shown with shaded areas.

4.4a-b and 4.5a-b) suggests that pore clogging plays little to no role in sudden death, as the cathode surfaces and pores are clearly observable between large NaO_2 particles, implying that the porous structure is still accessible to reactants at sudden death. At 0.4 atm and 180 $\mu A/cm^2$ (Figure 4.5a-b), much of the discharge product appears to be present as 3-10 μm cubic crystals on the Na side and crystals as large as 30 μm on the O_2 side reminiscent of those observed in prior reports.[29,50] These findings are comparable with results observed at 440 $\mu A/cm^2$ (Figure 4.4a-b), though in this case, the crystal sizes on both sides of the cathode appear similar in size and are smaller overall (3-5 μm). Surface charging observed during image acquisition suggests that thin insulating NaO_2 films were present on the surface, a suggestion supported by images at higher-magnification where slightly thicker films are directly observable (Figure 4.7). The formation of NaO_2 films is also supported by the EIS results, since the cathode/electrolyte interfacial capacitance ($C_{Cathode}$) in these cells drops drastically at the beginning of discharge, suggesting that most of the electrochemically active cathode is instantaneously covered with a thin layer of NaO_2 (Figure 4.6 and Figure A.3).

While discharges at 880 $\mu A/cm^2$ and above experience cell failure too rapidly at 0.4 atm for changes in the cathode to be readily probed by EIS, it is reasonable to assume that, with increasing current density, cell failure can also be attributed to cathode passivation. This is consistent with additional relaxation measurements performed at 0.4 atm. In the first (Figure 4.8), following sudden death, the cells were immediately relaxed to a lower current density and allowed to continue discharge. The small but significant additional capacity achieved upon decreasing the current density, as much as 0.2 mAh/cm^2, suggests cell failure occurred primarily due to surface passivation, as the decreased current at the same R_{CT} yields a lower overpotential. In the second (Figure 4.9), cells were relaxed to open-circuit for an hour to allow re-equilibration of dissolved O_2. During this time, some NaO_2 films

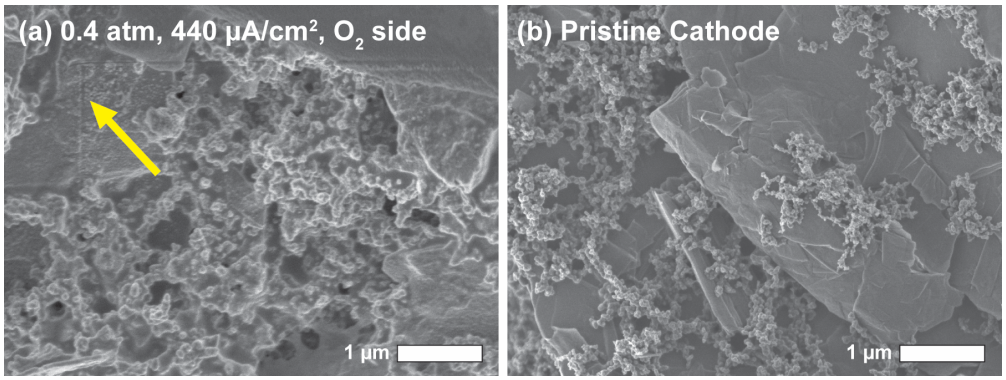

Figure 4.7: High-magnification SEM images demonstrating presence of surface films. (a) O_2 side cathode discharged under an approximately constant O_2 pressure of 0.4 atm and a sudden death capacity of 1.23 mAh/cm^2, comparable to Fig. 4b. Sample damage, indicative of the presence of insulating NaO_2, is indicated (yellow arrow). Conformal films over the carbon structure are apparent in comparison to (b) a pristine cathode imaged at the same magnification with identical image acquisition parameters. Scale bars are 1 μm.

may also dissolve. Following relaxation, the cells were discharged again at the same current density, and achieved small but significant additional capacities, large enough to suggest that the availability of dissolved O_2 or the buildup of thin NaO_2 films may have played a role in cell failure.

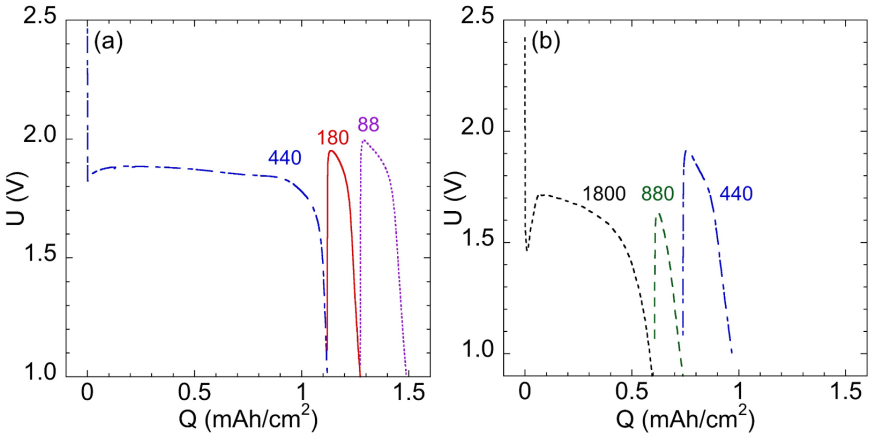

Figure 4.8: Results from successive relaxations to decreasing currents at (a) 440, 180, and 88 μA/cm^2, and (b) 1800, 880, and 440 μA/cm^2 under a headspace of 0.4 atm O_2. Each lower-current discharge began immediately following the previous sudden death.

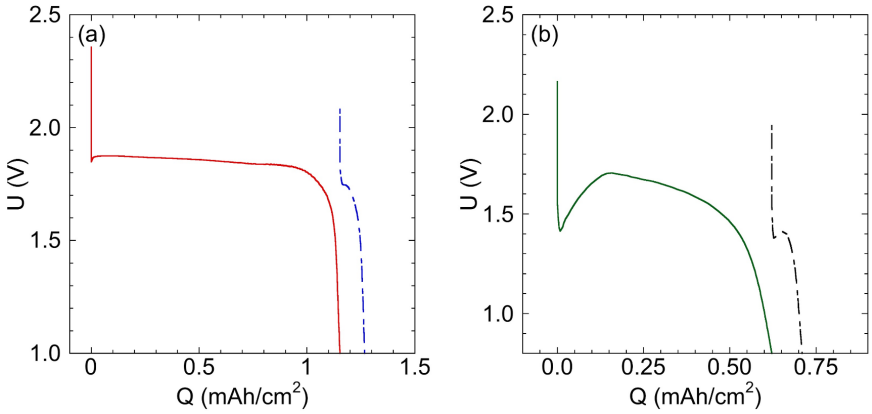

Figure 4.9: Discharge at 0.4 atm and (a) 440 μA/cm^2 or (b) 1800 μA/cm^2, followed by one hour of relaxation, then an attempt to discharge at the same current density. At 440 μA/cm^2, an additional 0.09 mAh/cm^2 was achieved (10% of the first discharge), and at 1800 μA/cm^2, an additional 0.11 mAh/cm^2 was achieved (14% of the first discharge).

4.4.2.2 Na-O_2 cell behavior at intermediate O_2 pressures (0.8 atm)

Upon increasing the pressure to 0.8 atm, the discharge capacity obtained at all current densities is sufficiently high to enable a detailed EIS study at current densities from 180 to

1800 μA/cm^2. Results are given in Figure 4.10, with corresponding representative Nyquist and Bode plots available in Figure A.4. At 0.8 atm O_2, EIS shows that at 180 μA/cm^2, the capacity-limiting mechanism is primarily passivation, indicated by the increase in the charge-transfer resistance (R_{CT}) coinciding with cell death, though the ionic resistance within the pores (R_i) is of a similar magnitude and contributes somewhat to cell failure. At the higher current densities (440-1800 μA/cm^2), the cell impedance is dominated by an increasing R_{CT}. As with the 0.4 atm cells, this suggests that the cathode/electrolyte interface was blocked, possibly by a thin layer of NaO_2, causing the increase in overpotential that ultimately results in cell death. These observations are supported by evidence from SEM of cathodes discharged to sudden death at 180 μA/cm^2 and 0.8 atm (Figure 4.5c-d). While NaO_2 crystals are observed on the Na side of the cathode, no directly observable thick surface films are apparent (Figure 4.5c), though some surface charging during image acquisition again indicates the presence of thin films between the NaO_2 crystals. In contrast, on the O_2 side of the cathode (Figure 4.5d), thick surface films that obscure the underlying cathode structure between the cubic NaO_2 crystals are clearly present. The average crystal size between the two sides of the cathode seems comparable at 180 μA/cm^2 (5-10um), as is the apparent distribution of the crystals, and thus the presence of thicker films on the O_2 side suggests that product deposition may occur to a greater extent in regions of higher dissolved O_2 concentration, an effect that will be discussed in more detail later. Upon increasing the current density to 440 μA/cm^2, similar trends in product deposition as at 180 μA/cm^2 are observed using SEM.

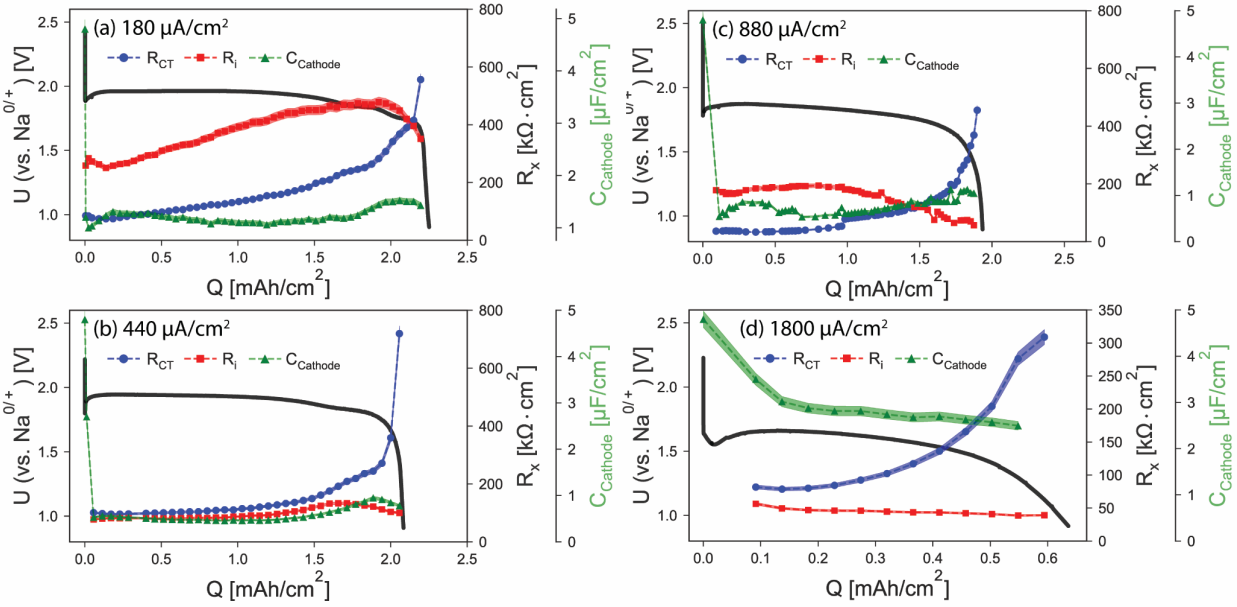

Figure 4.10: Electrochemical impedance spectroscopy analyses for cells discharged at an approximately constant pressure around 0.8 atm and an average current density of (a) 180 μA/cm^2, (b) 440 μA/cm^2, (c) 880 μA/cm^2, and (d) 1800 μA/cm^2. The uncertainty of each variable is shown with shaded areas.

Large NaO_2 crystals (5-10 μm) are observed on both sides of the cathode (Figure 4.4c-d), with apparent surface films visible between the crystals on the O_2 side (Figure 4.4d). Further increases in the current density at 0.8 atm demonstrate that, while R_i remains non-negligible at both 880 and 1800 $\mu A/cm^2$ an increased R_{CT} is the primary reason for sudden death (Figure 4.10c-d). These observations indicate that, in the current density range used in this study, cell failure in cells operated at 0.8 atm occurred as a result of surface passivation due to the buildup of NaO_2 films at the carbon/electrolyte interface.

4.4.2.3 Na-O_2 cell behavior at moderate O_2 pressures (1.4 atm)

Cell behavior in this pressure regime was discussed in detail in Chapter 3 and in our previous studies (Knudsen et al. and Nichols and McCloskey), and EIS results from Knudsen et al. are reproduced in Figure 4.11.[1,51] Placing these findings in the context of the present study, it is at this pressure that the first complete transitions in the sudden death failure mechanism as indicated by EIS are observed. EIS shows that at 180 and 440 $\mu A/cm^2$, the capacity-limiting mechanism is primarily the ionic resistance within the pores (R_i), suggesting a pore-clogging failure mechanism (Figure 4.11a-b). In contrast with the behavior observed at 0.8 atm, while an increase in the charge-transfer resistance (R_{CT}) coincides with the onset of sudden death, R_i is approximately three times the value of R_{CT}. This observation is consistent with the large crystals and thick porous surface films observed in Figures 4.4e-f and Figures

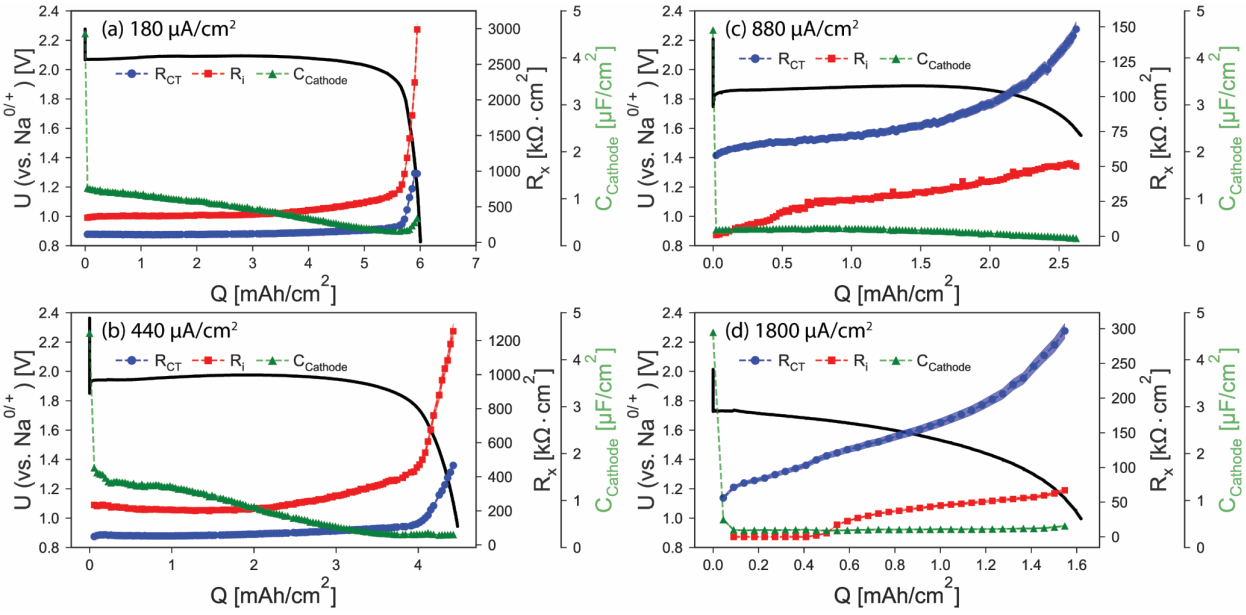

Figure 4.11: Electrochemical impedance spectroscopy analyses for cells discharged at an approximately constant pressure around 1.4 atm and an average current of (a) 180 $\mu A/cm^2$, (b) 440 $\mu A/cm^2$, (c) 880 $\mu A/cm^2$, and (d) 1800 $\mu A/cm^2$. Data from Knudsen et al.,[51] republished by Nichols, Knudsen, and McCloskey.[1] The uncertainty of each variable is shown with shaded areas.

4.5e-f, since crystals and films like these are likely to participate in the clogging of pores and increased R_i. When the current is increased to 880 and 1800 $\mu A/cm^2$, R_{CT} is the primary reason for sudden death, though as with the case of 0.8 atm, R_i is non-negligible in both cases. These findings are in agreement with the observations in Chapter 3. At sudden death at 880 $\mu A/cm^2$, large NaO_2 crystals and thick surface films were observed as in Figure 3.6e. However, these are consistent with cell failure due to R_{CT} and a lower value of R_i because they are significantly smaller than crystals observed, for example, at 180 $\mu A/cm^2$ in Figure 4.5e. (Note that the scale bars in Figure 3.6e are 5 μm as compared to 10 μm in Figures 4.4 and 4.5.)

4.4.2.4 Na-O_2 cell behavior at high O_2 pressures (2.0 atm)

EIS results from the highest pressures studied (2.0 atm) at all current densities are given in Figure 4.12; here, the primary cause of sudden death is a pore filling mechanism. As shown in Figure 4.12, while charge-transfer resistance (R_{CT}) contributes to the cell failure, the ionic resistance within the pores (R_i) dominates the cell impedance at all current densities, suggesting that cell failure is caused by large amounts of NaO_2 deposited within the pores. These findings are consistent with SEM observations from cathodes at sudden death at 440 $\mu A/cm^2$ and 2.0 atm, given in Figure 4.4g-h, where thick films and large crystals (5-20 μm) are observed on both sides of the cathode. This result is unsurprising, given the high

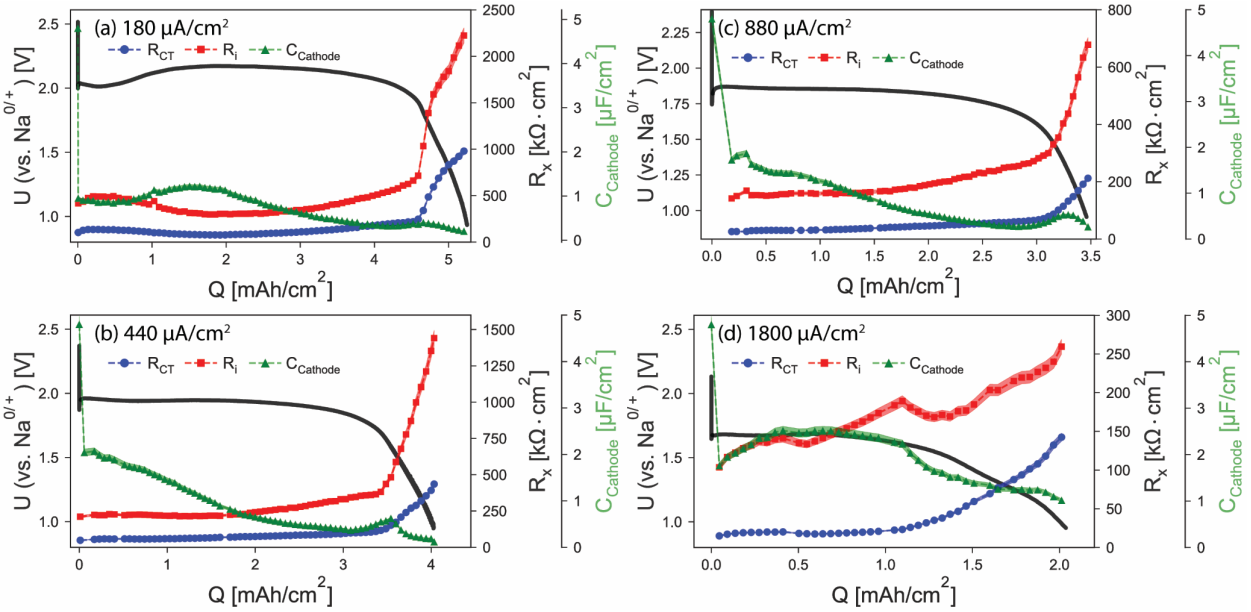

Figure 4.12: Electrochemical impedance spectroscopy analyses for cells discharged at an approximately constant pressure around 2.0 atm and an average current of (a) 180 $\mu A/cm^2$, (b) 440 $\mu A/cm^2$, (c) 880 $\mu A/cm^2$, and (d) 1800 $\mu A/cm^2$. The uncertainty of each variable is shown with shaded areas.

capacity achieved during discharge and the commensurately large amount of NaO_2 deposited throughout the cathode. As with the observations at 1.4 atm (Figure 4.4e-f), the surface coverage with NaO_2 at 2.0 atm appears more complete on the Na side of the cathode, with less of the underlying carbon structure visible than on the O_2 side (compare Figure 4.4g with 4.4h). This observation will be revisited in greater detail later. Note that at 180 $\mu A/cm^2$, the 2.0 atm discharge was not studied with SEM because the capacity at 180 $\mu A/cm^2$ and 1.4 atm was within statistical variance of the highest achievable capacities at any current density, and the EIS analyses indicated similar pore-clogging failure mechanisms at 1.4 and 2.0 atm. For these reasons, a discernible variation in discharge product morphology was not expected, and the discharge product at 180 $\mu A/cm^2$ and 2.0 atm likely bears a strong resemblance to that in Figure 4.5e-f.

To summarize, the SEM images presented in Figures 4.4 and 4.5 suggest that at lower operating pressures (0.4 atm), NaO_2 may be preferentially deposited on the O_2 side of the cathode as opposed to the Na side of the cathode. Schröder et al. previously reported and visualized an analogous trend depending on current density with deposition of NaO_2 favored near the O_2 reservoir, particularly at high current densities.[52] In addition, the results in Figure 4.6 and 4.10 to 4.12 indicate that both O_2 pressure and current density affect the primary failure mechanism, with NaO_2 film-induced charge-transfer resistance generally accounting for cell death at high current densities and low O_2 pressures, and pore clogging by NaO_2 causing cell death at high O_2 pressures and low current densities.

4.4.3 Spatial distribution of NaO_2 within the cathode as a function of O_2 pressure and current density

To further investigate a possible correlation between the spatial distribution of NaO_2 deposition and the sudden death mechanism, cells were assembled containing two 12 mm P50 discs stacked together. These cells were discharged to roughly 30%, 60%, and 100% of the sudden death capacity (i.e., to 1.0 V) under 0.4, 0.8, and 1.4 atm O_2 at 440, 880, and 1800 $\mu A/cm^2$, when normalized as before to the cross-sectional area of the cell. Following cell death, the Na-O_2 cells were disassembled and the P50 discs titrated separately to quantify the relative deposition on the Na and O_2 sides of the cathode. The titration results of these cells are presented in Figure 4.13, with the quantities of NaO_2 presented as a percent yield of the NaO_2 expected given the total Coulombic capacity of the discharge. The average percent yield over all cells was 94%, as observed in the single-cathode system. An additional plot presented with the μmol quantities of NaO_2 detected in each side of the cathode is available in the Appendices (Figure A.6).

The data presented in Figure 4.13 evince two important trends. First, as the pressure is increased at any current density, NaO_2 is more likely to deposit on the Na side of the cathode. Second, as the current density is increased at any pressure, NaO_2 preferentially and increasingly deposits on the O_2 side of the cathode, in agreement with prior observations.[52] The combined effect of these trends is most evident in examining the extremes: the

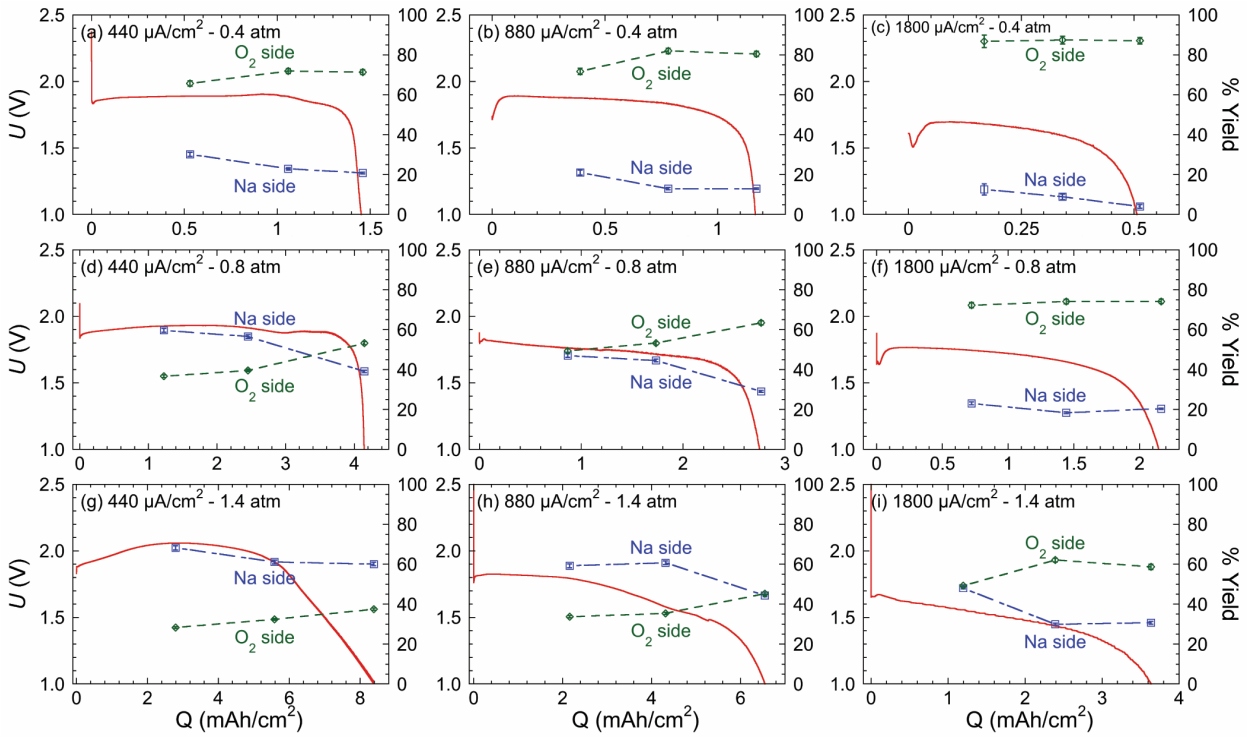

Figure 4.13: Discharge profiles (red solid line) and percent yield of NaO_2 measured by iodometric titration from the O_2 side of the cathode (green diamonds) and Na side of the cathode (blue squares) for two-cathode experiments at various current densities and pressures. Current increases from left to right; pressure increases from top to bottom. Error bars represent the individual measurement error, and in most cases are smaller than the points.

high-current/low-pressure case of Figure 4.13c where cell failure due to surface passivation is expected, and the low-current/high-pressure case of Figure 4.13g where cell failure due to pore clogging is expected.

At 1800 μA/cm^2 and 0.4 atm (Figure 4.13c), where charge-transfer resistance causes sudden death, nearly the entire capacity of the cell is achieved through NaO_2 deposition on the O_2 side of the cathode, with an 87% yield of NaO_2 detected on the O_2 side alone. In addition, practically all NaO_2 detected on the Na side of the cathode deposits early in discharge, with no significant increase in the quantity of NaO_2 detected on the Na side following the initial measurement at 30% capacity. The strong preference for deposition in the O_2 side suggests the dissolved O_2 present in the electrolyte may be rapidly depleted at the beginning of discharge and is never adequately replenished for the O_2 reduction reaction to occur at the Na side. This would render a significant portion of the cathode inactive for O_2 reduction, an observation consistent with NaO_2 distributions reported previously.[52] At decreased O_2 pressures, the initial concentration of dissolved O_2 is already low in the electrolyte, and NaO_2 therefore deposits mainly on the O_2 side due to rapid depletion of O_2 throughout the liquid phase contained in the porous electrode. For example, at 0.4 atm, the

concentration of O_2 in the electrolyte is around 4 mM by Henry's Law, using coefficients available in the literature.[40] This represents a theoretical capacity of less than 0.01 mAh/cm^2 if all dissolved O_2 reacts and none is replaced by diffusion. Notably, the capacity titrated on the Na side of the 0.4 atm and 1800 μA/cm^2 cell was approximately 2.5 times this theoretical capacity, suggesting that some O_2 must be replenished on the Na side during discharge. However, at low pressures and high current densities, these results suggest steep concentration gradients for dissolved O_2 in the cell, resulting in large non-uniformities in product deposition, favoring the O_2 side of the cathode. This explanation is consistent with the EIS results observed in the single-cathode system, and particularly with the initial drop in cathode/electrolyte interfacial capacitance ($C_{Cathode}$) consistent with the formation of insulating NaO_2 films that was observed at the beginning of every discharge. However, at 0.4 and 0.8 atm, following this initial drop, $C_{Cathode}$ tends to either remain relatively constant or increase, consistent with a less active cathode that accumulates less NaO_2.

By contrast, at 440 μA/cm^2 and 1.4 atm (Figure 4.13g), where pore clogging primarily causes sudden death, about a 60% yield of NaO_2 is detected in the Na side of the cathode at sudden death, compared to 38% in the O_2 side. NaO_2 appears to be deposited on both sides of the cathode at similar rates, though slight shifts in the yield suggest that deposition occurs more quickly on the Na side at first, then begins to favor the O_2 side as discharge proceeds to higher capacities. This shift in product deposition is clearer at more intermediate current-pressure combinations, such as at 880 μA/cm^2 and 1.4 atm (Figure 4.13h) and at 440 μA/cm^2 and 0.8 atm (Figure 4.13d). In these cases, the yield of product on the Na side (about 60%) is higher than on the O_2 side (about 35-40%) during earlier stages of discharge, but ultimately more NaO_2 deposition is observed on the O_2 side at sudden death. At 1.4 atm, the equilibrium dissolved O_2 concentration is about 14 mM, and at 0.8 atm it is about 8 mM, again calculated by Henry's Law coefficients from literature.[40] Together with the higher partial pressure increasing O_2 concentration and the lower rate of O_2 consumption by the reduction reaction, it is evident from the behavior of these cells that mass transport limitations, either Na^+ or O_2, are not significant early in discharge. However, as the cell approaches sudden death, the yield of product on the O_2 side increases to about 45-55%, which would be consistent with an increased resistance to transport within the pores of the cathode causing less NaO_2 deposition on the Na side. We note that pore clogging is a significant primary cause of cell failure for analogous single-cathode cells at low and intermediate current densities (180-440 μA/cm^2) at 1.4 atm and at low current densities (180 μA/cm^2) at 0.8 atm, as discussed previously (see Figures 4.10 and 4.11).

4.4.4 The influence of NaO_2 product distributions and morphology on sudden death behavior

Considering the dependence of sudden death capacity on pressure discussed extensively above, we have formulated the following explanations for the different cell failure mechanisms of Na-O_2 cells as a function of supplied O_2 pressure and applied current density. During

discharge at any pressure, a gradient in dissolved O_2 concentration will develop through the cathode. At 0.4 and 0.8 atm, we generally attribute cell failure to a combination of O_2 mass-transport limitations to the Na side of the cathode and e^- transport limitations through the passivating NaO_2 on the O_2 side of the cathode. At 0.4 atm, this results in low capacities, highly preferential deposition of NaO_2 on the O_2 side of the cathode, and cell failure due to passivation of that side of the cathode, where NaO_2 formation occurs more quickly than NaO_2 dissolution and deposition as larger crystals. At 0.8 atm, the increased O_2 pressure permits NaO_2 deposition through a greater depth of the cathode. The accumulation of more NaO_2 exacerbates mass transport issues of both O_2 and Na^+, consistent with the higher ionic resistances within the pores of these cells observed at all current densities. At higher pressures, such as 1.4 and 2.0 atm, increased dissolved O_2 concentrations mitigate the mass transport issues evident at lower pressures, though they may still be a factor at the highest current densities studied. At 1.4 atm and low current densities (180-440 $\mu A/cm^2$), NaO_2 deposition occurs at all depths in the cathode without O_2 transport limitations playing a significant role until much higher capacities are achieved, where large pore-blocking NaO_2 crystals form. However, at high current densities (880 and 1800 $\mu A/cm^2$) the eventual cause of sudden death is surface passivation in a mechanism comparable to that at lower current densities and lower pressures. Finally, at 2.0 atm, the higher initial dissolved O_2 concentration maintains electrochemical activity throughout the cathode throughout discharge, and leads to a transition to a pore-clogging-dominated failure mechanism at all current densities studied. Overall, the combination of e^- transport through NaO_2 and O_2 and Na^+ mass transfers in the electrolyte lead to a transition between passivation and pore-clogging failure mechanisms at some pressure depending on the discharge current density.

Finally, these results suggest that at high pressures, decreasing the concentration of Na^+ in the electrolyte could cause the deposition of NaO_2 to become dependent upon Na^+ concentration and reduce achievable capacities. In particular, this follows from the implication that lower Na^+ concentration would limit how quickly surface NaO_2 could be dissolved and deposited as larger NaO_2 crystals, making low-Na^+-concentration cells more susceptible to early failure due to surface passivation. To confirm this, we performed discharges to sudden death at 1.4 atm O_2 using cells with lower NaOTf concentrations. We found that lower-concentration cells exhibited significantly smaller achievable sudden death capacities at all current densities studied (Figure 4.14), consistent with both the results of this work and with our prior studies.[1,51]

4.5 Conclusions

In this chapter, we have expanded upon the previous chapter regarding the failure mechanisms and capacity limitations of Na-O_2 batteries to elucidate their dependence on the O_2 pressure provided to the cell. At all current densities studied (180-1800 $\mu A/cm^2$), an increase in sudden death capacity is observed with increasing O_2 pressure supplied during discharge. We do not attribute cell failure directly to O_2 mass-transport limitations in any case. However,

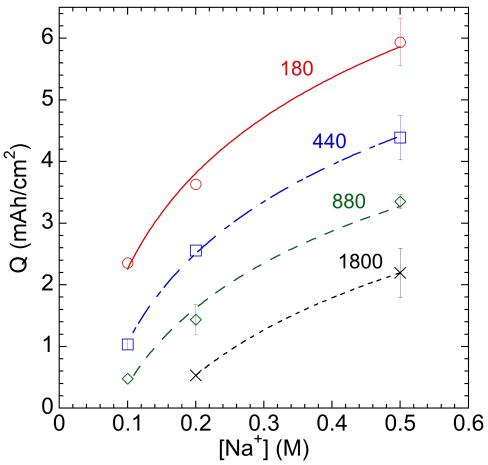

Figure 4.14: Sudden death discharge capacity of Na-O_2 cells at various currents (indicated in μA/cm^2) and 1.4 atm O_2 as a function of the concentration of NaOTf in the electrolyte. Sudden death was a 1.0 V full-cell potential, except for low-concentration cells which never achieved a potential above 1.0 V. In these cases, a 0.75 V cutoff was used. Points without error bars represent single cells. Points with error bars indicate averages of multiple cells; error bars indicate one standard deviation. Note that the lines are solely to guide the eye.

O_2 gradients across the porous cathode induce different cell failure mechanisms depending on current density and O_2 pressure. Generally, cells are observed to be more susceptible to failure due to surface passivation at low O_2 pressures, and more susceptible to failure due to pore clogging at high pressures. The pressure at which the transition between failure mechanisms occurs depends on the current density, and is higher for higher current densities. At 180 μA/cm^2, this transition occurs near or above 0.8 atm. At 440 μA/cm^2, the transition occurs between 0.8 and 1.4 atm. At 880 and 1800 μA/cm^2 this transition occurs between 1.4 and 2.0 atm. Generally, cells which fail due to pore clogging have a higher capacity at sudden death, associated with deposition of NaO_2 throughout the cathode, as compared to preferential deposition of NaO_2 on the O_2 side of the cathode observed at low pressures.

These mechanisms are a consequence of the porous structure of the cathode, the O_2 solubility, and the transport properties of the electrolyte, and we expect results with chemically similar electrolytes and similar cathode structures to be qualitatively comparable. Different cathode structures are likely to induce different transition pressures for these failure mechanisms, and optimization of cathode structure and porosity for operating parameters will be critical to maximize achievable capacity. In addition, enhancing O_2 solubility and diffusion will increase the discharge capacity, particularly at lower O_2 pressures where cell failure due to passivation is likely. These findings highlight the importance of monitoring and reporting O_2 discharge pressures in Na-O_2 studies, not only to clarify discharge product formation and identification, but to understand how the operating pressure may affect observed capacity limitations and cathode performance.

Chapter 5

The Charge Sudden Death Phenomenon in Na-O_2 Batteries

This chapter adapted with permission from Nichols, J. E.; McCloskey, B. D. *J. Phys. Chem. C* **2017**, *121* (1), 85–96. *Copyright 2017 American Chemical Society.*

5.1 Abstract

Metal-air (O_2) batteries have been studied over the past decade as potential high-energy alternatives to current state-of-the-art Li-ion batteries. Although Li-O_2 batteries possess higher theoretical specific energies, Na-O_2 cells have been reported to achieve higher capacities on discharge and exhibit much lower overpotentials on charge than analogous Li-O_2 cells. Nevertheless, sudden and large overpotential increases ("sudden deaths") occur in Na-O_2 cells on both discharge and charge, substantially limiting achievable capacity on discharge and increasing the average charge voltage, thereby reducing round-trip energy efficiency. In previous chapters, we considered the origins of the sudden death phenomenon on discharge, which is linked to the electrochemistry occurring at the cathode. In this chapter, we consider the sudden death phenomenon on charge. The discharge and charge current densities were both found to influence the attainable capacity prior to sudden death. We propose a charge mechanism consistent with our data, where a concerted surface oxidation mechanism and a dissolution-oxidation mechanism both contribute to the observed overpotentials. Sudden death on charge is proposed to occur when these two pathways cannot support the applied

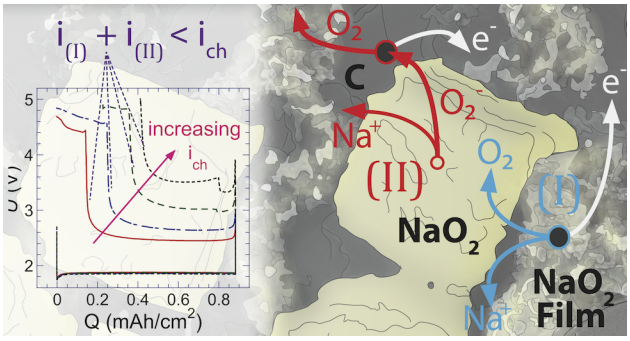

current rate.

5.2 Introduction

As discussed in the previous chapters, some of the highest theoretical specific energies are those of the nonaqueous metal-O_2 batteries, such as the Li-O_2 and Na-O_2 batteries. Nonaqueous Li-O_2 batteries in which Li_2O_2 is formed as the discharge product have the highest theoretical specific energy of any beyond Li-ion battery technology, 3456 Wh kg^{-1} Li_2O_2.[20,21] The theoretical specific energy of Na-O_2 batteries is lower, only 1105 Wh kg^{-1} NaO_2, owing to the higher molecular weight of NaO_2 and its production by a one-electron reduction of O_2 as compared to Li-O_2's two-electron process. Likewise, Na-O_2 has a lower operating potential; whereas the theoretical potential of the Li-O_2 battery is 2.96 V vs. Li/Li^+, the theoretical potential of the Na-O_2 battery forming NaO_2 is 2.27 V vs. Na/Na^+.

Given these differences, it may be surprising that the Na-O_2 battery is subject to such serious consideration. However, its chemistry has been demonstrated to offer significant advantages over the Li-O_2 battery.[30] In Figure 5.1, the first discharge-charge cycles of a Li-O_2 battery and a Na-O_2 battery are shown. The advantageous higher discharge potential of the Li-O_2 battery is evident, as much as 1 V higher than the analogous Na-O_2 battery. However, the majority of the Li-O_2 battery's charge occurs almost 2 V higher than the majority of the Na-O_2 battery's charge. This is surprising, given prior reports indicating that the inherent kinetic overpotentials of the two systems are similar.[29,30] Evidence suggests that the higher charge potential of the Li-O_2 battery is due in part to the susceptibility of the system to parasitic side reactions and byproducts and the deposition of solid electrolyte degradation

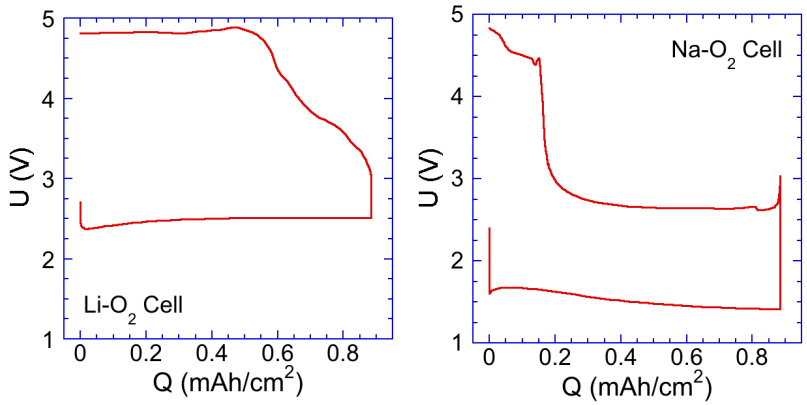

Figure 5.1: Comparison of the first discharge-charge cycle of a Li-O_2 cell (left) and a Na-O_2 (right). Discharge proceeds left-to-right and charge proceeds right-to-left. Both cells were discharged and charged at 1800 $\mu A/cm^2$ with identical cathodes. The Li-O_2 cell was assembled using a Celgard 2500 separator and a 1.0 M lithium bis(trifluoromethanesulfonyl)imide salt in 1,2-dimethoxyethane, roughly analogous to the composition of the Na-O_2 cell (see Section 2.2.1.2).

products on the cathode surface.[15,17,22,25,119] A significant fraction of the gas evolved during the Li-O_2 charge is not O_2 but instead byproducts like CO_2 produced from parasitic reactions involving both the electrolyte and the cathode.[15,17,30,120] These instabilities have proven to be significant technical challenges and remain the subject of ongoing research.[9]

In contrast, the Na-O_2 charge profile initially occurs at a relatively low-potential plateau, consistent with its inherently low kinetic overpotential on charge, and has been demonstrated to evolve comparatively more O_2.[30] This plateau persists until late during charge, at which time a sudden death occurs, a precipitous increase in the cell potential that is not observed in the Li-O_2 case.[8,30,38] Prior reports indicate that these differences are in part due to differences in reactivity and solubility of the discharge products.[8,30,113] While this explanation accounts for the low-overpotential charge plateau, it does not account for the occurrence of sudden death on charge, particularly because sudden death can occur before all of the NaO_2 on the cathode is consumed.[29,30,39,113] A mechanistic understanding of the charge sudden death phenomenon is essential for improving the achievable charge capacity of Na-O_2 batteries, as it represents the primary practical limitation to increasing that capacity.

In this chapter, we elucidate factors that influence sudden death during the first charge of the battery, including the charge and discharge current densities and their secondary effects on NaO_2 deposition and oxidation. We find evidence that sudden death on charge is likely related to an ever-decreasing rate of NaO_2 thin film oxidation and NaO_2 large crystal dissolution. We propose and discuss a charge sudden death mechanism consistent with these observations, wherein at some point during charge, the combined overall rates of these reaction pathways cannot support the applied current density, resulting in the charge sudden death.

5.3 Methods

Experimental methods are discussed in detail in Chapter 2. A custom-built cell of a modified Swagelok design was used in this study and has been previously described in detail (Section 2.2.1.1).[15,30] Materials and cell assembly procedures are given in Section 2.2.1.2 and are consistent with our prior reports and the procedures used in the study of sudden death on discharge in the preceding chapters.[1,2,51] Constant-pressure galvanostatic discharges were performed prior to charge under pure O_2 at pressures around 1.4 atm as described in Section 2.1.1.1. Quantitative characterizations of cell performance during charge were performed using both differential electrochemical mass spectrometry (DEMS, Section 2.1.2) and pressure-rise/decay techniques (Section 2.1.1), which we have previously described.[15,30] Electrochemical methods are described in Section 2.3.1. Samples for characterization with scanning electron microscopy (SEM) were prepared using methods described in Section 2.5 and consistent with our prior studies.[1,2,51]

5.4 Results and Discussion

As discussed above, the Na-O_2 charge profile (Figure 5.2) is marked by two striking features unlike those observed in an analogous Li-O_2 system.[15,25,28] First, a constant plateau potential is observed during the early stages of discharge.[29,30,41,43,44,49,50,113] At low current rates (<440 μA/cm^2), this plateau potential occurs at extremely low overpotentials (<100 mV) and lasts for nearly the entire duration of the charge process. The plateau potential is also observed to increase with increasing current, reaching nearly 3.8 V at the highest current we explored, 7100 μA/cm^2. The second striking feature of the charge voltage profiles is the onset of an undesirable "sudden death," a dramatic voltage increase (to values greater than 4 V) that marks the end of the low-potential plateau. Our prior study using impedance spectroscopy attributes sudden death on charge, regardless of current density, primarily to an increased resistance to charge transfer.[51] We wish to systematically isolate the cause of this sudden death, as well as understand the influence of cell properties on the capacity at which sudden death occurs. In this chapter, we therefore consider the following effects on the sudden death behavior: discharge and charge current density, possible differences in product formation during discharge and charge between cells, concentration polarization effects, and NaO_2 product morphology differences. We end with a description of a NaO_2 oxidation mechanism that is consistent with our experimental data.

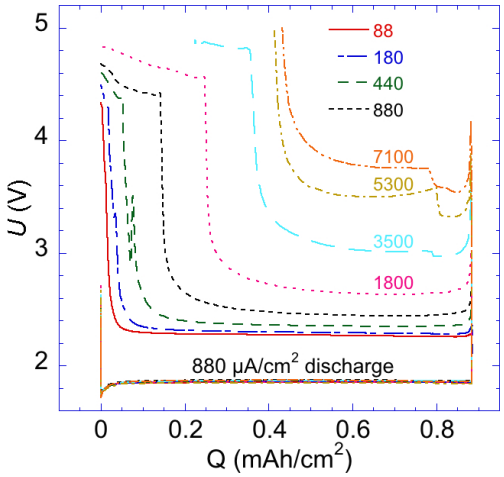

Figure 5.2: Representative charge profiles at various current densities following an 880 μA/cm^2 discharge to 0.88 mAh/cm^2 under constant O_2 pressure. Prior to charge, cell headspaces were flushed with Ar to a negligible O_2 pressure. Discharge is shown left-to-right, and charge right-to-left. Charge current densities for each profile are indicated in μA/cm^2. At all current densities studied a "sudden death" phenomenon was observed, occurring earlier during charge at higher current densities. Cells were charged to a capacity of 0.88 mAh/cm^2, a potential of 5.0 V, or to evident cell failure due to dendrite formation.

5.4.1 Influence of charge current density on charge sudden death

The capacity at which sudden death occurs is clearly dependent on the charge current density (Figure 5.2). At low current densities, such as those less than 180 μA/cm^2, nearly all of the discharge capacity can be achieved on charge prior to the sudden death. The charge capacity at the onset of sudden death (i.e., when the voltage rise initially commences) in these cells is consistent with the capacity necessary to oxidize all NaO_2 formed during discharge, recalling that a 94% Coulombic yield of NaO_2 was observed during discharge. As current increases, the charge capacity at which sudden death occurs decreases (i.e., the low potential plateau duration decreases). Even at moderate current densities, such as 440 μA/cm^2 or 880 μA/cm^2, this achievable capacity prior to sudden death is only $\sim$80% of the capacity expected.

5.4.2 Influence of discharge current density on charge sudden death

Furthermore, the capacity at which sudden death occurs is dependent on the discharge current density (Figure 5.3b), although interestingly, the discharge current density does not significantly influence the potential of the low-overpotential charge plateau (Figure 5.3c). In Figure 5.3, Na-O_2 cells were discharged to the same capacity (0.88 mAh/cm^2) at three different current densities, then flushed with Ar and charged at the same current density. Sudden death was taken to be whenever the full cell potential exceeded 4.0 V (Q_{SD}, indicated in Figure 5.3). At low charge rates ($\leq$180 μA/cm^2), all cells, regardless of their discharge current rate, can be charged to nearly full capacity (0.88 mAh/cm^2) prior to sudden death. At higher charging rates, sudden death occurs at a lower charge capacity, with cells discharged at lower current densities resulting in a lower capacity prior to sudden death. For example, for cells charged at 3500 μA/cm^2, the cell discharged at 1800 μA/cm^2 achieved 0.65 mAh/cm^2 prior to sudden death compared to only 0.47 mAh/cm^2 for the cell discharged at 440 μA/cm^2, both of which fall well below the total discharge capacity of each cell (0.88 mAh/cm^2). An important conclusion of these data is that energy efficiency for a Na-O_2 cell discharged at a low current followed by a fast charge will be poor unless we understand the causes of sudden death and control it.

5.4.3 Differences in product formation are negligible and likely do not influence charge overpotential

Recalling that the NaO_2 product yield during discharge is not significantly altered by the discharge current, it is not likely that the behavior shown in Figure 5.3 is caused by substantial changes in the charge electrochemistry between the various cells. In support of this premise, for cells discharged at the same current (880 μA/cm^2) and to the same capacity (0.88 mAh/cm^2), we observe regardless of charge current density that the gas evolution for each cell is consistent with a nearly 1 e$^-$/gas molecule process (Figure 5.4). Slight deviations away from a 1 e$^-$/gas process over the duration of charge are observed to a similar degree

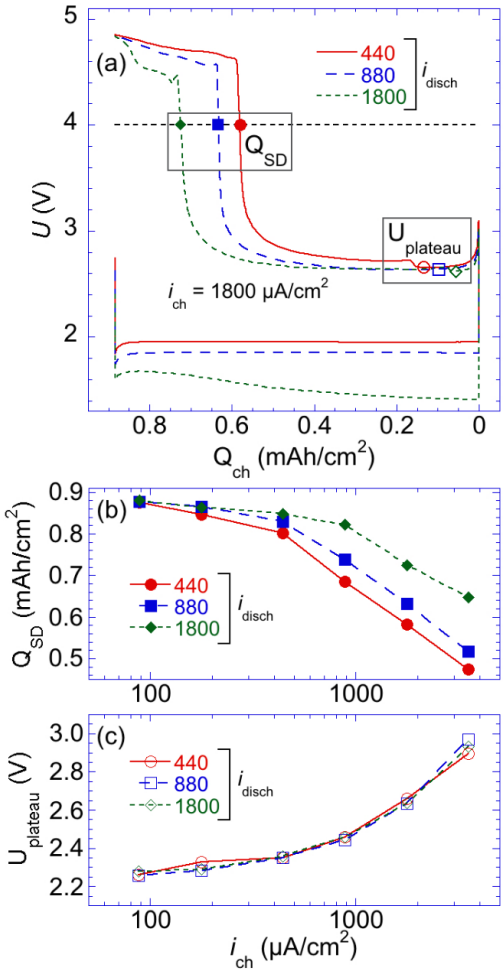

Figure 5.3: (a) Discharge-charge profiles for three cells discharged at different current densities (i_{disch}, indicated in $\mu A/cm^2$), then charged at the same current density (i_{ch}), in this case, 1800 $\mu A/cm^2$. The charge capacity at sudden death, Q_{SD}, and the minimum cell potential achieved on the low-overpotential plateau during charge, $U_{plateau}$, are indicated. (b) The charge capacity at sudden death, Q_{SD}, and (c) the minimum cell potential, $U_{plateau}$, achieved during charge for cells discharged and charged as in Figure 5.2a at a variety of charge current densities.

in all cells, and prior to sudden death, the average gas production in all cells studied is approximately 1.08 ± 0.02 e^-/gas. Separate measurements using DEMS confirm that nearly all gas evolved is O_2, and a predominantly 1 e^-/O_2 process is observed prior to sudden death (Figure 5.6). Studies of charged cells following discharge at different current densities showed comparable performance, with marginal improvements observed in cells discharged at high current densities relative to those discharged at low current densities (Figure 5.5). Combined, these results imply that the sudden death capacity dependence on current is not related to substantial changes in the overall electrochemistry occurring in the cell. Of note, following sudden death, e^-/gas values slightly greater than 1.10 are observed in the cells that continued

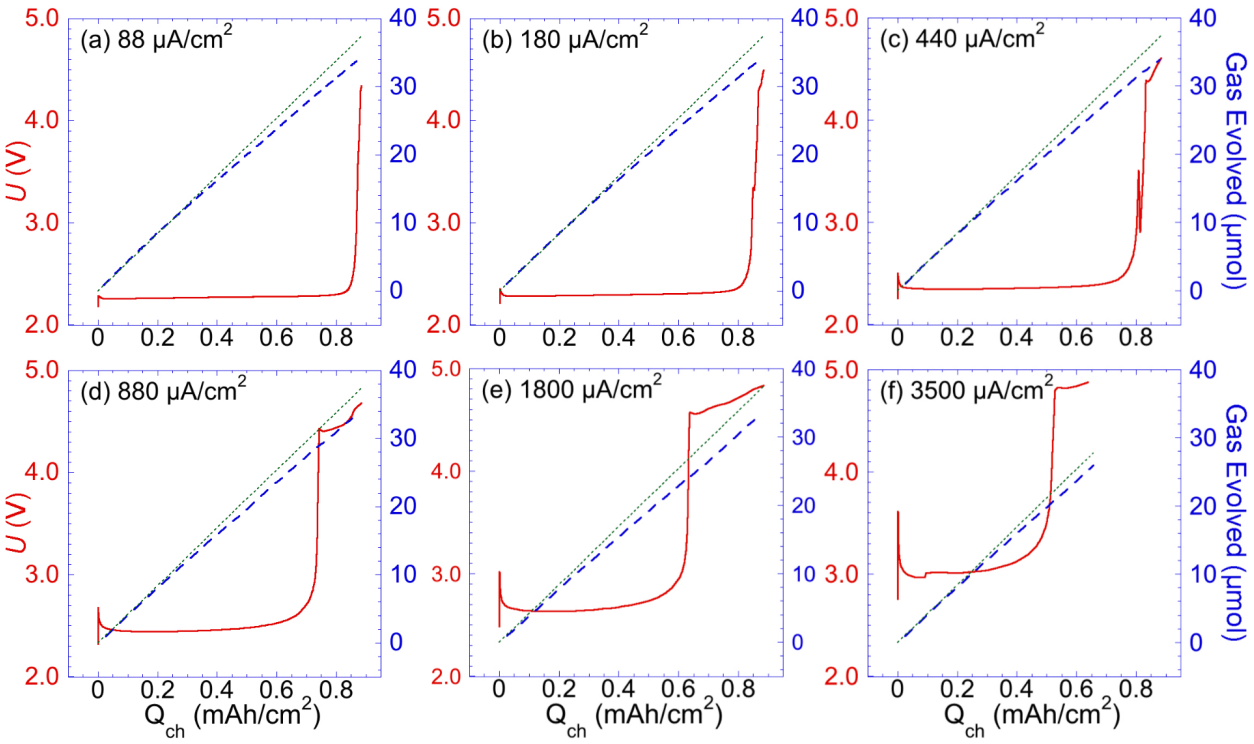

Figure 5.4: Charge profiles and accompanying gas evolution data for cells initially discharged at 880 μA/cm^2 to 0.88 mAh/cm^2, then charged under an initially Ar atmosphere at (a) 88 μA/cm^2, (b) 180 μA/cm^2, (c) 440 μA/cm^2, (d) 880 μA/cm^2, (e) 1800 μA/cm^2, and (f) 3500 μA/cm^2. Charge proceeds from left to right. Gas evolution is indicated with a heavily dashed line (blue), and the thin dashed line (green) indicates expected gas evolution assuming an ideal 1 e$^-$/gas process.

to charge below 5 V (i.e., cells charged between 440 and 3500 μA/cm^2). O_2 production is still observed to be the primary gas evolved after sudden death, although slight production of H_2 and some CO_2 is also observed.

Another potential cause for the charge sudden death could be related to the deposition of solid electrolyte degradation products on the cathode surface, in a fashion reminiscent of the cause for large charge overpotentials in Li-O_2 batteries.[9] In this context, sodium carbonates/carboxylates that are stable to high voltages would be deposited at the electrolyte-NaO_2 interface, thereby substantially decreasing the exposed NaO_2 surface area and driving the overpotential to high values. As shown in Figure 5.4, parasitic processes are likely occurring, since a deviation away from the ideal 1 e$^-$/O_2 process starts somewhere during the course of the low potential plateau regardless of current rate. Nevertheless, the blocking of exposed NaO_2 as the cause of sudden death is unlikely for a couple reasons. First, we have observed that O_2 continues to evolve at high rates following sudden death (Figure 5.6), alongside any parasitic chemistries that may be occurring. Second, accumulation of these products over the course of the charge would result in an ever-increasing charge potential (as is observed in Li-O_2 cells),[121] as the potential would necessarily increase to

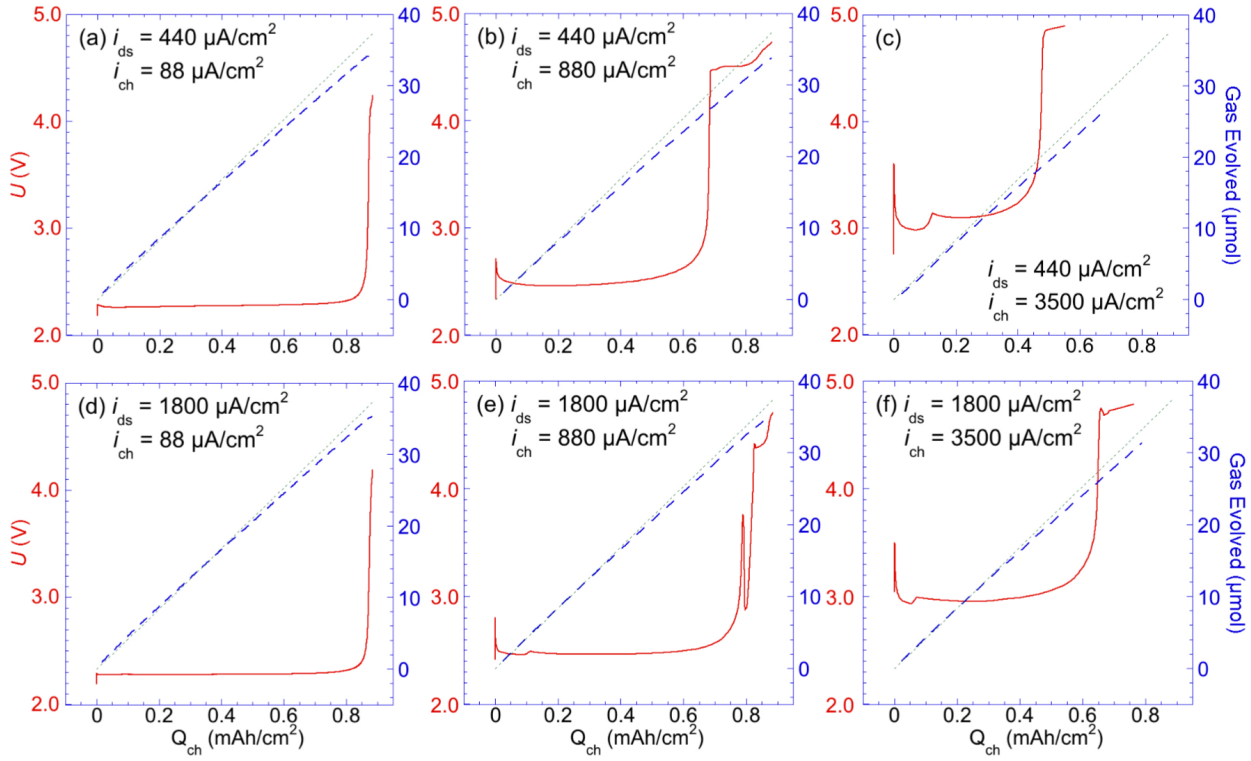

Figure 5.5: Charge profiles and accompanying gas evolution data for cells initially discharged at either 440 μA/cm^2 (a-c) or 1800 μA/cm^2 (d-f) to 0.88 mAh/cm^2, then charged under an initially Ar atmosphere at (a,c) 88 μA/cm^2, (b,d) 880 μA/cm^2, and (c,f) 3500 μA/cm^2. Charge proceeds from left to right. Gas evolution is indicated with a heavily dashed line (blue), and the thin dashed line (green) indicates expected gas evolution assuming an ideal 1 e$^-$/gas process. Marginally improved e$^-$/O_2 performance is observed following discharge at higher current densities.

drive O_2^- dissolution at an ever-vanishing, carbonate/carboxylate blocked NaO_2 surface. The existence of a low-overvoltage plateau implies that no surface blocking occurs, consistent with our previous results.[30] Third, a relaxation experiment (see Figure 5.7a and related discussion) analogous to those performed in Figure 3.7 indicates that the blocking of the NaO_2 surface does not occur.

In this relaxation experiment (Figure 5.7a), a cell was initially discharged to 0.88 mAh/cm^2, then charged at 1800 μA/cm^2 to a cell potential of 3.0 V, right at the onset of sudden death. At this potential, the current density was immediately decreased to 880 μA/cm^2, until 3.0 V was again achieved. These decreases continued, first to 440 μA/cm^2, then to 180 μA/cm^2, at which time the cell was charged to completion. Upon each decreased current, the sudden death was delayed, and the cell potential decreased below that of the initial 1800 μA/cm^2 low-overpotential plateau. This technique effectively extended the capacity of the charge, and we note that this suggests that a staged reduction of the charge current may provide an optimal method to for rapid but complete charging of Na-O_2 cells, as will be explored later

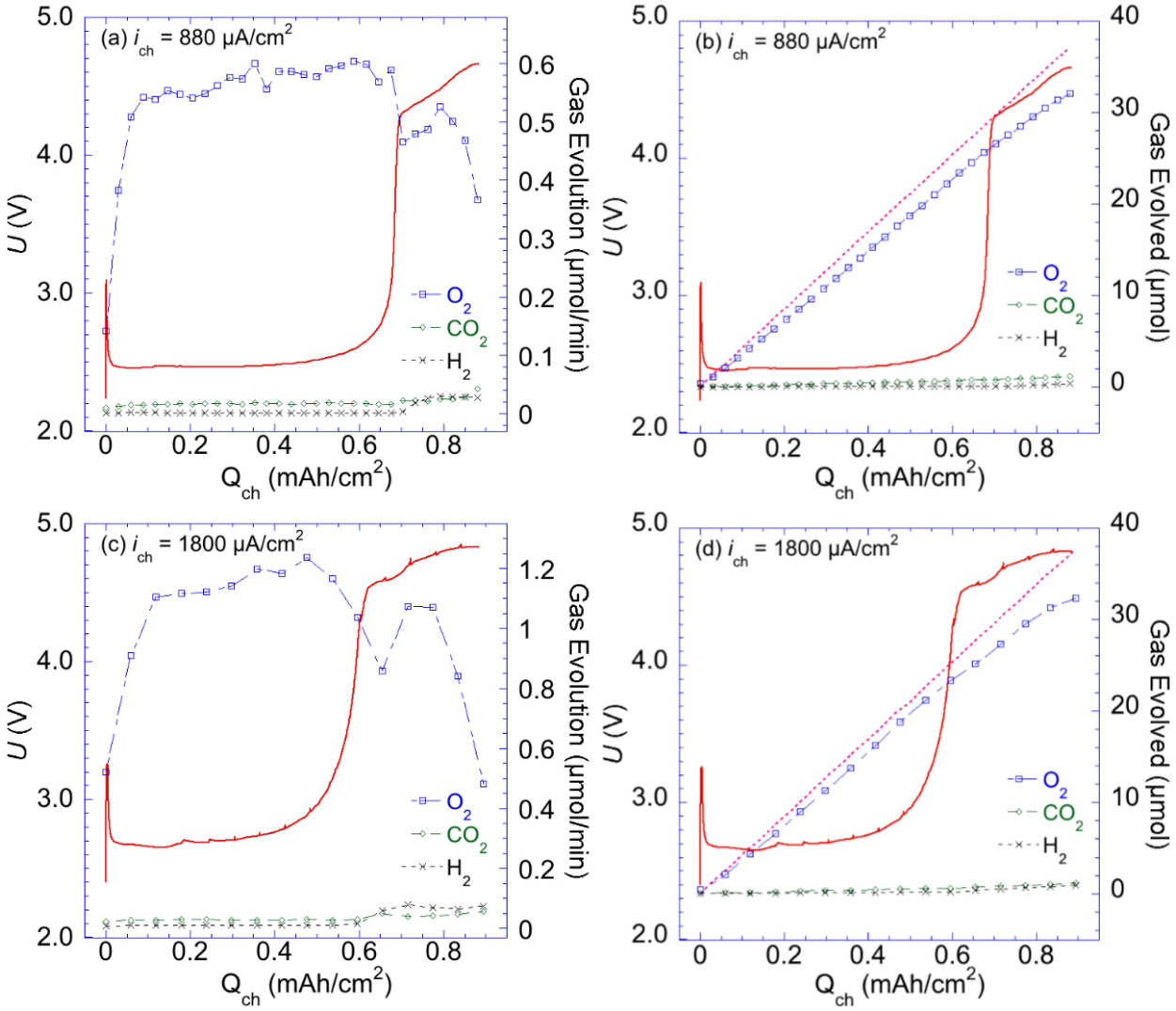

Figure 5.6: Differential electrochemical mass spectrometry data quantifying the rates at which gas is evolved (a,c) and the cumulative gas production (b,d) in Na-O_2 cells initially discharged at 440 μA/cm^2 and charged at (a-b) 880 μA/cm^2, where the ideal rate of gas production is 0.62 μmol O_2/min, and (c-d) 1800 μA/cm^2, where the ideal rate of gas production is 1.24 μmol O_2/min. Note that O_2 production is the dominant process throughout charge both prior to and following sudden death, and that it occurs at a nominally 1 e$^-$/O_2 rate (~1.1 e$^-$/O_2).

(see Chapter 6). Eventual sudden death at 180 μA/cm^2 occurred at a capacity statistically identical to that of a cell charged constantly at 180 μA/cm^2. If sudden death were caused by an accumulation of parasitic side products at the NaO_2/electrolyte interface, then we would expect that reducing current immediately prior to achieving sudden death would not substantially delay it, as the NaO_2 surface would already be blocked; this is not the case presented in Figure 5.7a.

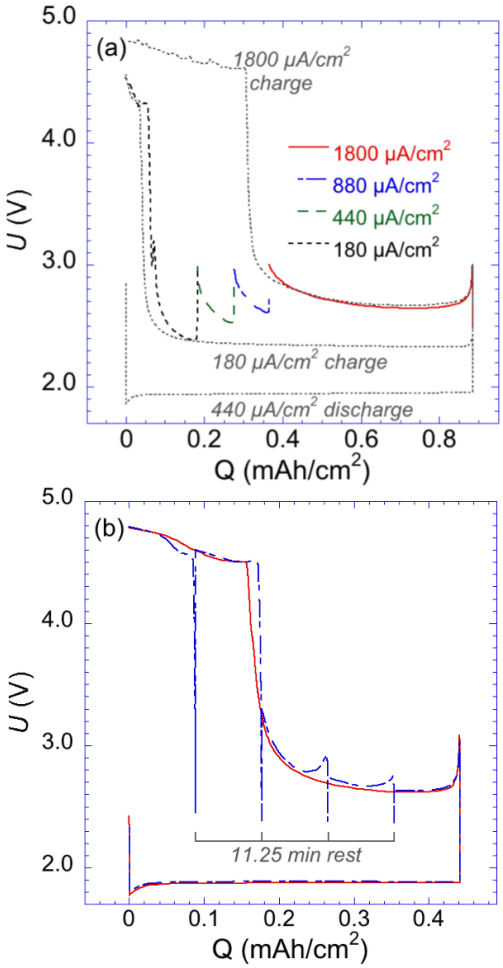

Figure 5.7: (a) Charge profiles for a cell initially discharged at 440 μA/cm^2 to 0.88 mAh/cm^2, then charged to 3.0 V at 1800 μA/cm^2. Upon reaching 3.0 V, shortly before the expected occurrence of sudden death, the charge current was decreased to 880 μA/cm^2, then to 440 and 180 μA/cm^2 upon again reaching 3.0 V. Eventual sudden death occurred at a capacity comparable to that of a cell discharged constantly at 180 μA/cm^2 (dashed line). (b) Charge profiles for cells discharged to 0.44 mAh/cm^2 at 880 μA/cm^2, then charged at 1800 μA/cm^2. One cell was charged constantly (solid line), and the other was allowed to relax to open-circuit potential for 11.25 min every 0.088 mAh/cm^2 (20% of the total expected capacity).

We note recent reports that indicate an increase in overpotential due to parasitic chemical reactions between NaO_2 and the electrolyte or to O_2^- diffusion away from the cathode if cells are allowed to sit for substantial (multiple hours/days) amounts of time in their discharged state.[46,53] The former report clearly shows that if carbonates/carboxylates were to form, large overpotentials would be necessary to oxidize them. This phenomenon is likely contributing to sudden death at our lowest current rates (e.g., 88 μA/cm^2), where sudden death occurs at approximately the capacity expected to oxidize all NaO_2 formed during discharge (>90% of

discharge capacity).

5.4.4 Concentration polarization has little influence on charge sudden death

To test the effects of polarization and solubility limitations on NaO_2 oxidation, an additional relaxation experiment was conducted (Figure 5.7b). Two cells were initially discharged to 0.44 mAh/cm^2 at 880 μA/cm^2; the lower capacity was selected to decreases the risks of shorting on charge due to dendrite formation. One cell was charged constantly at 1800 μA/cm^2, and the other charged at the same current density but allowed to relax to open circuit potential every 20% of its estimated charge capacity (0.088 mAh/cm^2). The results are given in Figure 5.7b. Relaxation to open-circuit was not found to significantly delay or reverse the onset of sudden death. Relaxation should allow re-equilibration between NaO_2 solid phases, solvated Na^+ and O_2^-, and any other Na^+ gradients in the electrolyte. Were these factors limiting, relaxation should delay or reverse sudden death, but this is not the case. Instead, these data suggest that even at high current densities, polarization and mass transport limitations have a limited effect on the occurrence of sudden death. This observation is not entirely surprising given the extremely low total amount of solvated NaO_2 present in the electrolyte even at saturation concentrations (1 mM of NaO_2 in 80 μL of electrolyte corresponds to 80 nmols of NaO_2).

5.4.5 NaO_2 morphology has a large effect on sudden death behavior.

Because no substantial differences in the cell chemistry are observed prior to sudden death at all current rates, the differences in sudden death behavior presented in Figure 5.3 are likely due to NaO_2 morphological differences resulting from different discharge currents (as is shown in Figure 3.3). The NaO_2 morphology can influence transport processes that directly impact the cell sudden death. For example, a more conformal surface coating of discharge product, such as that achieved during higher current discharges, could result in either improved electron transport through the NaO_2 layer or provide more surface area for O_2^- dissolution during the charge process. In both cases, a lower transport resistance, either of electrons through NaO_2 or O_2^- in solution, would extend cell charge capacity before sudden death occurs.

To monitor changes in NaO_2 morphology during charge, cathodes extracted at various states-of-charge were imaged using SEM (Figure 5.8). Here, cathodes were imaged following a 0.88 mAh/cm^2 discharge at 880 μA/cm^2 and at various points during charge at 1800 μA/cm^2. At early stages of charge, while the cell is still operating at its low-overpotential plateau, the NaO_2 crystals appear to dissolve somewhat, as is observed from surface roughening in the inset of Figure 5.8b-c, but generally retain their recognizable truncated cubic morphology. While there appears to be a slight variation in size and crystal density with respect to state of

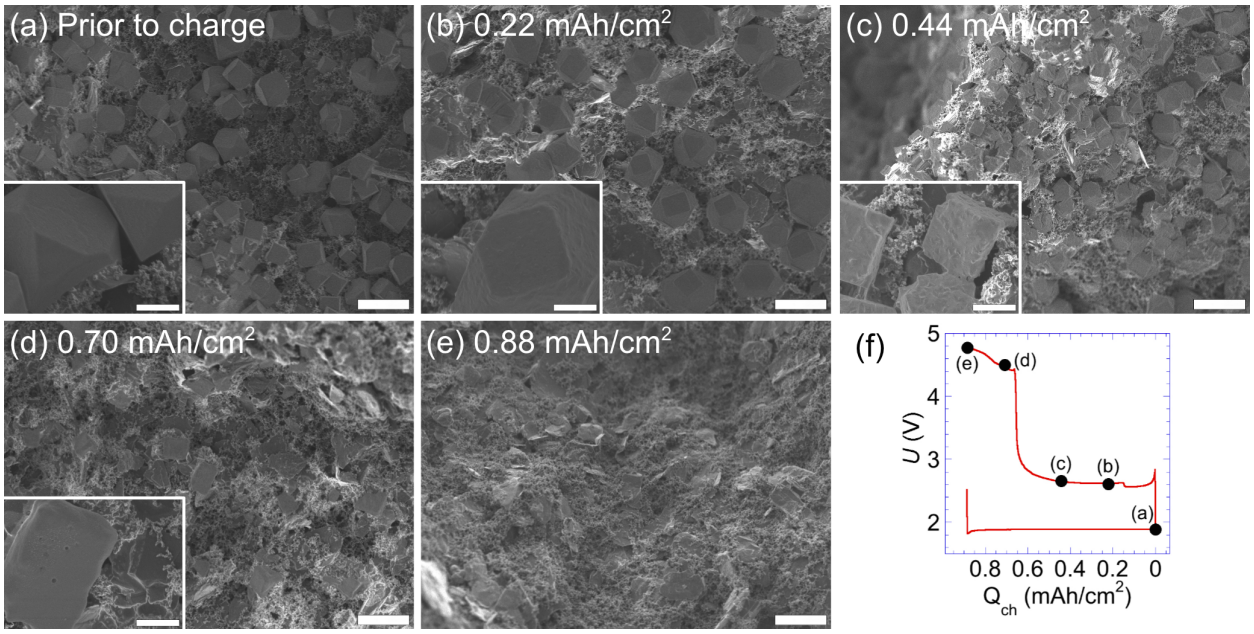

Figure 5.8: SEM images of cathodes first discharged to 0.88 mAh/cm^2 at 880 μA/cm^2, then charged to various stages at 1800 μA/cm^2: (a) prior to charge, discharged only; (b) charged to 0.22 mAh/cm^2; (c) charged to 0.44 mAh/cm^2, (d) charged to 0.70 mAh/cm^2; (e) charged to 0.88 mAh/cm^2, a theoretically complete charge. The associated representative discharge/charge profile (f) is given with the capacities indicated. Note that (b) and (c) lie on the low-overpotential charge plateau and (d) lies in the high-overpotential regime following sudden death. Scale bars are 5 μm; inset scale bars are 1μm.

charge, both are statistically equivalent to the crystal size and density of a freshly discharged cathode. This result implies that NaO_2 oxidation initially occurs primarily from the high surface area conformal NaO_2 film formed between large crystals. Following sudden death, two dramatic changes in surface morphology are observed. The majority of cubic crystals appear to have vanished, replaced with irregularly shaped NaO_2 crystals and films (Figure 5.8d). In addition, unusual patches of film that appear light-colored in the SEM images are observed following sudden death (Figure 5.8d). Following completion of charge, the cathode surface appears devoid of both NaO_2 crystals and these films (Figure 5.8e). Extensive examination of the fully charged cathode revealed that the majority of the cathode surface resembles that of a pristine cathode, although some NaO_2 crystals were sometimes observed to remain in small areas on the cathode.

5.4.6 Proposed Na-O_2 charge mechanism

Given the data presented, our postulated charge mechanism is as follows, and is highlighted in Figure 5.9. Prior to sudden death, NaO_2 is oxidized through two different pathways. The first (pathway (I), given as reaction 5.1) is the concerted oxidation of surface films via reaction

5.1:

$$\text{(I)} \qquad NaO_2 \rightleftharpoons Na^+ + O_2 + e^- \tag{5.1}$$

where charge transport occurs through the thin NaO_2 film. The second (pathway (IIa) to (IIc), given as reactions 5.2 to 5.4, respectively) is a three-step process involving the dissolution of NaO_2 from large crystals followed by diffusion to and oxidation of superoxide at accessible cathode sites:

$$\text{(IIa)} \qquad NaO_2 \rightleftharpoons Na^+ + O_2^- \tag{5.2}$$

$$\text{(IIb)} \qquad O_2^- \text{ diffusion} \tag{5.3}$$

$$\text{(IIc)} \qquad O_2^- \rightleftharpoons O_2 + e^- \tag{5.4}$$

It is noted that this mechanism can also occur to oxidize a portion of NaO_2 deposited as thin films. Given the fast kinetics of O_2^- oxidation at carbon surfaces,[122] pathway (II) is limited by either the dissolution or diffusion steps (IIa, b), although dissolution is much more likely the limiting factor, particularly as the crystal surface area decreases.[113] Our data also suggests that pathway (I) will be able to support a substantially larger current rate than pathway (II) as long as the surface film area is larger than the micron-sized cubic crystal surface area. We therefore suggest that at high current rates (>880 $\mu A/cm^2$), pathway (I) will support most of the current during the initial stages of charge. At low current rates, both pathways contribute substantially to the overall electrochemistry, with pathway (II) being able to support the entire current density even if the NaO_2 thin films are entirely oxidized before the end-of-charge.

These pathways lead to a gradual disappearance of surface films and a roughening and slight shrinking of the large crystals, as observed in Figure 5.8b-c. As surface films disappear, the surface mechanism (I) accounts for a smaller fraction of the overall current rate, and the solution mechanism (II) becomes increasingly limited by the overall rate of dissolution from the shrinking surface area of the NaO_2 crystals. Eventually, the combined overall rate of pathway (I) and (II) no longer is sufficient to support the current density. At high current rates this stage is reached earlier due to the increased demand on the rate of dissolution for mechanism (II) and the accompanying requirement that the oxidation of surface films occur instead. As a consequence, the cell potential rapidly increases, resulting in the charge sudden death. At sudden death, reduced O_2 evolution and increased production of parasitic byproducts, particularly H_2 and CO_2, is observed (Figure 5.6). However, we note that O_2 production continues following sudden death at a rate only slightly less than that prior to death (Figure 5.6). Furthermore, we have observed that cells charged without prior discharge experience significant parasitic electrochemical reactions beginning above 4 V (Figure 5.10), which produce quantities of gas statistically identical to the observed H_2 and CO_2 production during DEMS studies of discharged and charged Na-O_2 cells. We therefore hypothesize that some irreversible electrochemical process occurs following sudden death, inducing electrolyte degradation, which may produce both gaseous byproducts and some

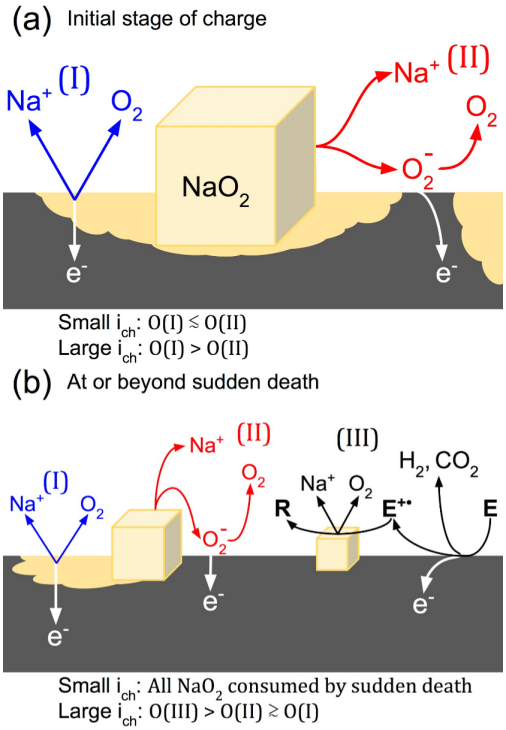

Figure 5.9: The proposed mechanism during charge. O(x) indicates the order of magnitude of the overall rate of process x. (a) Prior to sudden death, concerted NaO_2 film oxidation (I) and large crystal dissolution through a dissolution-oxidation solution mechanism (II) can occur. The cell experiences sudden death once the combined overall rate of (I) and (II) cannot support the applied current. (b) Following sudden death, unknown parasitic reactions are observed, designated by (III), likely producing H_2 and CO_2 at the electrode surface. Since O_2 production is observed to continue at a high rate, we hypothesize that redox active species, designated here as $E^{+\bullet}$, are irreversibly produced from the electrolyte (E). $E^{+\bullet}$ diffuses to the surface of a NaO_2 crystal, where it reacts with the NaO_2 to evolve O_2 and form a parasitic side product, R. The solution mechanism (II) and surface mechanism (I) may continue but account for a decreasing amount of total oxidation at higher charge capacities.

redox active solution-soluble species. In turn, this redox active species reacts with NaO_2 to produce O_2, as indicated in Figure 5.9b as process III, effectively establishing an irreversible electron shuttling mechanism. The gaseous products account for a small percentage of the total reaction products, and parasitic processes may occur to some minor extent prior to sudden death as well. We also note that at small current densities, sudden death is found to occur at capacities approximately equal to that necessary to oxidize all NaO_2 deposited during discharge, suggesting that earlier parasitic processes or migration of NaO_2 away from the surface may be responsible for cell death, as has been previously reported. Finally, we cannot rule out some concerted surface mechanism where charge transport occurs through the large NaO_2 crystals to support O_2 evolution after sudden death; however, due to the expected

substantial insulating character of NaO_2, we view this as less likely than the electrolyte degradation pathway (III in Figure 5.9b) to account for the O_2 production.

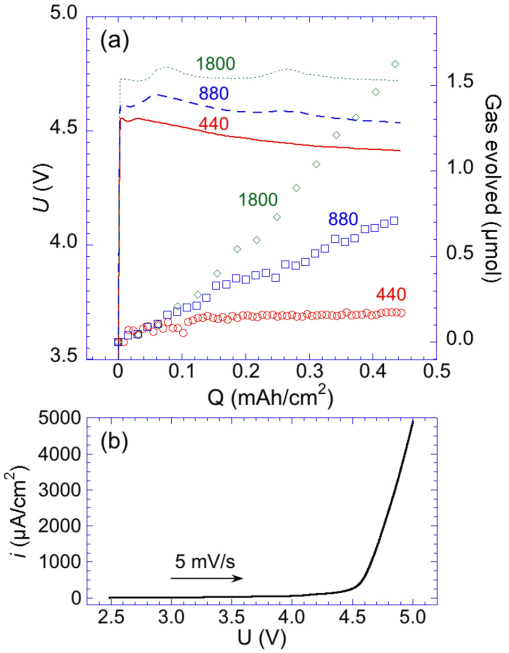

Figure 5.10: (a) Oxidative chronopotentiometry of cells under Ar, without previous discharge or exposure to O_2. Currents are indicated in $\mu A/cm^2$. The accompanying gas evolution data based on pressure rise measurements is also indicated. Note that for a given capacity and current, the amount of gas evolved in these tests is statistically equivalent to the total H_2 and CO_2 observed using DEMS following sudden death, and substantially less than the quantity of O_2 that might be evolved from a cell that has been discharged. (b) Oxidative linear sweep voltammetry of a cell under Ar, conducted at a 5 mV/s scan rate to an upper limit of 5.0 V. Beginning around 4.5 V, a parasitic electrochemical process is observed at high current densities. Note that these potentials roughly correspond with those observed in discharged and charged Na-O_2 cells following sudden death.

5.5 Conclusion

In this chapter, we have shifted our focus to the Na-O_2 charge sudden death phenomenon. On charge, a current-dependent sudden death is observed following low overpotential voltage plateaus, thereby limiting the achievable capacity at higher charging rates. We confirm that the 1 e^-/O_2 oxidation of NaO_2 is the primary cell electrochemistry during all of charge, though minor deviations from this ideal chemistry are observed. The sudden death when charging at low current rates is likely related to the oxidation of accumulated solid parasitic side products (likely carboxylate or carbonates) after all NaO_2 formed during discharge has been oxidized. At higher currents, sudden death is related to the disappearance of NaO_2 thin

films, which oxidize at low overpotentials, and an ever-decreasing cubic NaO_2 crystal surface area, which continuously reduces the dissolution rate of O_2^-. Once the combined overall rate of these processes cannot support the applied current density, the charge-transfer resistance to NaO_2 oxidation significantly increases, resulting in sudden death. Once the cell reaches a sufficiently high potential, NaO_2 oxidation to O_2 continues, likely as a process coupled with the formation of active redox species via parasitic decomposition of the electrolyte. We recommend further study of these post-sudden-death chemistries, so as to better understand the continued production of O_2 following cell death. This parasitic redox shuttle may also play a part in Li-O_2 batteries, where O_2 evolution from large, insulating Li_2O_2 toroids is observed, although poorly understood, as the dominant process at high (>4 V) voltages.[23] Furthermore, we agree with a previous recommendation[113] to investigate reversible redox mediators as a means to enhance the rate of charge transport from NaO_2 in large crystals, thereby possibly providing a route to delay the charge sudden death in Na-O_2 cells. Initial efforts in this research direction and in exploring alternate charging schemes to improve achievable capacity will be discussed in the following chapter.

Chapter 6

Improving Na-O_2 Battery Performance on Charge

6.1 Abstract

Na-O_2 battery charge capacities are limited by the onset of sudden death, after which parasitic side reactions occur and O_2 production decreases. Prior reports, including ours, have suggested that the introduction of a redox mediator could alleviate sudden death and improve performance on charge. In this chapter, we explore the viability of some redox mediators on charge through pressure-rise/decay measurements, DEMS, and discharge-charge cycling. Our observations suggest that significant challenges with reversibility and stability will be encountered with the introduction of redox mediators to Na-O_2 cells. An alternative combined galvanostatic and potentiostatic charging scheme is proposed and demonstrated to enable excellent charge capacity and recovery of O_2 without the onset of sudden death or the requirement of redox mediation.

6.2 Introduction

As discussed in the previous chapter, the Na-O_2 battery suffers from a curious sudden death on charge. This sudden death occurs when the combined rates of two NaO_2 reaction pathways can no longer support the applied current: the oxidation of thin NaO_2 films on the surface, and the dissolution, transport, and surface reaction of NaO_2 from larger crystal deposits.[1] As NaO_2 films disappear, the first reaction pathway accounts for a smaller fraction of the overall current rate, and because NaO_2 is only sparingly soluble in the electrolyte, the rate of the second reaction pathway can become limited by the rate of dissolution.[1,53] During the later stages of charge in particular, the shrinking surface area of the dissolving NaO_2 crystals becomes rate-limiting, and the potential in the cell precipitously increases beyond the stability window of the electrolyte. After this point, charge and the evolution of O_2

continue; however, they are accompanied by parasitic processes, the evolution of CO_2 and H_2, and possibly the irreversible degradation of the electrolyte into additional redox-active species.[1] As a result, the sudden death of the cell on charge is the effective limitation for the achievable reversible capacity of the Na-O_2 system.

A mechanistically inspired strategy for improving the Na-O_2 performance on charge is therefore to reduce the demand on the rate of NaO_2 dissolution, such that the rate-limiting oxidation of NaO_2 does not induce sudden death. In the previous chapter, charge at very low current densities (e.g., 88 $\mu A/cm^2$) could effectively delay sudden death until the practical end of charge. Low-current charging accomplishes this by avoiding the rate limitations associated with sudden death until effectively all of the NaO_2 present on the cathode has been consumed.[1] However, recent reports suggest that parasitic chemical reactions between NaO_2 and the electrolyte or O_2^- diffusion away from the cathode may be problematic on the time scales required for very-low-current-density discharges.[46,53] For both these reasons and the practical allure of a rapidly charged battery, it is desirable to mitigate sudden death while using higher current densities or shorter charging times.

Strategies for improving Na-O_2 performance in this manner include the introduction of a redox mediator or a modified charging scheme for the battery. Redox mediators are of increasing interest in both the Na-O_2 and Li-O_2 systems because of their likely abilities to enhance the capacity on discharge and charge.[18,123–125] A redox mediator intended to enhance charge, for example, exists in its reduced state in the cell. During charge, it is oxidized at the electrode surface, after which it oxidizes the discharge product (NaO_2 or Li_2O_2) to form O_2 and is thereby returned to its reduced state. In effect, a redox mediator acts as an electron-transfer agent between the solid electrode and the discharge product.[124] Because the action of a redox mediator need not necessarily require the dissolution of NaO_2 or its transport to the electrode surface, this approach seems promising upon initial examination, though the sensitive chemistry of the Na-O_2 system may make the design and optimization of an appropriate redox mediator challenging. Alternately, the demand for NaO_2 dissolution may be decreased using a charging scheme that relaxes the constant-current requirement utilized in the previous chapter, such as the approach briefly studied in Figure 5.7a. Decreasing the current rate effectively prevents the onset of sudden death on charge without the introduction of additional species in the cell or the associated complications to the chemistry.[1]

Countless redox mediators are presently under consideration for use in metal-air systems. As a preliminary study, four candidate redox-active species were selected and their viability as redox mediators studied in the Na-O_2 battery system. Previous reports have suggested that halide salts, and in particular I^-, may function as redox mediators in Li-O_2 batteries. Both the I^-/I_3^- redox couple and the higher-potential I_3^-/I_2 couple have been investigated for their viability as redox mediators and their effect on the cell chemistry.[18,123] The associated redox reactions (both written as reduction reactions) are:

$$I_3^- + 2e^- \rightleftharpoons 3I^- \tag{6.1}$$

$$I_2 + I^- + e^- \rightleftharpoons I_3^- \tag{6.2}$$

Likewise, Br^- may also function as a redox mediator, with similar possible reactions, including:

$$Br_3^- + 2e^- \rightleftharpoons 3Br^- \tag{6.3}$$

Ferrocene/ferrocinium ($Fe(C_5H_5)_2$ and its ion) is one of the most widely studied redox couples, and was the third possible redox mediator selected for study. Finally, prior reports have suggested that derivatives of thianthrene ($C_{12}H_8S_2$) may perform stable shuttling between the electrodes of Li-ion batteries.[126] Though shuttling (the reduction of an otherwise inactive species at one electrode and its oxidation at the other) is not necessarily a desirable behavior except for overcharge protection, the capability is somewhat analogous to redox mediation (oxidation at the cathode and reduction in contact with another active species at the cathode) and shuttling capabilities may indicate a species of interest. As a preliminary test of the stability and viability of thianthrene derivatives as redox mediators in Na-O_2 batteries, thianthrene was also selected for study.

In this chapter, we discuss preliminary attempts at employing these four possible redox mediators in Na-O_2 batteries. While none of the redox mediators tested exhibit sufficient stability and reversibility for use in the Na-O_2 cell design utilized in this work, the results provide insight into likely pitfalls in the use of redox mediators and possible future research directions. In addition, we demonstrate the superior performance of cells charged using a combined galvanostatic/potentiostatic scheme that prevents sudden death without requiring redox mediators. Charging at a constant current and then at a constant potential enables significantly improved recovery of O_2 gas on charge without the occurrence of sudden death or the long charging time required for a low-current galvanostatic charge.

6.3 Methods

Experimental methods are discussed in detail in Chapter 2. A custom-built cell of a modified Swagelok design was used to produce the data in this chapter and has been previously described in detail (Section 2.2.1.1).[15,30] Materials and cell assembly procedures are given in Section 2.2.1.2 and are consistent with our prior reports and the procedures used in the preceding chapters.[1,2,51] Specific details concerning the preparation of electrolytes containing redox mediators are given in Section 2.2.1.5. Electrolytes consisting of 0.5 M sodium trifluoromethanesulfonate (NaOTf) with either 0.2 M NaI, saturated NaBr (<0.2 M), 0.2 M ferrocene, or 50 mM thianthrene were prepared. Constant-pressure galvanostatic discharges to 0.88 mAh/cm^2 (or upon reaching 1.0 V for lower-capacity cells) were performed prior to charge under pure O_2 at pressures around 1.4 atm as described in Section 2.1.1.1. Quantitative characterizations of cell performance during charge were performed using both differential electrochemical mass spectrometry (DEMS, Section 2.1.2) and pressure-rise/decay techniques (Section 2.1.1), which we have previously described.[15,30] Electrochemical methods are described in Section 2.3.1, with particular details regarding linear sweep voltammetry, cycling, and chronoamperometric charging schemes given in Section 2.3.3.

6.4 Results and Discussion

6.4.1 Redox mediators

Cells with electrolytes containing NaI, NaBr, and ferrocene were assembled and tested for the activity and rate capability of the redox mediators using linear sweep voltammetry (LSV) under Ar. Results are given in Figure 6.1. Two peaks in the current are observed for the NaI electrolyte at approximately 3.2 V and 3.6 V. As reported in the analogous Li-O_2 system, these likely correspond to the I^-/I_3^- and I_3^-/I_2 redox couples, respectively (reactions 6.1 and 6.2).[18,123] NaBr was observed to be only sparingly soluble in the DME electrolyte. However, given that NaO_2's sparing solubility is sufficient to promote a solution mechanism on discharge and charge (see Chapters 3 and 5), even a sparingly soluble redox mediator could provide significant enhancements to cell performance or capacity depending on its activity. Due to its low concentration, the low current densities observed in the NaBr LSV are expected. However, a slight increase in the current as compared to the NaOTf-only cell at around 4.0 V suggests some additional redox activity, perhaps consistent with reaction 6.3. In contrast, the cell containing ferrocene demonstrates significant activity, with a maximum current occurring around 4.0 V. However, above 4.5 V, a rapidly increasing current was observed, suggesting parasitic chemistries or instabilities for this redox mediator. Taken together, these LSV results suggest that the three redox mediators tested may be active at potentials above those of the Na-O_2 charge plateau, and could be tested in Na-O_2 cells containing O_2 and NaO_2.

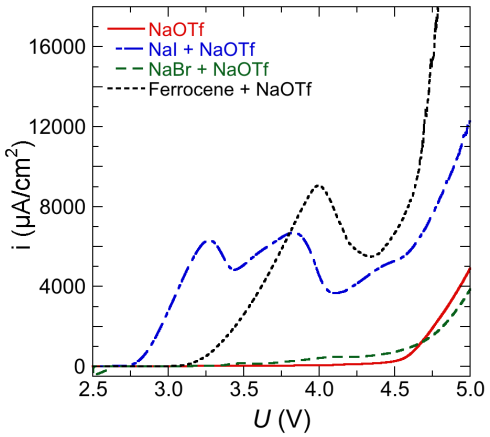

Figure 6.1: Linear sweep voltammetry at a 5 mV/s scan rate of Na-O_2 cells containing possible redox mediators in the electrolyte. Cells were not exposed to O_2 or atmosphere prior to LSV. Electrolytes were all mixed in DME and included: 0.5 M NaOTf alone; with 0.2 M NaI; with saturated NaBr; and with 0.2 M ferrocene.

6.4.1.1 Influence of NaI and NaBr on Na-O_2 charge behavior

The first discharge-charge cycles of two representative Na-O_2 cells containing NaI and NaBr are given in Figure 6.2. Accompanying gas consumption and gas evolution data from pressure-rise/decay measurements are plotted on the second axis. The cells in Figure 6.2 were overcharged by approximately 25% of the original discharge capacity to probe electrolyte stability and to attempt to recover any unreacted NaO_2 on the cathode. In all three cases, while additional redox processes are likely occurring, there are problems evident for each possible redox mediator.

Both the NaI and NaBr redox mediator electrolytes experience a lower-overpotential plateau prior to or preventing sudden death. In the case of NaI (Figure 6.2a), this occurs at approximately 3.0 V, and likely corresponds to the I^-/I_3^- redox couple. It is unclear from these data alone whether NaI is acting as a reversible redox mediator. However, during the ~3.0 V plateau, gas evolution from the cathode significantly decreases. This serves as evidence against the possibility of reversible, effective NaI redox mediation.

To confirm the decrease in gas evolution rate is due to a decreased rate of O_2 evolution, DEMS was performed on an identically prepared NaI cell, and the cell was overcharged by approximately 45% of its discharge capacity in an attempt to recover all O_2 expected based on its discharge capacity. Data are given in Figure 6.3. The presence of NaI induces, as observed in the pressure-rise/decay, a second charge plateau at ~3.0 V. The larger overcharge capacity leads to a second increase in potential, toward what appears to be the beginning of an additional charge plateau above 3.5 V; this likely corresponds to the I_3^-/I_2 redox couple.

As with cells containing no NaI (see Figure 5.6), the dominant charge product throughout the majority of the charge process is O_2, and O_2 production occurs at an approximately 1 e^-/O_2 process during the first (i.e., the low-overpotential) charge plateau. However, following

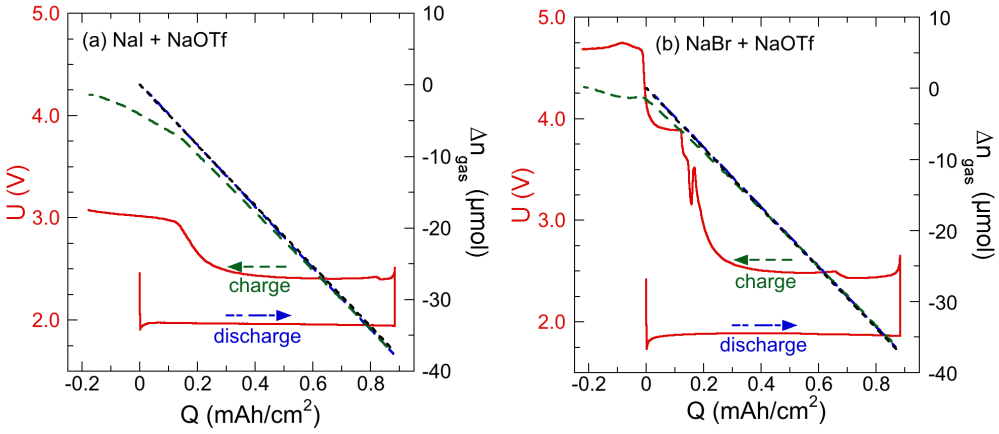

Figure 6.2: First discharge-charge cycles for Na-O_2 cells with 0.5 M NaOTf electrolytes containing (a) 0.2 M NaI and (b) saturated NaBr. Discharge at 880 $\mu A/cm^2$ proceeds from left to right, and charge at 880 $\mu A/cm^2$ from right to left. Gas consumption and evolution data are provided on the second axis, and the black dashed line indicates an ideal 1 e^-/O_2 process.

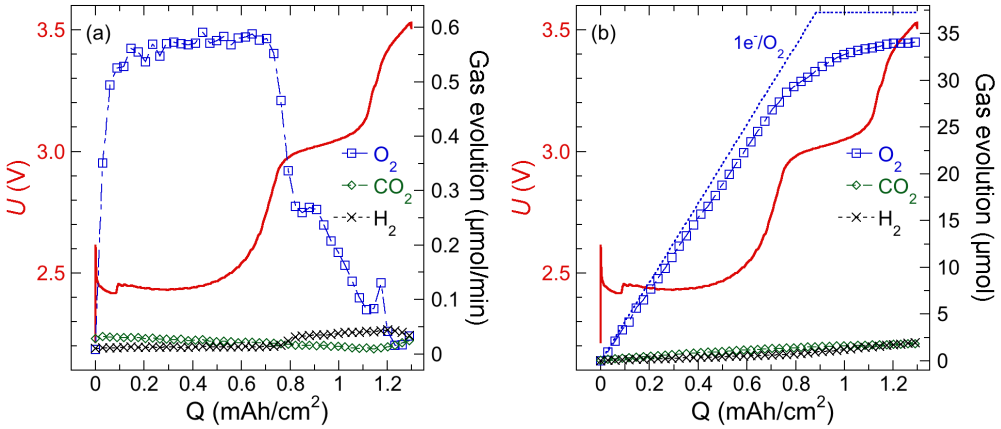

Figure 6.3: First charge of an Na-O_2 cell containing a 0.2 M NaI + 0.5 M NaOTf electrolyte with accompanying DEMS data. The charge current density was 880 μA/cm^2; charge proceeds from left to right. Evolution rates for the major charge products are given in (a), and the cumulative quantities of gases evolved are given in (b), with O_2 evolution consistent with an ideal 1 e$^-$/O_2 process indicated in (b).

the increase in potential to the second charge plateau, O_2 production decreases significantly. This suggests that, while the presence of I^- induces an additional charge plateau, the I^-/I_3^- redox couple does not act as a redox mediator in the evolution of O_2 from NaO_2. Instead, I^- forms I_3^- without additional reaction with NaO_2, and when all I^- is consumed, the potential increases to ~3.5 V and the I_3^- reacts to form I_2. After this point, it is possible I_3^-/I_2 shuttling in the cell may continue indefinitely, as has been reported in the Li-O_2 case.[18] However, charge could not be continued due to dendrite growth. This hypothesis is consistent with the quantities of I^- present in the cell, the quantity of O_2 evolved, and the capacity passed at the ~3.0 V plateau. Assuming 100% Faradaic efficiency for oxidation of I^- to I_3^-, the cell may be charged 0.25 mAh/cm^2 purely by this process. The quantity of O_2 evolved at that plateau (about 4.8 μmol) corresponds to a capacity of approximately 0.13 mAh/cm^2, again assuming 100% efficiency. These combined capacities are within 10% of the approximately 0.35 mAh/cm^2 passed during the 3.0 V charge plateau. Thus, it is likely that formation of I_3^- proceeded alongside a lower rate of O_2 formation by its usual mechanisms, and that I_3^- was not reduced back to I^- through any redox mediation reactions with NaO_2. Finally, the O_2 recovered at the end of charge represented only 91% of the O_2 expected, and approximately 5% of the total gas evolved is H_2, the majority of which was produced beginning at the ~3.0 V charge plateau. This is not a significant improvement over that recovered during charge of a cell without NaI. Altogether, while the addition of NaI to the electrolyte delayed the onset of sudden death, it did so without redox mediation and did not enhance overall cell efficiency or the recovery of O_2.

In the case of NaBr (Figure 6.2b), analogous behavior is observed. However, the second plateau occurs slightly below 4.0 V, and only about 0.1 mAh/cm^2 of capacity was passed

before the cell's eventual sudden death occurred. This plateau is likely associated with the Br^-/Br_3^- redox couple, and the lower capacity is consistent with the sparing concentration of NaBr in the electrolyte ($\ll$0.2 M). This behavior suggests that Br^- oxidation does not occur reversibly or that Br_3^- does not act as a redox mediator. To confirm this, cells containing NaBr were cycled up to four times. The results are given in Figure 6.4, alongside the results from a cell containing no NaBr (Figure 6.4a). While the presence of NaBr delays the final sudden death of the cell on the first discharge/charge cycle, in subsequent cycles the cell containing NaOTf only and the cell containing NaBr exhibit similar behaviors and capacities. Thus, while both NaI and NaBr affect the charge voltage behavior of the Na-O_2 cell and do not significantly alter the stability of the discharge product, neither acts as a redox mediator in the Na-O_2 battery system as studied here.

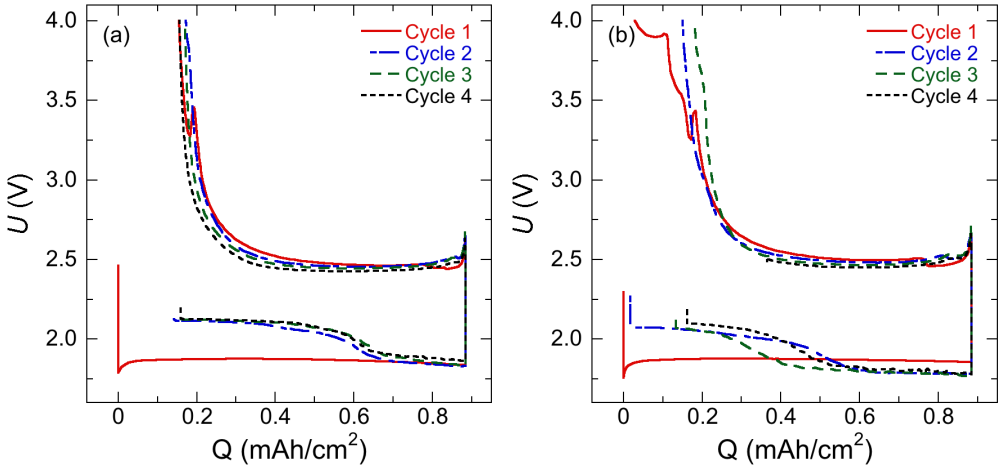

Figure 6.4: First four discharge/charge cycles of Na-O_2 cells containing (a) a 0.5 M NaOTf electrolyte and (b) a 0.5 M NaOTf electrolyte saturated with NaBr. Following the first cycle, no significant differences are observed in the cell, indicating that the redox mediator does not reversibly react or is otherwise unstable. Note that the fourth cycle in (b) ended early due to dendrite formation.

6.4.1.2 Instability of ferrocene in the presence of O_2

The first discharge-charge cycle of a representative Na-O_2 cell containing ferrocene is given in Figure 6.5. As with NaI and NaBr, the introduction of ferrocene modifies the charge profile of the cell from that of a cell with an NaOTf electrolyte alone. The low-overpotential charge plateau is followed by a modest increase in potential, less dramatic than that associated with sudden death. Unlike with NaI and NaBr, the presence of ferrocene may improve recovery of O_2 prior to this point; recovery of gas from the cell seems nearly perfect for the first 90% of the cell's charge. However, in the final 10% of the cell's charge, the production of gas

begins to decrease. Upon overcharge of the cell, apparent gas consumption begins. This is likely an oxidation reaction involving O_2 and the ferrocene or ferrocinium in the electrolyte, quite possibly the oxidation of the metal center to iron oxide and degradation of the organic components. Thus, while it is possible ferrocene assisted in redox mediation as suggested by the excellent O_2 evolution prior to this point, the instability of ferrocene to O_2 makes it unsuitable for application in the Na-O_2 battery.

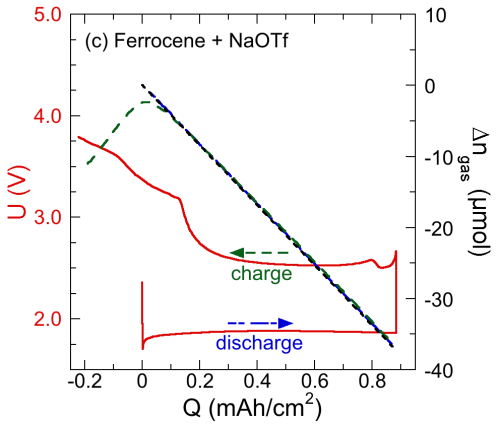

Figure 6.5: First discharge-charge cycle for a Na-O_2 cell containing 0.2 M ferrocene in addition to 0.5 M NaOTf in the electrolyte. Discharge at 880 μA/cm^2 proceeds from left to right, and charge at 880 μA/cm^2 from right to left. Gas consumption and evolution data are provided on the second axis, and the black dashed line indicates an ideal 1 e^-/O_2 process.

6.4.1.3 Instability of thianthrene to both the Na-O_2 cathode and anode.

Results from the first discharge and charge of a cell containing 50 mM thianthrene in the electrolyte are given in Figure 6.6.[a] Unlike cells containing any of the first three redox active species studied, cell containing thianthrene tend to suffer sudden death at low capacities; in Figure 6.6, the cell shown achieved a discharge capacity of less than 0.30 mAh (0.27 mAh/cm^2) before reaching 1.0 V, about one-tenth of that expected at this current density (see Figure 3.1). O_2 consumption on discharge is consistent with a 1 e^-/O_2 process. However, upon charge, the cell exhibits significantly different characteristics from the typical Na-O_2 cell. No low-overpotential charge plateau occurs. Instead, following the initial increase in potential at the beginning of charge, the overpotential increases gradually until the cell begins to short due to dendrite formation, evidenced by the downward spikes in potential late on charge. Additionally, gas production is significantly below that of a 1 e^-/O_2, and in fact more closely resembles an apparent 2 e^-/O_2. We note similarities between this charge profile and those reported for some Na-O_2 batteries forming Na_2O_2.[8]

[a]Figure 6.6 acquired in collaboration with Elyse A. Kedzie; the thianthrene was purified by recrystallization by Dr. Pedro Arrechea.

These data suggest that thianthrene has multiple detrimental effects on the Na-O_2 cell chemistry. First, the low capacity on sudden death suggests a possible passivation effect on the cathode, such as by the deposition of parasitic discharge or decomposition products. This is supported by the increasing overpotential on charge and decreased production of gas. Additionally, the tendency of the cell to short at low capacities despite the modest current density suggests an instability of the redox mediator to the anode, which could result in a poorer-than-usual solid-electrolyte interface at the Na anode, inconsistent Na plating on charge, and an increased tendency to dendrite formation. These results suggest that the use of thianthrene or its derivatives in an Na-O_2 cell may require chemical modification to improve stability to NaO_2 and protection of the Na anode to prevent diffusion of the redox mediator to the anode surface.

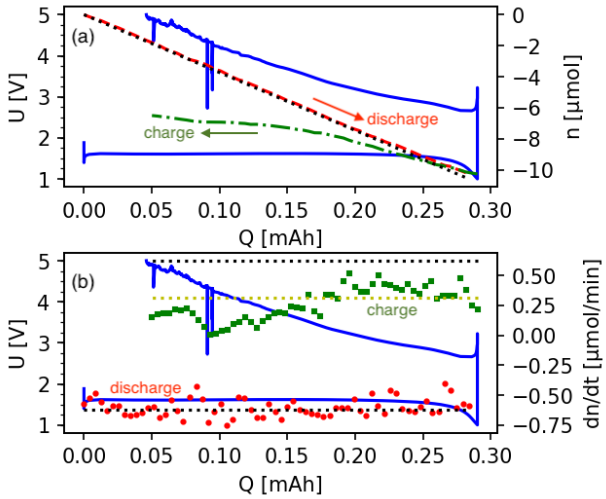

Figure 6.6: First discharge-charge cycle of an Na-O_2 cell containing 50 mM thianthrene in addition to 0.5 M NaOTf in the electrolyte. The discharge and charge current density was 880 μA/cm^2. (a) Cumulative consumption and evolution of gas from the cell, and (b) the instantaneous rate of gas evolution from the cell. The black dotted line indicates an ideal 1 e^-/O_2 process, and the yellow dotted line indicates an apparent 2 e^-/O_2 process.

6.4.2 Alternate charging schemes

While redox mediators could enable rapid charging without the onset of sudden death or the degradation of the electrolyte, our prior results suggest that sudden death can be similarly delayed by decreasing the current density upon reaching some voltage cutoff, as in Figure 5.7a. In this approach, three currents lower than the initial charging current were selected and utilized in a stepwise manner; upon reaching 3.0 V, the cell's current was decreased to the next-lowest current. The decreased-current charging scheme effectively extended the charge

capacity of the cell prior to sudden death, achieving a capacity similar to that achieved at a constant lower current density in a fraction of the time. The approach could be extended to a greater number of lower currents or steps. At the limit of an infinite number of charging steps, this becomes a potentiostatic (constant-potential) charging technique performed using chronoamperometry, where the current is allowed to decrease until reaching some minimum current cutoff.

Results from an initial study of a combined galvanostatic-potentiostatic charging technique are given in Figure 6.7.[b] In this example, the cell was galvanostatically charged at 1800 μA/cm^2 to a full cell potential of 3.0 V. Upon achieving this potential, the cell was potentiostatically charged at 3.0 V until the current decreased to approximately 15 μA/cm^2, a current consistent with that observed in a cell containing no active material (O_2 or NaO_2) at 3.0 V using LSV (Figure 6.1). At this point, charge was taken to be complete. The accompanying gas consumption/evolution data from pressure-rise/decay indicates that the cell experienced excellent recovery of gas on charge; pressure-rise on charge achieved a quantity equivalent to 93% of the O_2 consumed on discharge and 94% of the gas expected based on the discharge capacity. This is within the statistical variance of the yield of NaO_2 from iodometric titrations of identically discharged cathodes, as reported in previous chapters (see Chapters 3 and 4). This suggests that, if the majority of the gas evolved was O_2, it could represent virtually all of the NaO_2 present on the cathode following discharge. Additionally, this was achieved in a fraction of the time required to charge the cell constantly at a lower current density. In our prior study, sudden death on charge could be delayed until >95% of the discharge capacity by charging at current densities at or below 88 μA/cm^2, requiring 10 hours and recovering approximately 91% of the gas expected based on the discharge capacity (see Figure 5.4a). The combined galvanostatic-potentiostatic charge was complete in 94

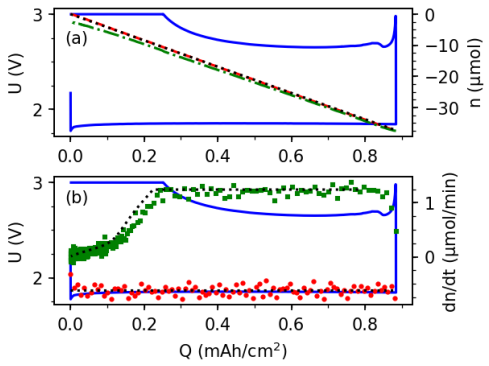

Figure 6.7: Galvanostatic discharge at 880 μA/cm^2 of an Na-O_2 cell followed by galvanostatic charge at 1800 μA/cm^2 to 3.0 V. Immediately upon reaching 3.0 V the cell was switched to a potentiostatic charge and allowed to charge until the current reached 15 μA/cm^2.

[b]Figure 6.7 acquired in collaboration with Elyse A. Kedzie.

minutes and demonstrated superior gas evolution. While superior oxygen recovery has yet to be verified by DEMS, these results suggest that combined galvanostatic-potentiostatic charging schemes may circumvent the need for redox mediators on charge altogether.

6.5 Conclusions and Recommendations

In this chapter, we have presented preliminary work concerning two approaches for improving the achievable charge capacity of Na-O_2 cells. Both approaches, the introduction of redox mediators and the application of alternate charging schemes, focus on reducing the demand on NaO_2 dissolution, which becomes rate-limiting and induces sudden death in the cell. None of the redox mediators tested achieve the desired performance. First, neither NaI nor NaBr act as reversible mediators; observations suggest that I^- and Br^- react to form I_3^- and Br_3^-, respectively, which do not participate in any redox mediation with NaO_2. The presence of NaI or NaBr could delay or eliminate the sudden death behavior of the cell, but evidence from further cycling of cells containing NaBr suggests this effect occurs only on the first discharge-charge cycle. Second, while ferrocene may have operated as a redox mediator, slight overcharge of the cell induced consumption of gas, suggesting significant instability of ferrocene in the system. Third, cells containing thianthrene exhibited symptoms consistent with instabilities of both the anode and the cathode.

While the redox mediator candidates considered in this study do not comprise an exhaustive list of possible candidates, these results provide some insight into likely challenges in further research of redox mediators to assist in the charge of Na-O_2 cells. A redox mediator must have an active redox couple at a potential relevant in the Na-O_2 system. Unlike the case of NaI and NaBr, it must not only be oxidized reversibly, but the oxidized species must participate in redox mediation with the NaO_2 chemistry. Ideally, a redox mediator should also be stable enough that it does not degrade on overcharge of the cell, as was the case with ferrocene. Stability of the mediator to both the cathode and anode materials will also be necessary if it is to be viable in the Na-O_2 system. If stability to the Na metal anode cannot be achieved, protection of the anode by a physical barrier or solid-electrolyte interface engineering could be beneficial. Some reports of Na anode protection strategies exist, such as the use of a sodium-beta-alumina solid electrolyte membrane, and may provide additional benefits in preventing dendrite growth or undesired shuttling.[39]

A promising alternative to the introduction of redox mediators may be modifying the charging parameters of the cell. In particular, the combined galvanostatic-potentiostatic charging scheme demonstrated herein offered superior recovery of gas on charge and prevented sudden death, achieving complete charge of the cell in a fraction of the time required to do so galvanostatically. Further research into this technique is recommended. In particular, an investigation of the effect of current densities and potentials used on charge may be beneficial. Quantitative chemical analysis of the gases evolved and of any solid products remaining on the cathode following charge would provide crucial insight into the viability of this approach for improving Na-O_2 charge performance. Additional tests exploring its viability on later

cycles of the cell would also be informative, especially when used in conjunction with an anode protection strategy to prevent crossover of dissolved O_2^- or growth of Na dendrites.

Chapter 7

A Quantitative Analysis of the Magnesium Negative Difference Effect

7.1 Abstract

Magnesium metal (Mg) offers numerous advantages in energy storage applications over other active metals, including its high abundance, low toxicity, and inherently safer properties as compared to Li or Na. Aqueous Mg-O_2 batteries, for example, could be constructed with lightweight, inexpensive materials, and due to the inherently safer properties of aqueous electrolytes (e.g., non-flammability), might more easily be designed as "breathing" cells open to the atmosphere. However, the parasitic corrosion of Mg in aqueous environments generates H_2 and decreases the efficiency of the cell, especially on discharge. This corrosion is exacerbated by the occurrence of an unusual increase in the rate of H_2 evolution during oxidative polarization of Mg, known widely as the negative difference effect (NDE). In this chapter, we study the NDE in electrolytes of varying pH containing Cl^-, which is known to result in substantial Mg corrosion. We observe that in an electrolyte of a sufficiently low bulk pH, the NDE disappears. This observation has significant implications with respect to possible mechanisms for the NDE, and in particular is inconsistent with the popular theory that Mg dissolves as Mg^+.

7.2 Introduction

As discussed in Section 1.4, Mg corrosion is a significant challenge in the use of Mg electrodes for energy storage devices.[60] In particular, the Mg anode is afflicted by an atypical increase in the rate of H_2 evolution during oxidative polarization known as the negative difference effect (NDE).[61,73–75] The NDE is particularly problematic in aqueous Mg-O_2 batteries because it results in a dramatic and problematic increase in the anode's corrosion rate during discharge.[19] Despite the first report of the NDE dating back to 1866,[61] and extensive investigation of the

phenomenon in the past sixty years, no consensus exists for the mechanism of the NDE.[60,75]

For the purposes of simplifying the many possible mechanisms enumerated in Section 1.4, we generally classify the postulated mechanisms as belonging to two categories: those involving the dissolution of Mg as an ion of unusual valence, the unipositive Mg^+ (also known as univalent or monovalent), and those which do not. The former mechanism was first put forward by Petty, Davidson, and Kleinberg in 1954.[63] Proponents within the second camp have argued that the unipositive ion theory was definitively disproven in the subsequent decade by the works of Straumanis, Bhatia, James, Robinson, or King.[66,67,78] However, the past few decades have seen a popular resurgence of the unipositive theory, especially but not exclusively as promoted by Atrens and colleagues,[60,68,69,82,83,85] in spite of numerous recent works that independently and reproducibly dispute their assertions.[71,73,86–90] Alternate mechanisms in the second camp include anode disintegration, elemental impurities, surface film effects, the formation of MgH_2, catalytic effects, and other arguments.[66,67,73,77–81] We acknowledge that this summary somewhat oversimplifies the positions of the field, as disagreement regarding which mechanism may be correct exists within the second camp. However, these latter mechanisms are unified by the general agreement that Mg dissolution as Mg^+ does not occur.

The mechanism behind the Mg^+ theory entails the supposed dissolution of Mg as one of two ionic species:[127]

$$Mg \rightleftharpoons Mg^{2+} + 2e^- \tag{7.1}$$

$$Mg \rightleftharpoons Mg^{+} + e^- \tag{7.2}$$

The unipositive ion produced in reaction 7.2 could then be further oxidized electrochemically to Mg^{2+}, or oxidized by chemically reducing other species, especially the solvent H_2O,[63,65,127]

$$2Mg^+ + 2H_2O \rightarrow 2Mg(OH)_2 + H_2 \tag{7.3}$$

or, in acidic media,

$$2Mg^+ + 2H^+ \rightarrow H_2 + 2Mg^{2+} \tag{7.4}$$

Reaction 7.4 in particular suggests that the NDE should be exacerbated in acidic media where the activity of H^+ is higher. If instead one supposes that Mg dissolves only as Mg^{2+} (or $Mg(OH)_2$), and that its corrosion is promoted by any one of the alternate mechanisms, the dependence of the NDE on the pH will depend on the mechanism selected. In that case, dissolution and corrosion of Mg will occur by reactions 1.4 to 1.8, and for the case of one mechanism, perhaps including the production and consumption of MgH_2.

Previous reports have indicated that the identity of various salts in the electrolyte can impact the occurrence and severity of the NDE.[19,69,71] In particular, Cl^--based electrolytes are known to result in substantial Mg corrosion.[19,69,90] Other reports have suggested that pH effects are observed, largely though not exclusively with a focus on the effect of increasingly basic pH.[66–69,89–91] While some reports include quantitative measurements of the reacting species, not all do so. Additionally, because of the long history in the field, a large body of

data exists that predates more recent advances in electrochemical and analytical techniques, including the modern use of electrochemical impedance spectroscopy (EIS). More recent work has initiated a trend of applying methods like these to deepen the understanding of the Mg corrosion mechanism, to great effect.[71,87]

In this chapter, we detail quantitative measurements of the Mg NDE in different pH environments and different Cl^- concentrations. Our observations clearly indicate that Mg corrosion and dissolution are consistent with a $2e^-$ process regardless of electrolyte composition. We confirm previous reports of the non-polarizable behavior of the Mg electrode, highlighting the importance of electrochemical impedance spectroscopy in monitoring the behavior of the Mg electrode. In addition, we observe that in electrolytes of a sufficiently low bulk pH, the Mg NDE ceases, and suppression of H_2 evolution with increasing current is observed, contrary to prior reports.[69] A sufficiently high oxidative current density can induce the return of the NDE, an effect we correlate with an increase in the local pH at the dissolving Mg electrode surface and the appearance of dark surface films. The bulk pH below which the NDE is suppressed is likely dependent upon the transport and mixing properties of the electrochemical cell in which the NDE is studied. These observations are not consistent with an NDE mechanism involving the dissolution of Mg as Mg^+.

7.3 Methods

Experimental methods are discussed in detail in Chapter 2. A large-volume three-electrode glass H-cell was custom designed and constructed by Adams & Chittenden Scientific Glass (Berkeley, CA); the design and considerations for data analysis are described in detail in Section 2.2.2. Materials and cell assembly procedures are given in Section 2.2.2.2, with particular attention to the preparation of Mg electrodes and the assembly and calibration of the three-electrode large-volume H-cell. Analysis of H_2 evolution was performed using pressure-rise/decay techniques as described in Section 2.1.1. Similar instrumentation and techniques as applied to both Mg and other electrochemical systems have been previously described.[15,19,30] Electrochemical methods are described in Section 2.3.4, with particular attention for the application of electrochemical impedance spectroscopy (EIS) in the study of the Mg system. Potentiostatic EIS (PEIS, Section 2.3.4.1), staircase potentiostatic EIS (SPEIS, Section 2.3.4.2), and galvanostatic EIS (GEIS, Section 2.3.4.3) were used to acquire the data presented in this chapter. Additional electrochemical methods, discussion of limiting-current measurements, and comments on mass-transport coefficient models are included in Section 2.3.5. Python code used in the analysis of results and the aforementioned models is available in Appendix B.

7.4 Results and Discussion

7.4.1 General observations of the NDE and the importance of EIS

An important characteristic of the Mg electrode is its non-polarizable behavior on oxidative (anodic) polarization, which complicates the study of the NDE by controlled-potential techniques. Other reports clarify that the Mg electrode obeys Tafel kinetics on reductive (cathodic) polarization.[19,68,69,79] We find that on anodic polarization, the Mg electrode experiences nearly negligible changes in overpotential even at very high current densities, consistent with prior reports.[71,79,87] Apparent (as-measured) and IR-corrected oxidative Tafel plots of a Mg electrode are given in Figure 7.1, for the case of a 3.0 M KCl electrolyte at approximately pH 10, with the accompanying rate of gas evolution plotted on the second axis. Additional Tafel plots are available in A.7. Though prior reports have utilized PEIS at or near the open-circuit potential to acquire plots as in Figure 7.1, the use of SPEIS allows us to captures the tendency of the series resistance to increase during polarization. For example, in Figure 7.1, the resistance increased from 0.66 Ω initially to 0.91 Ω (see Figure A.8). Though small, this increase in the series resistance is likely indicative of changes to the Mg surface due to the formation of films and changes to the conductivity of the electrolyte, likely due to small shifts in the pH. Due to the high ohmic losses in the cell and small changes in the series resistance, the as-measured data acquired from the Mg electrode in Figure 7.1 can present a misleading picture of the chemistry, and in cases where the series resistance is

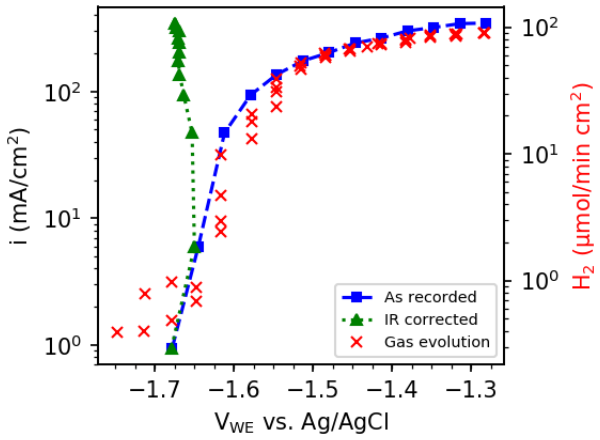

Figure 7.1: As-measured and IR-corrected oxidative Tafel plots of Mg in 3 M KCl, with accompanying gas evolution data. Gas evolution (plotted against as-measured potentials for clarity) is scaled such that overlap with the plot of i vs. V indicates that the rate of H_2 evolution scales with the current like a 2 e^- process. The open-circuit potentials of the electrode prior to and following this measurement were -1.74 and -1.67 V vs. Ag/AgCl, respectively.

large or unknown, any potentiostatic or controlled-potential techniques can lead to significant inaccuracies.

A curious observation concerning the NDE is the scaling between the rate of H_2 evolution and the applied current. The y-axes in Figure 7.1 are scaled such that overlap between the gas evolution data and the IV curve indicates an apparent 2 e^- process. This coincidental current scaling occurs despite the applied current being oxidative and the H_2 evolution reaction being fundamentally a reduction reaction, and has been reported previously in similar electrolytes.[19] This observation will be revisited throughout our discussion below.

Additionally, we observe that the open-circuit potential (OCV) of Mg electrodes is somewhat dependent on their history and preparation. Example OCVs prior to and following polarization of Mg electrodes are given in Table 7.1. The OCV before polarization was recorded shortly after insertion of the chemically polished and conditioned Mg electrode into the cell (see Section 2.2.2.2). The OCV after polarization was measured at least three minutes following the end of polarization, during which the OCV was observed to rapidly stabilize. The values given in Table 7.1 were acquired prior to and following SPEIS polarization schemes as in Figure 7.1, and the typical capacity passed during data acquisition was between 1 and 10 mAh/cm^2. However, the OCV following these tests was observed to be reasonably stable; repeat SPEIS polarizations on the same electrode resulted in no statistically significant changes in OCV.

A trend concerning both the value of the potential and how much it changes is observed with pH. At pH 1, the OCV was not observed to change; additionally, these electrodes exhibited a very high open-circuit corrosion rate, consistent with their low potentials vs. the equilibrium potential for H_2 (provided as OCV vs. RHE in Table 7.1). At pH 2, some change in open-circuit potential was observed with polarization, though these measurements had the greatest variance of all those studied, with an average change in pH on the same order as the standard deviation of the measurements. In higher-pH electrolytes between pH 3 and 10, a

Table 7.1: Open-circuit potentials (OCV) of Mg electrodes prior to and following polarization in $[Cl^-] = 0.5$ M electrolytes. Consistent with prior reports, the OCV was observed to be independent of the concentration of Mg^{2+} in the electrolyte. Potentials given are the average of multiple measurements, with the standard deviations indicated as ± quantities. The average change in potential (ΔV) is also provided. The approximate OCV vs. the reversible H_2 electrode (RHE) data were calculated from the pH as indicated.

	OCV vs. Ag/AgCl					OCV vs. RHE	
pH	Before	±	After	±	ΔV	Before	After
1	-1.86	0.02	-1.86	0.02	0.00	-1.60	-1.60
2	-1.83	0.01	-1.74	0.10	0.09	-1.52	-1.43
3	-1.79	0.01	-1.65	0.01	0.14	-1.42	-1.28
10	-1.73	0.02	-1.64	0.01	0.09	-0.94	-0.85
12	-1.61	0.01	-1.61	0.01	0.00	-0.71	-0.71

small increase in the electrode potential was sometimes observed prior to the beginning of polarization, suggesting that the change in potential after polarization is due to the formation or break down of surface films, and that adequate equilibration of the electrode in the cell could achieve a stable OCV similar to those observed following polarization. In addition, a significant change in the OCV at pH between 3 and 10 was generally correlated with an increased rate of open-circuit H_2 evolution after polarization, as will be shown for the case of pH 10 below. This occurred in spite of the fact that the potential vs. the equilibrium potential for H_2 (OCV vs. RHE) decreased following polarization. We attribute this change to the nature of the Mg electrode surface, possibly a roughening due to the oxidation of Mg or the corrosion of small Mg particles trapped in the oxidized films on the electrode surface. Finally, at pH 12, no significant change in the open-circuit potential of the cell was observed. This may be due to the lower corrosion rate at this pH and the stability of electrode surface films, such as $Mg(OH)_2$.

The appearance of dark surface film deposits varies depending on the pH, but their presence is observed to coincide with larger changes in the OCV. Dark films on the surface of Mg electrodes have been previously reported to be comprised primarily of $Mg(OH)_2$, with the dark color due to embedded particles of Mg metal.[62,67] Images of electrodes and the surface films formed in various pH environments are given in Figure 7.2. These films correspond to those present on the electrode following polarization by SPEIS as in Figure 7.1 following at least three minutes of rest at OCV. Electrodes are included for pH in the range of 4-7 to illustrate the trend in surface film appearance from acidic to neutral environments. However, data at these pH were not included in Table 7.1 because these electrodes tended to experience significant changes in pH prior to and following polarization, and pH in this range should be regarded as approximate. At higher pH (e.g., pH 12 and 10) the films appear in small patches and consist of both dark films and white $Mg(OH)_2$ that tends to flake or crumble off the dry electrode. As the pH is decreased from pH 10 to pH 4, the films tend to cover the electrode more completely. Below pH 4, film coverage decreases, and at the lowest pH (1 and 2), dark surface films are absent or only cover a small fraction of the electrode area. In these lower-pH cases, any films present tend to be concentrated at the tip and edges of the electrode, which are nearer to the counter electrode and may experience slightly higher local

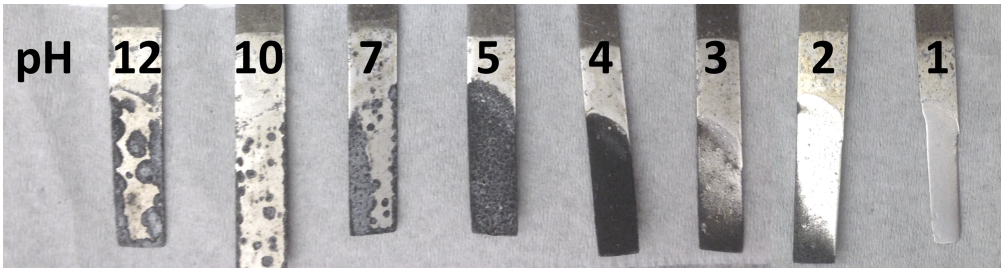

Figure 7.2: Photographs of Mg electrodes following electrochemical characterization in 0.5 M Cl^- electrolytes at different pH.

current densities as a result (such as the pH 2 electrode in Figure 7.2). This observation will become important later when considering the NDE behavior at low pH.

The values in Table 7.1 are given in a 0.5 M Cl^- electrolyte; however, similar trends are observed at other Cl^- concentrations. For example, in a 3.0 M KCl electrode at approximately pH 10, the electrode potential upon cell assembly was on average -1.74 ± 0.04 V vs. Ag/AgCl, and the average electrode potential following electrochemical analysis was -1.66 ± 0.01 V vs. Ag/AgCl. While the values of the OCVs were observed to be similar with different Cl^- concentrations, the open-circuit corrosion rate was generally higher in higher Cl^- environments, in agreement with prior reports that show Cl^- increases the rate of Mg corrosion.[69,90]

Additional polarization of the same electrode was not observed to produce further significant changes in the OCV, as illustrated in Figure 7.3. In these polarization experiments, current was applied using galvanostatic electrochemical impedance spectroscopy (GEIS) for a short period before the electrode was allowed to relax to open-circuit for a few minutes. Different currents were applied in succession, either in a strictly increasing scheme (Figure 7.3a-c) or varying high currents with low currents (Figure 7.3d-f). The electrode potentials

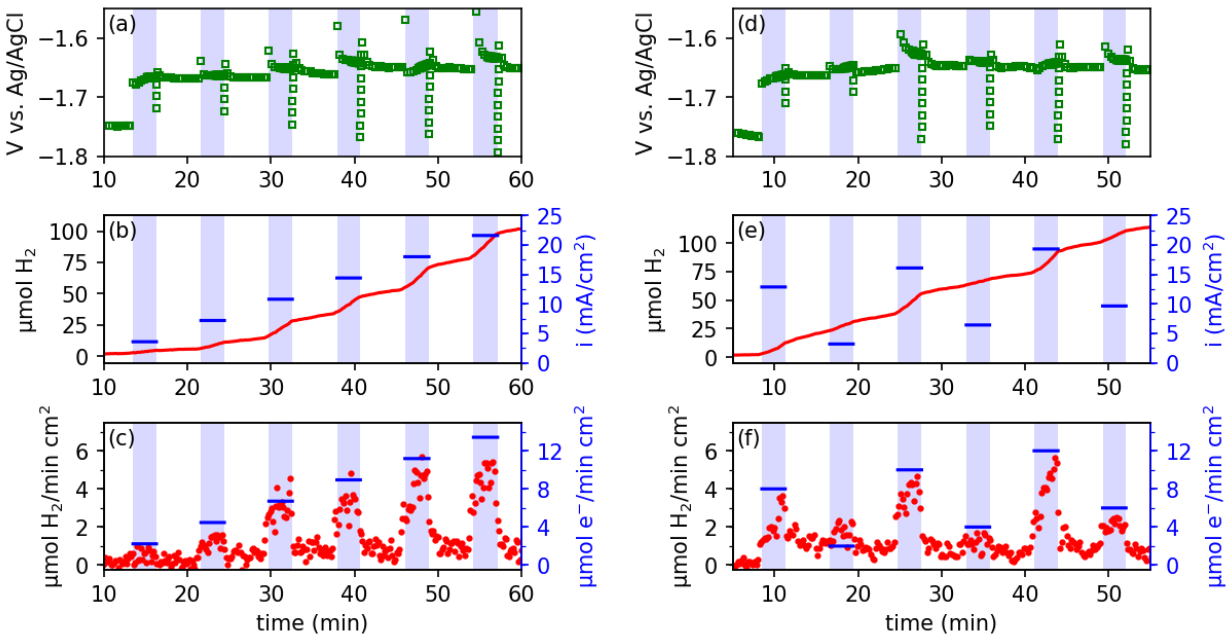

Figure 7.3: Polarization of Mg electrodes by GEIS at various current densities in 3 M KCl at pH 10. Time during which current was applied is shaded in blue. The currents employed in (a-c) were monotonically increasing and the currents in (d-f) were varied; changes in the measured electrode potential (a,d), particularly at open circuit, are similar in both cases. (b,e) The quantity of H_2 evolved over time with accompanying current densities indicated on the second axis. (c,f) The rate of H_2 evolution with accompanying current densities presented in μmol/min cm^2; the left and right axes are scaled such that overlap of the gas evolution and current density data indicates a 2 e^- process.

presented are IR-corrected using the series resistance acquired with GEIS (see Section 2.3.4.3).

Changes in the OCV are typically small, with the exception of the change following the first polarization (Figure 7.3a,d). Capacities as small as 0.6 mAh/cm^2, as in the first GEIS period in Figure 7.3a-c, are adequate to result in this largest increase in the OCV. Additionally, a small increase in the open-circuit corrosion rate is apparent following the first few lower-current GEIS periods in Figure 7.3a-c, or the first higher-current polarization in Figure 7.3d-f. That the change in open-circuit corrosion is not strictly correlated with the change in OCV implies it is related to a surface film effect that does not alter the activity of the electrochemically active anode, such as the buildup of small Mg particles trapped in the surface films.[67] Though small changes in OCV were observed following subsequent GEIS periods, these changes were significantly less than those observed prior to and following the first GEIS period, and could be correlated to slight increases in the electrolyte pH and the changing films on the Mg electrode surface. Finally, in this electrolyte (pH 10 in 3 M KCl), the rate of H_2 evolution approximately scales with the current density as previously discussed and as indicated by the scaled current densities and rates of H_2 evolution in Figure 7.3c and f. No significant difference in this scaling is observed between the two different current schemes.

7.4.2 Total dissolution of Mg electrodes for determining the stoichiometry of Mg oxidation

To assess the overall stoichiometry of the combined Mg oxidation and corrosion processes, Mg electrodes were placed in various electrolyte environments, and Mg oxidation was performed under GEIS until the entire electrode dissolved (see Section 2.3.4.3). Notably, this dissolution procedure applies an effectively constant current to the electrode, but the decreasing surface area of the electrode results in an increasing current density, particularly toward the end of the dissolution. The moment of complete electrode dissolution was marked by a rapid increase of the potential beyond the operating range of the galvanostat/potentiostat and by the rate of H_2 evolution falling to zero. The data acquired were analyzed to determine the quantities of Mg dissolved (i.e., Mg corroded or oxidized), the total amount of H_2 evolved by Mg corrosion, and the total oxidative charge passed through the electrode. The quantity of Mg dissolved due to oxidation as opposed to corrosion or the NDE may be determined by subtracting the quantity of H_2 evolved ($H_{2,total}$) from the total quantity of Mg dissolved (Mg_{total}) as determined from a gravimetric measurement of the electrode before and after Mg dissolution. For the quantities of each species,

$$Mg_{oxidized} = Mg_{total} - H_{2,total} \tag{7.5}$$

Alternately, the quantity of Mg dissolved due to corrosion as in reaction 1.7 or 1.8 may be determined by subtracting the quantity of electrons passed by oxidative current (e^-_{total}), scaled with an appropriate stoichiometric ratio n; i.e., for the quantities of each of the following,

$$Mg_{corroded} = Mg_{total} - \frac{e^-_{total}}{n} \tag{7.6}$$

This second approach requires some assumption of the Mg dissolution mechanism to determine the overall value of n, though except for the controversial unipositive Mg dissolution step, it is generally accepted that n = 2. The value of n observed in a given experiment may be determined by the ratio of $Mg_{oxidized}$ to e^-_{total}. The calculations given above are consistent with corrosion as given in reactions 1.4 to 1.8.

Data from the dissolution of Mg under various experimental conditions is given in Table 7.2, including calculated ratios indicating the apparent stoichiometry of the electrochemical Mg oxidation not including corrosion ($e^-/(Mg - H_2)$), and the apparent stoichiometry of Mg and H_2 corrosion, not including oxidation ($H_2/(Mg - \frac{e^-}{2})$). Mg electrodes were dissolved in KCl electrolytes varying in pH from 1 to 12. The total chloride ion concentration is given in each case. Electrolytes at pH 1 and 2 were prepared using HCl, with the remainder of the Cl^- provided by KCl (i.e., pH 1 electrolytes consisted of 0.1 M HCl and 0.9 M KCl). Electrolytes at pH 10 were prepared using only KCl at the given Cl^- concentration. As-mixed, their pH was measured to be at or below 7, consistent with the pH effects of KCl dissolution. The pH of the solution was observed to rapidly increase to approximately 10 following insertion of the Mg electrode, and the pH of each solution was measured following Mg dissolution and confirmed to be between 10 and 10.5 (see Section 2.2.2.2). Electrolytes at pH 12 were

Table 7.2: Quantities of Mg dissolved, H_2 evolved, and charge passed for dissolution of Mg electrodes in various electrolytes, and associated ratios of e^- to Mg assuming one-to-one evolution of H_2 from Mg corrosion, or of H_2 to Mg assuming a 2-e^- Mg oxidation. The uncertainty of each ratio is approximately ±10% of the reported value.

Electrolyte		Oxidation	Quantity (μmol)			Ratio	
pH	$[Cl^-]$ (M)	i (mA/cm^2)	Mg	H_2	e^-	$e^-/(Mg - H_2)$	$H_2/(Mg - \frac{e^-}{2})$
1	1.0	0	263	263	-	-	1.00
1	1.0	90	617	484	374	2.81	1.13
1	1.0	260	374	190	407	2.21	1.11
1	1.0	440	403	211	437	2.28	1.14
2	1.0	60	407	209	463	2.34	1.19
2	1.0	290	346	165	479	2.65	1.55
10	0.3	84	333	151	402	2.21	1.14
10	0.3	140	313	148	383	2.32	1.22
10	0.3	240	337	161	418	2.38	1.26
10	1.0	56	403	189	462	2.16	1.10
10	1.0	130	350	149	411	2.04	1.03
10	1.0	250	333	149	417	2.27	1.20
10	3.0	58	391	171	467	2.12	1.09
10	3.0	150	280	129	346	2.29	1.21
10	3.0	260	309	145	378	2.30	1.21
12	1.0	100	444	202	529	2.19	1.13

prepared using a 1.0 M KCl solution by addition of KOH. No significant change in electrolyte pH before or after a given experiment was observed for electrolytes prepared at pH 1, 2, or 12. Electrodes were dissolved at approximately constant currents by GEIS as described in Section 2.3.4.3. Current densities given in Table 7.2 are normalized on the basis of the initial surface area of the electrode.

The quantity of Mg was determined gravimetrically, by weighing a Mg electrode prior to and following oxidation in the electrolyte and calculating the mass loss. Factors leading to inaccuracy in this measurement include the possibility of film development on the unreacted portions of the electrode. H_2 was measured using pressure-rise/decay techniques with a Henry's law correction to account for dissolved H_2, and the quantity given was the total amount of H_2 collected (see Section 2.2.2.1). Some factors leading to inaccuracy in the measurement of H_2 include error in the volume calibration and errors in the Henry's law solubility coefficient, which was determined from literature values in similar but not identical electrolytes.[99] Finally, the quantity of e^- was determined based on the average current drawn during GEIS and the time for which it was drawn. For the case of high currents in particular, small inaccuracies in determining when the current should be stopped during the final dissolution of the electrode could lead to overestimation of the capacity. For these reasons, the ratios reported in Table 7.2 are expected to have significant experimental errors, ~10% of the values reported. In particular, overestimation of the capacity passed at high current is likely to result in slight overestimation of the $e^-/(Mg-H_2)$ and $H_2/(Mg-\frac{e^-}{2})$ ratios. This is consistent with the >2 values for the first ratio, and >1 for the second.

In every case studied in Table 7.2, with the exception of a few outliers, the approximate ratio between the e^- passed oxidatively through the electrode and the calculated quantity of oxidized Mg is approximately 2. In spite of the possible error of the $e^-/(Mg–H_2)$ ratio, in order for these values to be ~1 rather than ~2, the errors of the associated measurements would need to all simultaneously be between 20% and 50% of every measured value contributing to a given calculation. Any outlier values are >2.5 and likely due to the combination of measurement inaccuracies. We are therefore confident that no $e^-/(Mg-H_2)$ ratio is close to 1. Curiously, there is no significant trend in the apparent stoichiometric e^-/Mg ratio with either pH, the concentration of Cl^- in the electrolyte, or the applied current density. This result becomes particularly curious in the context of the NDE behavior with pH, as will be discussed in the following sections.

7.4.2.1 Quantification of the NDE at pH 12

The NDE was observed in electrolytes above pH 12, as illustrated in Figure 7.4. The total quantity of H_2 present in the headspace is normalized by the total quantity of Mg dissolved; a value of 1 would indicate pure corrosion (Mg dissolution that causes H_2 evolution) and a value of 0 would indicate perfect Mg oxidation (reaction 1.4) without the presence of H_2 evolution or the NDE. Values between 0 and 1 indicate a combination of Mg corrosion and oxidation. The rate of H_2 evolution is normalized on the basis of the initial surface area of the electrode. At pH 12 in a 1.0 M Cl^- electrolyte, the open-circuit corrosion rate prior to the

initiation of GEIS was within the experimental error of being zero; we report therefore that any open-circuit corrosion occurring at this pH was below the sensitivity of our experimental apparatus. Immediately upon beginning the flow of anodic current, the rate of H_2 evolution increased, consistent with the NDE. These rates were initially quite similar to that predicted by the 2 e^-/H_2 scaling as discussed above. However, despite the application of a constant current and, due to the dissolution of the electrode, an increasing current density, the rate of H_2 evolution was observed to gradually decrease throughout GEIS. Following complete dissolution of the electrode, which occurs entirely during the shaded blue region in Figure 7.4, a small pressure decay is apparent from the decrease in the total quantity of H_2 in Figure 7.4a and from the slightly negative apparent values for H_2 evolution in Figure 7.4b. We attribute this to the dissolution of H_2 into the electrolyte, indicating that the concentration of dissolved H_2 cell was not at equilibrium with the headspace during the experiment. However, this reequilibration involves the dissolution of only a small quantity of gas.

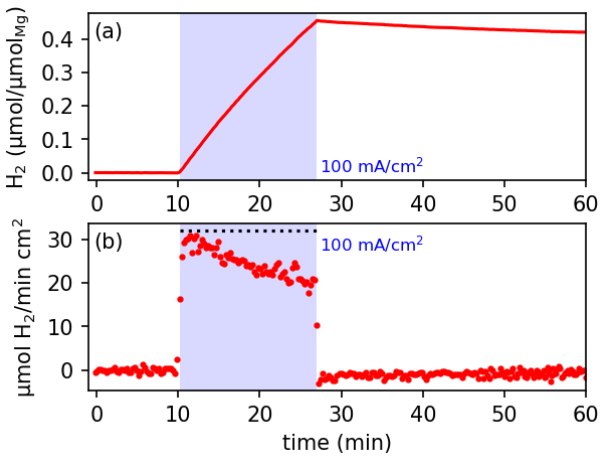

Figure 7.4: Dissolution of a Mg electrode at an anodic 100 mA/cm^2 (normalized to the initial electrode surface area) in a pH 12, 1.0 M Cl^- solution. The 2 e^-/H_2 scaling is indicated by the black dotted line. Shaded regions indicate where GEIS was performed at the indicated current density.

7.4.2.2 Quantification of the NDE at pH 10

KCl electrolytes prepared to their natural pH were observed to increase to a pH above 10 almost immediately upon exposure to a Mg electrode. This pH change is likely due to the corrosion of Mg in the electrolyte solution. For that reason, we report dissolution of Mg electrodes in KCl solutions (without addition of HCl or KOH to adjust the pH) as the dissolution at pH 10. Data from these experiments is given in Figure 7.5, and was acquired at three different KCl concentrations (0.3 M in Figure 7.5a-b, 1.0 M in Figure 7.5c-d, and 3.0 M in Figure 7.5e-f) and three general current regimes. These data are replotted in Figure 7.6 to

provide a direct comparison between different current regimes. At pH 10, the NDE is in effect, with low open-circuit corrosion rates prior to the beginning of GEIS and a significant increase in the rate of H_2 evolution immediately following the application of current. Curiously, the quantity of H_2 evolved in each case, when normalized to the total quantity of Mg dissolved, is approximately the same regardless of current density or electrolyte concentration. Indeed, when directly comparing similar current densities, the severity of the NDE, which may be thought of as the rate of H_2 evolution, is similar in each current regime, as shown in Figure 7.6. The most significant variable in the rate of H_2 evolution is instead the applied current density. As observed at pH 12, H_2 initially evolves approximately according to the 2 e^-/H_2 scaling. This scaling is a more accurate predictor of the initial H_2 evolution rate for lower current densities, whereas at higher current densities, the rate of H_2 evolution is lower than 2 e^-/H_2. Again, despite the current applied being constant and the current density increasing as the electrode dissolves, the rate of H_2 evolution decreases over time in every case.

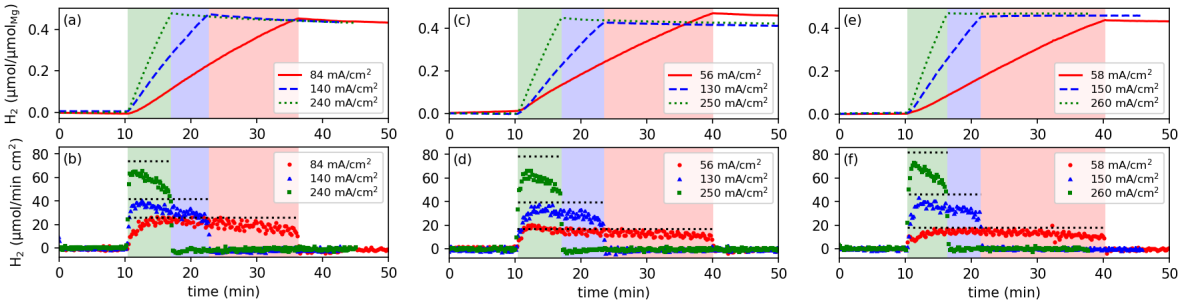

Figure 7.5: Dissolution of Mg electrodes at various anodic currents in pH 10 electrolytes of (a-b) 0.3 M KCl, (c-d) 1.0 M KCl, and (e-f) 3.0 M KCl. The 2 e^-/H_2 scaling is indicated by the black dotted line for each current in panels b, d, and f. Shaded regions (green, blue, and red for each respective current) indicate where GEIS was performed at the given current density, normalized to the initial electrode surface area.

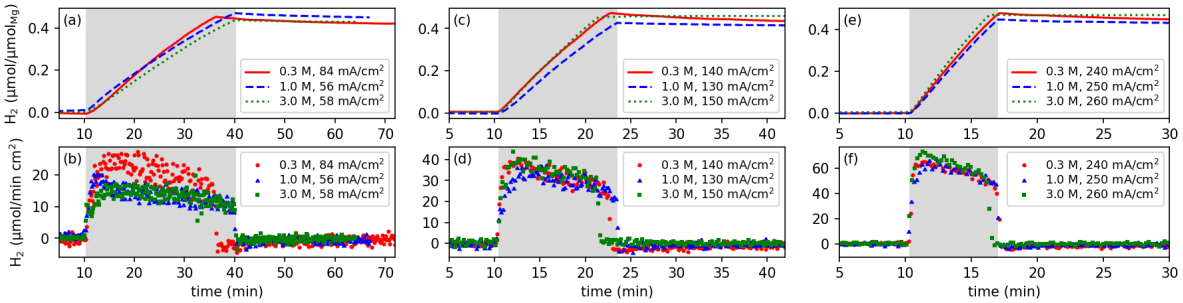

Figure 7.6: Dissolution of Mg electrodes at approximately (a-b) 50-80 mA/cm^2, (c-d) 125-150 mA/cm^2, and (e-f) 235-265 mA/cm^2 in electrolytes of 0.3, 1.0, or 3.0 M KCl electrolytes at pH 10. These data are replotted from Figure 7.5 to clarify the influence of KCl concentration on the NDE.

7.4.2.3 Quantification of the NDE in strong acidic conditions

To observe the NDE in lower pH environments, the pH was adjusted by addition of HCl, while the total Cl^- concentration was maintained constant at 1.0 M. Results from electrodes in a bulk pH 2 solution are given in Figure 7.7. As before, the NDE is evident, with the evolution of H_2 generally decreasing during polarization. However, a delayed onset of the NDE is observed at the lower current density (60 mA/cm^2 in Figure 7.7b), where the H_2 evolution is initially very similar to that observed at open-circuit and increases slowly to meet that predicted by the 2 e^-/H_2 scaling. After that point, the H_2 evolution decreases as was the case at pH 10 and 12. An analogous experiment in an initially pH 3.4 electrolyte demonstrated similar initial behavior (see Figure A.9). This delayed onset of the NDE requires several minutes of applied anodic current and is not comparable to the rise in H_2 evolution seen at similar currents at pH 10 (Figure 7.6a). We suggest it may indicate the need to form a particular surface film or morphology or, as will be visited later, an effect of the local surface pH on the NDE.

Finally, we monitored the Mg corrosion behavior in electrolytes of pH 1 (0.1 M HCl, 0.9 M KCl). The results are given in Figure 7.8, and are markedly different from our observations at every other pH. For each current density, several regions of different behavior are observed: an initial increase in the H_2 evolution rate at OCV, a slight decrease in H_2 evolution coinciding with the beginning of GEIS, and a small increase in H_2 evolution just before the completion of electrode dissolution. In this more aggressive electrolyte solution, the rate of open-circuit corrosion is rapid enough that complete dissolution of an electrode at open-circuit requires a comparable amount of time as dissolution under anodic polarization at another pH; these

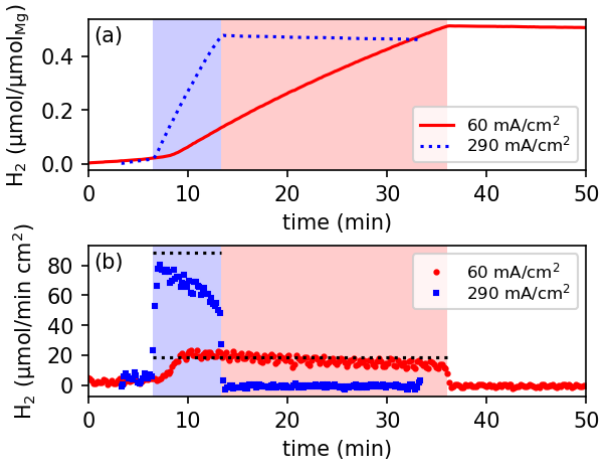

Figure 7.7: Dissolution of Mg electrodes at various currents in pH 2, 1.0 M Cl^- electrolytes. The 2 e^-/H_2 scaling is indicated by the black dotted line for each current. Shaded regions indicate where GEIS was performed at the given current density, normalized to the initial electrode surface area.

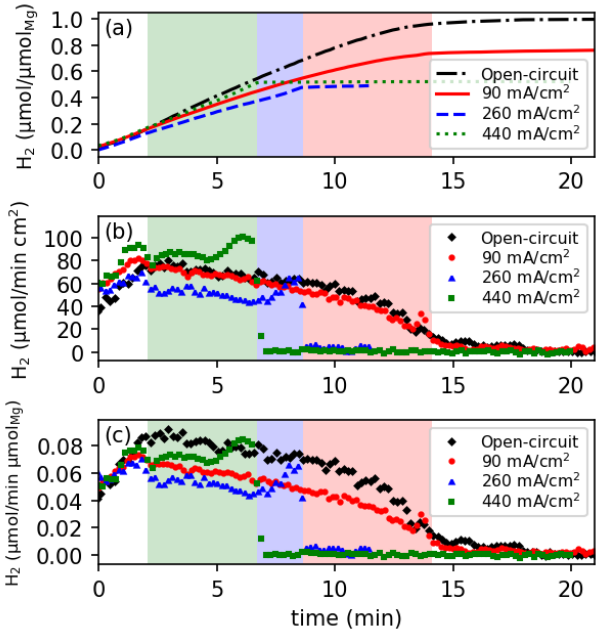

Figure 7.8: Dissolution of Mg electrodes at various currents in pH 1, 1.0 M Cl^- electrolytes. Shaded regions indicate where GEIS was performed at the given current density, normalized to the initial electrode surface area.

OCV (Open-circuit) data are included for comparison, and an additional comparative figure is included in the appendices (Figure A.10). No correlation with the 2 e^-/H_2 scaling was observed at this pH, and the lines indicating this scaling are omitted in Figure 7.8.

First, following cell assembly and prior to the beginning of GEIS, the open-circuit H_2 evolution was observed to slowly increase (Figure 7.8b-c). We attribute this to the dissolution of passivating surface films; as discussed in Section 2.2.2.2, electrodes for study at pH 1 were not pre-treated due to safety considerations, and this initial increase in H_2 evolution is attributable to the dissolution of the surface films that were chemically removed prior to study at other pH. Additionally, these open-circuit H_2 evolution rates were observed to differ considerably between electrodes when normalized by the initial surface area (Figure 7.8b). If instead the data were normalized by the total quantity of Mg evolved, these open-circuit H_2 corrosion rates were statistically identical (Figure 7.8c), indicating that this normalization provided a more appropriate comparison between different current densities at this pH. For this reason, as we continue our discussion of the results, we will focus on the results presented in Figure 7.8c.

Second, at the beginning of GEIS, the rate of H_2 evolution is observed to significantly decrease compared to that at open-circuit (Figure 7.8c and A.10). The significance of this decrease appears to depend on the applied current; at the lowest current (90 mA/cm^2, normalized to the initial surface area of the electrode), it is modest; at the intermediate

current (260 mA/cm^2) it is larger; and at the highest current (440 mA/cm^2) it is initially comparable to that achieved at the lowest current. In all three cases, however, it represents a clear suppression of H_2 evolution compared to open-circuit H_2 evolution, clearly indicating the absence of the NDE. During this stage of dissolution, we observed limited or no evidence of dark surface films on the electrode, consistent with the example electrode at pH 1 given in Figure 7.2. This suggests that the absence of these films and the suppression of H_2 evolution may be related.

Third, just before the end of GEIS, the H_2 evolution is observed to increase again, even to values above those observed or expected at open-circuit. This distinct increase is unique compared to observations at any other pH (see Figures 7.4, 7.5, 7.7 and A.9), and appears to indicate a return of the NDE despite the earlier non-NDE behavior. We note again that the current applied on the electrode is constant while the current density changes with the electrode area; this increase in H_2 evolution can only be due to the NDE, and is not observed at any point at open-circuit. Additionally, the overall quantities of H_2 evolved are different depending on the applied current (Figure 7.8a), in contrast with results at higher pH (e.g., Figure 7.5). At open-circuit, as expected, the quantity of H_2 evolved when normalized to the quantity of dissolved Mg is 1.0. At low current, it is almost 0.8, significantly higher than that observed at any other pH, indicating that the majority of H_2 evolution can be ascribed to Mg corrosion similar to an open-circuit process, consistent with the high open-circuit (non-NDE) corrosion rate at pH 1. At higher currents, it is nearer to those observed in higher-pH electrolytes, although without the presence of the NDE throughout most of the anodic dissolution. At this stage of dissolution, electrodes were observed to have dark films on the surface, consistent with the appearance of example electrodes prepared between pH 2 and 4 in Figure 7.2 despite the lower bulk pH. The presence of these dark surface films may therefore be related with the occurrence of the NDE.

Altogether, the apparent absence of the NDE at the beginning of GEIS and the return of the NDE at the end of dissolution presents a curious question regarding the NDE behavior with pH. The initial reduction of H_2 evolution during anodic dissolution compared to open-circuit suggests that at low pH, the NDE is suppressed, and increasing anodic polarization results in a decreased rate of H_2 evolution compared with open-circuit. However, to truly say that the NDE does not occur at these low pH, this observation must be reconciled with both the increased H_2 evolution at the end of dissolution and the relatively high rate of H_2 evolution at the highest current density studied (440 mA/cm^2, initially). We note that the active surface area of the electrode changes during dissolution, and thus the flux of H_2 away from electrode and of H^+ to the electrode change dramatically during a given dissolution experiment. In the following section we explore the implications of this changing area and flux and the possibility of a changing local pH environment at the surface of the electrode that leads first to suppression of H_2 evolution and later to the return of the NDE.

7.4.3 Estimation of surface pH at dissolving Mg electrodes

We investigated the increase in H_2 evolution at the conclusion of each pH 1 dissolution experiment using a simple model to estimate the concentration of H^+ and at the surface of the Mg electrode during dissolution and, in effect, the local pH. Values for these concentrations were estimated from mass-transfer coefficients determined by correlations between the Sherwood (Sh), Reynolds (Re), and Schmidt (Sc) numbers for mass transfer occurring to or from a flat plate, a reasonable approximation for our planar Mg electrodes:[106]

$$\mathrm{Sh} = 0.664\mathrm{Re}^{1/2}\mathrm{Sc}^{1/3} \tag{7.7}$$

A value for Re in the cell was estimated by measuring the limiting current of O_2 reduction on a Cu electrode of similar dimensions to the Mg electrodes used in this study, in an otherwise identically prepared cell using the same stir bar rotation rate. Other necessary quantities, including diffusion coefficients and the fluid properties of a 1 M KCl electrolyte, were determined from literature values and experiments.[107–109] Full details of the limiting-current measurement and use of the above correlation are available in Section 2.3.5; a cyclic voltammagram illustrating the limiting current for O_2 reduction on a planar Cu electrode of similar size to our Mg electrodes is available in Figure 7.9a. Values of key parameters are available in Table 2.1.

To calculate $[H^+]$ using an estimated mass-transfer coefficient, we required a reasonable model for the area of the electrode. Because the electrode is dissolving during our experiments, its area is continuously decreasing, and the current density and associated flux of species to and from the electrode are dependent on that area. We chose to model the changing area of the electrode using H_2 evolution data from the dissolution of a Mg electrode in a bulk pH 1 electrolyte at OCV. This is a reasonable approximation because when no external current is passed through the electrode in a low-pH environment, the rate of H_2 evolution should be roughly proportional to the surface area of the dissolving electrode. A third-order polynomial least squares fit was applied to the data, as it was observed to result in a monotonically decreasing function that closely approximated the rate of H_2 evolution. These data were sourced from the open-circuit experiment in Figure 7.8, and are replotted with the accompanying model of the electrode area in Figure 7.9b. This area model was nondimensionalized and re-scaled according to the initial surface area of the electrode and the amount of time during which the electrode was polarized. The electrode area was assumed to be constant prior to the start of polarization, and zero following the end of polarization.

This approach was applied to the 260 $\mathrm{mA/cm^2}$ data in Figure 7.8, which has a clear suppression of H_2 evolution followed by a slow rise signaling the return of the NDE. The H_2 evolution data were re-normalized by the time-dependent area according to the area model in Figure 7.9b to give the H_2 flux at the Mg surface. Then, we assumed that all hydrogen evolution occurred at the surface of the electrode according to:

$$2\mathrm{H}^+ + 2\mathrm{e}^- \rightarrow \mathrm{H}_2 \tag{7.8}$$

Thus, the flux of H^+ would be equivalent to two times the flux of H_2 as determined from the area and rate of gas evolution, with the sign adjusted according to convention. The simplifying assumptions used to develop this model may not be valid at all times due to the dynamic nature of the system, but were regarded as a reasonable given the low bulk pH of the electrolyte. We acknowledge the possibility of nonuniform H_2 flux distributions on the electrode surface and regard our calculated values of $[H^+]$ as approximations best used in estimating trends. The results are given in Figure 7.9c, together with accompanying gas evolution data normalized to the initial surface area of the cell as in Figure 7.8b.

Based on this estimate, the increase in H_2 evolution coincides with an increase in the pH of the local environment around the dissolving electrode. Initially, we estimate the pH is below 2, but this increases above 2.5 just before the onset of increased H_2 evolution. At that point, the calculated value of $[H^+]$ becomes negative, indicating that some assumptions of our model are no longer valid and suggesting a significant increase in the local pH. Further estimated pH values are omitted, as at all subsequent times, $[H^+]$ was calculated to be negative. Thus, we believe that in a sufficiently low local pH, roughly pH 2 and below, the NDE does not occur, and that the NDE only returns when the pH near the electrode is high enough to promote it. As a side note, applying the same model to an electrode in a bulk pH 2 electrolyte highlights similar behavior regarding the delayed onset of H_2 evolution at the beginning of polarization. These results are provided in Figure A.11. In brief, we estimate a low surface pH at open-circuit that immediately increases when polarization of the electrode begins, which is accompanied by the NDE. This may also confirm that the appearance of the NDE coincides with a more basic environment surrounding the electrode.

Altogether, these findings suggest that in the bulk pH 1 environment, the decreasing

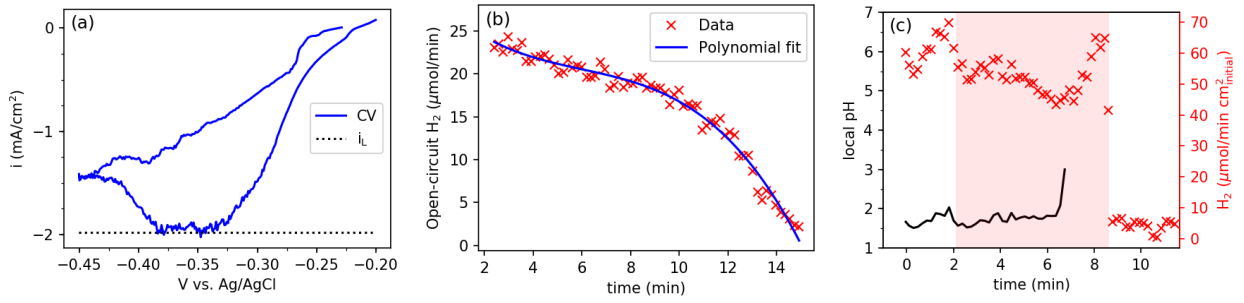

Figure 7.9: (a) CV measurement of the limiting current for O_2 reduction on Cu foil in a 1 M KCl electrolyte. The limiting current, an average of multiple measurements, is indicated by the black dotted line (i_L). (b) Data from the open-circuit evolution of H_2 in a bulk pH 1 electrolyte and the corresponding third-order polynomial fit used to model electrode area. (c) Estimation of the local pH at the surface of a dissolving Mg electrode in a bulk pH 1 electrolyte. The pH was calculated from the concentration of H^+, assuming all H_2 evolution occurred due to H^+ reduction to H_2 (reaction 7.8). Accompanying gas evolution normalized to the initial surface area of the electrode are given, and the shaded area indicates when current was applied. All measurements and calculations were performed using a total 1 M $[Cl^-]$ (KCl and HCl) electrolyte.

surface area and sluggish transport to the electrode can result in an increase in the local pH. This coincides with the return of the NDE shown in Figure 7.8. As soon as the environment permits the NDE to begin, the rate of H_2 evolution increases, further driving the increase in local pH. In addition, these results suggest that the bulk pH at which the NDE disappears is dependent on the transport and hydrodynamic properties of the cell and electrolyte in which the effect is studied. It is possible that the NDE disappears at a higher surface pH than that estimated in this work, and that NDE suppression could be more readily observed in a system with improved transport of species to and from the electrode surface.

Our hypothesis regarding the suppression of the NDE at low pH would adequately account for the increase in H_2 evolution at the end of dissolution at pH 1, and may partially explain the higher rates of H_2 evolution observed at the highest current in pH 1 as compared to lower currents (440 mA/cm^2, Figures 7.8c). At a bulk pH 1 and an initial current density of 440 mA/cm^2, the rapid oxidation of the electrode could result in a change in the surface environment, such as roughening due to Mg dissolution, changing concentrations of Cl^-, K^+, and H^+ to satisfy electroneutrality, or another transient effect. Regardless, if any effect were to result in a small area where the local pH increases, the resulting increase in H_2 flux combined with limitations in H^+ transport could cause the higher pH to spread to adjacent regions of the electrode. Thus, the local pH overall may fall initially within a transition regime, where the NDE occurs to a lesser extent or on only a fraction of the electrode area. Once the NDE onsets, the increase in H^+ flux required to maintain the low pH environment cannot be met overall, and increasing rates of H_2 evolution followed by the complete NDE onset as observed in Figure 7.8c occur.

Furthermore, our hypothesis accounts for the delayed onset of H_2 evolution at pH 2 (Figure 7.7). At pH 2, partial surface film coverage has been observed concentrated at the tip and edges of the electrode, which in our cell geometry are closer to the counter electrode and may experience a higher current density and higher local surface pH (Figure 7.2). In the bulk pH 2 electrolyte, the initial surface pH may be low enough to exhibit NDE suppression, before high local H_2 flux and poor transport result in an increase in pH and a return of the NDE; which coincides with the appearance of dark surface films. Indeed, the presence of dark films on the electrode surface is correlated with environments where the NDE occurs (pH 3-12 in Figure 7.2). Decreased film coverage or films localized to areas that likely experience higher current densities are correlated with apparent NDE suppression in more acidic environments (pH 1-2 in Figure 7.2). Additional qualitative observations of electrodes at pH 1 suggest that dark surface films also form during the final stages of dissolution, when the NDE returns. While the precise mechanism of surface film formation and its causal relationship to the NDE is not clear from the evidence in this study alone, the formation and presence of these films serves as an indicator of NDE behavior.

7.4.3.1 Assessment of NDE mechanisms

Given the results and reasoning we have presented above, we report that in our cell configuration at a bulk electrolyte pH of 1, the NDE no longer occurs as long as a sufficiently

low local pH at the electrode is maintained. These conditions are possible at pH 1 and may occur at pH 2, depending on the local current density. Due to the dependence of the local pH on the transport properties in the cell and the H_2 evolution rate observed, the bulk pH at which this NDE/no NDE transition occurs may be different in different electrolytes and cell configurations. Nevertheless, we note that this observation of NDE disappearance in low-pH conditions provides new insight into the nature of Mg corrosion and possible mechanisms for explaining the NDE. In particular, we note that reaction 7.4, which represents the NDE mechanism for unipositive ions chemically resulting in H_2 evolution, should occur more aggressively in low-pH environments. Our data suggest that this cannot be the case, and that the dissolution of Mg as a unipositive Mg^+ ion that subsequently reacts with the electrolyte to form H_2 does not occur. We emphasize that if it did, the NDE's disappearance in low pH should not be observed. If Mg^+ formation occurs, it can only do so in basic pH, which is not consistent with its proponents' previous insistences.[69]

Numerous other mechanisms for the NDE are under consideration by the field at large, including the aforementioned anode disintegration, elemental impurities, surface film effects, and catalytic effects.[66,67,73,77–81] We assert that these other possible mechanisms are more likely to be consistent with our observations, particularly those concerned with the nature of the the local Mg electrode environment, the formation of various surface films, or the agglomeration of NDE-promoting materials or regions on the electrode. In particular, we observe that the presence of dark surface films on the electrode is highly correlated with the incidence of the NDE. Mechanisms which account for this film formation either as the NDE's cause or effect, and which account for its absence in low-pH environments where suppression of H_2 evolution by anodic polarization can occur, are more likely be consistent with our observations.

7.5 Conclusions and Recommendations

In this chapter, we have quantitatively examined H_2 evolution from Mg electrodes suffering from the NDE. We confirm the non-polarizable behavior of the Mg electrode on anodic polarization and the occurrence of the NDE in basic, near-neutral, and mildly acidic electrolytes containing Cl^-. We report for the first time, insofar as we are aware, that in electrolytes of sufficiently low pH ($\leq$2), the NDE does not occur. We suggest that the disappearance of the NDE is due to a sufficiently low surface pH that alters the local environment such that it does not support or promote the NDE. If the associated flux of reactants to and from the surface permit this local pH to increase, the NDE returns. We also note the appearance of dark surface films when the NDE occurs and their absence when the NDE does not. While these observations are not inconsistent with many postulated NDE mechanisms, they are contrary to the predictions that follow from the unipositive Mg^+ theory.

We acknowledge that the use of low-pH electrolytes is clearly not a sufficient strategy for the suppression of the NDE in practice, and merely provides fundamental insight into

the NDE mechanism. Mg-O_2 electrolytes, for example, are typically near-neutral or basic in character.[57] Additionally, despite the suppression of the NDE at low pH, the open-circuit corrosion rate is exceptionally high. However, previous reports have suggested that alloys, electrolyte additives, or alternate electrolyte compositions can permit reasonable suppression of the NDE.[19,75,90,94,96] Further investigation of the NDE behavior for other alloys and for electrolytes containing additives is warranted to develop an improved fundamental understanding of the NDE mechanism, particularly the examination of possible NDE behavior or lack thereof at low pH. This may be of particular interest in non-Cl^- electrolyte environments, especially those which still lead to the occurrence of the NDE. We also encourage additional *ex situ* and especially *in situ* investigation of the NDE in various pH electrolytes, especially measurements which may provide insight into the changing character and local environment of the Mg surface during the disappearance and onset of the NDE. Additional modified cell designs to ensure superior electrolyte transport properties may also be beneficial.

Bibliography

(1) Nichols, J. E.; McCloskey, B. D. *J. Phys. Chem. C* **2017**, *121* (1), 85–96.

(2) Nichols, J. E.; Knudsen, K. B.; McCloskey, B. D. *J. Phys. Chem. C* **2018**, *122* (25), 13462–13472.

(3) Abraham, K. M. *J. Phys. Chem. Lett.* **2015**, *6* (5), 830–844.

(4) Wagner, F. T.; Lakshmanan, B.; Mathias, M. F. *J. Phys. Chem. Lett.* **2010**, *1* (14), 2204–2219.

(5) Zaghib, K.; Mauger, A.; Groult, H.; Goodenough, J.; Julien, C. *Materials* **2013**, *6* (3), 1028–1049.

(6) Goodenough, J. B.; Kim, Y. *Chem. Mater.* **2010**, *22* (3), 587–603.

(7) Whittingham, M. S. *Chem. Rev.* **2014**, *114* (23), 11414–11443.

(8) Adelhelm, P.; Hartmann, P.; Bender, C. L.; Busche, M.; Eufinger, C.; Janek, J. *Beilstein J. Nanotechnol.* **2015**, *6*, 1016–1055.

(9) McCloskey, B. D.; Burke, C. M.; Nichols, J. E.; Renfrew, S. E. *Chem. Commun.* **2015**, *51* (64), 12701–12715.

(10) Peng, Z.; Freunberger, S. A.; Hardwick, L. J.; Chen, Y.; Giordani, V.; Bardé, F.; Novák, P.; Graham, D.; Tarascon, J.-M.; Bruce, P. G. *Angew. Chem., Int. Ed.* **2011**, *50* (28), 6351–6355.

(11) Peled, E.; Golodnitsky, D.; Mazor, H.; Goor, M.; Avshalomov, S. *J. Power Sources* **2011**, *196* (16), 6835–6840.

(12) Reddy, T. B.; Linden, D., *Linden's Handbook of Batteries*; McGraw-Hill: New York, 2011.

(13) Van Noorden, R. *Nature* **2014**, *507* (7490), 26–28.

(14) McCloskey, B. D.; Valery, A.; Luntz, A. C.; Gowda, S. R.; Wallraff, G. M.; Garcia, J. M.; Mori, T.; Krupp, L. E. *J. Phys. Chem. Lett.* **2013**, *4* (17), 2989–2993.

(15) McCloskey, B. D.; Bethune, D. S.; Shelby, R. M.; Girishkumar, G.; Luntz, A. C. *J. Phys. Chem. Lett.* **2011**, *2* (10), 1161–1166.

(16) McCloskey, B. D.; Scheffler, R.; Speidel, A.; Bethune, D. S.; Shelby, R. M.; Luntz, A. C. *J. Am. Chem. Soc.* **2011**, *133* (45), 18038–18041.

(17) McCloskey, B. D.; Bethune, D. S.; Shelby, R. M.; Mori, T.; Scheffler, R.; Speidel, A.; Sherwood, M.; Luntz, A. C. *J. Phys. Chem. Lett.* **2012**, *3* (20), 3043–3047.

(18) Burke, C. M.; Black, R.; Kochetkov, I. R.; Giordani, V.; Addison, D.; Nazar, L. F.; McCloskey, B. D. *ACS Energy Lett.* **2016**, *1* (4), 747–756.

(19) Richey, F. W.; McCloskey, B. D.; Luntz, A. C. *J. Electrochem. Soc.* **2016**, *163* (6), A958–A963.

(20) Abraham, K. M.; Jiang, Z. *J. Electrochem. Soc.* **1996**, *143* (1), 1–5.

(21) Girishkumar, G.; McCloskey, B.; Luntz, A. C.; Swanson, S.; Wilcke, W. *J. Phys. Chem. Lett.* **2010**, *1* (14), 2193–2203.

(22) Bryantsev, V. S.; Uddin, J.; Giordani, V.; Walker, W.; Addison, D.; Chase, G. V. *J. Electrochem. Soc.* **2013**, *160* (1), A160–A171.

(23) Burke, C. M.; Pande, V.; Khetan, A.; Viswanathan, V.; McCloskey, B. D. *Proc. Natl. Acad. Sci. U.S.A.* **2015**, *112* (30), 9293–9298.

(24) Luntz, A. C.; McCloskey, B. D. *Chem. Rev.* **2014**, *114* (23), 11721–11750.

(25) Christensen, J.; Albertus, P.; Sanchez-Carrera, R. S.; Lohmann, T.; Kozinsky, B.; Liedtke, R.; Ahmed, J.; Kojic, A. *J. Electrochem. Soc.* **2011**, *159* (2), R1–R30.

(26) Johnson, L.; Li, C.; Liu, Z.; Chen, Y.; Freunberger, S. A.; Ashok, P. C.; Praveen, B. B.; Dholakia, K.; Tarascon, J.-M.; Bruce, P. G. *Nat. Chem.* **2014**, *6* (12), 1091–1099.

(27) Luntz, A. C.; McCloskey, B. D.; Gowda, S.; Horn, H.; Viswanathan, V. In *The Lithium Air Battery*, Imanishi, N., Luntz, A. C., Bruce, P., Eds.; Springer New York: 2014; Chapter 3, pp 59–120.

(28) Ottakam Thotiyl, M. M.; Freunberger, S. A.; Peng, Z.; Bruce, P. G. *J. Am. Chem. Soc.* **2013**, *135* (1), 494–500.

(29) Hartmann, P.; Bender, C. L.; Vračar, M.; Dürr, A. K.; Garsuch, A.; Janek, J.; Adelhelm, P. *Nat. Mater.* **2013**, *12* (3), 228–232.

(30) McCloskey, B. D.; Garcia, J. M.; Luntz, A. C. *J. Phys. Chem. Lett.* **2014**, *5* (7), 1230–1235.

(31) Yadegari, H.; Li, Y.; Banis, M. N.; Li, X.; Wang, B.; Sun, Q.; Li, R.; Sham, T.-K.; Cui, X.; Sun, X. *Energy Environ. Sci.* **2014**, *7* (11), 3747–3757.

(32) Landa-Medrano, I.; Li, C.; Ortiz-Vitoriano, N.; Ruiz de Larramendi, I.; Carrasco, J.; Rojo, T. *J. Phys. Chem. Lett.* **2016**, *7* (7), 1161–1166.

(33) Yadegari, H.; Sun, Q.; Sun, X. *Adv. Mater.* **2016**, *28* (33), 7065–7093.

(34) Liu, W.; Sun, Q.; Yang, Y.; Xie, J.-Y.; Fu, Z.-W. *Chem. Commun.* **2013**, *49* (19), 1951–1953.

(35) Yadegari, H.; Franko, C. J.; Banis, M. N.; Sun, Q.; Li, R.; Goward, G. R.; Sun, X. *J. Phys. Chem. Lett.* **2017**, *8* (19), 4794–4800.

(36) Bi, X.; Wang, R.; Ma, L.; Zhang, D.; Amine, K.; Lu, J. *Small Methods* **2017**, *1* (7), 1700102.

(37) Yang, S.; Siegel, D. J. *Chem. Mater.* **2015**, *27* (11), 3852–3860.

(38) Bender, C. L.; Schröder, D.; Pinedo, R.; Adelhelm, P.; Janek, J. *Angew. Chem., Int. Ed.* **2016**, *55* (15), 4640–4649.

(39) Hartmann, P.; Bender, C. L.; Sann, J.; Durr, A. K.; Jansen, M.; Janek, J.; Adelhelm, P. *Phys. Chem. Chem. Phys.* **2013**, *15* (28), 11661–72.

(40) Hartmann, P.; Grübl, D.; Sommer, H.; Janek, J.; Bessler, W. G.; Adelhelm, P. *J. Phys. Chem. C* **2014**, *118* (3), 1461–1471.

(41) Xia, C.; Black, R.; Fernandes, R.; Adams, B.; Nazar, L. F. *Nat. Chem.* **2015**, *7* (6), 496–501.

(42) Bender, C. L.; Hartmann, P.; Vracar, M.; Adelhelm, P.; Janek, J. *Adv. Energy Mater.* **2014**, *4* (12), 1301863.

(43) Ortiz-Vitoriano, N.; Batcho, T. P.; Kwabi, D. G.; Han, B.; Pour, N.; Yao, K. P. C.; Thompson, C. V.; Shao-Horn, Y. *J. Phys. Chem. Lett.* **2015**, *6* (13), 2636–2643.

(44) Zhao, N.; Li, C.; Guo, X. *Phys. Chem. Chem. Phys.* **2014**, *16* (29), 15646–15652.

(45) Abate, I. I.; Thompson, L. E.; Kim, H.-C.; Aetukuri, N. B. *J. Phys. Chem. Lett.* **2016**, *7* (12), 2164–2169.

(46) Landa-Medrano, I.; Pinedo, R.; Bi, X.; Ruiz de Larramendi, I.; Lezama, L.; Janek, J.; Amine, K.; Lu, J.; Rojo, T. *ACS Appl. Mater. Interfaces* **2016**, *8* (31), 20120–20127.

(47) Kang, S.; Mo, Y.; Ong, S. P.; Ceder, G. *Nano Lett.* **2014**, *14* (2), 1016–1020.

(48) Kim, J.; Park, H.; Lee, B.; Seong, W. M.; Lim, H.-D.; Bae, Y.; Kim, H.; Kim, W. K.; Ryu, K. H.; Kang, K. *Nat. Commun.* **2016**, *7*, DOI: 10.1038/ncomms10670.

(49) Black, R.; Shyamsunder, A.; Adeli, P.; Kundu, D.; Murphy, G. K.; Nazar, L. F. *ChemSusChem* **2016**, *9* (14), 1795–1803.

(50) Xia, C.; Fernandes, R.; Cho, F. H.; Sudhakar, N.; Buonacorsi, B.; Walker, S.; Xu, M.; Baugh, J.; Nazar, L. F. *J. Am. Chem. Soc.* **2016**, *138* (35), 11219–11226.

(51) Knudsen, K. B.; Nichols, J. E.; Vegge, T.; Luntz, A. C.; McCloskey, B. D.; Hjelm, J. *J. Phys. Chem. C* **2016**, *120* (20), 10799–10805.

(52) Schröder, D.; Bender, C. L.; Osenberg, M.; Hilger, A.; Manke, I.; Janek, J. *Sci. Rep.* **2016**, *6*, 24288.

(53) Sayed, S. Y.; Yao, K. P. C.; Kwabi, D. G.; Batcho, T. P.; Amanchukwu, C. V.; Feng, S.; Thompson, C. V.; Shao-Horn, Y. *Chem. Commun.* **2016**, *52* (62), 9691–9694.

(54) Aldous, I. M.; Hardwick, L. J. *Angew. Chem., Int. Ed.* **2016**, *55* (29), 8254–8257.

(55) Viswanathan, V.; Thygesen, K. S.; Hummelshoj, J. S.; Norskov, J. K.; Girishkumar, G.; McCloskey, B. D.; Luntz, A. C. *J. Chem. Phys.* **2011**, *135* (21), 214704.

(56) Arcelus, O.; Li, C.; Rojo, T.; Carrasco, J. *J. Phys. Chem. Lett.* **2015**, *6* (11), 2027–2031.

(57) Zhang, T.; Tao, Z.; Chen, J. *Mater. Horiz.* **2014**, *1* (2), 196–206.

(58) Aurbach, D.; Lu, Z.; Schechter, A.; Gofer, Y.; Gizbar, H.; Turgeman, R.; Cohen, Y.; Moshkovich, M.; Levi, E. *Nature* **2000**, *407*, 724–727.

(59) Hamlen, R. P.; Jerabek, E. C.; Ruzzo, J. C.; Siwek, E. G. *J. Electrochem. Soc.* **1969**, *116* (11), 1588–1592.

(60) Song, G.; Atrens, A. *Adv. Eng. Mater.* **2003**, *5* (12), 837–858.

(61) Beetz, W. *Philos. Mag.* **1866**, *32* (216).

(62) Baborovský, G. *Z. Elektrochem. Angew. Phys. Chem.* **1905**, *11* (30), 465–482.

(63) Petty, R. L.; Davidson, A. W.; Kleinberg, J. *J. Am. Chem. Soc.* **1954**, *76* (2), 363–366.

(64) Straumanis, M. E.; Wang, Y. N. *J. Electrochem. Soc.* **1955**, *102* (6), 304–310.

(65) Hoey, G. R.; Cohen, M. *J. Electrochem. Soc.* **1958**, *105* (5), 245–250.

(66) James, W. J.; Straumanis, M. E.; Bhatia, B. K.; Johnson, J. W. *J. Electrochem. Soc.* **1963**, *110* (11), 1117–1120.

(67) Straumanis, M. E.; Bhatia, B. K. *J. Electrochem. Soc.* **1963**, *110* (5), 357–360.

(68) Song, G.; Atrens, A.; St. John, D.; Nairn, J.; Li, Y. *Corros. Sci.* **1997**, *39* (5), 855–875.

(69) Song, G.; Atrens, A.; St. John, D.; Wu, X.; Nairn, J. *Corros. Sci.* **1997**, *39* (10), 1981–2004.

(70) Rossrucker, L.; Mayrhofer, K. J. J.; Frankel, G. S.; Birbilis, N. *J. Electrochem. Soc.* **2014**, *161* (3), C115–C119.

(71) King, A. D.; Birbilis, N.; Scully, J. R. *Electrochim. Acta* **2014**, *121*, 394–406.

(72) Newman, J.; Thomas-Alyea, K. E., *Electrochemical Systems*, 3rd ed.; Wiley: Hoboken, NJ, 2004.

(73) Birbilis, N.; King, A. D.; Thomas, S.; Frankel, G. S.; Scully, J. R. *Electrochim. Acta* **2014**, *132*, 277–283.

(74) Lebouil, S.; Duboin, A.; Monti, F.; Tabeling, P.; Volovitch, P.; Ogle, K. *Electrochim. Acta* **2014**, *124*, 176–182.

(75) Thomas, S.; Medhekar, N. V.; Frankel, G. S.; Birbilis, N. *Curr. Opin. Solid State Mater. Sci.* **2015**, *19* (2), 85–94.

(76) Marsh, G. A.; Schaschl, E. *J. Electrochem. Soc.* **1960**, *107* (12), 960–965.

(77) Perrault, G. G. *J. Electroanal. Chem. Interfacial Electrochem.* **1970**, *27* (1), 47–58.

(78) Robinson, J. L.; King, P. F. *J. Electrochem. Soc.* **1961**, *108* (1), 36–41.

(79) Tunold, R.; Holtan, H.; Berge, M.-B. H.; Lasson, A.; Steen-Hansen, R. *Corros. Sci.* **1977**, *17* (4), 353–365.

(80) McNulty, R. E.; Hanawalt, J. D. *Trans. Electrochem. Soc.* **1942**, *81* (1), 423–433.

(81) Glicksman, R. *J. Electrochem. Soc.* **1959**, *106* (2), 83–88.

(82) Shi, Z.; Cao, F.; Song, G.-L.; Atrens, A. *Corros. Sci.* **2014**, *88*, 434–443.

(83) Atrens, A. D.; Gentle, I.; Atrens, A. *Corros. Sci.* **2015**, *92*, 173–181.

(84) Song, G.-L.; Unocic, K. A. *Corros. Sci.* **2015**, *98*, 758–765.

(85) Bender, S.; Goellner, J.; Heyn, A.; Schmigalla, S. *Mater. Corros.* **2012**, *63* (8), 707–712.

(86) Fajardo, S.; Frankel, G. S. *Electrochim. Acta* **2015**, *165*, 255–267.

(87) Shkirskiy, V.; King, A. D.; Gharbi, O.; Volovitch, P.; Scully, J. R.; Ogle, K.; Birbilis, N. *ChemPhysChem* **2015**, *16* (3), 536–539.

(88) Fajardo, S.; Glover, C. F.; Williams, G.; Frankel, G. S. *Electrochim. Acta* **2016**, *212*, 510–521.

(89) Yang, Y.; Scenini, F.; Curioni, M. *Electrochim. Acta* **2016**, *198*, 174–184.

(90) Cain, T. W.; Gonzalez-Afanador, I.; Birbilis, N.; Scully, J. R. *J. Electrochem. Soc.* **2017**, *164* (6), C300–C311.

(91) Makar, G. L.; Kruger, J. *Int. Mater. Rev.* **1993**, *38* (3), 138–153.

(92) Nishikawa, Y.; Takara, A. *Mater. Sci. Forum* **2003**, *426-432*, 569–574.

(93) Lan, Y.; Huanyu, C.; Shimin, M.; Richard, H.; Yuhao, L.; Xu, X.; Suk-Won, H.; Harshvardhan, J.; Seung-Kyun, K.; Yewang, S.; Rui, L.; Yonggang, H.; A., R. J. *Adv. Funct. Mater.* **2014**, *24* (5), 645–658.

(94) Kirkland, N. T.; Birbilis, N.; Staiger, M. P. *Acta Biomater.* **2012**, *8* (3), 925–936.

(95) Weber, C. R.; Knörnschild, G.; Dick, L. F. P. *J. Braz. Chem. Soc.* **2003**, *14*, 584–593.

(96) Song, G.-L.; Xu, Z. *Electrochim. Acta* **2010**, *55* (13), 4148–4161.

(97) Renfrew, S. E.; McCloskey, B. D. *J. Am. Chem. Soc.* **2017**, *139* (49), 17853–17860.

(98) Kim, H. W.; Ross, M. B.; Kornienko, N.; Zhang, L.; Guo, J.; Yang, P.; McCloskey, B. D. *Nature Catalysis* **2018**, *1* (4), 282–290.

(99) Crozier, T. E.; Yamamoto, S. *J. Chem. Eng. Data* **1974**, *19* (3), 242–244.

(100) Graves, C. RAVDAV Data Analysis Software, Version 0.9.7., Technical University of Denmark, Computer Program, 2012.

(101) De Levie, R.; Delahay, P., *Advances in Electrochemistry and Electrochemical Engineering*; Wiley-Interscience: New York, 1967.

(102) Brug, G. J.; van den Eeden, A. L. G.; Sluyters-Rehbach, M.; Sluyters, J. H. *J. Electroanal. Chem. Interfacial Electrochem.* **1984**, *176* (1), 275–295.

(103) Hirschorn, B.; Orazem, M.; Tribollet, B.; Vivier, V.; Frateur, I.; Musiani, M. *Electrochim. Acta* **2010**, *55*, 6218–6227.

(104) Orazem, M. E.; Tribollet, B., *Electrochemical Impedance Spectroscopy*; John Wiley & Sons: Hoboken, NJ, 2008.

(105) King, F.; Quinn, M. J.; Litke, C. D. *J. Electroanal. Chem.* **1995**, *385* (1), 45–55.

(106) Sherwood, T.; Pigford, R.; Wilke, C., *Mass Transfer*; McGraw-Hill Book Company: New York, 1970.

(107) Lu-Kwang, J.; S., H. C. *Biotechnol. Bioeng.* **1985**, *27* (10), 1495–1499.

(108) Lang, W.; Zander, R. *Ind. Eng. Chem. Fundam.* **1986**, *25* (4), 775–782.

(109) Vanysek, P. In *CRC Handbook of Chemistry and Physics*, 90th ed.; CRC Press: Boca Raton, 2005.

(110) Peng, Z.; Freunberger, S. A.; Chen, Y.; Bruce, P. G. *Science* **2012**, *337* (6094), 563–566.

(111) Pinedo, R.; Weber, D. A.; Bergner, B.; Schröder, D.; Adelhelm, P.; Janek, J. *J. Phys. Chem. C* **2016**, *120* (16), 8472–8481.

(112) Viswanathan, V.; Nørskov, J. K.; Speidel, A.; Scheffler, R.; Gowda, S.; Luntz, A. C. *J. Phys. Chem. Lett.* **2013**, *4* (4), 556–560.

(113) Hartmann, P.; Heinemann, M.; Bender, C. L.; Graf, K.; Baumann, R.-P.; Adelhelm, P.; Heiliger, C.; Janek, J. *J. Phys. Chem. C* **2015**, *119* (40), 22778–22786.

(114) Gerbig, O.; Merkle, R.; Maier, J. *Adv. Funct. Mater.* **2015**, *25* (17), 2552–2563.

(115) Aetukuri, N. B.; McCloskey, B. D.; García, J. M.; Krupp, L. E.; Viswanathan, V.; Luntz, A. C. *Nat. Chem.* **2015**, *7* (1), 50–56.

(116) Gunasekara, I.; Mukerjee, S.; Plichta, E. J.; Hendrickson, M. A.; Abraham, K. M. *J. Electrochem. Soc.* **2015**, *162* (6), A1055–A1066.

(117) Chernov, A. A. In *Modern Crystallography III: Crystal Growth*, Queisser, H.-J., Ed.; Springer-Verlag Berlin Heidelberg: 1984; Chapter 3, pp 104–158.

(118) Knudsen, K. B.; Vegge, T.; McCloskey, B. D.; Hjelm, J. *J. Electrochem. Soc.* **2016**, *163* (9), A2065–A2071.

(119) Bryantsev, V. S.; Giordani, V.; Walker, W.; Blanco, M.; Zecevic, S.; Sasaki, K.; Uddin, J.; Addison, D.; Chase, G. V. *J. Phys. Chem. A* **2011**, *115* (44), 12399–12409.

(120) McCloskey, B. D.; Scheffler, R.; Speidel, A.; Girishkumar, G.; Luntz, A. C. *J. Phys. Chem. C* **2012**, *116* (45), 23897–23905.

(121) McCloskey, B. D.; Speidel, A.; Scheffler, R.; Miller, D. C.; Viswanathan, V.; Hummelshøj, J. S.; Nørskov, J. K.; Luntz, A. C. *J. Phys. Chem. Lett.* **2012**, *3* (8), 997–1001.

(122) Lee, B.; Kim, J.; Yoon, G.; Lim, H.-D.; Choi, I.-S.; Kang, K. *Chem. Mater.* **2015**, *27* (24), 8406–8413.

(123) Nakanishi, A.; Thomas, M. L.; Kwon, H.-M.; Kobayashi, Y.; Tatara, R.; Ueno, K.; Dokko, K.; Watanabe, M. *J. Phys. Chem. C* **2018**, *122* (3), 1522–1534.

(124) Chen, Y.; Freunberger, S. A.; Peng, Z.; Fontaine, O.; Bruce, P. G. *Nat. Chem.* **2013**, *5*, 489–494.

(125) Frith, J. T.; Landa-Medrano, I.; Ruiz de Larramendi, I.; Rojo, T.; Owen, J. R.; Garcia-Araez, N. *Chem. Commun.* **2017**, *53* (88), 12008–12011.

(126) Lee, D.-Y.; Lee, H.-S.; Kim, H.-S.; Sun, H.-Y.; Seung, D.-Y. *Korean J. Chem. Eng.* **2002**, *19* (4), 645–652.

(127) Atrens, A.; Dietzel, W. *Adv. Eng. Mater.* **2007**, *9* (4), 292–297.

Appendices

Appendix A

Supplementary Figures

A.1 Evidence of Dendrite Formation in Na-O_2 Cells

(a) Cathode side of separator

(b) Anode side of separator

Figure A.1: Photographs of a separator from an Na-O_2 cell with significant dendrite growth. Dendrites are visible as light grey spots on the cathode side of the separator (left). Clear evidence of Na deposition in the separator is visible by examination of the anode side of the separator (right).

A.2 H-Cell To-Scale Schematic

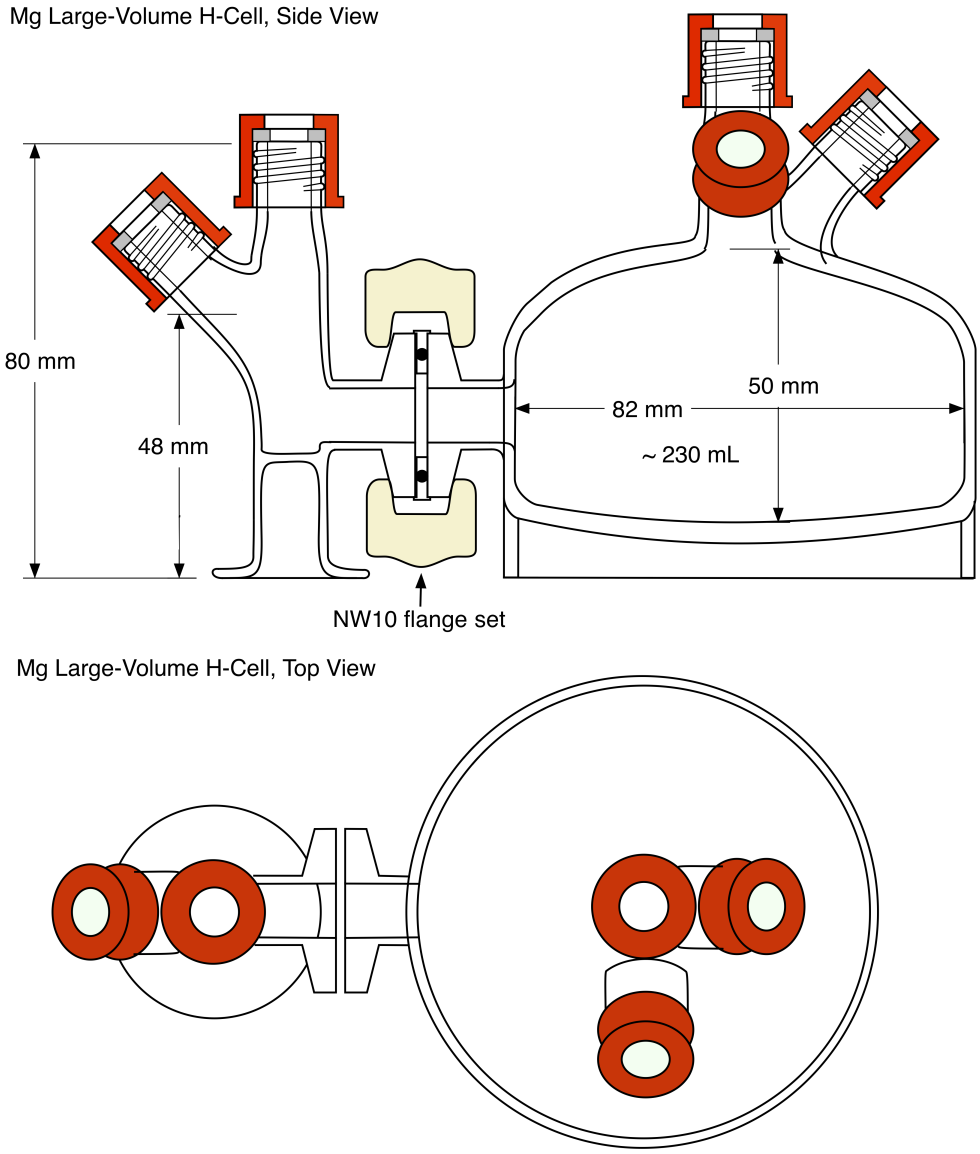

Figure A.2: To-scale schematic of a large-volume three-electrode glass H-cell for study of Mg oxidation. Image adapted from an illustration provided by Tom Adams, Adams & Chittenden Scientific Glassware, Berkeley, CA. Compare to Figure 2.4.

A.3 Nyquist and Bode Plots for Na-O_2 Cells

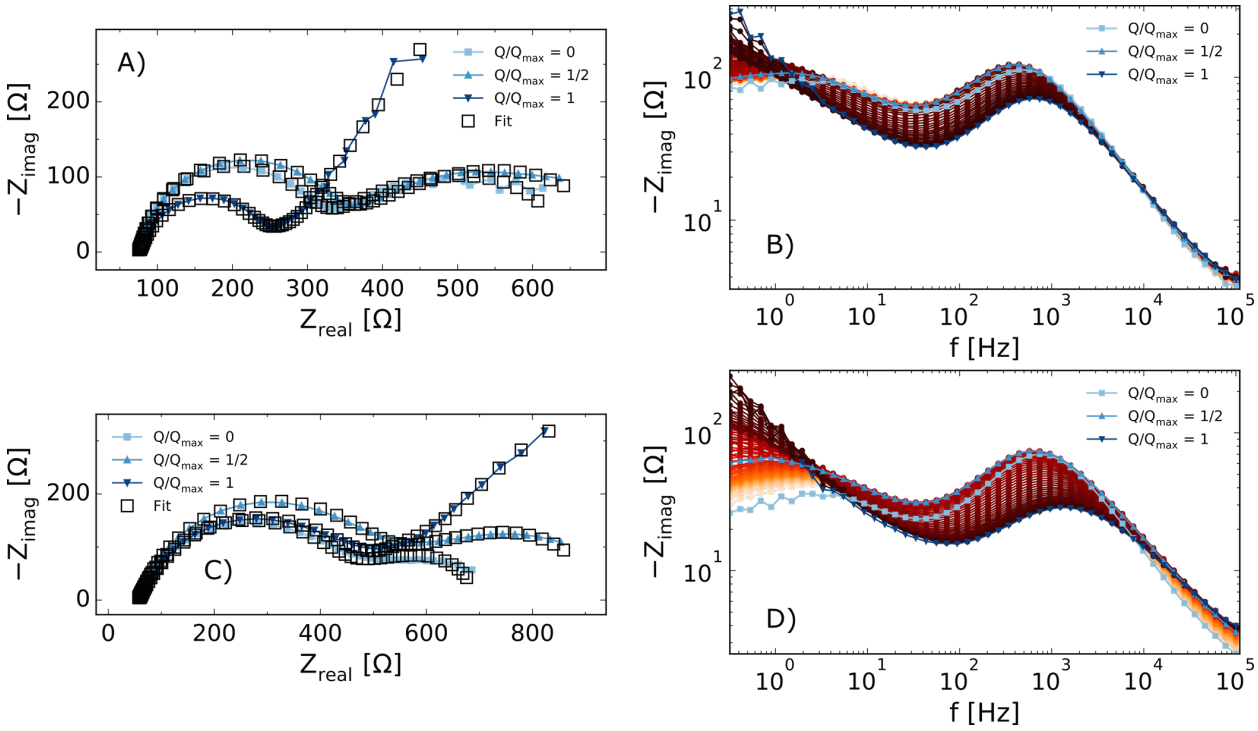

Figure A.3: Representative Nyquist (a,c) and Bode plots (b,d) acquired at 0.4 atm O_2 and average current densities of (a,b) 180 μA/cm^2 and (c,d) 440 μA/cm^2. Note that during galvanostatic conditions, EIS was performed throughout discharge until 1.0 V. The Nyquist plots (a,c) only show representative spectra while the Bode plots (b,d) show all collected spectra during the respective discharges, including those shown in (a,c).

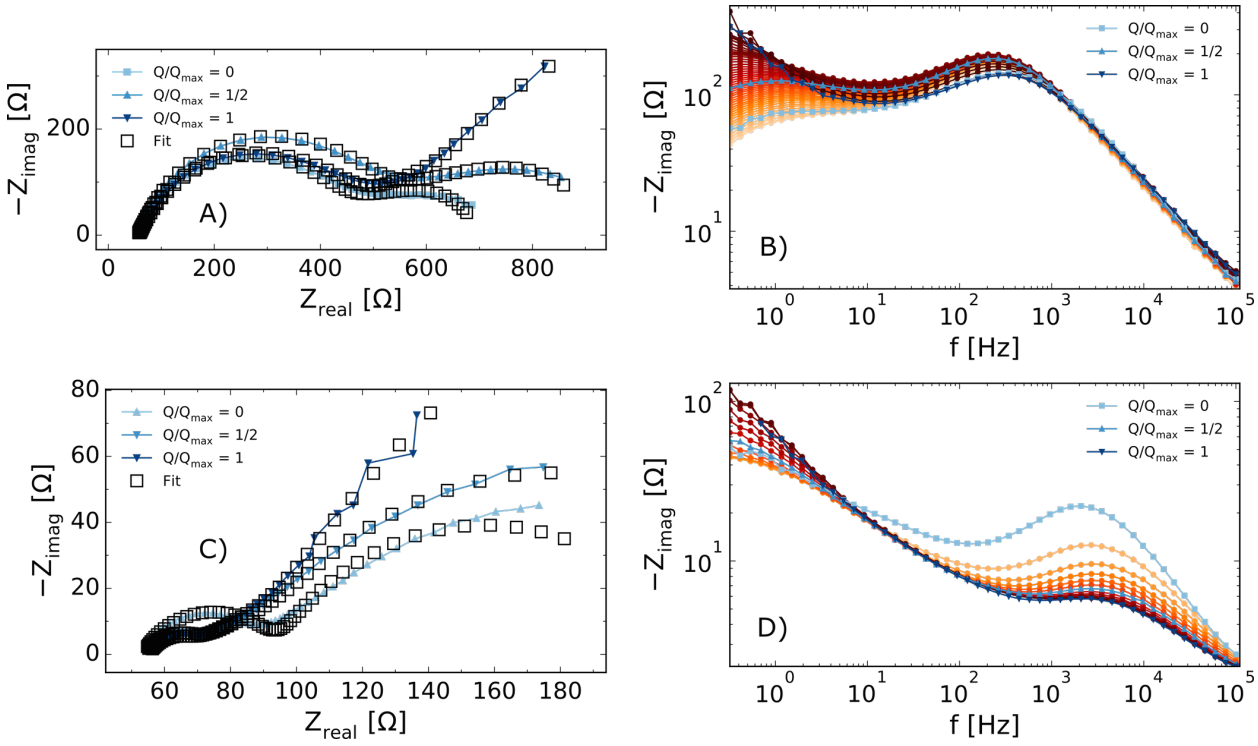

Figure A.4: Representative Nyquist (a,c) and Bode plots (b,d) acquired at 0.8 atm O_2 and average current densities of (a,b) 180 μA/cm^2 and (c,d) 1800 μA/cm^2. Note that during galvanostatic conditions, EIS was performed throughout discharge until 1.0 V. The Nyquist plots (a,c) only show representative spectra while the Bode plots (b,d) show all collected spectra during the respective discharges, including those shown in (a,c).

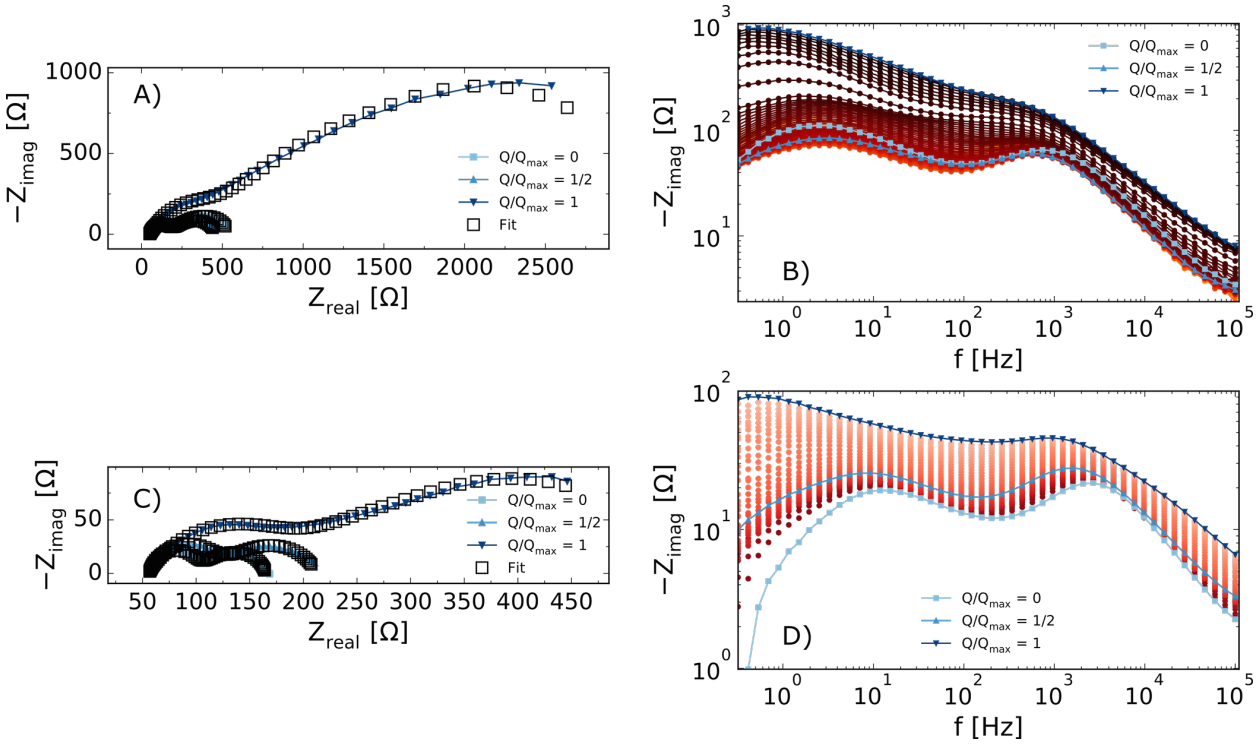

Figure A.5: Representative Nyquist (a,c) and Bode plots (b,d) acquired at 2.0 atm O_2 and average current densities of (a,b) 180 μA/cm^2 and (c,d) 1800 μA/cm^2. Note that during galvanostatic conditions, EIS was performed throughout discharge until 1.0 V. The Nyquist plots (a,c) only show representative spectra while the Bode plots (b,d) show all collected spectra during the respective discharges, including those shown in (a,c).

A.4 NaO_2 Spatial Distribution by Quantity

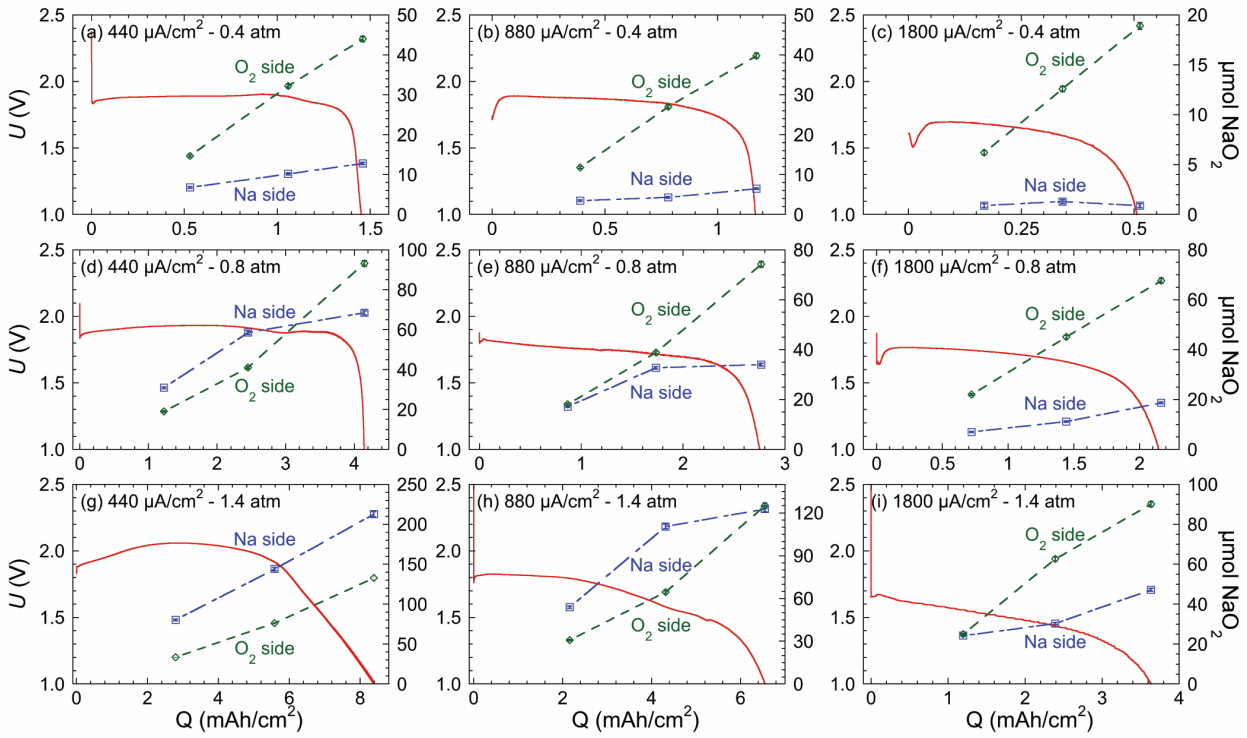

Figure A.6: Discharge profiles (red solid line) and quantity of NaO_2 detected by iodometric titration from the O_2 side of the cathode (green diamonds) and Na side of the cathode (blue squares) for two-cathode experiments at various currents and pressures. Current increases from left to right; pressure increases from top to bottom. Error bars represent the individual measurement error, and in most cases are smaller than the points. Compare to Figure 4.13.

A.5 Supplementary Oxidative Tafel Plots on Mg Electrodes

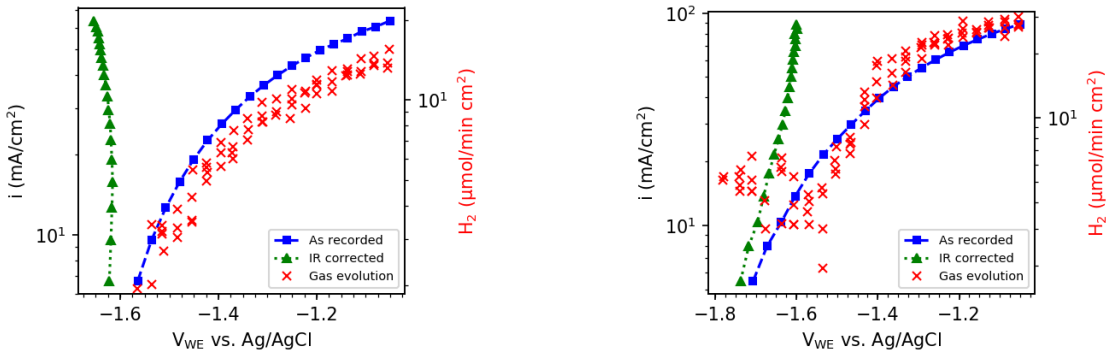

(a) pH 10, 0.5 M NaCl electrolyte **(b)** pH 2, 0.5 M [Cl^-] (NaCl/HCl) electrolyte

Figure A.7: Apparent and IR-corrected oxidative Tafel plots on Mg electrodes in (a) a 0.5 M NaCl electrolyte, with a measured pH 10 following Mg oxidation and (b) a 0.5 M [Cl^-] electrolyte at pH 2 comprised of NaCl and HCl. In both cases, the potential as-measured at a given current density must be IR corrected to account for Ohmic losses due to transport through the electrolyte. Gas evolution data are plotted against apparent potentials on an axis scaled such that overlap with the apparent Tafel plot indicates that the rate of H_2 evolution scales with the current according to a $2e^-$ process.

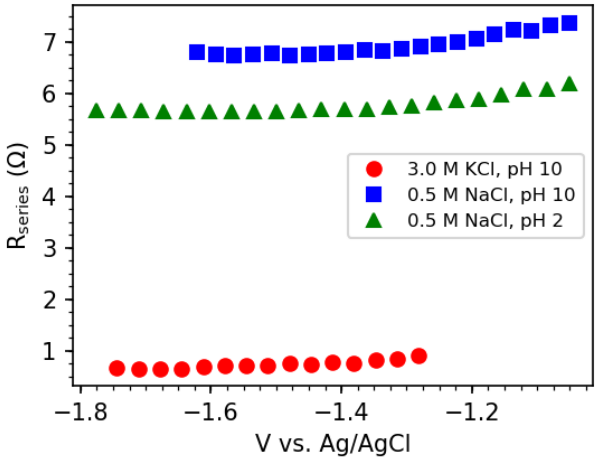

Figure A.8: Changes in the series or solution resistance (R_{series}) during polarization by SPEIS in several electrolytes. Data associated with Figures 7.1 and A.7.

A.6 Dissolution of a Mg Electrode Between pH 3.4 and 9.6

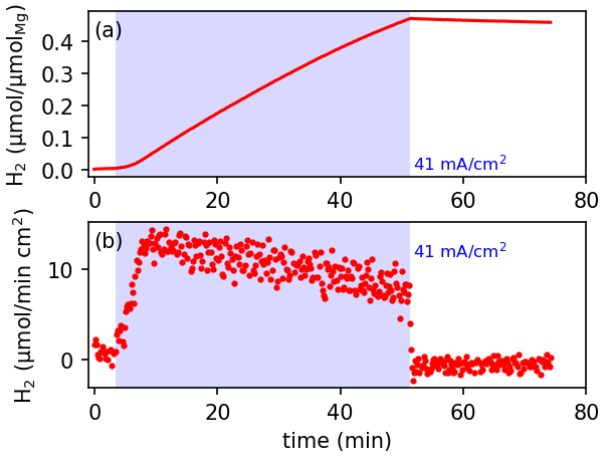

Figure A.9: Dissolution of a Mg electrode at an initial current density of 41 mA/cm^2 in a 1.0 M Cl^- electrolyte initially at pH 3.5. The final pH of the electrolyte following dissolution was 9.6. No significant change in the NDE behavior was observed throughout the dissolution.

A.7 Comparison of Mg Dissolution Data at pH 1 by the Estimated Extent of Electrode Dissolution

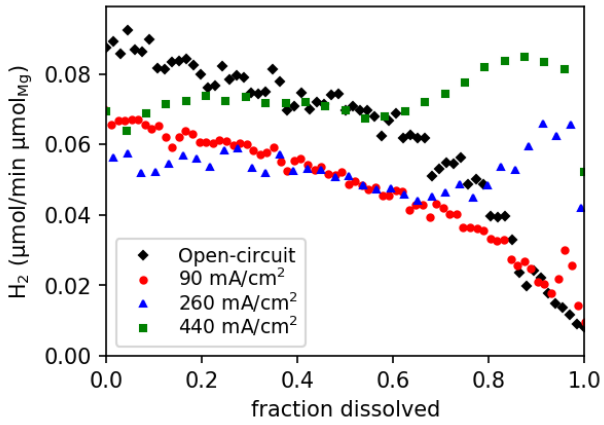

Figure A.10: Comparison of the pH 1 dissolution data in Figure 7.8c on the basis of the estimated fraction of the electrode dissolved. This fraction was esimated by non-dimensionalization of the time during which application of current occurred. The fraction of the electrode dissolved when application of current began was taken to be 0, with complete dissolution and the end of current flow corresponding to a fraction of 1. For data acquired at open-circuit, these times were estimated based on the decreasing rate of H_2 evolution. Suppression of H_2 evolution or the return of the NDE are evident by whether data at a given current are above or below the data at open-circuit, respectively.

A.8 Estimation of the Surface pH of a Dissolving Mg Electrode in a Bulk pH 2 Electrolyte

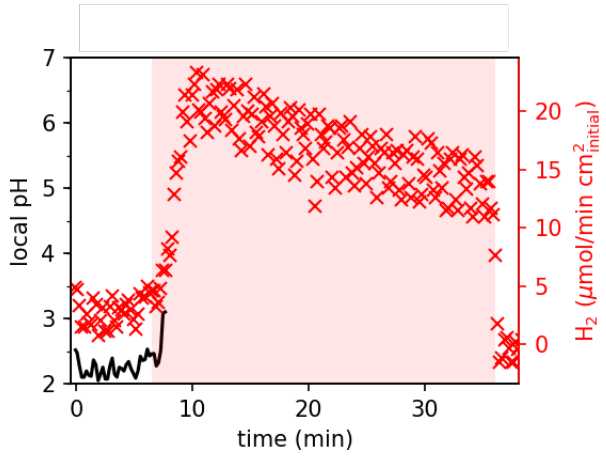

Figure A.11: Estimated pH at the surface of a dissolving Mg electrode in a bulk pH 2 environment, calculated according to the methods outlined in Sections 2.3.5 and 7.4.3. Note that the pH at the very beginning of GEIS (indicated by the shaded region) is initially lower, suggesting that the slow rise in H_2 evolution may be due to a transition from a non-NDE-promoting local surface pH to an NDE-promoting local pH.

Appendix B

Python Code for Data Analysis

B.0.0.1 Python packages used in the following functions

```
import pandas as pd
import numpy as np
import matplotlib.pyplot as plt
from scipy import stats
```

B.1 Calculation of Moles of Gas Consumed/Evolved from Gas Evolution Data

B.1.0.1 Analyze gas evolution from a Mg electrode in a large H-cell

```
# For data from labview (.txt), given cell headspace volume, calculate moles
    of gas.
#   This function accounts for the Henry's Law correction for H2 dissolution
def gas_Mg(filename,Vol, time_before = 0, est_time = 0):
    # Analyze Labview data from Mg NDE study and return H2 evolved vs. time
    # optional: specify length of time before data acquisition began and time
    # to be used in estimation of H2 evolved prior to data acquisition.

    # get labview data
    lbv = read_lbv(filename) # This function defined below

    time = lbv.loc[:,'time'].values # time, min
    pressure = lbv.loc[:,'Pressure'].values # pressure, Torr
    Temp = np.mean(lbv.loc[:,'Temp'].values) # MEAN temperature, C
    V = lbv.loc[:,'Voltage'].values # voltage/potential
    R = 62.363 # ideal gas constant, L, Torr, K, etc

    # calculate umol gas in headspace, return as an array
    mol_head = pressure * Vol / (R * (Temp + 273.15) )
    # calculate quantity of H2 by subtracting initial gas (Ar)
    mol_H2head = mol_head - mol_head[0]
```

```
21
22      # use Henry's law coefficient to calculate additional gas in electrolyte;
23      #   assume all pressure rise after initial point is due to hydrogen
        evolution
24      p_H2 = lbv.loc[:,'Pressure'].values - lbv.loc[0,'Pressure']
25      # calculate mol_H2 in electrolyte
26      #   Henry's constant = 0.00093 umol/mL-torr, per Crozier and Yamamoto 1974
27      #   Approximately 230 mL electrolyte is used in each experiment
28      mol_H2elyte = 0.00093 * 230 * p_H2
29      # add headspace + electrolyte H2
30      mol_total = mol_H2head + mol_H2elyte
31
32      # if an unmeasured time is specified as != 0, estimate amount of gas
        evolved during that time
33      if time_before != 0 and est_time != 0:
34          ocvindices = time <= est_time # indices to be used for estimation
35          H2_ocv_rate = np.gradient(mol_total[ocvindices],time[ocvindices])
36          # perform linear regression on H2_ocv_rate to extrapolate to lower
        corrosion rate
37          H2slope, Hintercept, _, _, _ = stats.linregress(time[ocvindices],
        H2_ocv_rate)
38          # extrapolate the above regression to time_before
39          H2initrate = Hintercept - H2slope*(time_before)
40          # H evolved: integral of the above,
41          # i.e. area of trapezoid with base lengths Hintercept and Hinitrate
        and width time_before
42          missing_H2 = (H2initrate + Hintercept)/2 * (time_before)
43          # add missing H2 due to electrolyte equilibrium
44          missing_H2 = missing_H2 + (((missing_H2 * R * (Temp+273.15))/Vol) *
        0.00093 * 230)
45          # increase mol_total to include missing_H2
46          mol_total = mol_total + missing_H2
47
48      return mol_total, time, V
```

B.1.0.2 Analyze gas evolution in any cell (Swagelok or H-cell without small headspace-to-electrolyte volume ratio)

```
1 # For data from labview (.txt), given cell headspace volume, calculate moles
      of gas.
2 #   No correction for Henry's law is performed
3 def gas_any(filename,Vol):
4     # Analyze Labview data from any data set and return gas evolved vs. time
5
6     # get labview data
7     lbv = read_lbv(filename)
8
9     # extract required data
10    time = lbv.loc[:,'time'].values # time, min
11    pressure = lbv.loc[:,'Pressure'].values # pressure, Torr
```

```
    Temp = np.mean(lbv.loc[:,'Temp'].values) # temperature, C
    V = lbv.loc[:,'Voltage'].values # voltage/potential

    R = 62.363 # ideal gas constant, L, Torr, K, etc

    # calculate umol gas in headspace, return as an array
    mol_gas = pressure * Vol / (R * (Temp + 273.15) )
    # Zero the data: subtract out the starting value
    mol_gas_0 = mol_gas - mol_gas[0] # subtracts out starting pressure

    return mol_gas_0, time, V
```

B.2 Analysis of Electrochemical Data

B.2.0.1 Analyze data from chronopotentiometry experiments

```
# Extract V vs. Q from a Chronopotentiometry file (EC-Lab, .mpt), and average I
def VvsQ(filename):
    # Read the mpt file
    rawdata = read_mpt(filename)
    # get potential and capacity
    Varray = rawdata.loc[:,'Ewe/V'].values # potential of working electrode
    Qarray = rawdata.loc[:,'Capacity/mA.h'].values # Q, mAh
    V = Varray.tolist()
    Q = Qarray.tolist()

    # get the average current:
    # get the current
    Iarray = rawdata.loc[:,'I/mA']
    # get the time
    tarray = rawdata.loc[:,'time/s']
    # time-average the current
    Iavg = np.divide(sum(np.multiply(Iarray,tarray)),sum(tarray))
    return V, Q, Iavg
```

B.2.0.2 Analyze data from chronoamperometry experiments

```
# Extract I vs. Q from a Chronoamperometry file (EC-Lab, .mpt), and average V
def IvsQ(filename):
    # Read the mpt file
    rawdata = read_mpt(filename)
    # get potential and capacity
    Iarray = rawdata.loc[:,'I/mA'].values # current, mA
    Qarray = rawdata.loc[:,'Capacity/mA.h'].values # Q, mAh
    I = Iarray.tolist()
    Q = Qarray.tolist()
    # get time
    tarray = rawdata.loc[:,'time/s'].values
    t = tarray.tolist()
```

```
13
14      # get the average current:
15      # get the current
16      Varray = rawdata.loc[:,'Ewe/V']
17      # get the time
18      tarray = rawdata.loc[:,'time/s']
19      # time-average the current
20      Vavg = np.divide(sum(np.multiply(Varray,tarray)),sum(tarray))
21      # get all potential data points...
22      Vall = Varray.tolist()
23      return I, Q, Vavg, t, Vall
```

B.2.0.3 Analyze data from LSV or CV

```
1 # Analyze LSV or CV data files (EC-Lab, .mpt)
2 def lsv_analyze(filename,loop): # no **opt_param
3     # get raw data
4     lsv = read_mpt(filename)
5
6     # get bounds of loops and total number of loops
7     loops = count_loops(filename)
8     loopends = read_loops(filename)
9     # if only one loop...
10    if loops == 1: # only one loop, loopends = bounds of loop
11        thisloop = range(loopends[0],loopends[1]+1) #+1 because range is non-
      end-inclusive
12    else: # more than one loop
13        thisloop = range(loopends[loop][0],loopends[loop][1]+1)
14    #thisloop = the range of values needed to return all data from the loop
15
16    # Get data
17    I = lsv.loc[thisloop,'<I>/mA'].values # current, mA
18    V = lsv.loc[thisloop,'Ewe/V'].values # potential of working electrode
19    t = lsv.loc[thisloop,'time/s'].values # time, s
20
21    # define startstop, times compatible with labview (in minutes):
22    #   when was the scan happening?
23    startstop = np.divide([np.amin(t),np.amax(t)],60)
24
25    return V, I, t, startstop
```

B.2.0.4 Analyze an EIS file (GEIS, PEIS, or SPEIS) for the series resistance and return the potential, current, resistances, timestamps, and other important parameters

```
1 # for GEIS file, PEIS file, or SPEIS file
2 # given filename (EC-Lab, .mpt)
3 # return Vseries, Iseries, Rseries
4 # plot the Nyquist plot of every loop
5 def eis_analyze(filename,loop,freq_cutoff = 5000, **opt_param):
```

```
6     # Analyzes EIS file (filename) for the given loop (loop)
7     #   compatible with GEIS, PEIS, or staircase equivalents
8
9     # print start of loops
10    print('Loop #' + str(loop))
11
12    # should all plots be given?
13    if ('plots' in opt_param):
14        plots = opt_param['plots']
15    else:
16        plots = True
17
18    # return averages, or all data values?
19    if ('detail' in opt_param):
20        detail = opt_param['detail']
21    else:
22        detail = False
23
24    # should all the resistances be printed?
25    if ('printR' in opt_param):
26        printR = opt_param['printR']
27    else:
28        printR = True
29
30    # get EIS raw data
31    eis = read_mpt(filename)
32
33    # extract relevant raw data:
34    real_raw = eis.loc[:,'Re(Z)/Ohm'].values # REAL, Ohm
35    imag_raw = eis.loc[:,'-Im(Z)/Ohm'].values # -IMAGINARY, Ohm
36    freq_raw = eis.loc[:,'freq/Hz'].values # FREQUENCIES, Hz
37    t_raw = eis.loc[:,'time/s'].values # TIME, s
38    V_raw = eis.loc[:,'<Ewe>/V'].values # potential working electrode
39    I_raw = eis.loc[:,'<I>/mA'].values # current, mA
40    cycle_number = eis.loc[:,'cycle number'].values # cycle number
41
42    # determine the bounds of all the loops
43    loopends = read_loops(filename) # we are in loop "loop", loopends[loop] if
      total loops > 1
44    # get indices corresponding with the loop:
45    # how many loops are there total?
46    loops = count_loops(filename)
47    # if only one loop...
48    if loops == 1: # only one loop, loopends = bounds of loop
49        loopbounds = loopends
50        thisloop = range(loopends[0],loopends[1]+1) #+1 because range is non-
    end-inclusive
51    else: # more than one loop
52        loopbounds = [loopends[loop][0],loopends[loop][1]]
53        thisloop = range(loopends[loop][0],loopends[loop][1]+1)
```

```
54
55      # determine max number of cycles there are in the loop
56      cycles = int(cycle_number[loopbounds[1]] - cycle_number[loopbounds[0]]) +
        1
57      # number of cycles = # of cycle in last row (1-indexed) - # in first row
        (1-indexed)
58      #   e.g. if cycles goes from 1 to 13, then this will return 13-1 = 12
59      # determine what cycle number to start from, such that we loop
60      #   from cyclestart to cyclestart + eiscycles (e.g. 15 to 27)
61      cyclestart = int(cycle_number[loopbounds[0]])
62
63      # Initialize variables
64      V = [] # V: average potential during each cycle (time-weighted), V
65      I = [] # I: average current during each cycle (time-weighted), mA
66      Rseries = [] # Rseries: series resistance from each cycle, Ohm
67      t = [] # t: weighted average timestamp from each cycle, s
68      cyclebounds = [] # boundary times of each cycle, s
69      # zero-frequency variables
70      t0 = []
71      I0 = []
72      V0 = []
73
74      if plots==True:
75          # Create Nyquist plot
76          figN = plt.figure()
77          axN = figN.add_subplot(111)
78
79      # loop through each eis cycle within the given loop
80      for j in range(cycles):
81          # calculate cycle number based on start cycle and j index
82          cyclenum = cyclestart+(j)
83          # determine which indices belong to the particular cycle
84          #   AND where frequency ~= 0
85          # Where frequency == 0, add these to the zeroindices units
86          cycleindex = (cycle_number == cyclenum) # it's this cycle
87          impindex = (freq_raw != (0)) # impedance is happening
88          # If both of the above are true, note the index, else don't
89          cycleimp = []
90          for k in range(len(cycleindex)):
91              if impindex[k] == True and cycleindex[k] == True:
92                  # it's this cycle, and impedance is happening
93                  cycleimp.append(k)
94              elif cycleindex[k] == True and impindex[k] == False:
95                  # it's this cycle, but impedance is not happening
96                  # append relevant data to zero-frequency data
97                  t0.append(t_raw[k])
98                  I0.append(I_raw[k])
99                  V0.append(V_raw[k])
100
101         # extract Re(Z)/Ohm and -Im(Z)/Ohm
```

```
102         real = real_raw[cycleimp]
103         imag = imag_raw[cycleimp]
104 
105         if plots==True:
106             # Add to Nyquist plot
107             axN.plot(real,imag)
108 
109         # imag[0]<0 means there exists an interpolatable x-intercept
110         # First, check that the cycle/loop actually happened,
111         #   i.e. method not skipped
112         if real.size == 0:
113             # this cycle does not exist (i.e. the method probably ended early)
114             print('Warning: EIS cycle ' + str(j) + ' does not exist')
115             print('Debug message, loop no ' + loop + ', cycle no ' + str(j)+ '
    , cyclenum = ' +str(cyclenum) )
116             break # end this loop early
117         elif imag[0] < 0:
118             # interpolate both resistance and frequency where it occurs
119             # LIMIT THIS to frequencies > freq_cutoff (default 5000 Hz) to
    avoid problems.
120             highfreq = freq_raw[cycleimp] > freq_cutoff
121             Rtemp = np.interp(0,imag[highfreq],real[highfreq])
122             Rseries.append(Rtemp)
123 
124             # frequency interpolation
125             freq = freq_raw[cycleimp]
126             finterp = np.interp(Rtemp,real,freq)
127 
128             # if printR setting is on:
129             if printR:
130                 # print interpolation result
131                 print('Loop ' + str(loop) + ', Cycle ' + str(cyclenum) +
132                       ': Interpolating R = ' + str(round(Rtemp,2)) +
133                       ' at f = ' + str(round(finterp,0)) + ' Hz')
134         else:
135             # extrapolate to zero: treat real as y, imag as x, and find y-int
136             y = real
137             x = imag
138             # use stats.linregress(x,y) from scipy
139             # ignore other outputs; save and print the R-value
140             _, Rtemp, r_value,_,_ = stats.linregress(x,y)
141             Rseries.append(Rtemp)
142 
143             # if printR is on:
144             if printR:
145                 # print R-squared value
146                 print('Loop ' + str(loop) + ', Cycle ' + str(cyclenum) +
147                       ' Extrapolating R = ' + str(round(Rtemp,2)) +
148                       '. R^2 =' + str(round(r_value**2,5)))
149 
```

```
150         if plots==True:
151             # label plot
152             axN.set_xlabel('Real')
153             axN.set_ylabel('-Imag')
154             plt.title('Loop ' + str(loop))
155 
156         if detail == False:
157             # store average I, V, and t associated with this cycle
158             # use a time-weighted average for V and I
159             V.append(np.divide(np.sum(np.multiply(V_raw[cycleimp],t_raw[
    cycleimp])),
160                                np.sum(t_raw[cycleimp])))
161             I.append(np.divide(np.sum(np.multiply(I_raw[cycleimp],t_raw[
    cycleimp])),
162                                np.sum(t_raw[cycleimp])))
163             t.append(np.mean(t_raw[cycleimp]))
164         cyclebounds.append([(t_raw[cycleimp[0]]),
165                             (t_raw[cycleimp[(len(cycleimp)-1)]])])
166 
167     # if detail == True, store raw data instead of averages
168     if detail == True:
169         # set data from this loop
170         t = t_raw[thisloop]
171         V = V_raw[thisloop]
172         I = I_raw[thisloop]
173 
174     # if Rseries is empty, the loop did not exist
175     if Rseries == []:
176         print('Warning: EIS cycle(s) for loop ' + loop + ' did not exist,
    result is empty.')
177 
178     # Calculate the average series resistance among all values above
179     Ravg = np.mean(Rseries)
180     # if printR is on, print average
181     if printR:
182         print('Average R = ' + str(round(Ravg,2)) + ' Ohms (Loop ' + str(loop)
    + ')')
183 
184     # Save the zero frequency points at the start of GEIS from this cycle
185     zerofreq = pd.DataFrame({'t':t0, 'I':I0, 'V':V0})
186 
187     # print end of analysis
188     print('/Loop #'+ str(loop))
189 
190     return V, I, Rseries, t, cyclebounds, zerofreq
```

B.2.0.5 IR-correct potentials by Ohm's Law, given a current and resistance

```
1 def IRcorrect(Vraw,I,R):
2     # IR-corrects the raw potential (V) using the pointwise values of R and
    average of R
```

```
    # I and Vraw must have the same dimensions

    # If only one resistance is given, calculate VpntR = VavgR
    if np.size(R) == 1:
        VavgR = Vraw - (np.multiply(I,R)/1000)
        VpntR = VavgR
    else:
        # average the resistance
        Ravg = np.mean(R)
        # calculate average-corrected resistance
        VavgR = Vraw - (np.multiply(I,Ravg)/1000)
        # calculate pointwise-corrected resistance
        VpntR = Vraw - (np.multiply(I,R)/1000)

    return VpntR, VavgR
```

B.3 Reading and Processing Data

B.3.0.1 Reading .mpt files output from EC-Lab

```
# Read MPT files from EC Lab
def read_mpt(filename):
    # Converts .mpt files from EC Lab into a dataframe file containing all EC Lab data

    # read first line of file as CSV with tab separators
    header = pd.read_csv(filename, sep='\t', nrows=1, encoding='latin1')

    # extract number of lines to skip
    word = str(header).split() # turns first line into string then breaks up into string array
    num = int(word[8]) # finds last number in the string and converts to integer

    # read the data chunk of the file by skipping the header-1 lines, viewing column labels
    df = pd.read_csv(filename, sep='\t', skiprows=num-1, encoding='latin1')
    return df
```

B.3.0.2 Reading output files from labview software

```
# Read Labview files generated by Delilah/Demi/Debbie
def read_lbv(filename):
    # reads labview.txt files and creates a dataframe with columns labeled
    # column labelsr: time, Volt, I, Pres, Temp
    df = pd.read_csv(filename, sep='\t', names=['time','Voltage','I','Pressure','Temp'])
    return df
```

B.3.0.3 Reading start and stop indices of loops in an EC-Lab file

```
# Read start/stop indices of loops within an EC-Lab file.
def read_loops(filename):
    # determine how many lines are skipped in the header total
    # read first line of file as CSV with tab separators
    header = pd.read_csv(filename, sep='\t', nrows=1, encoding='latin1')

    # extract number of lines of header information
    word = str(header).split() # turns first line into string then breaks up into string array
    num = int(word[8]) # finds last number in the string and converts to integer

    # extract the line describing the last loop
    lastloop = str(pd.read_csv(filename, sep='\t', skiprows=num-3, nrows = 1,
                               encoding = 'latin1')).split()
    # CHECK if lastloop[0] = 'Loop'
    # if yes: determine the start and stop points of each loop
    # if no: return inclusive [0, len(data)]
    if lastloop[0]=='Loop' and lastloop[1]!='0':
        # lastloop[1] = index of the last loop (zero-indexed)
        loopnumber = int(lastloop[1])

        # the describing lines begin at (num-3-loopnumber) and end at (num-3)
        loopnames = str(pd.read_csv(filename, sep='\t', skiprows=num-3-loopnumber,
                                    nrows = loopnumber, encoding = 'latin1')).split()

        # loop from 0 to loopnumber; for each create a new row in an array containing
        #   the start and stop indices of each loop
        # initialize with an array containing [0, loopnumber]
        loopends = []
        for i in range(loopnumber+1):
            # Current loop number is equivalent to i
            loopends.append([int(loopnames[5+(i*9)]), int(loopnames[7+(i*9)])])
    elif lastloop[1]=='0':
        # there is "loop" text but only one loop; treat it as if there are no loops
        # determine size of the data frame extracted
        df = read_mpt(filename)
        # set size of loopends
        loopends = [0,len(df)-1] # length doesn't account for zero index
    else:
        # determine size of the data frame extracted
        df = read_mpt(filename)
        # set size of loopends
        loopends = [0,len(df)-1] # length doesn't account for zero index
    return loopends
```

B.3.0.4 Reading the number of cycles in an EIS data file

```
# Read number of cycles in EIS file
def eis_cycles(filename):
    # read row #56 (nc cycles)
    row56 = str(pd.read_csv(filename, sep='\t', skiprows = 55, nrows=1,
                            encoding='latin1')).split()
    # row56[2] = the number of rows
    ncycles = int(row56[2])
    return ncycles
```

B.3.0.5 Count how many loops in the data exist in an EC-Lab data file

```
def count_loops(filename):
    # determines how many loops there are in the file
    loopends = read_loops(filename)
    # dimensions of loopends?
    loopsize = np.shape(loopends)
    # if len(loopsize) == 1, there are no loops, set loops = 1
    if len(loopsize) == 1:
        loops = 1
    else: # loops are present, set loops = loopsize[0], i.e. # of rows
        loops = loopsize[0]
    return loops
```

B.4 Calculations and Model for Estimation of Mass-Transfer Coefficients and the Surface pH of Dissolving Mg Electrodes

The following code estimates the mass-transfer coefficients in the large-volume three-electrode H-cell using limiting current measurements of O_2 on copper. It then builds a model for the changing surface area of a dissolving electrode based on the open-circuit evolution of H_2. These results combined are used to estimate the pH at the surface of dissolving Mg electrodes. An example is provided. H_2 evolution data from both the open-circuit experiment and the data used in the final pH model was obtained using functions and methods outlined in this appendix; these exist in the "MgAnalyzer" resource.

```
import numpy as np
import matplotlib.pyplot as plt
from MgAnalyze import lsv_analyze, count_loops, read_lbv, read_mpt, read_loops

###Henry's Law and diffusion coefficients
# Diffusion, converted to m2/s (i.e. *(10**-4)) for SI units
D_H = (9.311*(10**-5))*(10**-4) # m2/s, original cm2/s - Vanysek
D_O2 = (1.42*(10**-5))*(10**-4) # m2/s, original cm2/s, for 0.745 M KCl in
    water at 25C - Ju

# Henry's law solubility constants
```

```
H_O2 = 7.83762E-06 # O2, units in mol/m^3-Pa
H_H2 = 6.98341E-06 # H2, units in mol/m^3-Pa

viscosity_cP = 1.03 # cP
viscosity = viscosity_cP*(10**-3) # SI units of viscosity, kg/m-s = Pa-s
density_gmL = 1.05 # g/mL
density = density_gmL * 1000 # SI units, kg/m^3

# calculating Schmidt numbers
Sc_H = viscosity / (D_H * density)
Sc_O2 = viscosity / (D_O2 * density)

### Filenames and user-defined parameters
# these data files (from EC-Lab and Labview) must be saved in the same
    directory
CV_f = '2018-06-06_O2reduction-overnight_05_CV_C01.mpt' # CV filename
lbv_CV = '2018-06-06_O2reduction-overnight_Ch1__2018-06-06_19.36_49.txt' #
    filename for data from labview, CV

A_CV = 0.450418/10**4 # electrode area for CV experiment
l_CV = 2*2.26/1000 # m, characteristic length (width of electrode, mm * 2)

### CV limiting current analysis

# get labview data, particularly pressure and time
lbv_cv_P = lbv_cv_all.loc[:,'Pressure']
lbv_cv_t = lbv_cv_all.loc[:,'time']
# how many loops?
cvloops = count_loops(CV_f)

# initialize limiting current array for storing data
iL_cv = []

# loop to plot data
for j in range(1,cvloops-1): # multiple CVs were performed, this samples some
    of them for analysis
    # use LSV_analyze to get t (seconds), V, I
    cv_V, cv_I, cv_ts, cv_startstop = lsv_analyze(CV_f,j)
    # convert time to minutes
    cv_t = np.divide(cv_ts,60)
    # convert current to current density (A/m^2)
    cv_i = np.divide(cv_I,A_CV*1000)

    # sample the absolute minimum current achieved
    iL_cv.append(np.amin(cv_i))
    # print loop number and limiting current
    print('CV Loop #' + str(j) + ', i_L = ' + str(iL_cv[len(iL_cv)-1]))

    # separate CVs into two cycles
    cvall = read_mpt(CV_f)
```

```
58      loopends = read_loops(CV_f)
59      # use the jth loop
60      thisloop = loopends[j]
61      cvcyc = cvall.loc[range(thisloop[0],thisloop[1]+1),'cycle number'].tolist
        ()
62      # read first cycle and assign second cycle
63      cyc1 = cvcyc[0]
64      cyc2 = cyc1+1
65      # get the indices of each cycle
66      cyc1i = []
67      cyc2i = []
68      for k in range(len(cvcyc)):
69          if cvcyc[k] == cyc1:
70              cyc1i.append(k)
71          else:
72              cyc2i.append(k)
73
74 ### Determine Reynolds number
75 # calculate sherwood number and use correlation for Reynolds
76
77 # Calculate limiting current:
78 #   CV limiting current from highest currents achieved on loops 1 and 2 (zero-
       indexed)
79 iL_high = - np.mean(iL_cv) # A / m^2
80
81 # determine oxygen pressures ;
82 #   these were read manually from the graphs
83 p_high = 835 # torr
84
85 # calculate bulk concentration of O2
86 CO2inf_high = H_O2 * p_high * (133.322) # conversion: 133.322 Pa = 1 Torr
87 # calculate sherwood number
88 Sh_high = (iL_high * l_CV) / (4*96485*CO2inf_high*D_O2)
89
90 # use Sherwood and Schmidt nubmers to calculate Reynolds
91 # Sh = 0.664 Re^1/2 Sc^1/3
92 # Re = (Sh Sc^-1/3 / 0.664)^2
93 Re = (Sh_high * (Sc_O2**(-1/3)) / 0.664)**2
94
95 ### define function to model area changes
96 # set up area calculation
97 # OCV EVOLUTION RATES
98 # data from OCV evolution at pH 1 to obtain an area-change model
99 OCVdiss = [   2.30507810e+01,  2.34657283e+01,  2.25616646e+01,
100         2.43481871e+01,  2.29089152e+01,  2.27413366e+01,  2.36454002e+01,
101         2.14807809e+01,  2.14467372e+01,  2.19871753e+01,  2.20197968e+01,
102         2.21994688e+01,  2.17488629e+01,  2.10301751e+01,  2.00377014e+01,
103         2.01837885e+01,  2.16259049e+01,  2.06679792e+01,  2.09360612e+01,
104         2.08038098e+01,  1.96347569e+01,  1.95842436e+01,  1.97639155e+01,
105         2.13895190e+01,  2.04883072e+01,  1.83689488e+01,  1.86391679e+01,
```

```
106         1.96755055e+01,  1.84092460e+01,  1.89227789e+01,  1.88346022e+01,
107         1.94958336e+01,  1.95842436e+01,  1.83208360e+01,  1.86324681e+01,
108         1.83594046e+01,  1.83208360e+01,  1.78702301e+01,  1.64242986e+01,
109         1.75726268e+01,  1.81130649e+01,  1.62446267e+01,  1.65155606e+01,
110         1.62446267e+01,  1.62848483e+01,  1.34063044e+01,  1.39887454e+01,
111         1.44642971e+01,  1.43260982e+01,  1.47814724e+01,  1.28477512e+01,
112         1.31759437e+01,  1.28467628e+01,  1.04147914e+01,  1.03781946e+01,
113         1.04694566e+01,  8.66418116e+00,  6.23035388e+00,  5.24049886e+00,
114         6.40829989e+00,  5.86643207e+00,  4.69428643e+00,  3.88148471e+00,
115         3.61631758e+00,  3.07872391e+00,  2.34714322e+00,  2.16747126e+00]
116 OCVtimes = [ 2.393,  2.583,  2.773,
117         2.963,  3.152,  3.342,  3.532,  3.722,  3.912,  4.101,  4.291,
118         4.481,  4.671,  4.861,  5.051,  5.241,  5.43 ,  5.62 ,  5.81 ,
119         6.   ,  6.189,  6.379,  6.569,  6.759,  6.949,  7.139,  7.328,
120         7.518,  7.708,  7.898,  8.087,  8.277,  8.467,  8.657,  8.847,
121         9.036,  9.226,  9.416,  9.606,  9.796,  9.985, 10.175, 10.365,
122         10.555, 10.745, 10.934, 11.124, 11.314, 11.503, 11.694, 11.883,
123         12.073, 12.263, 12.452, 12.642, 12.832, 13.022, 13.212, 13.401,
124         13.591, 13.781, 13.971, 14.161, 14.351, 14.54 , 14.73 , 14.92]
125 # modify the times data to go from t = 0 to 1 (nondimensional time)
126 tA = np.divide((OCVtimes - np.amin(OCVtimes)),np.amax(OCVtimes)-np.amin(
        OCVtimes))
127
128 # fit a polynomial to OCVdiss vs. tA
129 porder = 3 # third order solution gives monotonically decreasing area
130 At_poly_raw = np.polyfit(tA,OCVdiss,porder) # gives polynomial coeffs.
131 # calculate values of the polynomial at tA
132 At_raw = np.polyval(At_poly_raw,tA)
133 # modify At_raw to have a maximum value of 1
134 At = np.divide(At_raw,np.amax(At_raw))
135
136 # Define an area function which can be used to determine the area
137 # GIVEN labview time, current start/stop times, Area
138 # RETURN Area(labview time)
139 def A_OCV(lbvt,tI0,tIf,A0):
140     # use Istart and Istop to rescale tA
141     tA_sc = np.multiply(tA,(tIf-tI0))+tI0
142     # use A to rescale At
143     At_sc = np.multiply(At,A0)
144
145     A_t = []
146     # loop through lbvt and assign values to A_t as needed
147     for i in range(len(lbvt)):
148         if lbvt[i]<tI0:
149             # current hasn't started, assume area is constant
150             A_t.append(A0)
151         elif lbvt[i]<=tIf:
152             # current has started, interpolate area
153             A_t.append(np.interp(lbvt[i],tA_sc,At_sc))
154         else: # current has stopped, area is zero
```

```
155             A_t.append(0)
156     return A_t
157
158 # define function to calculate mass transfer coefficients
159 #   and resulting concentrations and pH
160 def MassXfer(lbv_t, mol_total, Istart, Iend, Iavg, A, l, umoles_Mg, pH_b, Re):
161     # H2 from H+ number (0 to 2, typically 2)
162     Htrans = 2
163
164     # calculate H2 rate
165     H2_rate = np.gradient(mol_total,lbv_t)
166     # calculate H+ at infinity
167     Cinf_H = 1000* 10**(-pH_b)
168     # calculate the area
169     A_t = A_OCV(lbv_t,Istart,Iend,A)
170     # create I vs. time vector
171     I = [] # mA, either = Iavg or = 0
172     for i in range(len(lbv_t)):
173         if lbv_t[i]< Istart: # current isn't flowing yet
174             I.append(0)
175         elif lbv_t[i] <= Iend: # current flowing
176             I.append(Iavg)
177         else: # current stopped
178             I.append(0)
179     # calculate current (mA/cm2) based on the area estimate; if A = 0, set I =
        0
180     # also calculate H2 evolution rate per area
181     i_est = []
182     H2_est = []
183     for i in range(len(A_t)):
184         if A_t[i] > 0:
185             i_est.append(I[i] / A_t[i])
186             H2_est.append(H2_rate[i] / A_t[i])
187         else:
188             i_est.append(0)
189             H2_est.append(0)
190
191     # calculate flux of H+ based on H2 evolution rate
192     # convert H2 evolution rate to mol/s*m2
193     #   umol to mol (multiply by 10^-6)
194     #   minutes to seconds (divide by 60)
195     #   divide by area (already done up above)
196     #   /cm to /m2 (multiply by 10^4) => 10^-2 overall?
197     H2_mol_m2s = np.multiply(H2_est,10**(-2)/60) # hydrogen gas flux at
        electrode
198
199     # estimate H+ flux: 2*H2 flux:
200     #   assume H2 evolved comes from H+/H3O+, i.e. no OH- is produced
201     Hflux = np.multiply(H2_mol_m2s,Htrans)
202
```

```
203     # USE CORRELATIONS to determine pH at electrode surface VS time
204     # Using Re and Sc as calculated to get Sh number, and get mass x-fer coeff
        . from Sh
205     #   k = Sh * D / l
206     #   Sh = 0.664 Re^1/2 Sc ^1/3
207     #    ShH = 0.664 * (Re**(1/2)) * (Sc_H**(1/3))
208     kH = (0.664 * (Re**(1/2)) * (Sc_H**(1/3)) ) * D_H / l
209
210     # use fluxes above to calculate concentration at surface
211     #       N = k(Cinf - C)
212     # =>    C = (k*Cinf - N)/k
213     # divide by 1000 to get mol/L instead of mol/m^3
214     CH = np.divide(((kH*Cinf_H) - Hflux),kH*1000)
215
216     # calculate pH from CH
217     pH_H = -np.log10(CH)
218     # these data will likely produce errors if CH becomes negative;
219     # they should be noted but may be safely disregarded
220
221     # pH data of interest = before current stopped flowing
222     for i in range(len(lbv_t)):
223         if lbv_t[i]<Iend:
224             plotpH = i
225
226     return CH,pH_H
227
228 ### pH 1 data, 100 mA, 260 mA/cm^2
229 pH_b1 = 1 # bulk pH
230 # Chosen data:
231 #   effective initial current 264mA/cm2
232 I_avg1 = 99.9953686854957 # I_geis_avg, average geis current
233 A1 = 0.379313 # A, area of electrode
234 # important characteristic length: average of two width measurements
235 # multiplied by 0.95 to account for shrinking during reaction
236 l1 = 0.95*2*(1.88+2.1)/2/1000 # meters
237 # labview time and moles
238 lbv_t1 = [-0.044,  0.1  ,  0.289,  0.479,  0.669,  0.858,  1.048,  1.238,
239         1.427,  1.617,  1.807,  1.996,  2.186,  2.376,  2.566,  2.756,
240         2.945,  3.136,  3.325,  3.515,  3.705,  3.895,  4.085,  4.275,
241         4.464,  4.654,  4.844,  5.034,  5.223,  5.413,  5.603,  5.793,
242         5.982,  6.172,  6.361,  6.551,  6.741,  6.931,  7.12 ,  7.31 ,
243         7.5  ,  7.689,  7.879,  8.069,  8.258,  8.448,  8.591,  8.78 ,
244         8.97 ,  9.16 ,  9.35 ,  9.539,  9.729,  9.919, 10.109, 10.299,
245        10.488, 10.678, 10.868, 11.058, 11.247, 11.437]
246 mol_total1 = [0,   3.29348191,   6.90368737,  10.93360689,
247         14.78855327,  19.37882984,  23.61916012,  28.17510651,
248         33.22164218,  37.7078208 ,  42.61371349,  47.73001693,
249         51.44432034,  55.72008821,  59.61047219,  63.11436485,
250         67.00474882,  70.8596952 ,  75.10002548,  78.77889128,
251         82.73904304,  87.08457869,  91.11449821,  94.65493589,
```

```
252          98.47444467, 102.75021255, 105.93848909, 110.28402473,
253         113.4379711 , 117.50332822, 120.69271218, 124.40701559,
254         127.3859888 , 131.13572981, 133.86885468, 137.37385476,
255         140.31739037, 143.96192601, 147.22107774, 150.3395865 ,
256         154.12476511, 157.94427389, 161.62424712, 166.42493444,
257         170.98088083, 175.29097888, 179.00638971, 179.42610378,
258         179.7771575 , 180.33751455, 180.72289844, 180.89897901,
259         181.24892531, 181.70407698, 182.0196931 , 182.4405146 ,
260         182.61548774, 182.58005014, 182.68525552, 183.07063941,
261         183.49146091, 183.84251463]
262 # when current started and stopped (from EC lab, adjusted)
263 Istart1 = 2.0893766446400455
264 Iend1 = 8.6397802891006
265 # mass of Mg
266 umoles_Mg1 = 374.4085579098951 #umole, vs. 0.0091 g
267
268 # ANALYZE DATA
269 CH1,pH_H1 = MassXfer(lbv_t1, mol_total1, Istart1, Iend1,
270                                     I_avg1, A1, l1, umoles_Mg1, pH_b1, Re)
```